UNIVERSIDAD DE EXTREMADURA

TESIS DOCTORAL

Experimental techniques in alpha-particle spectrometry and alpha-gamma coincidence measurements. Application to the study of ^{242}Pu and ^{243}Am

* * *

Técnicas experimentales en espectrometría de partículas alfa y medidas de coincidencias alfa-gamma. Aplicación al estudio del ^{242}Pu y el ^{243}Am

BELÉN CARO MARROYO

DEPARTAMENTO DE FÍSICA

2015

UNIVERSIDAD DE EXTREMADURA

TESIS DOCTORAL

Experimental techniques in alpha-particle spectrometry and alpha-gamma coincidence measurements. Application to the study of ^{242}Pu and ^{243}Am

* * *

Técnicas experimentales en espectrometría de partículas alfa y medidas de coincidencias alfa-gamma. Aplicación al estudio del ^{242}Pu y el ^{243}Am

BELÉN CARO MARROYO

DEPARTAMENTO DE FÍSICA

Conformidad de los Directores:

Fdo: D. Alejandro Martín Sánchez

Fdo: D. Miguel Jurado Vargas

Fdo: D. Eduardo García-Toraño Martínez

2015

A todos los que
siempre habéis
estado a mi lado.

Perseverance is not a long race;
it is many short races
one after another.

Walter Elliot (1888-1958)

Acknowledgments

En primer lugar quisiera dar las gracias a Alejandro, Miguel y Eduardo, por todo su esfuerzo, dedicación e inestimable ayuda. No podría haber encontrado mejores directores. Les estoy especialmente agradecida por inculcarme que el trabajo duro, la constancia y la responsabilidad son herramientas indispensables en el mundo de la investigación científica. He aprendido muchísimo a su lado y su ejemplo ha sido el mejor referente para mi crecimiento profesional, y una influencia muy valiosa a nivel personal. Les admiro y les aprecio, y gracias a ellos esta aventura ha estado cargada de momentos muy especiales que siempre guardaré en mi memoria con cariño.

Mi gran gratitud a mi compañero Mikel por su inestimable ayuda; sus valiosos consejos e ideas han enriquecido mucho esta Tesis. A mi compañera Maite por su generosa e indispensable aportación. Así mismo, a Stefaan que con sus grandes conocimientos y entusiasta colaboración ha contribuido también a este trabajo. Gracias a mis compañeros de laboratorio en la Universidad de Extremadura, Ana y Julián, por su ayuda. Y por último, pero no por ello menos importante, especialísimas gracias a mis compañeros del CIEMAT, Virginia y Marcos, por estar ahí y por sus constantes ánimos.

Cómo no dar las gracias a mi querida familia y amigos. Su confianza y su empuje en los malos momentos han sido imprescindibles para seguir adelante. Muy especialmente a Pablo, por su amor incondicional y su paciencia y ayuda.

Pero si hay alguien a quien yo deba dar las gracias con especial cariño por haber aguantado todo este largo camino y haberme ayudado a llegar hasta aquí, esos son mis padres. Gracias por estar a mi lado, por todo vuestro esfuerzo, paciencia, confianza y amor. Sin vosotros, que siempre habéis sido mi sólido soporte, no lo habría conseguido.

Contents

Summary

Actinides and their natural decay products play a major role in several fields such as the nuclear fuel cycle of fission reactor systems, nuclear medicine, quality control, environmental monitoring, nuclear forensics and safeguards. They are therefore associated with many issues of importance in the fields of health and safety. Extensive measurement and evaluation programmes have been undertaken over the past fifty years to address the need for accurate actinide decay data and recommendations have been issued for a re-evaluation of the actinide data such as α-particle and γ-ray energies and emission probabilities of selected nuclides.

In this work, efforts have focused on the improvement of some techniques useful to the study of alpha-particle emitting nuclides. Three main aspects have been considered: alpha-particle spectrometry, alpha-gamma coincidence measurements and numerical analysis of spectroscopic data. Two spectrometric devices based on ion-implanted Si detectors have been used at the University of Extremadura and Centro de Investigaciones Energéticas, Medioambientales y Tecnológicas (CIEMAT) with the aim of obtaining high-quality alpha-particle spectra suited for accurate spectral analysis. An alpha-gamma coincidence chamber with semiconductor detectors in both channels was also designed and characterized at the University of Extremadura. To improve data treatment and analysis, a new code to fit alpha-particle spectra, called ALFITeX, and a decoding and analysis code, DIGDATA, were developed in this work. The experimental set-ups and the analysis tools developed in this work have been applied to obtain a new set of α-particle emission probabilities of ^{242}Pu by alpha-particle spectrometry, and to study the decay scheme of ^{243}Am, in particular with the determination of several γ-ray emission probabilities from this nuclide using advanced alpha-gamma coincidence measurements.

Resumen

Los actínidos y sus productos de desintegración juegan un papel importante en varios campos, como el ciclo de combustible nuclear en reactores de fisión, medicina nuclear, control de calidad, vigilancia ambiental, ciencia forense nuclear y salvaguardias. Por tanto, están asociados a muchas cuestiones de importancia en el campo de la salud y la seguridad. A lo largo de los últimos cincuenta años se han llevado a cabo extensos programas de medida y evaluación para señalar la necesidad de poseer datos nucleares correctos de actínidos y promulgar recomendaciones para reevaluar datos nucleares de determinados nucleidos, como energías y probabilidades de emisión de partículas alfa y fotones gamma.

Este trabajo se ha centrado en la mejora de algunas técnicas necesarias para el estudio de núcleos emisores de partículas alfa. Se han considerado tres aspectos principales: espectrometría de partículas alfa, medidas de coincidencias alfa-gamma y análisis numérico de datos espectroscópicos. Dos dispositivos espectrométricos, basados en detectores de silicio, se han utilizado en la Universidad de Extremadura y en el Centro de Investigaciones Energéticas, Medioambientales y Tecnológicas (CIEMAT) con el propósito de obtener espectros alfa de alta calidad adecuados para análisis espectrales precisos. En la Universidad de Extremadura también se diseñó y puso a punto una cámara de coincidencias alfa-gamma con detectores de semiconductor en ambos canales. Para mejorar el tratamiento y análisis de datos, en este trabajo se han implementado un nuevo código de ajuste de espectros alfa, llamado ALFITeX, y un programa de decodificación y análisis, denominado DIGDATA. Los dispositivos experimentales y las herramientas de análisis desarrolladas se han aplicado a la obtención de un nuevo conjunto de probabilidades de emisión alfa del ^{242}Pu mediante espectrometría de partículas alfa, y al estudio del esquema de desintegración del ^{243}Am, particularmente determinando varias probabilidades de emisión gamma de este radionucleido utilizando medidas avanzadas de coincidencias alfa-gamma.

Part I

Introduction

Chapter 1

Alpha-particle spectrometry

In the beginning of the 1900's, in the course of the experiments carried out by Rutherford, alpha particles were first identified as the least penetrating of the three types of radiation emitted by naturally occurring materials. Many heavy nuclei, especially those of the natural radioactive series, are unstable against the spontaneous emission of an alpha particle, i.e. ^4He nucleus (two protons and two neutrons). The decay process can be written as

$$ {}^{A}_{Z}X \rightarrow {}^{A-4}_{Z-2}Y + {}^{4}_{2}He \tag{1.1} $$

Alpha decay becomes increasingly important for heavy nuclei because alpha emission is a Coulomb repulsion effect. The disruptive Coulomb force increases as Z^2 while the specific nuclear binding force increases as A. Due to the stability and tightly bound structure of an alpha particle, it is particularly favored as an emitted particle in spontaneous decay.

In theory, alpha decay can occur in nuclei somewhat heavier than nickel (Z=28), but in practice this decay has only been observed in nuclei considerably heavier (the lightest known alpha emitters are the lightest isotopes of tellurium). Some of the typical alpha-particle emitting nuclei are the transuranic nuclei such us ^{241}Am, ^{239}Pu, ^{244}Cm, or some natural radionuclide as ^{226}Ra, ^{210}Po, ^{222}Rn, well known in environmental radioactivity.

Alpha particles are emitted in one or more energy groups which can be considered monoenergetic. The decay is characterized by a fixed energy (Q) which is shared between the alpha particle and the recoil nucleus in a unique way. Alpha-particle energy typically varies between 4 and 6 MeV.

A very strong correlation between the energy and the half-life of the parent exists, the highest energy the shortest half-life. For example, for ^{232}Th (14 x 10^9 y) Q = 4082 keV while for ^{212}Po (300 x 10^{-9} s) Q = 8954 keV.

Alpha-particle spectrometry is used to quantitatively study alpha-particle emitters. It combines experimental techniques (source preparation and detection systems) and analysis methods (deconvolution codes and Monte Carlo simulations). Alpha-particle spectrometry has many practical applications such as decay data measurements, activity determination (including low-level measurements), analysis of nuclear materials or geological studies.

This manuscript presents some technical and analysis improvements in alpha-particle spectrometry and alpha-gamma coincidence measurements. Chapters 1 and 2 summarize the evolution and the state of the art of these two spectrometric techniques. The experimental set-ups used in this research are illustrated in Chapters 3 and 4. Chapter 5 describes in detail the development of a new code to fit alpha-particle spectra, called ALFITeX. The experimental set-ups and the analysis tools described in these chapters have been applied to the measurement of nuclear data of two alpha-particle emitting nuclides: ^{242}Pu and ^{243}Am. The procedures followed and the results obtained are presented in Chapters 6 and 7. Finally, Appendix I presents additional material describing the development and first results of a new approach in spectral fitting using a modified peak shape model using a larger set of peak parameters.

1.1 Spectrometric devices

The best parameters characterizing the quality of a spectrum are the *energy resolution* and the *peak-to-valley ratio*. The energy resolution is defined as the full width at half maximum (FWHM) of a monoenergetic peak either in absolute values or relative values, this is the FWHM divided by the location of the peak centroid H_0 [1].

First devices for alpha-particle spectrometry were based on **magnetic spectrometers**. There are mainly two types of magnetic alpha spectrographs: the *semicircular* and the $1/\sqrt{\rho}$ *double focusing*, where ρ denotes the curvature radium of the alpha-particles. In the first devices the emitted alpha-particles were allowed to pass through a narrow slit and, after a chosen distance, recorded on a photographic plate with its surface normally facing both the source and the slit. The deflecting magnetic field is perpendicular to the particles. The main disadvantage of this kind of spectrographs is the absence of space-focusing. For that reason, the $1/\sqrt{\rho}$ *double focusing* was developed. It is based in the fact that alpha-particles describe oscillatory paths in ρ and in the z-coordinates of the particles when they interact with a magnetic field with rotational symmetry and a field gradient. Alpha-particles starting from a point on this optical axis will return to the axis after certain two "focusing angles". The double focusing takes place after an angle of $\pi\sqrt{2}$ and imposes that the magnetic field decrease as $1/\sqrt{\rho}$ in the vicinity of $\rho = \rho_0$ (the central path).

The energy resolution of the magnetic spectrometers is excellent, obtaining FWHM values lower than 2 keV [2]. However, their detection efficiency is very low. Figure 1.1 shows an alpha-particle spectrum of ^{251}Fm as an example.

Other kind of spectrometric devices are **grid ionization chambers** working in pulse mode. Their detection efficiency is close to 50 % although their intrinsic efficiency is practically 100 %. However, their use is restricted as a consequence of both the limited energy resolution (about 25 keV) and the

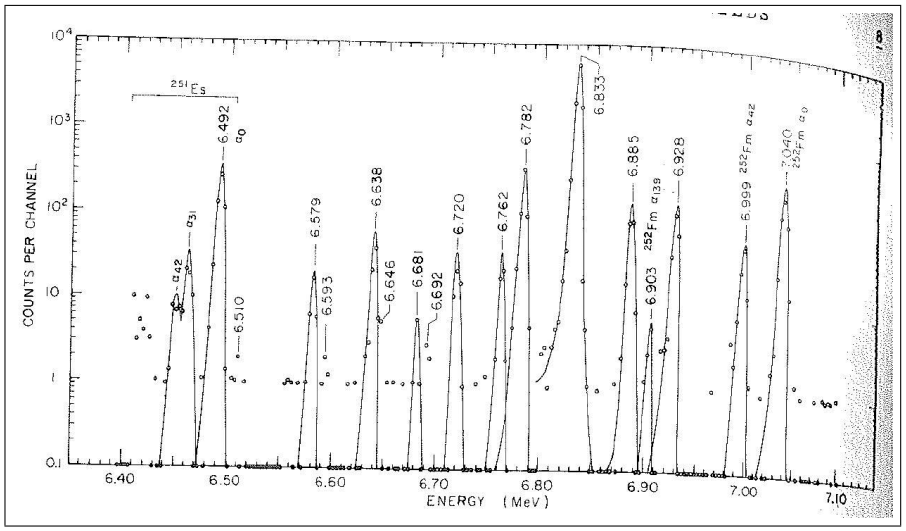

Figure 1.1: Alpha-particle spectrum of ^{251}Fm measured with the Argonne double-focusing magnetic spectrometer. Taken from Ahmad et al. [3].

peak tailing (Figure 1.2). Both facts are due to the high angle of acceptance of the particles emitted by the source. The resolution can be improved by the collimation of the beam by mechanical or electronical ways. Bertolini [4] improved the measured resolution to 11.5 keV reducing the noise contribution and using a mechanical collimator. On the other hand, the collimation reduced the overall detection efficiency to 2 % of 2π sr.

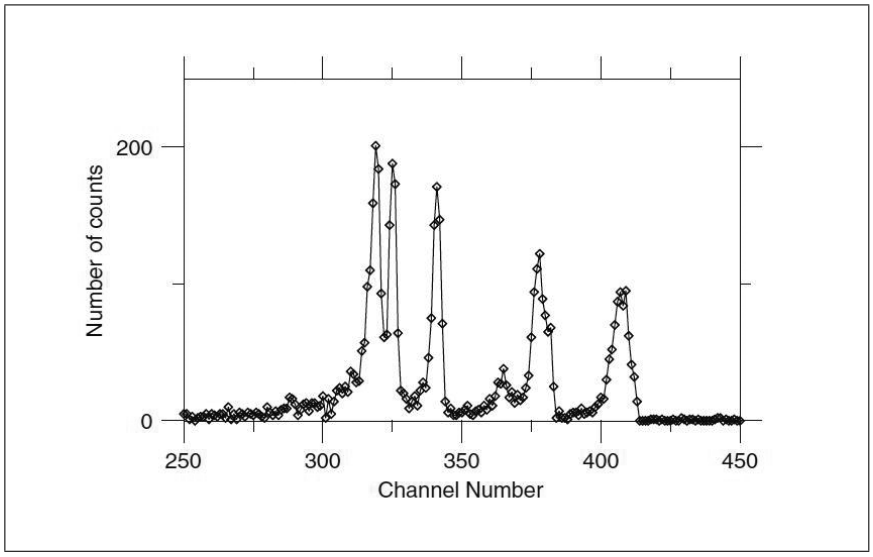

Figure 1.2: Alpha-particle spectrum of a region of the ^{232}U decay chain measured with a grid ionization chamber. Taken from García-Toraño [5].

Ion chambers have an important application to calibrate activity solid sources of different shapes and sizes. An accurate knowledge of backscattering and self-absorption effects in sources are required for this [6]. The *backscattering* is caused by both the large-angle deviations from the incident alpha-

particle direction (due to the cumulative effect of many scattering events) and the Rutherford scattering (i.e. collisions with nuclei). In sources with appreciable thickness, *self-absorption* caused by scattering and energy losses is not negligible [7, 8].

The use of the "electronic collimation" in grid ion chambers [9–11] allows the simultaneous determination of energy and emission angle of alpha particles. This technique allows to classify the detected particles as a function of their emission angle. Combining the expressions of the pulse amplitudes at the anode (V_a) and cathode (V_c), the following value for the cosine of the angle of emission of the particle (ϕ) can be obtained

$$cos\phi = \frac{[1 - (V_a/V_c)\,(G_a/G_c)]}{\bar{X}/d}. \tag{1.2}$$

Here $\bar{X}$ is the distance of the ion's center of mass from the start of the track, d is the distance between anode and cathode and G_a and G_c are the amplification factors corresponding to anode and cathode, respectively. Electronic collimation enhances the resolution but reduces the detection efficiency.

The simultaneous determination of energy and emission angle of alpha particles by grid ionization chambers permits to study the angular distribution of alpha particles and their dependence with backscattering and self-absorption effects in sources [12]. These angular distributions can also be studied by Monte Carlo simulations [13].

Replacing old-technology *surface barrier detectors*, **ion-implanted Si detectors** are nowadays the basic tool for alpha-particle spectrometry. They mainly differ from surface barrier detectors in the manufacturing method. The p-n junction in the first ones is formed by etching the surface and evaporating a thin gold layer promoting slight oxidation of the surface. For ion-implanted detectors impurities are introduced by exposing the surface of the semiconductor to a beam of ions produced by an accelerator.

Ion-implanted Si detectors provide a compromise between energy resolution and efficiency. For small detectors and energies of common alpha-particle emitters, spectra can be measured with a resolution about 8.5 keV [14–16] and lower peak tailing [17]. Since all particles entering the active surface of the detector are registered and backscattering at the detector window is in the order of 10^{-4}, the intrinsic efficiency of these detectors is virtually 100 %.

Detector sizes can vary from 25 mm^2 of active area to several thousands. The entrance window is about 40 nm equivalent Si, although a thinner window (25 nm) can be found in the best models. A reduction of the window thickness decreases the straggling resulting in a better energy resolution and lower tailing, i.e. in improving overall quality of the spectra [18–20]. Figure 1.3 shows a spectrum of ^{241}Am obtained with a passivated implanted planar silicon (PIPS) detector.

Detection of conversion electrons and X-rays is also possible with ion-implanted Si detectors. Since the intrinsic detection efficiency of Si detectors for low energy electrons (in the order of a few tens of keV) is not negligible,

the simultaneous arrival of alpha particles and electrons to the detector will give rise to a single pulse with contribution of both particles. This is the well-known effect of coincidence-summing that will be covered in detail in other section. As an example, Figure 1.4 shows the conversion-electron spectrum of ^{243}Am and ^{239}Np and continuum β^--ray spectrum of ^{239}Np measured with a 50 mm^2 PIPS detector.

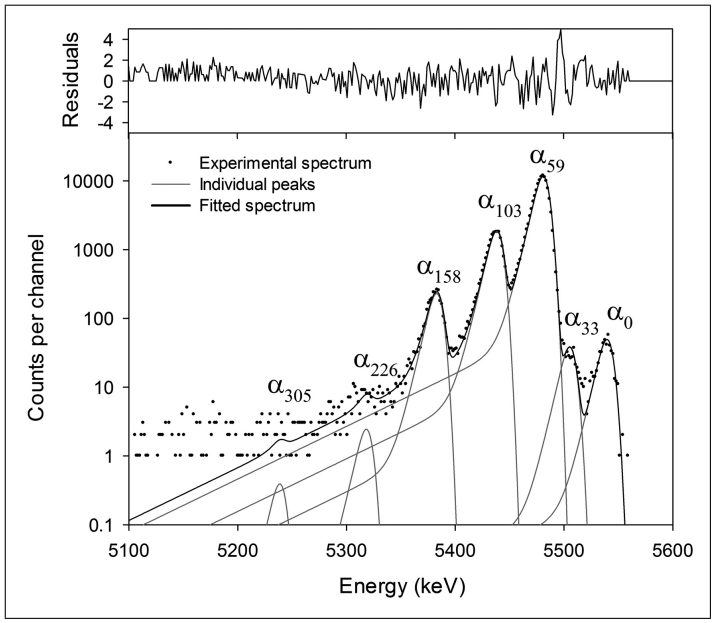

Figure 1.3: Alpha-particle spectrum of ^{241}Am measured with an ion-implanted Si detector. Taken from Caro Marroyo et al. [21].

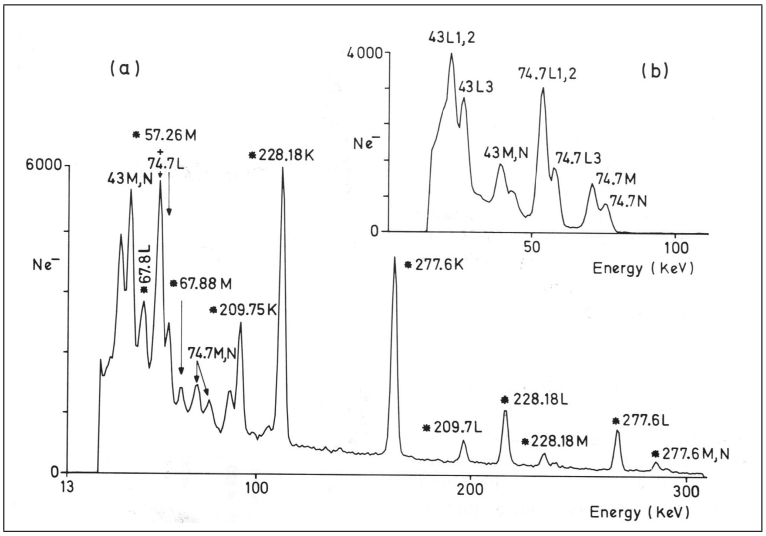

Figure 1.4: (a) Conversion-electron spectrum of ^{243}Am and ^{239}Np and continuum β^--ray spectrum of ^{239}Np measured with a 50 mm^2 PIPS detector. Peaks belonging to ^{239}Np are marked with an asterisk. (b) Conversion electrons measured in coincidence with alpha-particles from ^{243}Am. Taken from García-Toraño et al. [16].

Frolov et al. [22] proposed the measurement of the alpha-particle energies applying the well-known **time-of-flight** method (used with heavy ions and neutrons). The spectrometer is formed by a start and a stop detectors with microchannel plates which are placed in a vacuum chamber (Figure 1.5). The "start" detector ("stop" in the figure) has microchannels plates and electromagnetic focusing for the detection of Auger and emission electrons generated in the alpha decay and then accelerated. The "stop" detector ("start" in the figure) comprises two microchannel plates and detects incident alpha-particles. The time-of-flight spectrometer operates in the "inverse start-stop" mode in which the counting time starts when the alpha-particle is detected by the "stop" detector. Signals from "start" detector are not processed until the alpha-particles are detected. With this operation mode, high alpha-particle counting rates, which could lead to alpha-particle summing coincidences and give rise to a worse energy resolution, are avoided. The alpha particle energy is calculated using the following expression [22]

$$E = \frac{\lambda m_\alpha}{\left(1 - \frac{S^2}{c^2 t^2}\right)^{1/2}} - \lambda m_\alpha, \tag{1.3}$$

where λ is the energy equivalent of unit atomic mass, m_α the alpha-particle mass, c the speed of light, S the flight distance and t the flight time. As an example, a spectrum of ^{244}Cm obtained with a time-of-flight alpha spectrometer and a spectrum of ^{236}Pu measured with the BIMP magnetic spectrometer are shown in Figure 1.6.

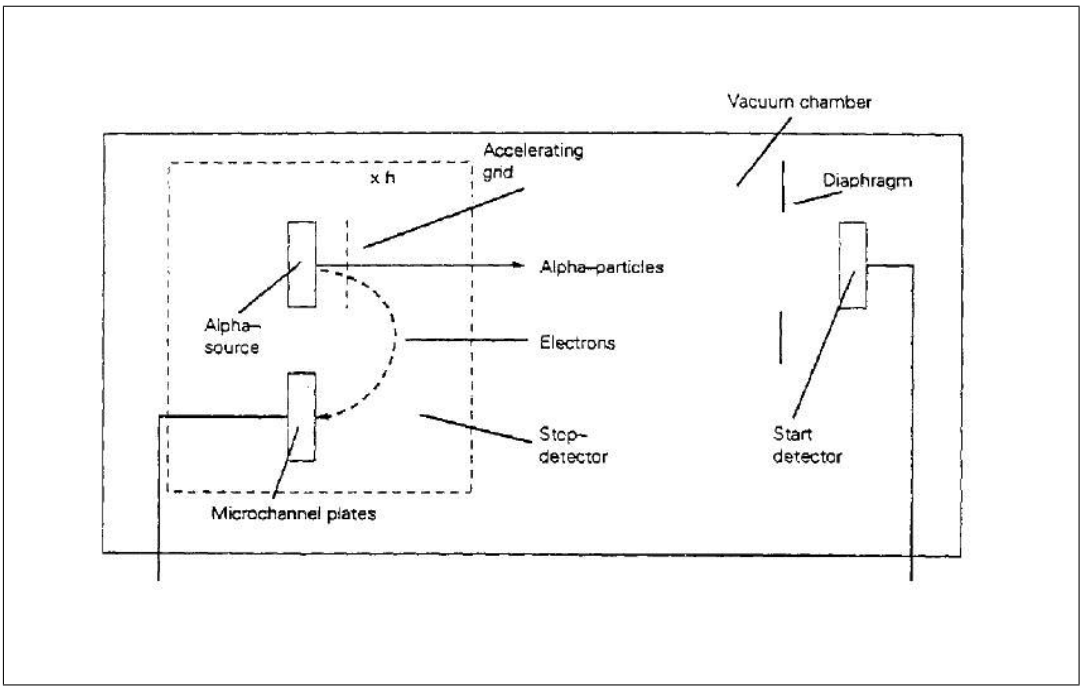

Figure 1.5: Block-diagram of the alpha-particle spectrometer. Taken from Frolov [22].

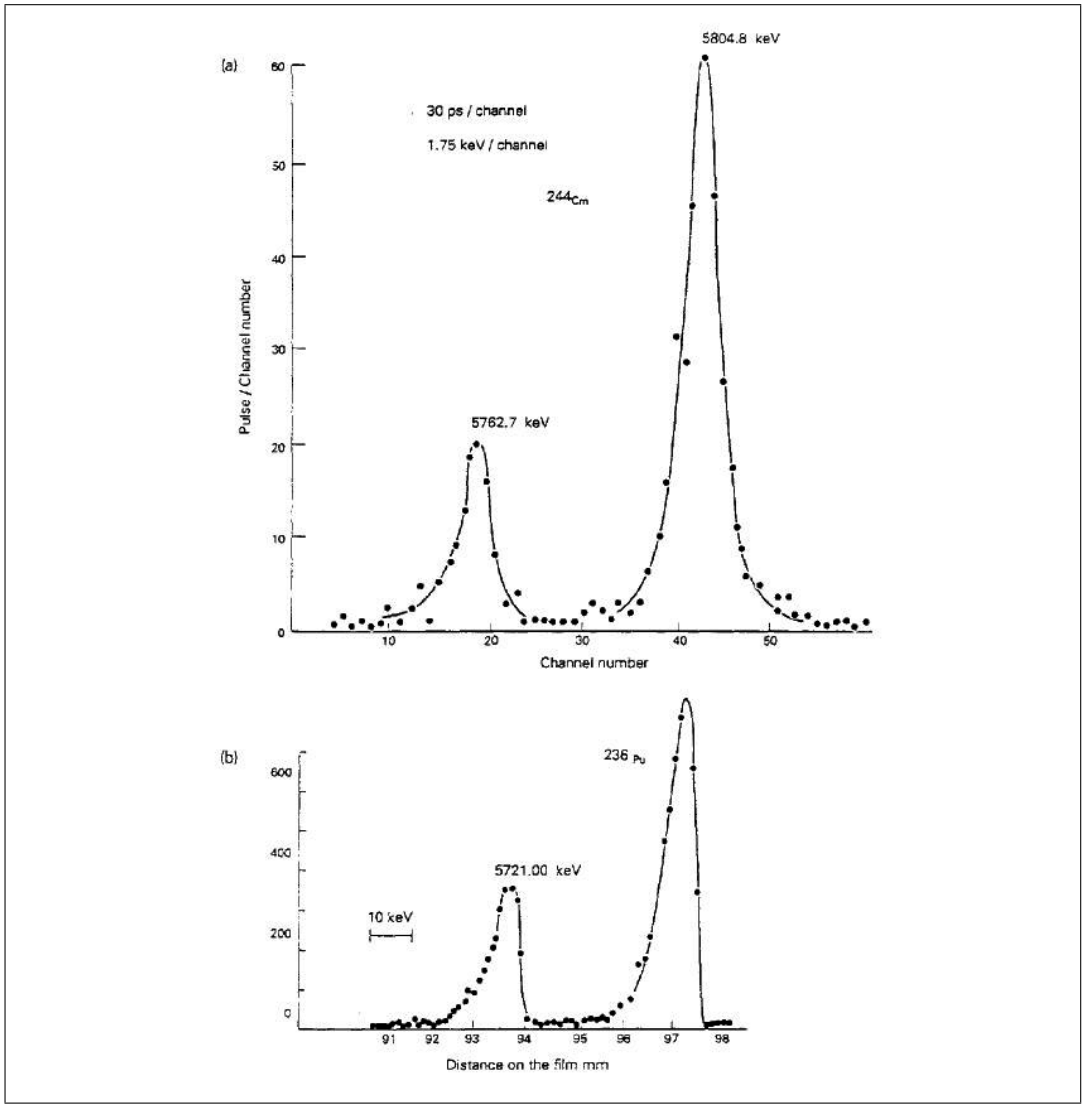

Figure 1.6: (a) Alpha-particle spectrum of ^{244}Cm obtained with the time-of-flight alpha spectrometer. Taken from Frolov [22]. (b) Alpha-particle spectrum published by Rytz and Wiltshire [23].

At the end of 80's **cryogenic detectors**, also called bolometers or microcalorimeters, begun to be used [24]. They are based in the fact that any substance exposed to ionizing radiation will show an increase in temperature caused by the energy absorbed from the incident particles or photons. There are mainly two kinds of temperature sensors: Transition Edge Sensor (TES), based on the temperature-dependent resistance of a superconducting film, and Metallic Magnetic Calorimeter (MMC), which uses a paramagnetic material in a small magnetic field. In this case, the magnetization of the material is measured using a superconducting circuit.

This kind of spectrometric devices have achieved an energy resolution of 1-3 keV for thin layer alpha sources. This represents a remarkable improvement compared with the energy resolution of conventional Si detectors. However, bolometers are extremely complex and expensive due to the electronic components necessary to measure the temperature. Moreover, another inconvenient of this kind of devices is that the signal decays as the sensor cools to its quiescent temperature with time constants in the order of ms [25]. This precludes its use with medium or high counting rates. Therefore further improvements are necessary if this technique is pretended to have practical applications for alpha spectrometry. An example of a ^{241}Am spectrum measured with the cryogenic micro-calorimeter discribed by Ranitzsch et al. [26] is shown in Figure 1.7.

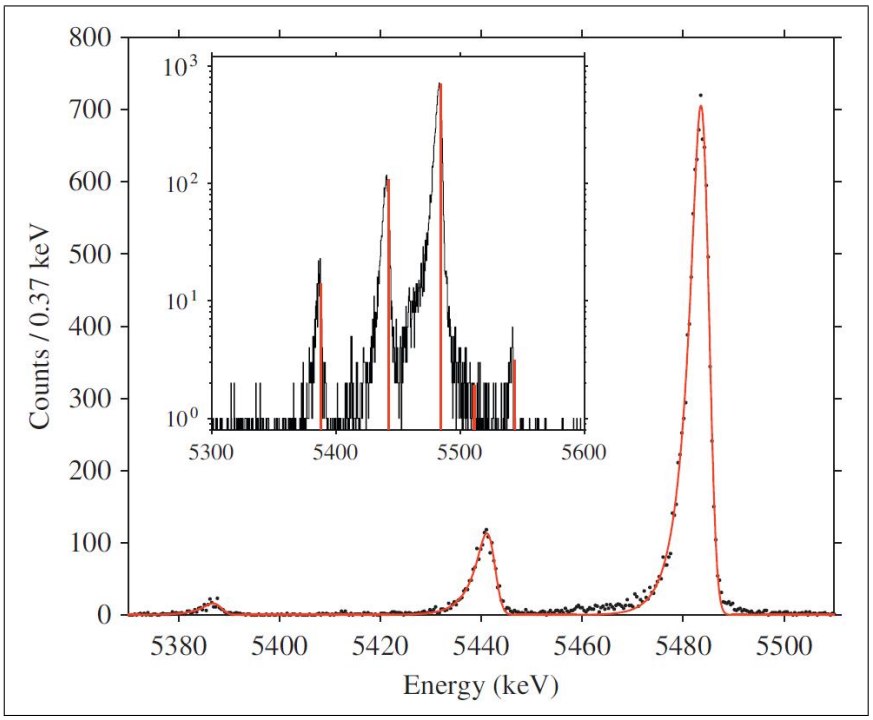

Figure 1.7: ^{241}Am spectrum measured with the set-up described by Ranitzsch et al. [26]. The corresponding FWHM by the dispersion of the convolution function (solid line) is 2.83 ± 0.05 keV.

1.2 Alpha-particle spectrometry with Si detectors

1.2.1 Coincidence summing

An alpha-particle spectrum can be disturbed by conversion electrons from a gamma transition depopulating a level which are detected in coincidence with the alpha particle feeding such level. These summing effects will cause the appearance of additional lines in the spectrum and changes in the relative intensities of the alpha lines. This effect depends on the experimental method used, the detection efficiency, the kind of conversion (K, L, M), the energy of the excited level and the multipolarity of the transition [27]. Coincidences between X-rays and alpha particles can also be produced but their effect is usually smaller than that of conversion electrons.

K conversion will lead to additional alpha lines when the energy summing of the conversion and the Auger electrons is larger than the energy resolution of the detector. The energy difference between the coincidence summing line and the normal alpha line (if the transition to the ground state takes place in one step) is approximately given by the energies of the L_α lines of the daughter products. *L and M conversion* will lead to a change in the relative intensities of alpha decays. The energy of the coincidence summing line will be close to the energy to the ground-state transition.

The effect of conversion electrons has to be carefully evaluated if nuclear decay data are pretended to be obtained. The joint effect of using magnets coupled to the support for sources [28] (Figure 1.8) and measuring under low solid angles reduces, not totally eliminates, coincidence summing pulses. A detailed calculation of the most probable events is then necessary to evaluate these processes. A precise knowledge of the energies and the emission probabilities of the alpha particles and conversion electrons is required in this procedure.

Figure 1.8: Magnets coupled to a support for sources.

1.2.2 Stability of measurements

For long periods of counting time, spectral stability is very important to achieve the best spectral quality. Electronic gain shift versus temperature and time leads a worse overall resolution because of the displacement (derive) of the measured spectra by a number of channels. A pair of examples of the displacement of peak positions for measurements with unstable and stable temperature conditions are shown in Figures 1.9 and 1.10, respectively.

For high counting rates, electronic stabilization systems at the level of the amplifier or the analog-to-digital converter (ADC) can be helpful. However, for low counting rates this kind of devices are useless. The problem can be approached in another way, acquiring a series of short-period spectra and combining them after an appropriate shifting correction.

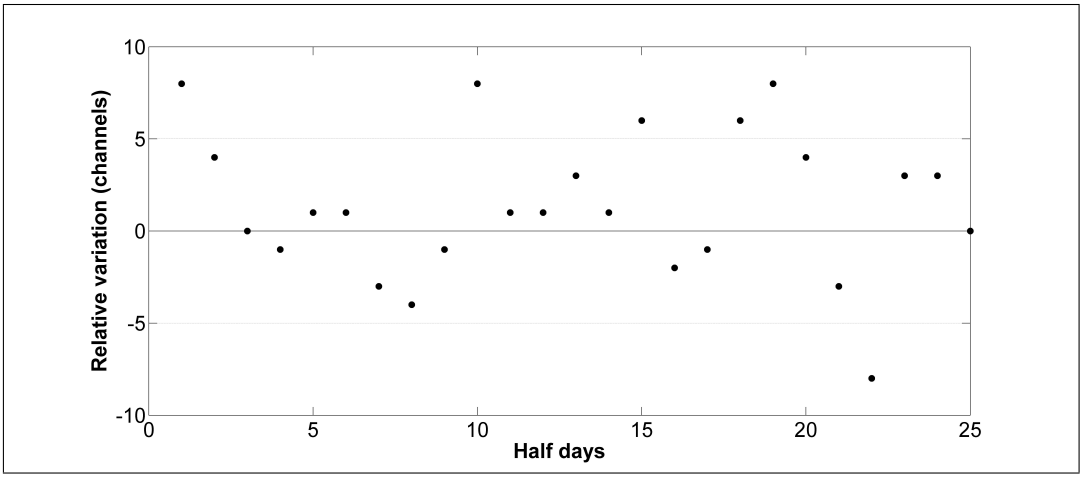

Figure 1.9: Relative variations of the peak position for alpha spectra of ^{243}Am measured with unstable temperature conditions. Measuring time of 14 h.

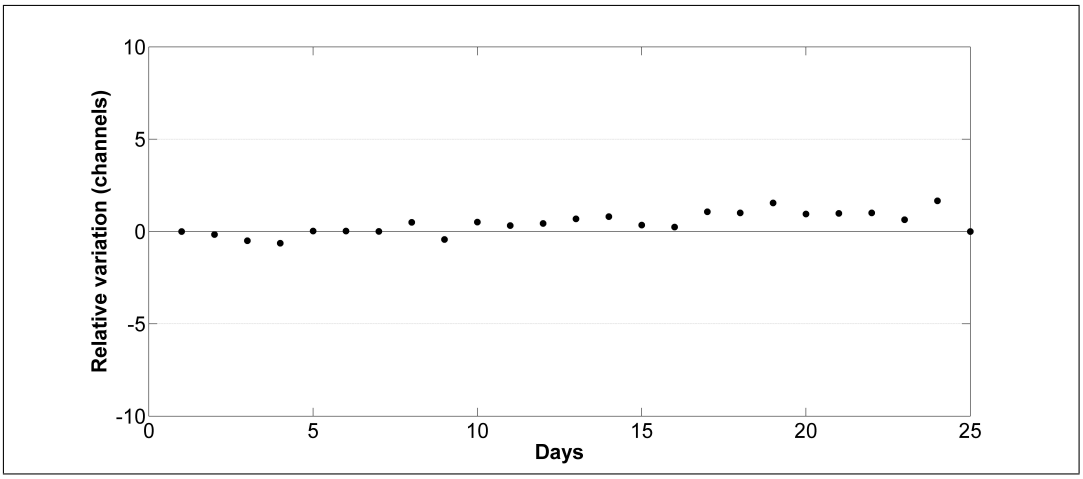

Figure 1.10: Relative variations of the peak position for alpha spectra of ^{242}Pu measured with stable temperature conditions. Measuring time of 24 h.

Pommé and Sibbens [29,30] proposed a numerical gain stabilization method. This method is based on the Stieltjes integral of spectra with a moving average taken as shift indicator. The Stieltjes integral combines the number of counts in each channel with the first derivative in the corresponding channel of the reference spectrum. The criterion for gain stability is that the Stieltjes integral of the spectra compared with a reference spectrum has to remain constant. As a reference spectrum, a sum of a large stable sub-set of spectra can be chosen (with slightly displaced centroid positions). In this way,

$$\int_a^b f_{shifted}(x)f'(x)dx = \frac{f^2(b)}{2} - \frac{f^2(a)}{2}, \tag{1.4}$$

and for a slightly shifted spectrum:

$$\int_a^b f_{shifted}(x)f'(x)dx \approx c\int_a^b \left[\frac{\partial f}{\partial x}\right]^2 dx + \frac{f^2(b)}{2} - \frac{f^2(a)}{2}. \tag{1.5}$$

If data are stored one-by-one in list mode, the gain shift can be reconstructed as a function of time and an individual correction can be made for each counting channel. The local shift is obtained applying an "exponentially moving average". Then data are relocated following a stochastic procedure, taking into account the spectral shape.

Other shifting correction method was proposed by Rubio Montero and García-Toraño [31] based on the properties of the Discrete Fourier Transform (DFT). The implementation of this method is independent of the kind of the analyzed spectra and no particular spectral shape is necessary to be assumed. Mathematically, defining a spectrum as Y_k with $k = 0, ..., N-1$ (where N is the number of channels and Y_k are the counts of the kth channel), the DFT [32] of this spectrum is

$$C_\omega = \sum_{k=0}^{N-1} Y_k exp\left(-i\frac{2\pi\omega k}{N}\right), \omega = 0, ..., N-1, \tag{1.6}$$

where C_ω are complex coefficients and i is the imaginary unity.

If the spectrum is shifted by an integer number of channels m, the transforms of both the original and the shifted spectra are related by

$$Z_\omega = \frac{C_\omega}{C_{S\omega}} = \left|e^{-i\omega m}\right|, \tag{1.7}$$

where $C_{S\omega}$ is the coefficient obtained in the transformation of the shifted spectrum, $|Z_\omega| = 1$ and $\phi(Z_\omega) = \omega m$ is the phase spectrum. The computation of the ratio of their DFT's and the determination of m from the fitting of the phase spectrum will be carried out to determine the relative displacement between two spectra. An example of ^{244}Cm get from Rubio Montero and García-Toraño [31] is shown in Figure 1.11.

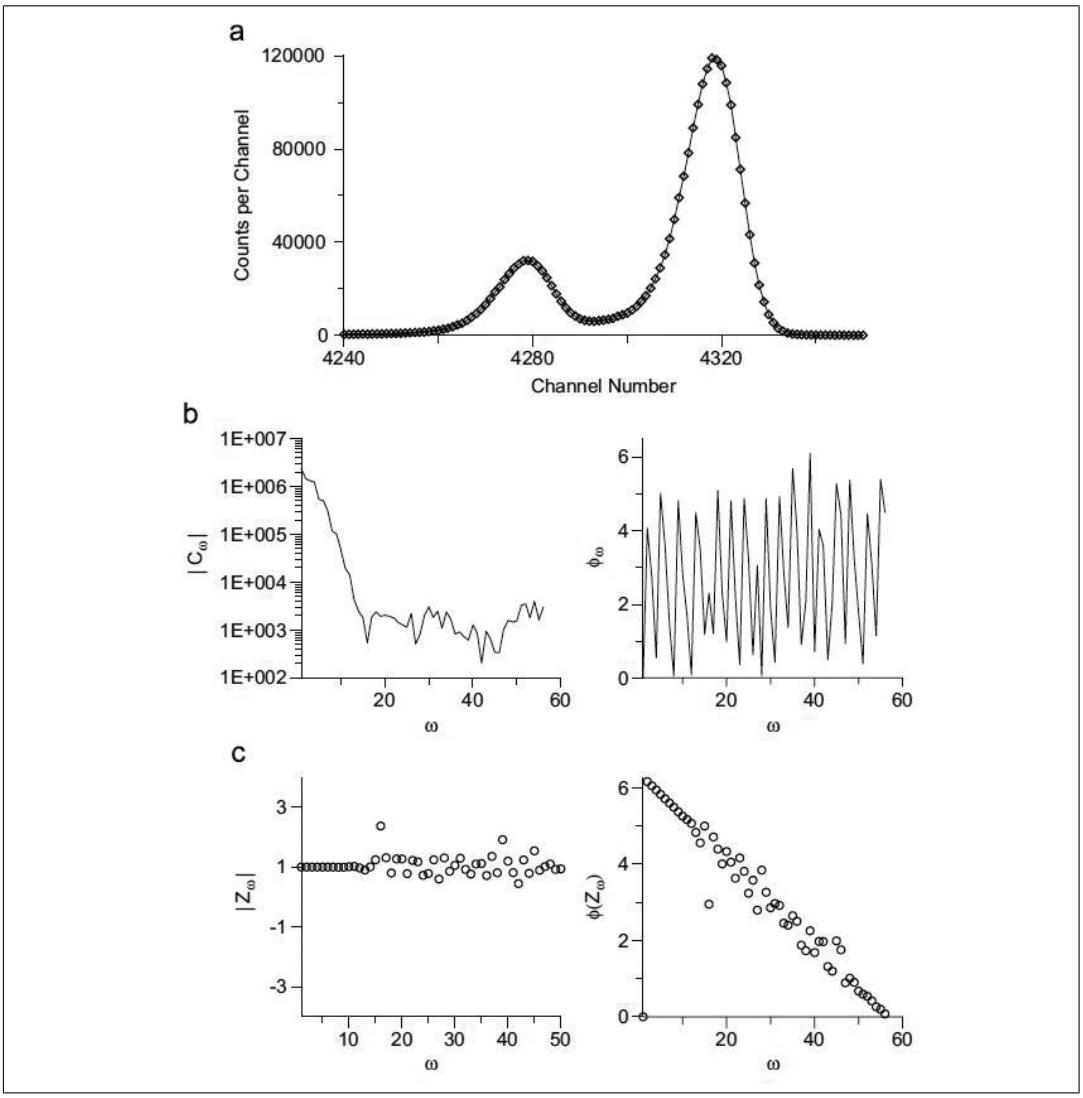

Figure 1.11: (a) Alpha-particle spectrum of ^{244}Cm measured for 2 days. (b) Sum spectrum obtained by combining 50 similar spectra using the method explained above. (c) Typical amplitude and phase spectra of the Z function, defined in Eq. 1.7, which is used to determine the channel shift correction. Taken from Rubio Montero and García-Toraño [31].

1.2.3 Energy determination

Although in alpha-particle spectrometry with Si detectors the efficiency calibration is reduced to a geometrical problem, the energy calibration presents an inherent non-linearity. The pulse height of the signal registered by an analog-to-digital converter (ADC) is not proportional to the alpha-particle energy. The measurement of the alpha energy with this kind of detectors has to be seen as a particular case of a more general problem, the interaction of light ions in Si [33].

The processes involved in the detection of alpha particles were described by Steinbauer et al. [14,15]. The origin of the nonlinear behavior of the system are some energy-loss effects, which have a non-Gaussian energy dependence [34,35]. Before leaving the source, an alpha particle with an initial energy E will loss a fraction of its energy E_s which depends on the source thickness. Then the alpha particle will impinge the detector with an effective energy given by $E - E_s$.

Once the particle reaches the detector, another amount of energy will be lost at the detector entrance window and dead layer (E_w). The window thickness has to be determined in order to suitably characterize the detector. Two methods can be followed to obtain this parameter: Rutherford Backscattering Spectrometry (RBS) [36] and the calculation of the energy shift of the peaks in a spectrum measured with a collimated alpha source with the detector being rotated at several angles [17]. The energy distribution of the ions entering the sensitive volume of the detector is determined by the the electronic energy-loss straggling (Gaussian) and the variations of the dead layer thickness (possible non-Gaussian) [18, 19].

The amount $E-E_s-E_w$ will be available to contribute to signal production although a fraction will still be lost in non-electronic interactions (which will not contribute to pairs production). The energy distribution for the production of electron-hole pairs and lattice vibration is found to be non-Gaussian. For that reason, alpha spectra have their peculiar asymmetric shape. For the creation of electron-hole pairs, the energy distribution is Gaussian. These contributions have been recently applied to reproduce alpha-particle spectra measured with silicon detectors, combining analytical and simulation techniques [37]. Lennnard et al. [38] suggested that the mean energy necessary to create electron-hole pairs depends on the charge carrier density in the ionization track and thus on stopping power (which also contributes to the non-linear response of silicon detectors). Finally, the last contribution to the energy resolution is due to the electronic noise of the amplifier system, whose energy distribution is Gaussian.

Figure 1.12 represents the energy defect versus the kinetic energy. It can be seen that at low energies the electronic energy loss in the dead layer dominantly contributes, whereas at high energies the main contribution is due to the creation of crystal damage and lattice vibrations.

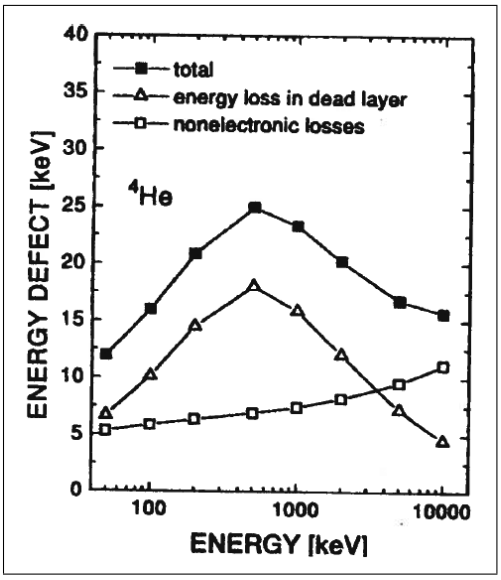

Figure 1.12: Energy defect for alpha-particles in a silicon detector due to energy loss in a dead layer of 48 nm and due to crystal damage and lattice vibrations (calculated with TRIM). Taken from Steinbauer et al. [14].

1.3 Deconvolution of alpha-particle spectra

Alpha-particle spectra measured with semiconductor detectors are often complex, showing several overlapping emissions or groups of peaks. Several factors contribute to difficult the analysis of spectra. The most important ones are the limited energy resolution of Si detectors ($\approx$ 8.5 keV in optimum conditions), the high stopping power of alpha particles (which deteriorates the energy resolution), coincidence summing between alpha particles and conversion electrons and the fact that most nuclides decay by multiple alpha branches. Source preparation, detector size, and solid angle of the measurement, among other factors, also have a strong influence on spectral parameters such as energy resolution and peak tailings.

Therefore, the deconvolution of multiplets is necessary in order to obtain accurate and reliable values for the peak positions and areas. This can be done in a variety of manners, from single channel counting to a full non-linear fitting. If the degree of overlapping of peaks in the spectra is high, complex algorithms are usually needed. A typical peak model depends on two groups of parameters, the peak position and area and a set of "shape parameters" which are used to adapt the model to the particular conditions of the spectrum being analyzed. A good analytical peak model should closely follow the shape of real alpha peaks. Here, a compromise is necessary between the complexity of the model and the performance that can be expected.

1.3.1 Numerical peak shapes

Different peak models have been proposed for the analysis of alpha-particle spectra. The assumption of all peaks in the same spectrum have similar shapes

is one of the basic premises in spectral analysis. Differences can be only observed if spectra are obtained in optimal conditions. Therefore, the peak shape parameters can be kept constant for a given spectrum.

Considering the constant shape of the peaks all over the spectrum, one of the first solutions proposed was the use of a monoenergetic isolated peak as a model to which compare the others. For spectra where this kind of peak exists, this is a simple but efficient solution [39]. However, the fitting process can be unstable, unless some extra cautions are taken, because of the calculation of derivatives are usually needed in the optimization process.

Most of proposed models are based on the convolution of a Gaussian curve with additional functions to describe the strong asymmetry found in the low energy side of alpha-particle peaks. The most important models are described in the following.

- *Model proposed by Trivedi (1969)* [40].

  This model is based on a modified Gaussian:

$$Y_x = A\,exp\left\{-\frac{\left(\frac{x-m}{\sigma}\right)^{t_1}}{1+\{[1-sgn(x-m)]\times[s(x-m)]\}^{t_2}}\right\}, \tag{1.8}$$

  where A is the peak amplitude and m the peak position. The parameter s is obtained from $Q = exp\left(\frac{1}{2\sigma^2 s^2}\right)$. This expression links the peak-valley parameter Q (experimentally determined) with σ (the peak width) and s.

- *Model proposed by Baba (1978)* [41].

  Two separate functions were proposed to describe the peak shape. In the central and high energy region

$$Y_x = A\ \times\ exp\left[-\frac{(x-m)^2}{2\sigma^2}\right], \tag{1.9}$$

  and in the low energy region

$$Y_x = exp\left[a\,(x-m)^3 + b\,(x-m)^2 + c\,(x-m) + d\right], \tag{1.10}$$

  where a, b, c and d are shape parameters.

- *Model proposed by Watzig and Westmeier (1978)* [42].

$$Y_x = A\left\{\frac{exp\left[-b\,(x-m)^2\right] + t\,ft(x,m)}{1+HTAIL}\right\}, \tag{1.11}$$

  where t is a parameter which characterizes the tail amplitude and

$$ft(x,m) = \frac{1}{\sqrt{b}} exp\left[d\,(x-m) + \frac{d}{4b}\right] \times FI1\left[\sqrt{b}\left(x - m + \frac{d}{2b}\right)\right] \quad (1.12)$$

describes the tailing structure of the peak. $b = \frac{4ln(2)}{FWHM}$ and $FI1$ includes the error function.

- *Model proposed by Basova (1979)* [43].

  This model combines two exponentials:

$$Y_x = A\left\{exp\left[\frac{x-m}{\sigma\,(1-\beta)}\right] - exp\left[\frac{m-x}{\sigma\,(1+\beta)}\right]\right\}^{-2}, \quad (1.13)$$

  where β is the asymmetry parameter.

- *Model proposed by García-Toraño and Aceña (1981)* [44].

  Their proposed curve consists of two branches. For the high energy region two Gaussians are used, being the second one the responsible of the asymmetry:

$$Y_x = A\,exp\left[-\frac{(x-m)^2}{2\sigma^2}\right] + B\,exp\left[-\frac{(x-m+p\sigma)^2}{2\sigma^2}\right], \quad (1.14)$$

  and for the low energy region a hyperbolic equation was proposed.

$$Y_x = \frac{K}{(a-x)^2} + C, \quad (1.15)$$

  where $p = 2\sqrt{2ln2}$, being $p\sigma = FWHM$ of the Gaussians; K, a and t are characteristic parameters, and C represents a constant low energy tail.

- *Model proposed by L'Hoir (1984)* [33].

  This model, which formed the basis for subsequent developments, is based on the convolution of a Gaussian and a truncated exponential:

$$Y_E = \lambda\,exp\left[\frac{\left(E-\bar{E}\right)^2}{2\sigma^2}\right] \otimes exp\left(\frac{E}{E_0}\right) H(-E), \quad (1.16)$$

  where $H(-x)$ is the Heaviside step function, E is the energy and λ is a constant factor.

- *Model proposed by Bortels and Collaers (1987)* [45].

  In this case the convolution of a Gaussian curve with two left-handed exponentials in the low-energy-tail region (or three if the tailing structure becomes more important) was proposed. Here

$$Y_x = \frac{A\sigma\sqrt{2\pi}}{2}\left[\eta_1\tau_1 exp\left((x-m)\,\tau_1 + \frac{\sigma^2\tau_1^2}{2}\right)\right.$$
$$\times erfc\left(\frac{1}{\sqrt{2}}\left(\frac{x-m}{\sigma}+\sigma\tau_1\right)\right)$$
$$+\,(1-\eta_1)\,\tau_2 exp\left((x-m)\,\tau_2 + \frac{\sigma^2\tau_2^2}{2}\right)$$
$$\left.\times erfc\left(\frac{1}{\sqrt{2}}\left(\frac{x-m}{\sigma}+\sigma\tau_2\right)\right)\right], \tag{1.17}$$

where $erfc$ is the complementary error function, η_1 is the weight of the first exponential (with $1-\eta_1$ being the weight of the second exponential) and τ_j the exponential parameters (j = 1, 2).

- *Model proposed by Koskelo et al. (1996)* [46].

  This model proposes the following curve:

$$Y_x = A\,exp\left[\frac{T\,(2x-2m+T)}{2\sigma^2}\right], \tag{1.18}$$

  where T is the tailing parameter.

- *Model proposed by García-Toraño (1996).* [47]

  In a more recent model, García-Toraño modified the central and high-energy part (maintaining the hyperbolic branch for the low energy region) of his curve [44]

$$Y_x = h \times P\left(A, \frac{x-m}{\sigma}\right)$$
$$\times\left\{H\,(q-x)\left[\frac{k_2}{(m+a-x)^{t_2}}\right]\right.$$
$$\left.+\,[1-H\,(q-x)]\,exp\left(\frac{x-m}{t_1}\right)\left[1+\,f\,exp\left(-k\frac{x-m}{t_1}\right)\right]\right\}, \tag{1.19}$$

  where P is the incomplete gamma function

$$P\,(A,z) = \frac{1}{\Gamma(A)}\int_0^z e^t t^{A-1}dt,\ z = \frac{x-m}{\sigma}. \tag{1.20}$$

  This part of the curve is joint to the hyperbolic branch in the point $q = m-4\sigma$. h and m are the height and the position of the peak. f, k_1 and t_1 are the shape parameters for the high-energy region while t_2 and a are the parameters for the low-energy region. A and σ are common to both regions. Constraining the continuity of the total function, the parameter k_2 can be calculated. And the number of independent parameters can also be reduced imposing the continuity of the derivatives.

- *Model proposed by Lozano et al. (2000)* [48].

  In a semilogarithmic representation, an alpha peak can be described as a positive-slope straight line at the left edge of the peak, a parabolic curve at the right edge and, attaching these two parts, a cubic splines curve. These three regions are expressed as

$$S_L(E,x) = (Z_1 - Z_1' X_1) + Z_1' x, \tag{1.21}$$

$$\begin{aligned} S_S(E,x) = & \left(\frac{X_{j+1}-x}{X_{j+1}-X_j}\right) Z_j + \left(\frac{x-X_j}{X_{j+1}-X_j}\right) Z_{j+1} \\ & + \left[\left(\frac{X_{j+1}-x}{X_{j+1}-X_j}\right)^3 - \left(\frac{X_{j+1}-x}{X_{j+1}-X_j}\right)\right] \\ & \times \frac{(X_{j+1}-X_j)^2 Y_j''}{6} + \left[\left(\frac{x-X_j}{x_{j+1}-X_j}\right)^3\right. \\ & \left. - \left(\frac{x-X_j}{X_{j+1}-X_j}\right)\right] \frac{(X_{j+1}-X_j)^2 Y_{j+1}''}{6}, \ (X_1 \le x \le X_n), \end{aligned} \tag{1.22}$$

$$S_R(E,x) = -\frac{1}{2\sigma^2}x^2 + \left(Z_n' + \frac{X_n}{\sigma^2}\right) + \left(Z_n - \frac{X_n^2}{2\sigma^2} - Z_n' X_n\right), \tag{1.23}$$

  where Y_j are the ordinates on a logarithmic scale and Y_j'' are the second derivatives at the knots X_j.These knots are defined as $X_j = E + r_j$, where r_j gives the relative position of the knots with respect to the energy of the peak.

  For NP peaks and on the linear scale, data distribution can be expressed as

$$Y_x = \sum_{k=1}^{NP} H_k e^{S(E_k,x)}. \tag{1.24}$$

- *Model proposed by García-Toraño (2003)* [49].

  This line shape is a simplification adapted in the development of WinAlpha code [50]. The analytical function consists of two branches. In the main part of the peak a pure Gaussian is used above the maximum and a second Gaussian with a different resolution parameter described the region below the maximum.

$$Y_x = A\, exp\left[-\frac{(x-m)^2}{2\sigma_{l,r}^2}\right]. \tag{1.25}$$

For the low energy region, the following function starts at a point $m - n\sigma$ $(1 < n < 2)$

$$Y_x = B\, exp\left[-C\left(\frac{x-m}{\sigma_d}\right)^{1/2}\right]. \tag{1.26}$$

$\sigma_{l,r}$ are the resolution values for the left and right regions of the peak, respectively. Hence, the ratio $\frac{\sigma_l}{\sigma_r}$ describes the asymmetry of the peak. $B = A\left[exp\left(-n^2/2\right)/exp\left(-2n^2\right)\right]$ and $C = 2n^{3/2}$. n, σ_l and σ_r can be considered constant for all peaks in a spectrum.

1.3.2 Fitting process

χ^2 statistics

The alpha-particle spectrum shape can be modeled following a least square fit to the experimental data. If $y\{x = 1, \ldots n\}$ is the number of counts stored in channel x, the spectrum is supposed to be formed by m peaks, and the peak shape is given by the function f_x, then any channel in the alpha spectrum can be approximated by a linear combination of the values predicted by the model for the m component peaks as

$$Y_x \approx \sum_{i=1}^{m} I_i f_x^i, \tag{1.27}$$

where f^m is the contribution of the m-th peak model and I_m its relative intensity. The function Y depends on an array $\mathbf{a}$ of nonlinear parameters $a_k (k = 1, \ldots, N)$ corresponding to the m peak areas and positions and the line shape parameters. The best parameters are those which minimize a function χ^2 defined as

$$\chi^2 = \sum_x \sum_{i=1}^{n} \left(\frac{y_i - Y_x(\mathbf{a})}{\sigma_i}\right)^2. \tag{1.28}$$

The variance can be taken in different forms leading a family of χ^2 statistics [51].

- *Neyman's definition:*

$$\chi^2_N = \sum_x \sum_{i=1}^{n} \frac{\left(y_i - Y_x(\mathbf{a})\right)^2}{y_i}, \tag{1.29}$$

  where $\sigma_i = y_i$.

- *Pearson's definition:*

$$\chi^2_P = \sum_x \sum_{i=1}^{n} \frac{\left(y_i - Y_x(\mathbf{a})\right)^2}{Y_x}, \tag{1.30}$$

where $\sigma_i = Y_x$.

Both chi-squares can present biased results, but Pearson's chi-square can be used correctly in an iterative way. In the study carried out by García-Toraño [52] Pearson's definition was obtained as the only safe chi-squares for all kind of spectra.

In order to obtain unbiased results, another good approach is to apply the Maximum Likehood Estimation statistic for the Poisson distribution:

$$\chi^2_\lambda = \sum_x 2 \sum_{i=1}^{n} \left[Y_x - y_i - y_i ln \left(\frac{Y_x}{y_i} \right) \right] \tag{1.31}$$

In which the last term is set equal to zero for $y_i = 0$.

The Maximum Likehood method can also be applied to the Gaussian distributed data:

$$\chi^2_{\lambda,G} = \chi^2_P \sum_x \sum_{i=1}^{n} \left\{ ln \frac{Y}{y'_i} - \frac{[y_i - y'_i]^2}{y'_i} \right\}, (y_i > 0) \tag{1.32}$$

With $y'_i = \sqrt{1/4 + y_i^2} - 1/2$.

Another statistic studied by Pommé and Keightley [51] with unbiased results is that proposed by Mighell:

$$\chi^2_\gamma = \sum_x 2 \sum_{i=1}^{n} \frac{[y_i + min\,(y_i, 1) - Y]^2}{y_i + 1} \tag{1.33}$$

Optimization methods

The process of optimization is complicated by the fact that almost every line shape models are non-linear, which involves iterative methods requiring heavy numerical analysis procedures. There are many optimization methods to search the minimum value of χ^2 [53].

The so-called Direct Search Methods are useful when the analytical calculation of the partial derivatives is difficult or not suitable. They are less efficient in terms of convergence, but are very useful to provide a set of values to feed a more efficient algorithm.

- *Nelder and Mead method. Simplex.*

  This method is based in building the simplest nondegenerate polyhedron with n+1 vertices from $\Re^n$ (where the initial approximations of the optimum point are located). This polyhedron is called a simplex. A set of initial values is assigned to the vertices to form the initial simplex and some rules are given to derive new vertices to generate a sequence of simplices (each being generated from the preceding) by evaluating the function that is being optimized.

- *Powell method.*

  It is a gradient method in which an extensive use is made of line search procedures whose directions are changed by an efficient algorithm. The method minimizes the function by a bi-directional search along N search vectors (which are simply the normals aligned to each axis), in turn. The new displacement vector becomes a new search vector meanwhile the search vector which was most successful is deleted from the search vector list. The algorithm iterates an arbitrary number of times until no significant improvement is reached.

- *Davidon, Fletcher and Powell (DFP) method.*

  It is considered one of the best quasi-Newton methods. It generalizes the secant method to a multidimensional problem finding the solution to the secant equation that is closest to the current estimate and satisfies the curvature condition. This method requires the evaluation of the gradient of the function which is being minimized, which is often a critical point in many calculations, especially if analytical expressions are not available.

If the partial derivatives of χ^2 are available, there are some methods which provide fast convergence if initial values are suitable.

- *Newton-Raphson method.*

  This method is a root-finding algorithm that uses the first few terms of the Taylor series of the function in the vicinity of a suspected root. It starts with an initial guess which is reasonably close to the true root, then the function is approximated by its tangent line, and the x-intercept of this tangent line is computed. This x-intercept will typically be a better approximation to the function's root than the original guess, and the method can be iterated.

- *Levenberg-Marquardt method.*

  This iterative method interpolates between the Gauss-Newton algorithm and the steepest descent method. Given a differentiable function $f(x)$ and an initial guess x_1, the steepest descent algorithm iteratively moves the guess toward lower values of the function by taking steps in the direction of the negative gradient $-\nabla f(x)$. The method typically converges to a local minimum, but may rarely reach a saddle point, or not move at all if x_1 lies at a local maximum.

  The Levenberg-Marquardt method acts more like a steepest descent method when the parameters are far from their optimal value and more like the Gauss-Newton method when the parameters are close to their optimal solution. As for any iterative method, the algorithm converges only if the set of initial parameters is already somewhat close to the final solution. The evaluation of the uncertainties of the parameters is based on the covariance matrix obtained in the fitting process.

1.3.3 Deconvolution codes

There are several codes to perform the analysis of alpha spectra. They can roughly be divided into two groups: a set of commercial programs, with a user-friendly approach, usually in a Windows environment, with great advantages and some drawbacks; and a second group, developed by researchers mainly for their own use, aimed at obtaining the best possible accuracy in the results, not well suited for the use as general-purpose fitting programs. A summary of the major fitting codes is presented below in Table 1.1.

The first step in the development of a new fitting software is the election of a line shape model. A compromise must be accepted between the complexity of the model and the fitting performances. A peak model with a large number of shape parameters will adapt very well to many different experimental situations, but the fitting process can become tedious or even impossible in some circumstances, e.g. in spectra with poor statistics and many peaks.

There are also several possibilities for the optimization process. The fitting procedure must be stable, so a suitable set of initial parameter values must be provided to the algorithm. In most cases users will not be able to introduce good values, so it will be necessary that the program does it itself. This step will be crucial, since the overall performance of the code relies on the optimization process.

Commercial codes	From researchers
AlphaVision 1.20 (EG&G Ortec, USA)	GEAL [39]
	ALFUN [42]
Alps 4.21 (Westmeier GmbH, Germany)	The code developed by Baba [41]
	NOLIN [44]
WinnerAlpha 4.0f5 (Eurisys Meures, France)	ALFA [54]
	MULT [55, 56]
Genie-2000 (Canberra industries inc., USA)	ALPACA [57]
	FITBOR [58]
	COLLEGRAM [59]
	FITBLO [60]
	The code developed by Koskelo et al. [46]
	ALFIT [61]
	WinAlpha [50]
	ALPHA [30]

Table 1.1: Summary of the major deconvolution codes for alpha-particle spectrometry.

Chapter 2

Coincidence spectrometry

In many cases, the disintegration of a nuclide by alpha or beta emission leaves the daughter nuclide in an excited level. As an example, Figure 2.1 shows the decay scheme of ^{226}Ra, an alpha-particle emitting nuclide. If the populated level is excited, de-excitation can take place by the emission of a gamma photon or the alternative process of internal conversion, in which the nuclear excitation energy (E_{ex}) is transferred directly to one of the atomic electrons. This electron then appears with an energy given by

$$E_{e^-} = E_{ex} - E_b, \tag{2.1}$$

where (E_b) is its binding energy. This expression indicates that the internal conversion process has a threshold energy equal to the electron binding energy in a particular shell. These conversion electrons are labeled according to the electronic shell from which they are emitted: K, L, M, etc. After the conversion electron is emitted, the atom is left with a vacancy in one of the atomic orbitals. Electrons from higher shells fill this vacancy and thereby characteristic X-rays or Auger electrons can also be observed following conversion electrons [62].

In most cases, the de-excitation of excited levels by gamma photons or conversion electrons befalls in very short times, in the order of nano or picoseconds. Therefore this emission can be considered simultaneous with the alpha or beta particle from the experimental point of view. In this case, both emissions are considered coincident.

Coincidence measurements are widely used in the study of **decay schemes**. Most of the schemes for the heavy nuclei were obtained using this methodology [63], [64]. This technique is also used to check or verify some nuclear data, such as internal conversion factors or branching ratios [65]. Another nuclear data that can be determined using the coincidence technique is the lifetime of an excited level [66], [67]. This can be done creating the time spectrum of coincidence events between emissions that populate the excited state and the radiations that de-excite that level.

One of the common applications of coincidence measurements is the determination of the **absolute activity** of a radioactive source [68], [69], [70]. The activity is calculated using an expression which only depends on the individual

counting rates, r_1 and r_2, and the true coincidence rate, $r_{true\ coin.}$:

$$A = \frac{r_1 \times r_2}{r_{true\ coin.}}. \tag{2.2}$$

At shown in Equation 2.2, the knowledge of the detection efficiencies of either detectors is not necessary to calculate the activity.

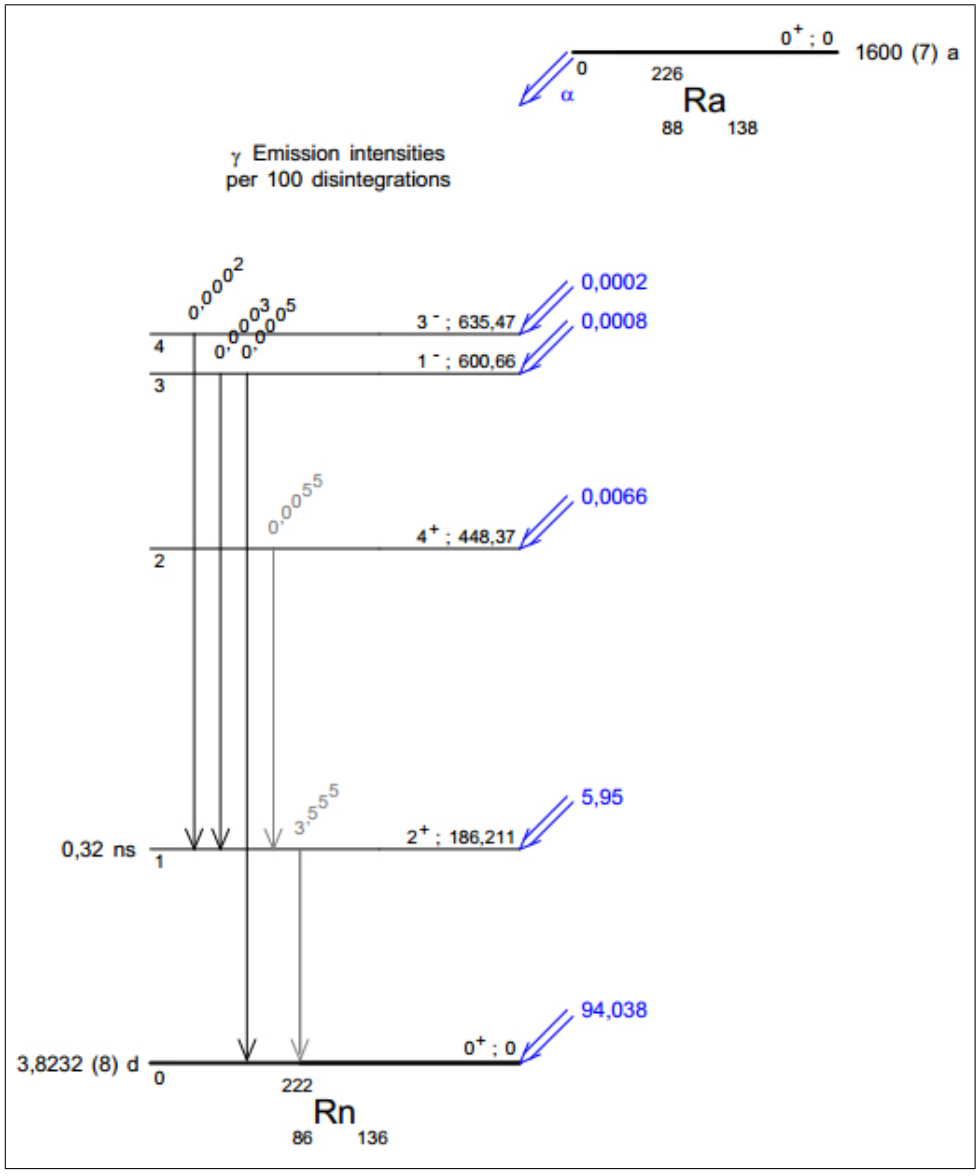

Figure 2.1: Decay scheme of ^{226}Ra. Taken from the Decay Data Evaluation Project [71].

In some cases, the structures of interest in spectral measurements are blurred by a number of other contributions whose influence could be reduced using an adequate coincidence technique; such is the case of small peaks overlapped by stronger emissions that do not have a common coincident radiation. In some situations, this can allow the identification of certain nuclides with very low detection thresholds.

Other application of coincidence measurements is the study of **angular correlations** between alpha or beta particles with gamma rays [72] or for gamma radiations in cascade [73]. Angular correlations have wide applications in nuclear spectroscopy for the determination of nuclear spins and gamma-ray multipolarities.

2.1 Basic coincidence set-ups.

A simplified configuration to register coincident emissions from a radioactive source using two independent detectors is shown in Figure 2.2. Signals from both detectors are in first place shaped by spectroscopy amplifiers. In most cases, signals produced by events that are simultaneous from the point of view of emission produce non-coincident pulses, given that the time spent to collect the charges and to shape the pulses is different for each electronic chain. For that reason, in order to align pulses from both detectors, a time delay module is inserted in the fastest branch before pulses enter the coincidence unit. A coincidence unit will produce a logic output if pulses arrive within a preset resolving time, the so-called *coincidence time* (τ).

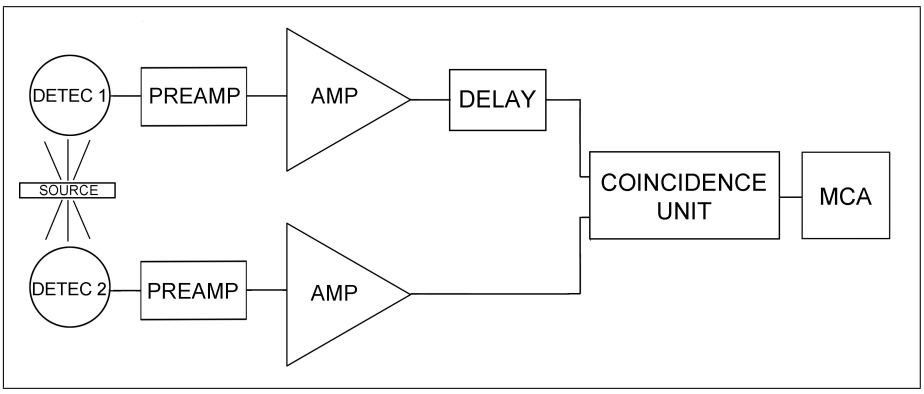

Figure 2.2: Simplified system to register coincident events using a coincidence unit.

An optimal coincidence time is determined from the so-called *time spectrum*, which can be obtained using a time-to-amplitude converter (TAC) (Figure 2.3).This device produces an output pulse with an amplitude proportional to the time interval between two pulses, called "start" and "stop", that come from both chains [1]. Time intervals can be recorded by a multichannel analyzer (MCA) creating a time spectrum as shown in Figure 2.4.

In an ideal case where the detectors and the electronic chains are nearly identical in both branches, the peak obtained in the time spectrum should be symmetric. The peak width indicates the total contribution of all sources of time uncertainty. A common practice is to take the FWHM of this peak as the time resolution of the system. Moreover, the peak shift from the origin of coordinates indicates the delay between signals. In basic coincidence set-ups, both electronic chains should be aligned before measurements using delay

modules. On the contrary, with current digital modules, the delay correction can be carried out off line by software (as it will be explained in Section 4.3.2).

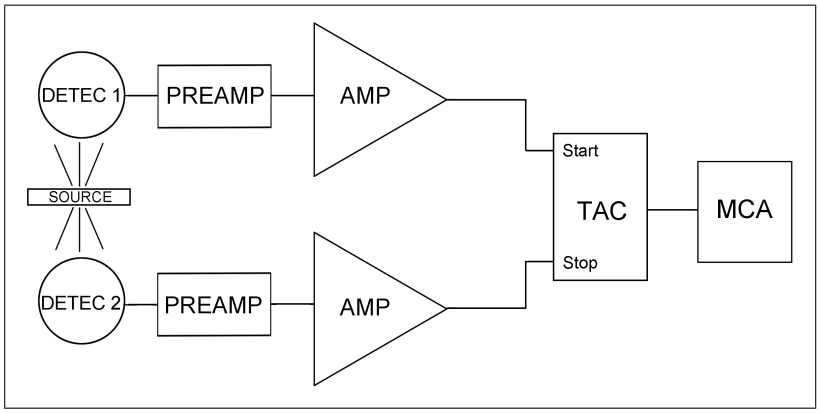

Figure 2.3: Simplified set-up to register multichannel time spectra of coincident radiations.

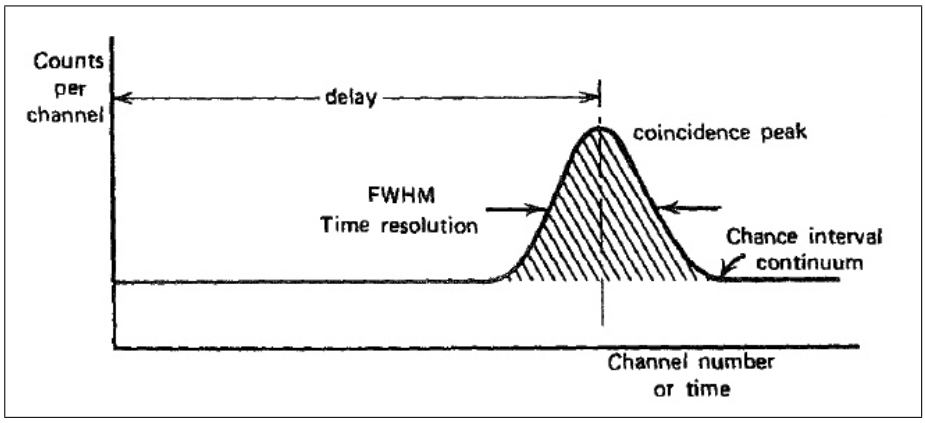

Figure 2.4: Multichannel time spectrum for a source measured with a coincidence set-up. The cross-hatched area gives the total number of coincident events. The FWHM of the coincidence peak is commonly taken as the time resolution. Taken from Knoll [1].

A number of instrumental effects modify the ideal situation and add uncertainty in deriving the timing signal and determining the *true coincidence rate*. The relevant effects are discussed below.

Distortion of the time resolution.

The easiest and most direct trigger condition is the so-called *leading edge trigger*. A digital pulse is generated on the output when the input signal crosses a certain threshold. If two signals are simultaneously registered with the same rise times but different amplitudes, they will reach the trigger threshold at different times, which gives a time displacement between the two digital output pulses (see Figure 2.5). This effect is known as *walk*.

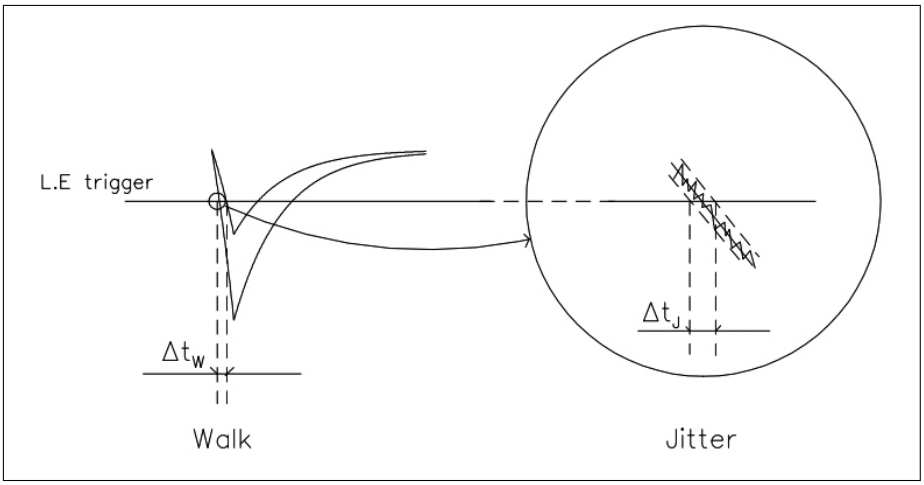

Figure 2.5: The effect known as *walk* is produced when two input signals with the same rise time but different amplitudes reach a trigger threshold at different times. The time shift caused by electronic noise overlapped on the signal is called *jitter*.

Another cause for the deterioration of the time characteristics of a signal is the so-called *time jitter* which is produced by high frequency electronic noise overlapped on signals. Two identical pulses will not reach the trigger threshold at exactly the same time due to fluctuations in the time assignment introduced by the noise. This effect is much smaller than *walk* effect.

These two distorting effects can be reduced using two different methods. The first one is the *crossover timing*. It requires input pulses with bipolar shape. Theoretically, the time at which the bipolar signal crosses from the positive to the negative side of the axis is independent of the amplitude. For that reason, this method greatly reduces the *walk* effect but at the expense of increased *time jitter*.

The other method is based on the production of an output signal in a fixed time after the leading edge of the pulse has reached a *constant fraction* (f) of the amplitude. The process involves several steps that are shown in Figure 2.6. The time at which the signal crosses the zero axis corresponds to the time at which the pulse reaches the constant fraction f of its height and it is independent of the amplitude. This method reduces the *walk* effect as well as the crossover method, but exhibits lower *time jitter*.

Random coincidences.

Since the time resolution of the instruments is limited, there is a chance that two events that are not correlated from the point of view of emission arrive to the detectors within the resolution time. These events are called *random coincidences* and their probability depends on the time resolution of the system and the activity of the source. Given that the Poisson law that describes the time interval between successive emissions favors short interval times, random coincidences are, to some extent, always present. Therefore, the measured coincidence rate consists of two contributions, the true coincidence

rate and the random coincidence rate. This random contribution must be subtracted from the measured rate.

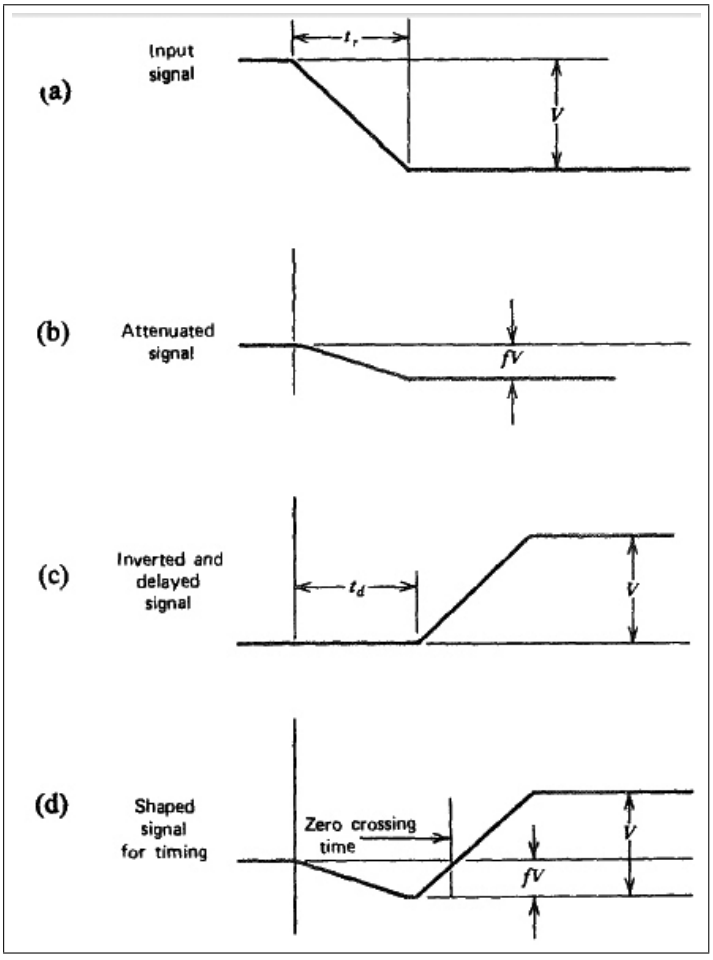

Figure 2.6: Waveforms obtained in each step of the *constant fraction* method. Only the leading edge of the pulse is shown. Taken from Knoll [1].

For a system formed by two independent electronic circuits and with a coincidence time τ [1], the rate of random coincidences is given by:

$$r_{rnd} = 2\tau r_{D1} r_{D2}, \tag{2.3}$$

where r_{D1} and r_D denote the corresponding detector 1 and detector 2 uncorrelated counting rates, respectively.

Equation 2.3 shows that the rate of random coincidences is directly proportional to the coincidence time. On the other hand, the coincidence time should be larger enough to allow some leeway for such drifts or other timing changes. The usual criteria to balance these conflicting considerations is to select τ in the order of the full width at tenth of maximum (FWTM) of the peak obtained in the time spectrum.

Basic coincidence set-ups hardly provide good energy and time resolutions simultaneously. In coincidence spectrometry, the satisfaction of both require-

ments is essential but difficult to implement with a simple system, given that slow signals allow excellent amplitude determination but provide poor timing information. A complete solution can be obtained by using a "fast-slow" coincidence set-up, as shown in Figure 2.7. This method is based in the implementation of a duplicated coincidence chain. The "fast" branch selects the coincident signals while the "slow" branch determines the amplitude of the pulses [73].

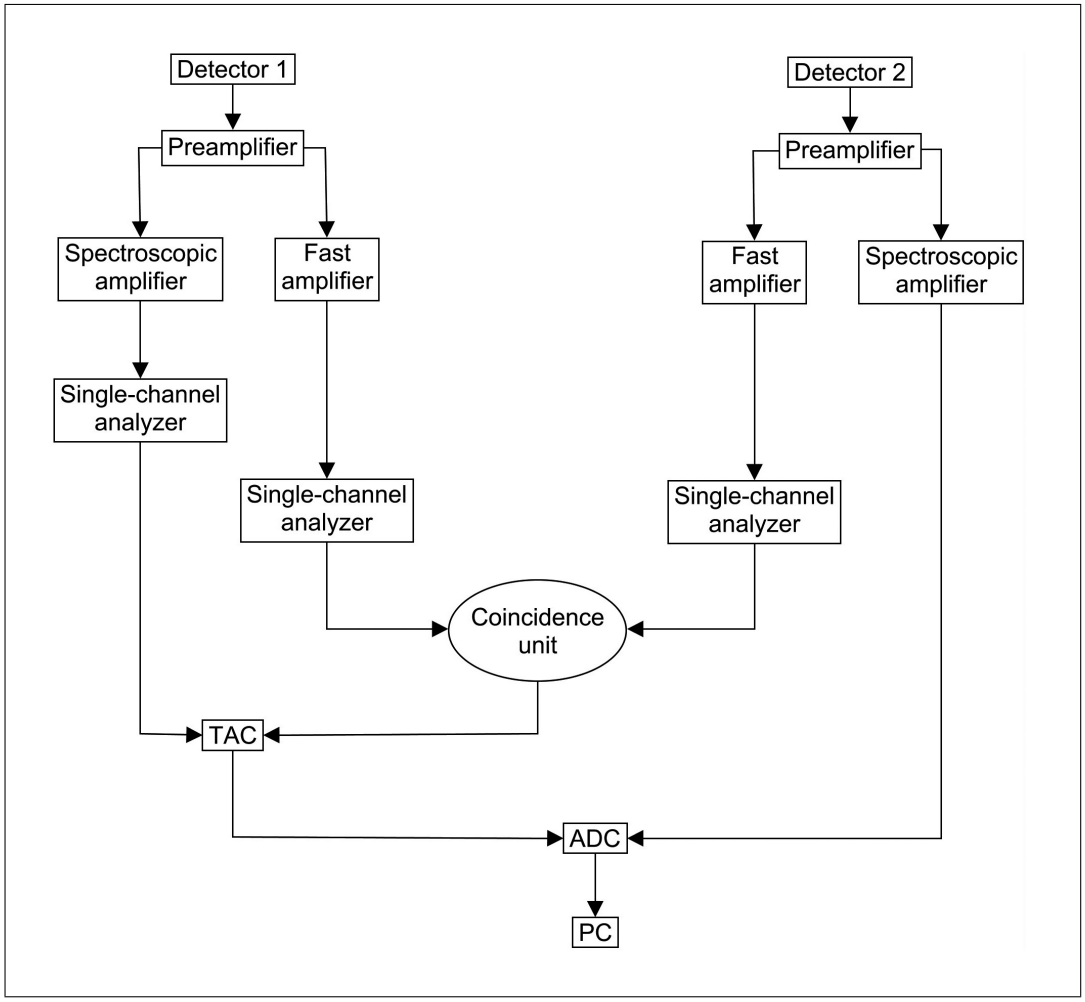

Figure 2.7: Scheme of a "fast-slow" coincidence set-up.

Therefore, the complete electronic chain consists of two detectors, their corresponding preamplifiers sensitive to charge, two spectroscopic amplifiers and two fast amplifiers. Both kinds of amplifiers are connected directly to the preamplifiers, forming the beginning of the slow and fast chains, respectively.

Considering that for detector 1 only the emissions of interest will be analyzed, the outputs of the corresponding two amplifiers, both the fast and the slow, are connected to single-channel analyzers with their acceptance window opened a few channels. Thus, only pulses whose amplitudes are classified within this interval of channels will be selected. On the other hand, for detector 2 the corresponding fast amplifier is connected to a single-channel analyzer

with its acceptance window completely opened allowing the registration of all pulses.

The outputs of the fast amplifiers enter the coincidence unit. This module will provide a logic pulse when signals coming from both amplifiers are registered within the coincidence time, parameter that is commonly set in the coincidence unit itself.

The output of the coincidence unit is connected to the "start" input of a time-to-amplitude converter (TAC). Besides, in the slow branch, the output of the single-channel analyzer associated with the spectroscopic amplifier corresponding to detector 1 is connected to the "stop" input of the TAC. If these two pulses are registered within a fixed time imposed by the TAC itself, an output signal will be generated. This time should be in the order of the delay between both the fast and the slow branches of detector 1.

The output of the TAC is connected to the coincidence input (GATE) of an analog-to-digital converter (ADC). The output of the spectroscopic amplifier corresponding to detector 2 is connected to the ADC input (INPUT). This module is working in coincidence mode and only accept pulses from detector 2 if they reach the ADC within the coincidence time imposed by the fast branch.

The experimental result will be an energy spectrum of events from detector 2 that are coincident with the fixed emission of interest registered by detector 1. This spectrum is called *coincidence spectrum.*

2.2 Modern systems to measure coincidences.

From the point of view of the spectroscopic devices, basic coincidence systems have been developed on the basis of a single-channel analyzer to measure a specific emission registered with one of the detectors and a multichannel analyzer to collect all pulses generated in the other detector. These set-ups have the disadvantage that in order to analyze coincidences with other emissions, new acceptance windows (also called gates) must be selected in the single-channel analyzer and then the measurements should be repeated.

In addition, the width of the gate has to be chosen before carrying out the measurements. It enables a possible loss of information or the erroneous contribution of events from other interfering emissions. A dual-parameter multichannel analyzer solves these problems because coincidences between all emissions are registered in just one measurement.

Figure 2.8 shows a simplified scheme of a set-up using a dual-parameter multichannel analyzer. The electronic chain consists of two detectors, their corresponding preamplifiers sensitive to charge, two spectroscopic amplifiers and two analog-to-digital converters (ADC). The outputs of both ADCs are connected to a dual-parameter multichannel analyzer [74–76].

The simplest application of this kind of units is to determine the pulse height spectra for both detectors. For this purpose, this device provides two separate inputs to accept ADC signals. Moreover, for coincidence measurements a coincidence circuit is also associated. Once the coincidence time is determined from the time spectrum, it can be supplied to this coincidence

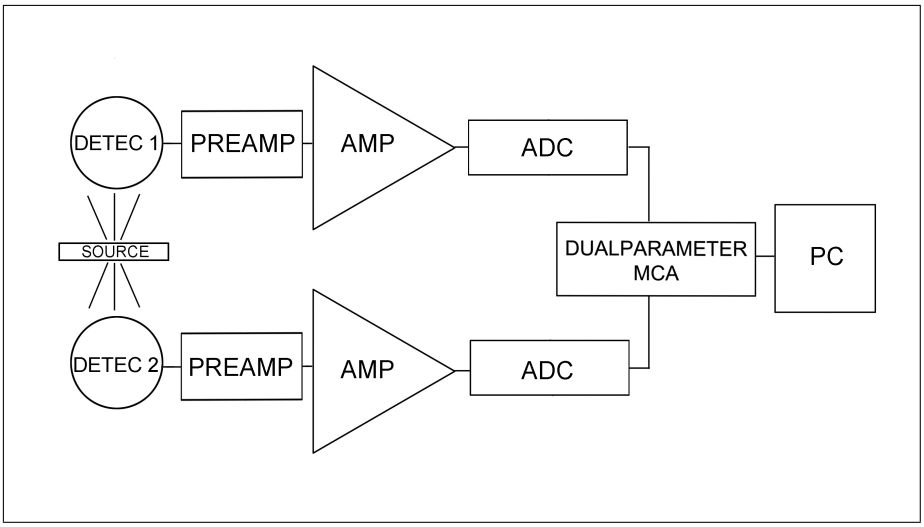

Figure 2.8: Scheme of the electronic chains for a coincidence set-up with a multichannel analyzer.

circuit by software. The dual-parameter multichannel analyzer recognizes the coincidence between the inputs and, as data accumulate, the intensity distribution then takes the form of a two-dimensional surface with local peaks representing combinations of amplitudes of pulses coming from both electronic chains. Data are sometimes displayed as a surface contour plot or as a three dimension view of the surface (see Figure 2.9).

The main disadvantage of this kind of systems is that no time information is provided and additional devices are then necessary. In order to create the time spectrum, the same set-up described above (see Figure 2.3) is required. As well as in the case of basic set-ups, the alignment of both electronic chains should be carried out using a delay module.

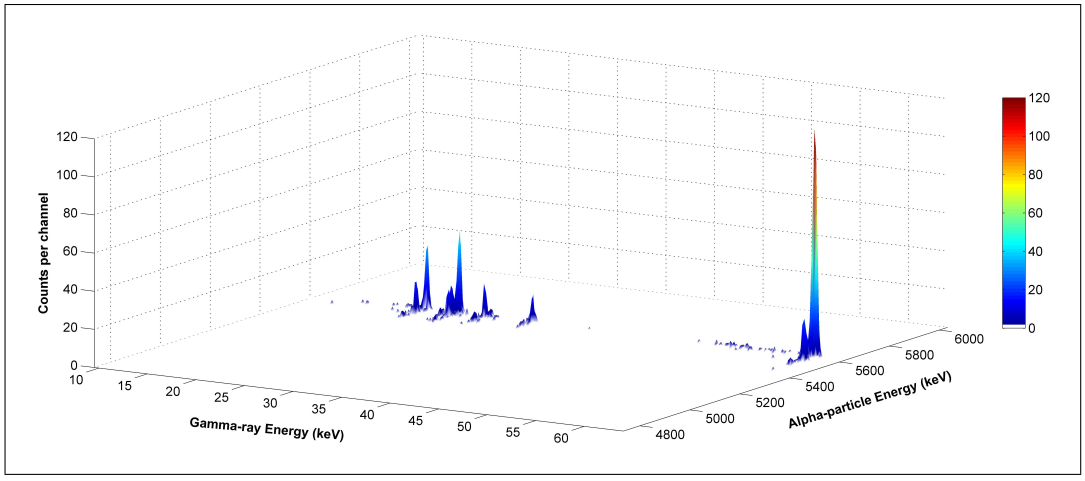

Figure 2.9: Alpha-gamma coincidence spectrum of ^{241}Am obtained with a coincidence set-up using a dual-parameter multichannel analyzer.

Over the last years, advances in digital signal acquisition technology have allowed the introduction of digital systems in the field of Nuclear Physics [77], [78], [79]. Digital devices facilitate the possibility of storing pulse information from multiple detector systems along with the time of occurrence ("time stamp") for each recorded event, allowing various method to be implemented "off-line" by the use of dedicated software routines. The result obtained depends less on the stability and reproducibility of the parameters of the electronics since many analog modules become unnecessary. Moreover, the data stored on a hard disk has a primary form, which enables different methods of statistical processing to be employed and compared.

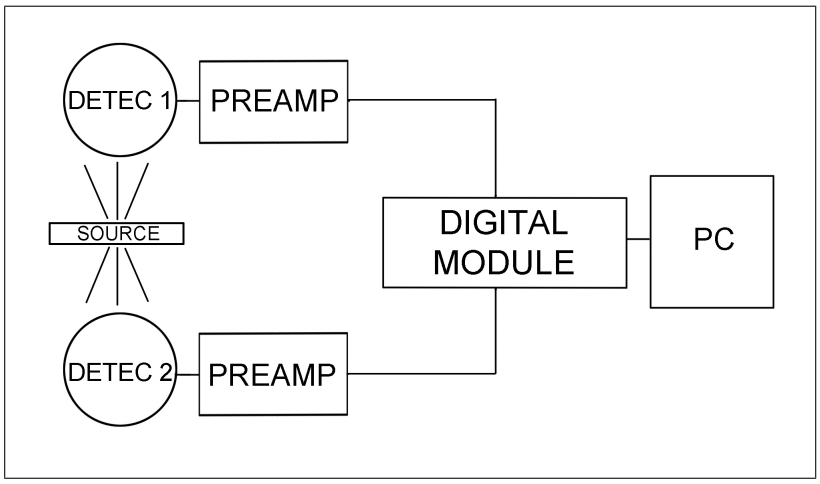

Figure 2.10: Scheme of the electronic modules used in a coincidence set-up with a digital module.

A typical set-up is shown in Figure 2.10. The outputs of the preamplifiers are directly connected to a digital module, which can be configured by software. Signals are shaped, analyzed and classified following the directives provided by the user. After the conclusion of the measurements, information such as the time stamp and the amplitude of the pulse is stored for each recorded event. The knowledge of these data makes possible to create time and energy spectra, apply delays to pulses, make dead times corrections or establish coincidences avoiding the use of additional modules. Everything is carried out off-line and using specific software.

Part II

Experimental set-ups. Description & Optimization

Chapter 3

Alpha-particle spectrometry devices

As described in Section 1.1, a number of different devices have been developed to cover the wide range of applications of alpha-particle spectrometry. The choice of a particular instrument is always a compromise between two basic requirements: good energy resolution to evaluate the different component of a radioactive source and high efficiency to minimize counting times. Ion-implanted Si detectors provide an equilibrium between energy resolution and efficiency and were chosen for all the measurements in this work. The spectrometric set-ups used in this research are described below.

3.1 Semiconductor chamber

The first spectrometric device was designed and characterized at the University of Extremadura. It consists of a stainless steel vacuum chamber with a Passivated Implanted Planar Silicon (PIPS©) detector placed in the upper part (see Figure 3.1). The design and use of this chamber is based in previous devices developed at other laboratories [80–82]. It is aimed at providing good resolution and to allow an easy modification of the source-to-detector distance, i.e. decreasing the geometrical factor. Measuring under these conditions allows a better evaluation of the sample components and facilitates the fitting and analysis process of alpha-particle spectra.

A PIPS detector with 50 mm^2 active area model PD 50-12-100 AM from Canberra was used, although detectors with other areas can also be adapted. The reason for using a detector with 50 mm^2 active area was that low active area detectors involves measurements with lower subtended source-to-detector solid angles. The lower the solid angle, the better the resolution. However, the absolute detection efficiency decreases proportionally to the solid angle, or to an "effective solid angle" in the case of extensive sources $\left(\epsilon_{abs} = \epsilon_{int}\frac{\Omega_{eff}}{4\pi}\right)$. In that case, long time measurements are necessary. As it was explained in Section 1.2.2, for long counting times some shift of the measured spectra can appear (drift effects); therefore the procedure of acquiring series of short-period spectra and combining them after an appropriate shifting correction was applied

in this study.

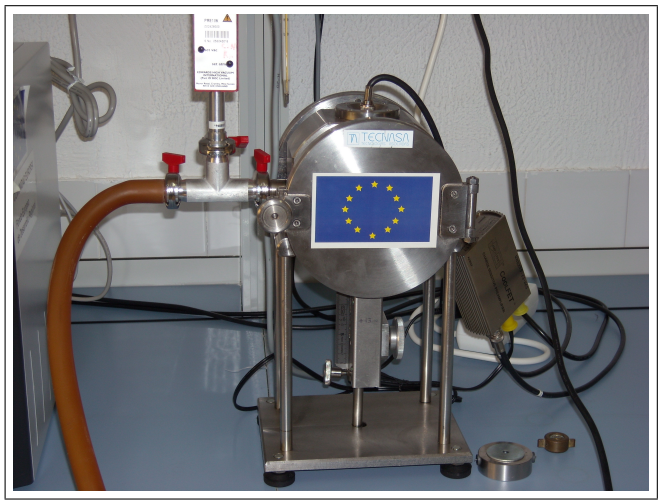

Figure 3.1: Semiconductor chamber designed and characterized at the Univeristy of Extremadura.

The detector is polarized with a voltage of +60 V, following the manufacturer recommendation. The electronic resolution is 6.0 keV (FWHM), with a total nominal resolution of 11.8 keV (FWHM).

The source support is placed in the bottom part of the vacuum chamber. The source-to-detector distance can be adjusted using the wheel and graduated scale located under the chamber, as shown in Figure 3.1. The distance varies between 13 and 61 mm. Considering a detector with 50 mm^2 active area and a source with 2 cm of diameter, these distances correspond to solid angles of $\sim$ 0.2004 and 0.0134 sr, respectively [83].

Since the aim of this work is to evaluate nuclear data of alpha-particle emitting nuclides, the coincidence summing effects of alpha particles with conversion electrons in alpha spectra have to be carefully evaluated. Measuring under low solid angles and placing magnets between the source and the detector reduce, although not totally eliminate, coincidence summing pulses. In our set-up, a pair of magnets are placed in a holder of 11.60 mm height that is coupled to the source support. A diaphragm with a central 6.05 mm diameter hole and 1.45 mm height is placed on the magnet holder (Figure 3.2).

A rotary vacuum pump is externally connected to the chamber, reaching about 8 Pa in a normal working mode. The vacuum reached in the chamber is measured with an external Pirani detector shown in the left side of the Figure 3.1.

The components of the electronic chain are the following:

- A high-voltage power supply hosted in a NIM module 3102D, from Canberra.
- A charge sensitive preamplifier Coolfet A250CF (AMPTEK, Inc.), which connects the high-voltage module to the detector. It is shown in the right part of Figure 3.1.

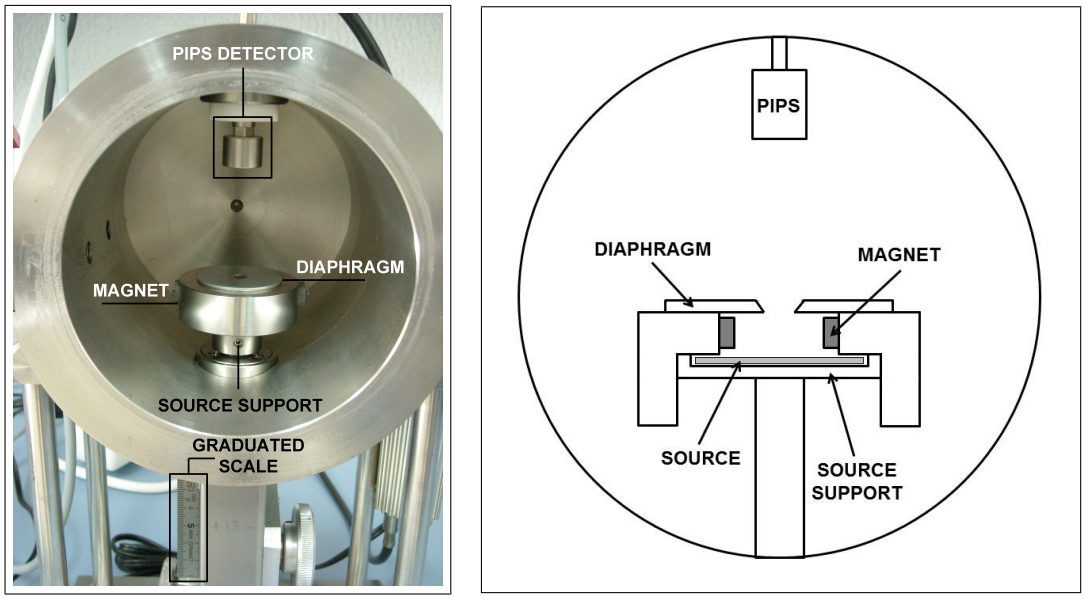

Figure 3.2: Details of the internal components of the semiconductor chamber.

- An amplifier model 2022 (Canberra) that shapes the output pulses from the preamplifier.
- All NIM modules (the high-voltage power supply and amplifier) are fed by a power rack 2100 also from Canberra.

The optimal measuring conditions were obtained using an electrodeposited source of $^{239+240}$Pu, ^{241}Am and ^{244}Cm formerly used in other work [84]. A 2 μs shaping time was chosen to carry out the measurements. The MCA memory was 8192 channels.

The output of the amplifier is directly connected to an MCA-3A v 2.84 card from FAST COMPTEC integrated into a computer and working as an MCA. This card has an ADC. The configuration of the card as well as the pulse processing is carried out by the MCDWIN v 2.93 software (Canberra), which runs under Windows environment.

This semiconductor chamber was used in this work to measure a source of ^{241}Am. The resulting alpha spectrum was one of those used to check the analyzing capability of a new code to fit alpha-particle spectra, which will be described in detail in Chapter 5.

3.2 High-stability and α-e$_c$ coincidence chambers

The measurements of ^{242}Pu were carried out at CIEMAT using two chambers that have been described elsewhere [16, 85]: a high-stability alpha-particle chamber (Figure 3.3 and 3.4) and an alpha-particle/conversion-electron coincidence chamber (Figure 3.5).

The first device is made of stainless steel and consists of two vacuum chambers: a PIPS detector is placed in the upper chamber and the source is positioned in the other; a shutter valve allows the vacuum isolation of the upper chamber while a source is being changed. With this configuration, the operating conditions, e. g. bias and vacuum, can be maintained for long counting times.

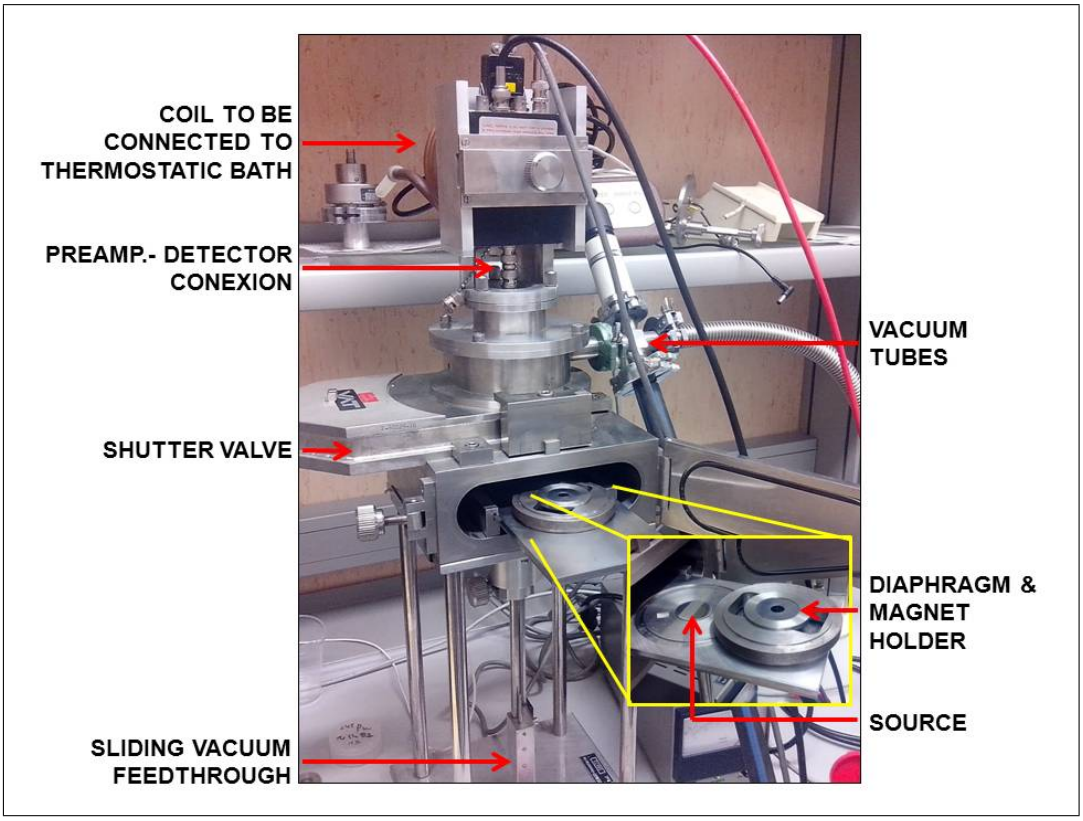

Figure 3.3: High-stability alpha-particle spectrometry chamber.

The source-to-detector distance is set by means of a sliding vacuum feedthrough and digital vernier to a precision of ± 0.03 mm. A pair of magnets can be coupled to a piece placed above the source support to reduce conversion electrons emitted by the sample (see Figure 3.4a). Its strength can be adapted to the measuring conditions. Two cubic magnets with 1.6 kg force were used for the measurements of ^{242}Pu that are described in detail afterward in this text. The corresponding magnetic field was about 1 kG for 15 mm distance between poles. In order to reduce the straggling of the alpha-particle flow impinging

the detector, a collimator composed of a tantalum diaphragm (0.1 mm thick and 9 mm opening diameter) was placed coaxial with the source and detector in the same piece where the magnets were coupled. The source-to-detector geometry can be adapted to the measuring needs.

(a) Magnets.

(b) Diaphragm.

Figure 3.4: Diaphragm and magnets coupled to the source support.

Since apparent peak positions can vary with changes in detector temperature (about - 0.06 keV/°C), a thermostatic bath can be used to stabilize the temperature of both the detector and the preamplifier at (21 ± 0.1) °C. If the room temperature is stabilized at ± 0.1 °C, its use is not necessary. The stability of the measurements was checked, finding that the system was very stable under the measuring conditions.

A ^{Hi}CUBE PFEIFFER turbomolecular pump (Air cooling 24 V DC, PM Z01 300) was used, reaching 1 Pa in the normal working mode. The system contains a small turbomolecular pump in series with a rough pump.

The α-e_c coincidence chamber consists of a cylindrical vacuum chamber with a PIPS detector placed in the upper part. The device has two opposite windows in the side where other gamma or PIPS detectors could be coupled to measure in coincidence (Figure 3.5). However, in this work, this chamber was only used as a second unit to measure an additional source of ^{242}Pu under higher efficiency set-up. The source is placed in a sliding support at the bottom part of the chamber facing the detector. Two cylindrical magnets with 1.2 kg force were used for all measurements of ^{242}Pu. The magnet field was about 0.05 kG for 20 mm distance between poles. A diaphragm with 22 mm diameter was fixed at an intermediate distance between the source and the detector. The turbomolecular pump described above was also used in this chamber.

The detectors and the electronic components corresponding to each chamber are enumerated below:

High-stability chamber.

- A PIPS detector from Canberra with 50 mm^2 active area and 300 micrometers Si thickness, model PD 50-11-300 AM (No 88272). The detector works with +60 V bias and a reverse current in the order of few

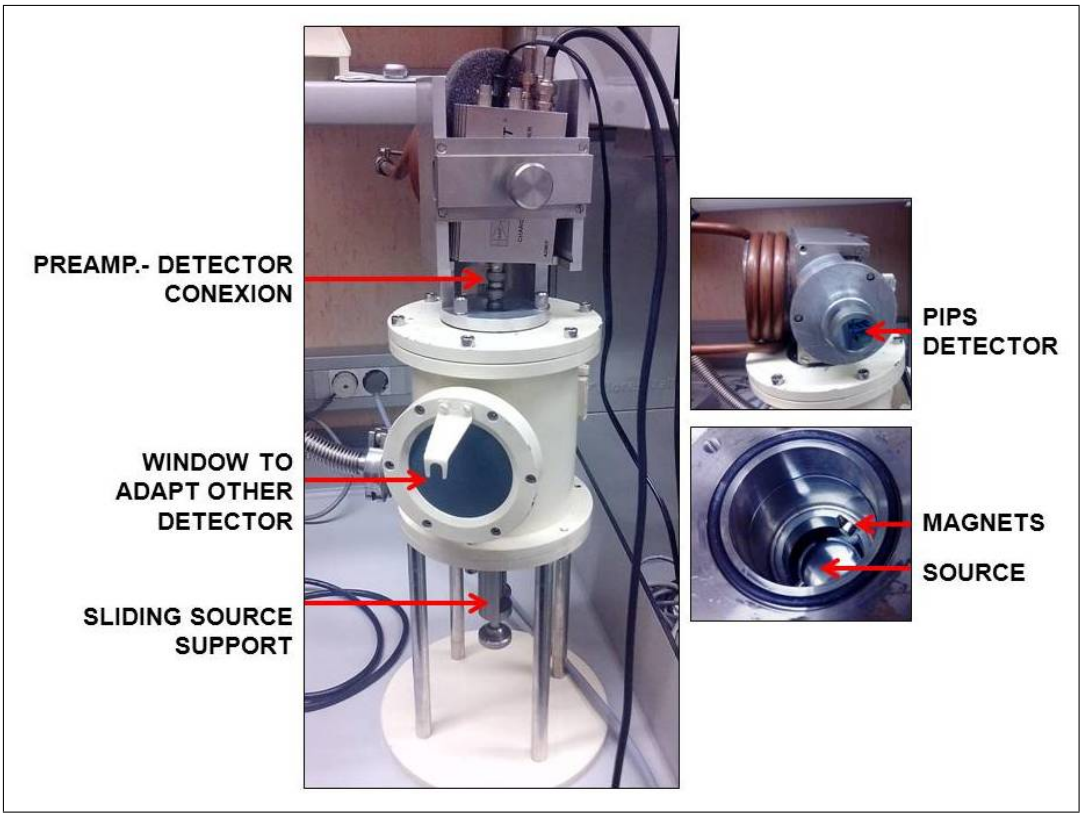

Figure 3.5: α-e$_c$ coincidence chamber.

ns. Its electronic and nominal resolutions are 6 and 10.3 keV FWHM, respectively.

- A high-voltage power supply TC953 from TENNELEC with two outputs.
- A charge sensitive preamplifier model 2001 A from Canberra.
- An amplifier model N968 (CAEN) to shape the signals coming from the preamplifier.
- An MCA ASPEC 927 from Ortec with two ADCs integrated.

α-e_c coincidence chamber.

- Two PIPS detectors from Canberra with 450 mm^2 active area and 100 micrometers Si thickness, model PD 450-17-100 AM (No 84488 and No 59871). The detectors need +40 V bias and a reverse current of few ns. The electronic and nominal resolutions for this detector are 10.4 and 15.7 keV FWHM, respectively.
- The high-voltage power supply TC953 from TENNELEC.
- A charge sensitive preamplifier preamplifier Coolfet A250CF (AMPTEK, Inc.).

- An amplifier model 2020 from Canberra.
- The MCA ASPEC 927 from Ortec.

All NIM modules are fed by a power rack 2100 from Canberra. The MCA was configured and the spectra collected by the MAESTRO v 7 software (Ortec), which runs under Windows environment.

For the measurements of ^{242}Pu, shaping times of 2 and 1.5 μs was selected for the high-stability and the α-e$_c$ chambers, respectively. The MCA memory was 8192 channels in both cases. Figure 3.6 shows two spectra of ^{242}Pu obtained with both chambers. The energy resolutions obtained for the main peak of ^{242}Pu were 9 and 13 keV FWHM for the high-stability and the coincidence chambers, respectively.

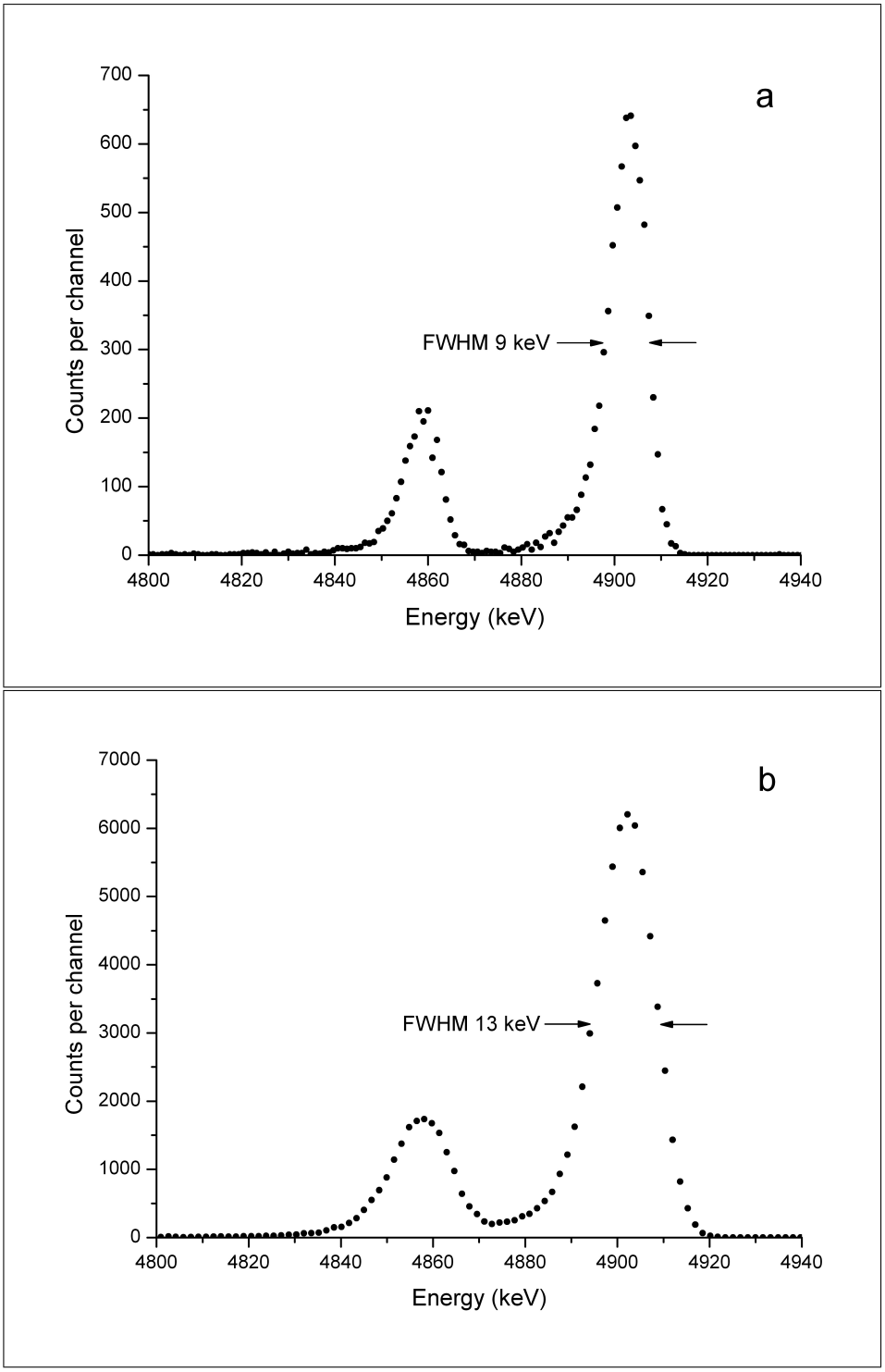

Figure 3.6: Spectra of ^{242}Pu obtained with the high-stability chamber (a) and the α-e$_c$ coincidence chamber (b).

Chapter 4

Alpha-gamma coincidence set-up

An alpha-gamma coincidence device has been designed and set up at the University of Extremadura [74–76] (Figure 4.1). The design of a good coincidence system is not an easy task due to the fact that this technique is not as widely used as, for example, the γ spectrometry technique. The design of the proposed coincidence set-up is original although a similar spectrometer has been recently presented to study coincidences for safeguard measurements [86].

4.1 Description of the coincidence chamber

Figure 4.1: Alpha-gamma coincidence chamber.

The device consists of a stainless steel vacuum chamber with a passivated implanted planar silicon detector (PIPS©) placed at the top to register alpha particles. To register gamma radiation, a Canberra low-energy germanium (LEGe) detector was coupled to the back of the chamber, behind a 624.84 μm thick carbon-epoxy window (Figure 4.2a). The utility of this chamber is triple: alpha-particle spectrometry using the PIPS detector, gamma-ray spectrometry with the LEGe detector, and alpha-gamma coincidences measuring simultaneously with both detectors.

The radioactive source is located in the centre of the chamber in a rotary support which can be handled with an external graduated wheel (Figure 4.2b). In order to measure coincidences, the source is usually located forming 45° angle with both detectors, although other orientations were used in this research. The distance from the centre of the source to the PIPS detector cannot be varied and is fixed at

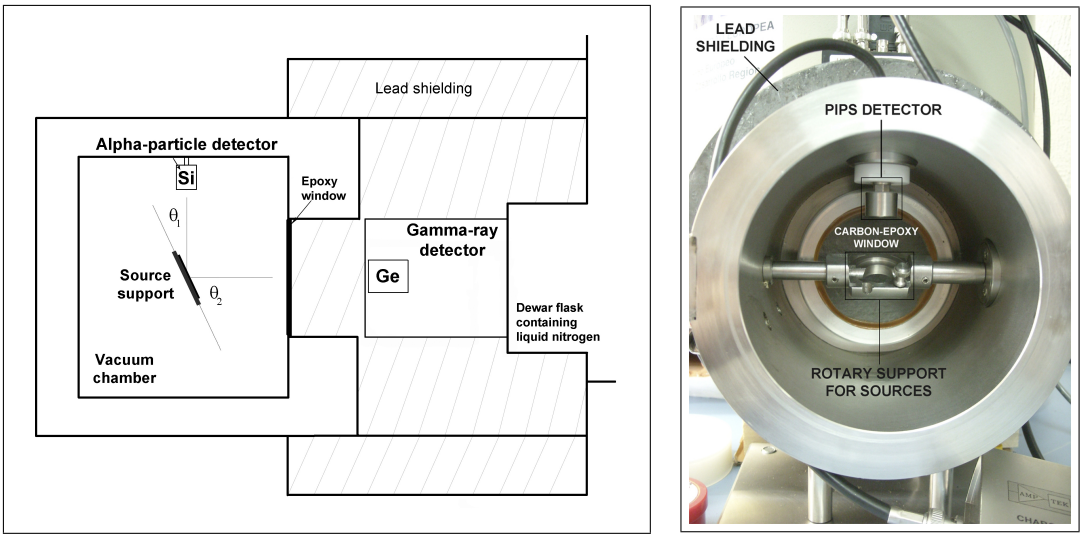

(a) Set-up scheme. (b) Internal components.

Figure 4.2: Details of the alpha-gamma coincidence device.

30 mm. On the contrary, the distance from the source to the LEGe detector can be changed, but was set to 40 mm for all the measurements. A rotary vacuum pump is externally connected to the chamber, being able to reach about 8 Pa in the normal working mode.

The alpha-particle detector is a partially depleted PIPS detector model SPD 50-11-100 AM from Canberra, working with a voltage of + 100 V. The detector active area is 50 mm^2 and its nominal resolution is 10.8 keV (FWHM).

For the detection of gamma rays a *p - type* germanium detector model GL0110P from Canberra has been used, working with -1000 V. This detector has 100 mm^2 active area and 10 mm thick. The energy range suggested by the manufacturer is 5.9-122 keV, with energy resolutions between 0.155 keV and 0.495 keV (FWHM) in this range. It can work for gamma emissions with higher energies but with much less efficiency. The LEGe detector is enclosed in a vacuum environment by an aluminum cover. This cover is surrounded by 5 cm thick lead shielding and coupled to a Dewar flask of 30 L volume containing liquid nitrogen (74.65 K) to keep a fixed low temperature for the correct performance of the detector. Working at low temperatures and high potential barriers are necessary in order to reduce the thermally-induced leakage current [1].

The electronic modules used to detect alpha particles are:

- A high-voltage power supply installed in a NIM module model 3106D from Canberra.
- A charge sensitive preamplifier Coolfet A250CF (AMPTEK, Inc.), which is shown at the right bottom of Figures 4.1 and 4.2b.
- An amplifier model 2026 (Canberra) that shapes the preamplifier pulses.

- An analog-to-digital converter (ADC) model 8701 (Canberra) that converts the analogical output signals from the amplifier into digital data.

All NIM modules were hosted in a power rack (Canberra 2100).

The electronic modules composing the gamma detection branch are:

- A high-voltage power supply 3106D.
- A 2008 BEF charge sensitive preamplifier.
- A 2026 amplifier.
- An 8701 analog-to-digital converter.

The NIM modules, all from Canberra, were placed in the power rack 2100 mentioned above.

The ADC output data are processed by a dual-parameter multichannel analyzer MPA-3 from FAST CompTec (Figure 4.3) connected to a PCI card integrated in a personal computer. The card configuration and the registration process is controlled by the MPANT for MPA-3 v 1.6 software (Canberra), which runs under Windows environment. Alpha and gamma devices work simultaneously in both individual and dual modes, obtaining single and dual-parameter spectra (alpha, gamma, and alpha-gamma in coincidence).

Figure 4.3: Dual-parameter Multichannel Analyzer (MCA).

4.2 Dual-parameter multichannel system

Generally, traditional coincidence systems have been developed on the basis of a single channel to measure alpha-particles and a multichannel analyzer for gamma rays. These devices had the disadvantage that the coincidences obtained in a unique measurement were those in which the alpha-particles have a specific energy range selected with the single-channel gate. In order to analyze coincidences with other alpha-particle emissions, new windows must be selected and the measurements repeated. In addition, the width of the

gate should be chosen before carrying out the measurements. It enables a possible loss of information or the erroneous consideration of events from other interfering alpha-particle emissions. A dual-parameter multichannel analyzer solves these problems because coincidences between any alpha-particle and any gamma-ray are registered in just one measurement [75].

The coincidence set-up was checked and optimized using an electrodeposited source of ^{241}Am provided by CIEMAT. The sample has 830 Bq activity with 22 mm diameter active area deposited on a circular stainless steel plate. The decay scheme of ^{241}Am is depicted in Figure 4.4, with numerical values taken from the Decay Data Evaluation Project (DDEP) [71].

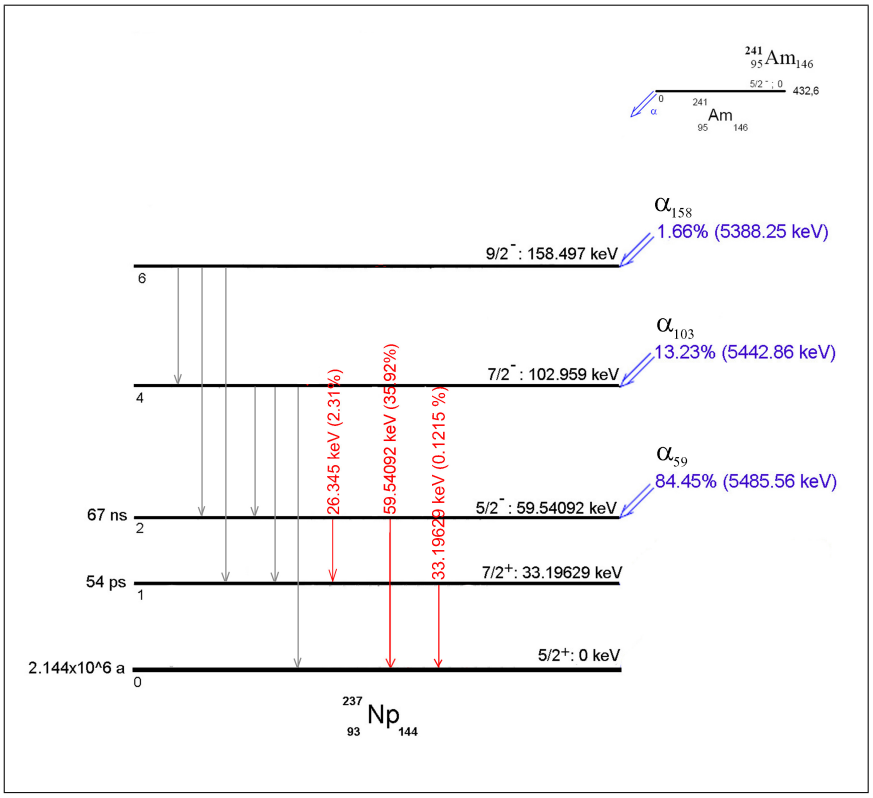

Figure 4.4: Simplified decay scheme for ^{241}Am. The emissions shown for alpha-particles and gamma-rays are those considered in the present work. The numerical values were taken from the Decay Data Evaluation Project [71].

The alpha-gamma coincidence matrix obtained with a dual multichannel analyzer is divided into m files and n columns corresponding to the m alpha and n gamma individual spectra. An example of this coincidence matrix is shown in Figure 4.5 for the case of the three main kinds of alpha particles (5388.23, 5442.80, and 5485.56 keV) of ^{241}Am and the corresponding 59.54 keV gamma-ray emission. The solid line delimits the ROI contour of the coincidences between the three main alpha-particle emissions (5388.23, 5442.80, and 5485.56 keV) and the 59.54 keV gamma-ray emission from ^{241}Am ("contour graphics"). The shaded region is the ROI contour for only the coincidences considered between the 5485.56 keV alpha-particles and 59.54 keV photons. The dotted

line delimits a rectangular ROI with a narrow alpha region, and the dashed line delimits a rectangular ROI with a wider alpha region.

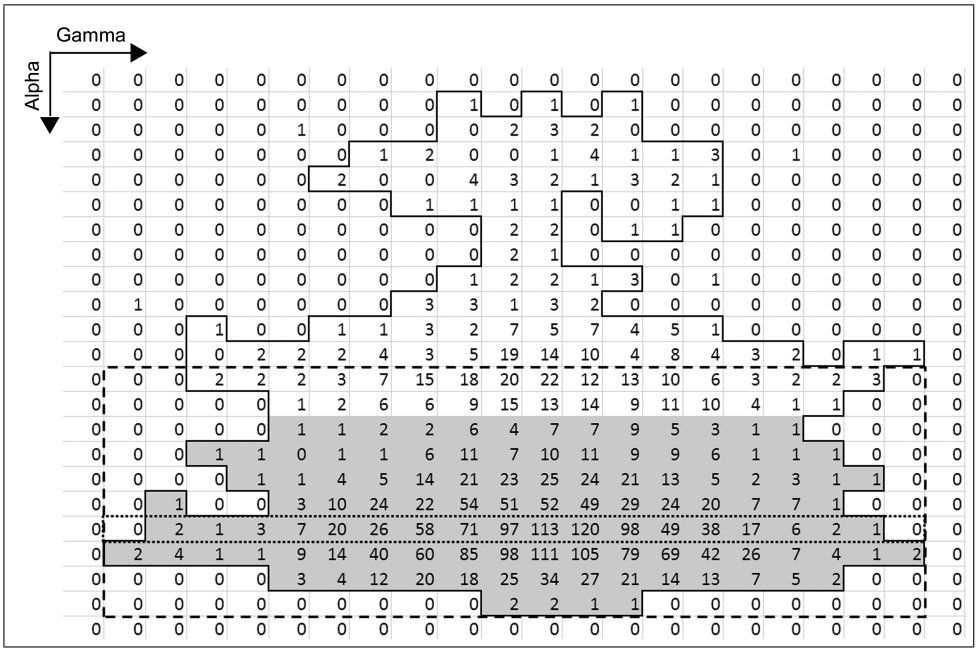

Figure 4.5: Example of experimental results obtained using the dual-parameter multichannel analyzer. Taken from Jurado Vargas et al. [75].

In order to calculate the number of experimental coincidences from the coincidence matrix, the analysis can be done in two ways: by selecting a gamma (alpha) region and analyzing the total sum of the alpha (gamma) events, or by analyzing only the peak region using contour graphics. The first way is somewhat equivalent to the analytical procedure followed in traditional systems (single and multichannel analyzers), although the selection of the gates in this case would be made *a posteriori* knowing the limits of the peaks. On the contrary, the second way is based on the visualization of the peak region using a contour plot. This technique shows the limits of each peak in both the alpha and the gamma regions and permits the discrimination of interfering emissions. Once the number of "experimental coincidences" has been determined from the coincidence matrix, the final "true coincidence" rate is obtained by subtracting the corresponding random coincidence events following Equation 2.3 already described in Section 2.1.

As shown in Figure 4.5, if the gate used in a single-channel is not wide enough (dotted rectangular ROI), events will be lost, so the measured coincidence rate will be less than the real one. If, however, the gate is too wide (dashed rectangular ROI), signals from other alpha-particle emissions could be registered, erroneously increasing the number of coincidences considered. Using contour graphics, an appropriate region can be selected, obtaining the number of coincidences for the emissions of interest more accurately.

4.2.1 COLMA: a data realignment code

COLMA is a code developed in this work to realign coincidence data from the analogical system generated by MPANT software. After using the program, data are arranged in a matrix with "number of alpha channels x number of gamma channels" dimensions, instead of just one column.

COLMA's first version was written in Fortran77, useful only for realignment and data saving in .txt files [87]. Due to a software limitation, COLMA was rewritten with Matlab 2010a© as a graphic user interface (GUI). The limitation was corrected and the code was improved including the possibility of building three dimensional plots and contour graphics with the coincidence data.

The processing speed is another advantage of this new version. Thanks to Matlab optimization for matrix treatment, realigning 16 millions of data (as a result of measuring with 4096 channels for both alpha and gamma spectra) lasts 18 sec using a computer with an MC INTEL 1155 CORE I5 2300 2.8 GHz. Different features of COLMA are described below.

Coincidence files (with .mp extension) are opened through "Open file" option from "File" menu. Once the file is opened, the number of channels used by each ADC has to be indicated using the corresponding "pop-up" menu (Figure 4.6). Then, data are realigned pressing "Column to Matrix" button. When coincidence matrix is created, it can be saved in a .txt file for its subsequent use with the "Save Matrix" button.

Figure 4.6: COLMA screenshot.

One of the main characteristics of COLMA is the possibility of creating three dimensional plots and contour graphics of the coincidence spectrum. For this purpose, a channel range for X axis (alpha) and Y axis (gamma) and the image resolution of the plot files (.tif extension) have to be indicated. Plot aspects are joined in "Plot Range" panel.

Once the range is determined and the "Save Graphics" button is pressed, two windows are opened: one with both plots, three dimensional and contour graphics (Figure 4.7), and another to save the image. Instead of plotting counts versus channel, counts versus energy can also be used indicating calibration parameters in the "Use of calibration" panel. Finally, a guide of COLMA can be consulted in "Help" menu.

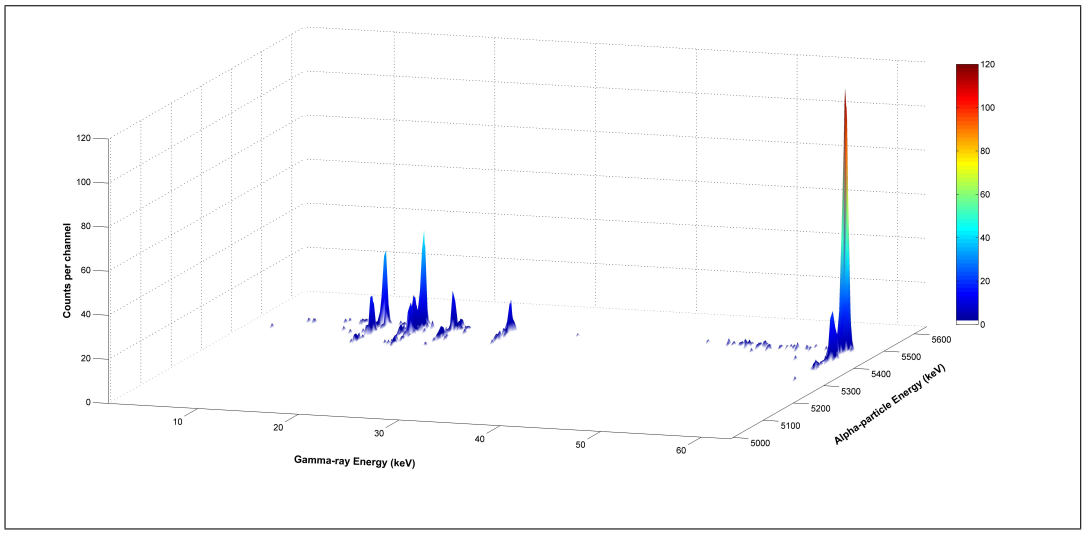

(a) Dual-parameter plot.

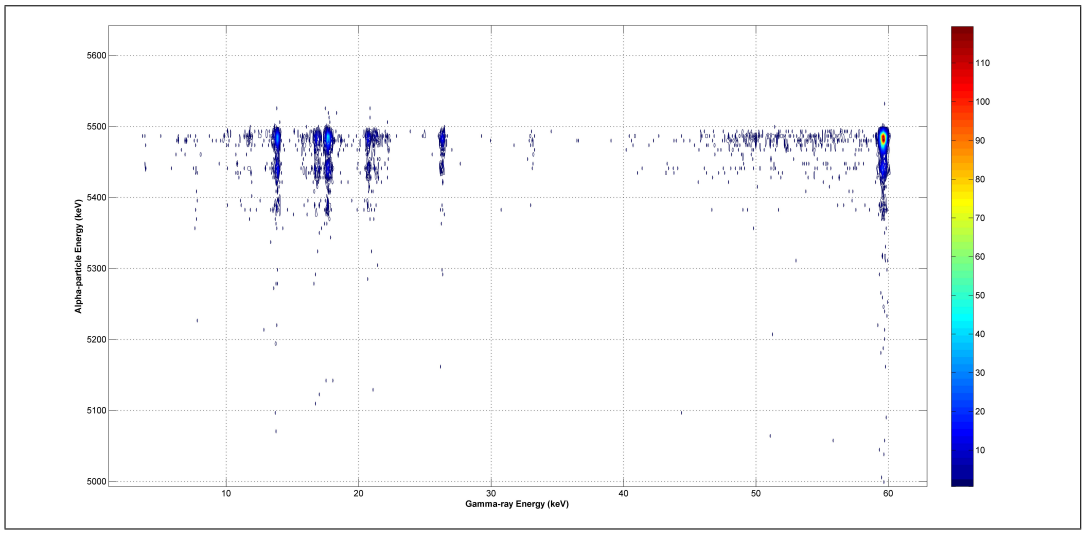

(b) Contour graphic.

Figure 4.7: Three dimensional plot and contour graphic of a coincidence spectrum of ^{241}Am created by COLMA.

4.2.2 System optimization

Both the PIPS and the LEGe detectors were calibrated in energy and efficiency. PIPS detector was calibrated in energy with a certified electrodeposited source made at CIEMAT containing ^{233}U, $^{239+240}$Pu and ^{241}Am. Alpha-particle spectra had an energy resolution about 16 keV.

LEGe detector was calibrated in energy between about 1 keV and 220 keV with an standard source of ^{241}Am also made by electrodeposition at CIEMAT. In this case, energy resolution was about 0.4 keV for 59.54 keV emission of ^{241}Am. The experimental efficiency calibration of the detector was carried out using a multigamma source containing ^{57}Co, ^{241}Am, ^{88}Y, ^{109}Cd and ^{139}Ce. An additional calibration was made using the Monte Carlo code DETEFF [88] confirming the experimental results. For the gamma emission of 59.54 keV of ^{241}Am the geometrical efficiency of the detector is about 0.00297. Subsequent tests and improvements, as well as preliminary results, were carried out using the source of ^{241}Am.

Electronic variables

During the system optimization, several influential factors to the coincidence registration were studied. The ADCs conversion time and the coincidence time have been found to be the most critical factors for the coincidence counting rate. Related to the variable affecting the shape of the dual-parameter spectrum, the influence of the source orientation to both detectors has also been studied.

Shaping time

The *shaping time* is defined as the time-equivalent of the "standard deviation" of the Gaussian output pulse (Figure 4.8). For silicon and germanium detectors, the electronic noise at the preamplifier input makes a noticeable contribution to the energy resolution of the detector. This noise contribution can be minimized choosing the appropriate amplifier shaping time constant.

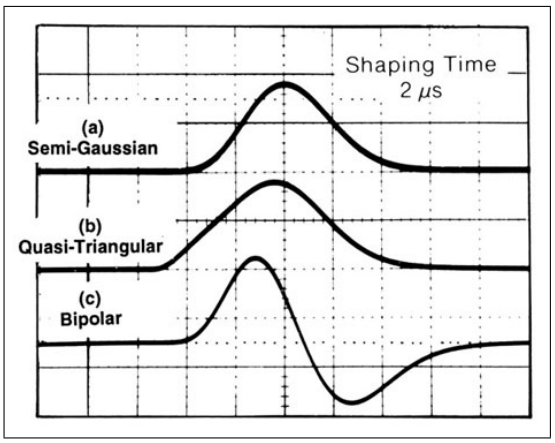

Figure 4.8: A Comparison of (a) Semi-Gaussian, (b) Quasi-Triangular, and (c) Bipolar Pulse Shapes at a 2 μs Shaping Time Constant.

The total noise at any shaping time constant is the square root of the sum of the squares of the series (caused by thermal noise) and parallel noise contributions (from noise sources that are effectively in parallel with the detector at the preamplifier input). Consequently, the total noise has a minimum value at the shaping time constant where the series noise is equal to the parallel noise. The time constant for minimum noise will depend on the characteristics of the detector, the preamplifier, and the amplifier pulse shaping network.

For PIPS detectors, 0.5, 1 and 2 μs are the recommended values for the shaping time constant. For LEGe detectors, optimal values vary from 8 to 24 μs. Such long time constants impose a severe restriction on the counting rate capability. Consequently, energy resolution is often compromised by using shorter shaping time constants, in order to accommodate higher counting rates. In our case, after carrying out several tests for coincidence registration, 1 μs for PIPS detector (alpha) and 6 μs for LEGe detector (gamma) were found to be the most suitable.

ADCs conversion time

As for any Wilkinson-type band ADC, conversion time is directly related to the number of channels chosen for spectra, i.e. with the number of "bins" into which the pulses can be sorted. The greater the number of channels, the longer the conversion time.

Tests were carried out changing the number of channels in each ADC. Results showed that the number of channels selected in both ADCs has to be equal in order to detect true coincidences. Thus, both pulses are converted spending the same time avoiding coincident signals to be registered outside the coincidence time interval. After several tests, 4096 channels were chosen for each ADC.

The active programmable rising or falling edge of each ADCs dead-time signal is used by the dual-parameter multichannel analyzer as the time-of-arrival of an ADC event. On detecting such a dead-time signal's active edge, a coincidence-resolving time window is opened and all dead-time edges arriving in this window are stored. After the coincidence time has elapsed, the system waits for all busy (DRDY) signals of the corresponding ADC ports (meaning that the port contains valid data) to become true. The maximum time to wait for these signals is software selectable. When the expected busy signals have arrived (or, at the latest, when the DRDY timeout elapses), the corresponding ports are read, and the data are transferred to the PC.

A choice of a *DRDY Timeout* value was then necessary. This value is calculated as a function of the number of channels selected in the ADCs as $DRDY\ \ Timeout \approx (No\ channels\ \times\ 0.01\ +\ 10)\mu$s. With the configuration of 4096 channels, the minimum value to correctly register alpha-gamma coincidences was found to be 50 μs for the *DRDY Timeout*.

Coincidence time

An optimum coincidence time must be large enough to permit the regis-

tration of all the true coincidences, and small enough to reduce the number of coincidences by chance. The way of finding the optimal value of this parameter is to construct the so called "coincidence curve", measuring the time delay between two pulses. The width of this curve indicates the value of the coincidence time.

Ideally, if no delay exists, the shape of this curve should be a Gaussian centered in the origin. However, mainly due to the electronic components, the curve is normally shifted and even, in some cases, has some asymmetries (e.g. for beta and gamma coincidences). Hence, for the proper registration of coincidences, before opening the coincidence time window advanced events should be delayed. In analogical setups this correction is applied before measuring using delay modules. On the contrary, with current digital modules this correction can be carried out off line by software (as it will be explained in Section 4.3.2).

Since we did not use any time module, the curve shown in Figure 4.9 was built as an alternative to the coincidence curve. The experimental true coincidence rate of specific emissions of ^{241}Am was determined as a function of the coincidence time. The number of coincidences for the 59.54 keV gamma-ray emission with any of the three main alpha-particle emissions (5388.23, 5442.80, and 5485.56 keV) was calculated. This coincidence region, including all three alpha emissions, was chosen due to a deconvolution procedure was then unnecessary. The true coincidence rate was determined following the method described in the introduction of Section 4.2. Figure 4.10 shows this coincidence region.

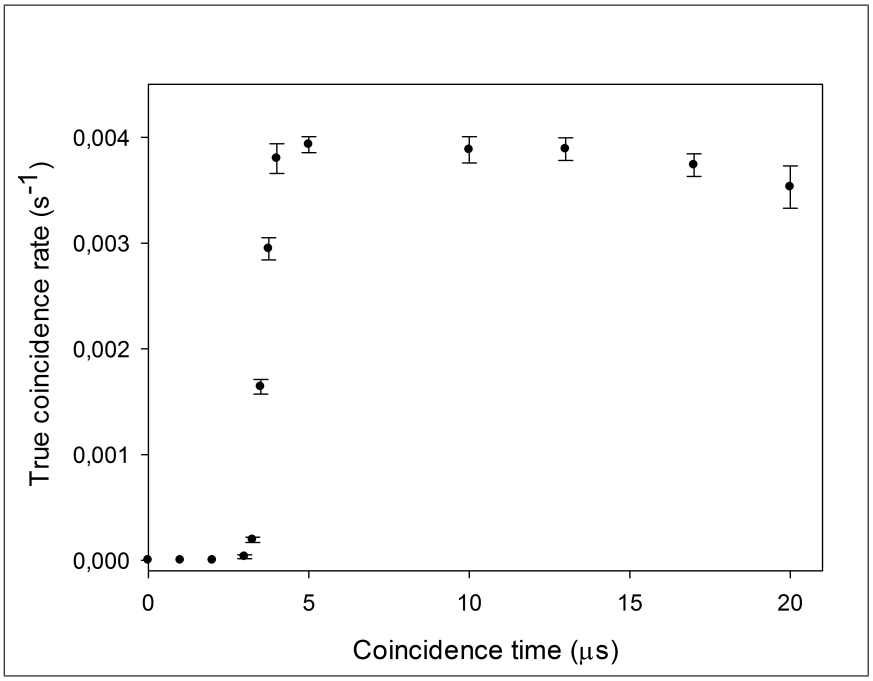

Figure 4.9: Variation of the true coincidence rate with the coincidence time. Taken from Jurado Vargas et al. [75].

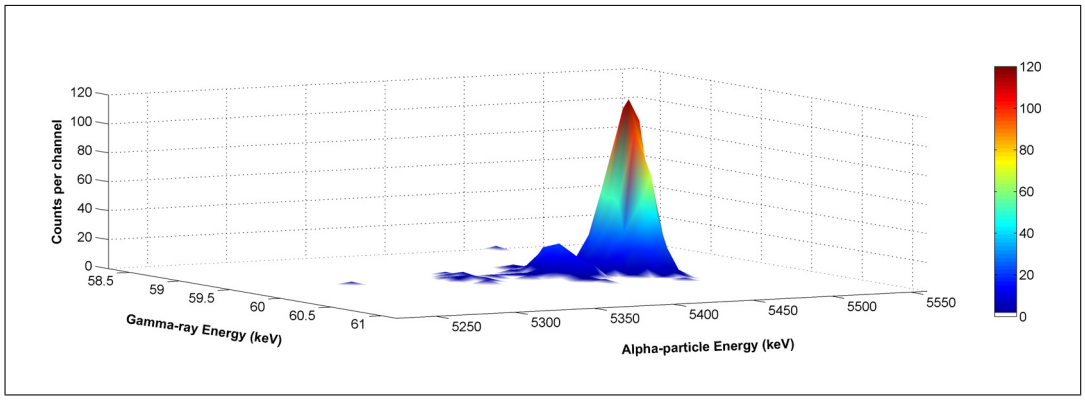

Figure 4.10: Coincidence region of the 5388.23, 5442.80, and 5485.56 keV alpha emissions with the 59.54 keV gamma-ray emission for ^{241}Am. The spectra were measured with 4096 channels, 5 μs coincidence time, and $\theta_1 = \theta_2 = 45°$ (see Figure 4.2a).

No true coincidences were registered when the coincidence time was shorter than 3 μs, as shown in Figure 4.9. Above 4 μs a plateau was observed showing a constant true coincidence rate. However, as the number of random coincidences increases with the coincidence time, the best value should be chosen at the beginning of the plateau, in this case $\approx 5\mu$s. Notice that, for larger values of the coincidence time, the true coincidence rate decreases slightly, which could be due to the fact that the dead-time of the system increases with the coincidence time.

Coincidence times extremely long become a problem with high counting rates because of the excessive registration of chance coincidences. Although this time could be lower using a delay module, in our case, due to the low activity of the source of interest, the use of $\tau = 5\mu$s was allowed. For this coincidence time, the true coincidence rate between alpha particles of 5485.56 keV and gamma photons of 59.54 keV was

$$r_{exp.\ true\ coin.} = (3.67 \pm 0.06) \times 10^{-3}\ s^{-1}.$$

Although this value can be influenced by angular correlation effects (due to a 90° measuring angle), it was compared with an estimation of the true coincidences assuming isotropy in order to see the consistency of the experimental result. The true coincidence rate assuming isotropy can be calculated as

$$r_{est.\ true\ coin.} = r_\alpha \cdot P_\alpha \cdot P_{\gamma}|_{\alpha} \cdot \epsilon_\gamma, \tag{4.1}$$

where r_α is the total experimental alpha rate, P_α is the emission probability corresponding to the alpha particles of 5485.56 keV, $P_{\gamma}|_{\alpha}$ is the emission probability for the 59.54 keV gamma photons conditioned to the desexcitation of the energy level, and ϵ_γ is the experimental detection gamma efficiency, previously obtained. The estimated true coincidence rate was

$$r_{est.\ true\ coin.} = (3.16 \pm 0.19) \times 10^{-3}\ s^{-1}.$$

Both values were compatible considering 2 σ. This compatibility of the results can be considered as an indicator that the experimental device is working properly. A more rigorous coincidence study for ^{243}Am (described in detail in Chapter 7) will provide an adittional validation of the coincidence set-up.

Source-to-detector angle

The influence of the source orientation on the coincidence rate and on the shape of the peaks in the spectra was also studied. Once again the source of ^{241}Am was used and the coincidences between the three main alpha-particle emissions (5388.23, 5442.80 and 5485.56 keV) and 59.54 keV photons were studied. Three positions were used: $\theta_1 = 70°$ and $\theta_2 = 20°$, $\theta_1 = \theta_2 = 45°$, and $\theta_1 = 20°$ and $\theta_2 = 70°$ (see Figure 4.11).

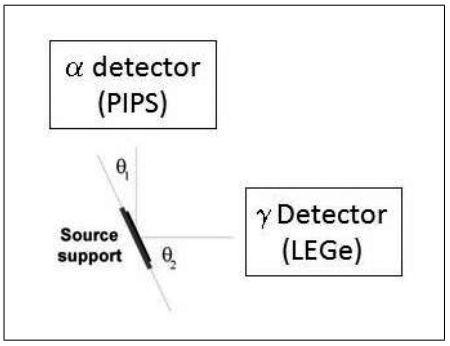

Figure 4.11: Source-to-detector angles.

The contour graphics for each case are drawn for comparison in Figure 4.12. For the alpha region, peak widths increased and their positions shifted towards the lower-energy region as the measurement angle θ_1 decreased (and θ_2 increased). The reason is that under big source-to-detector angles, alpha particles lose more energy because they must go through a longer path. A widening in the gamma region for small angles θ_2 was also observed, although it was less important than for alpha peaks.

Coincidence rates were calculated for the three cases, obtaining statistically identical results. For that reason, and taking into account that gamma-rays were less affected by orientation than alpha-particles, the angle θ_1 could be chosen somewhat greater than θ_2, thus obtaining spectra with improved energy resolution.

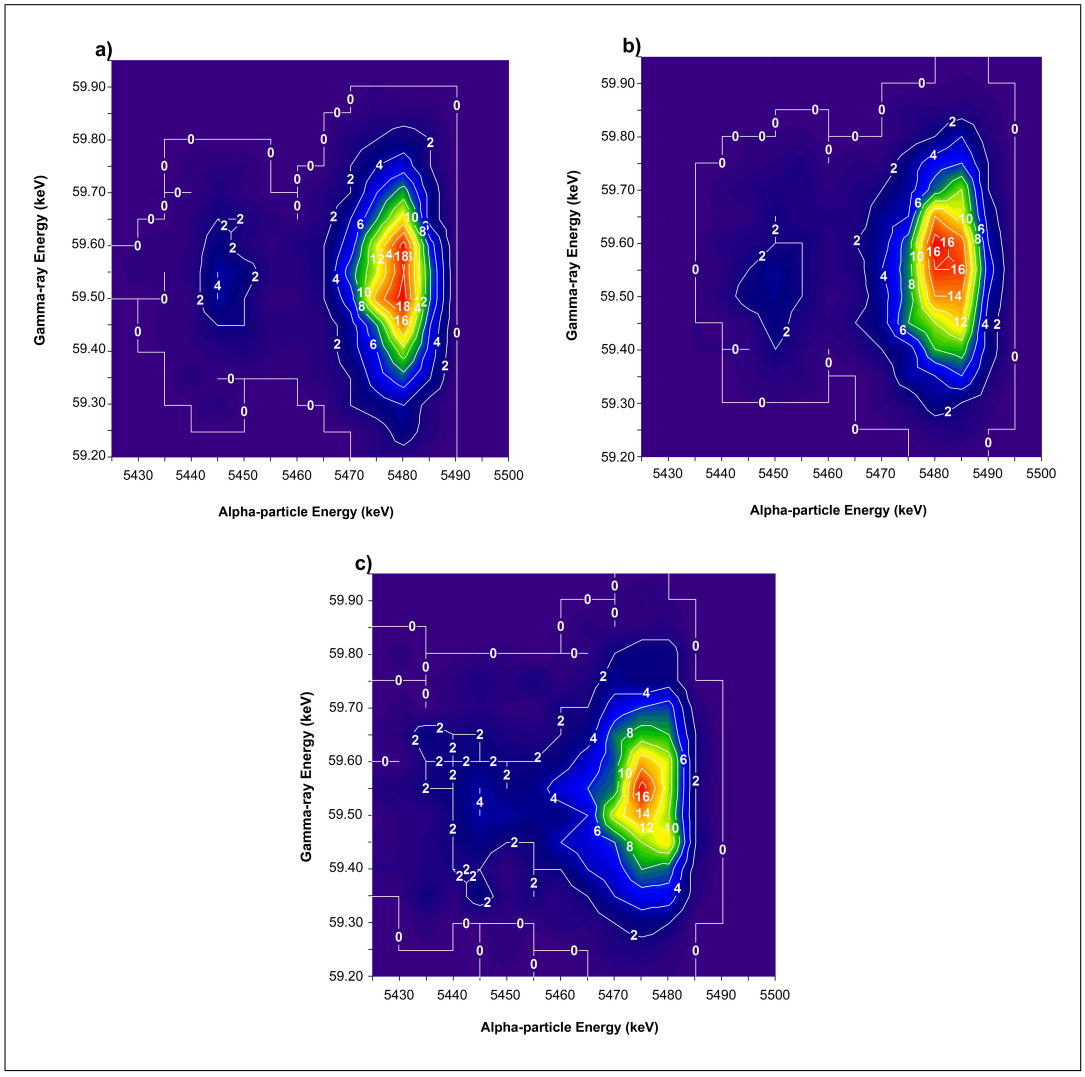

Figure 4.12: Contour graphics of the coincidence spectrum ($\times 10^{-5} s^{-1}$) measured with 4096 channels in both ADCs. Three source orientations were used: (a) $\theta_1 = 70°$ con $\theta_2 = 20°$, (b) $\theta_1 = \theta_2 = 45°$, and (c) $\theta_1 = 20°$ con $\theta_2 = 70°$. Taken from Jurado Vargas et al. [75].

4.3 Digital acquisition system

Traditionally, in the field of coincidence techniques, coincidences between pulses, arriving from detectors, have been determined using analog modules, which include single-channel analyzers, delay lines, coincidence units, scalers, etc. Newer set-ups, as the one described in Section 4.1, permit the determination of coincidences using digital dual-parameter multichannel analyzers, although no time information is registered with these systems.

Recent advances in digital signal acquisition technology are fostering its introduction in the field of experimental nuclear physics [77–79]. Digital systems facilitate the possibility of storing pulse information from multiple detector systems along with a time stamp for each recorded event, allowing various methods to be implemented "offline" via the use of dedicated software routines. The stored data can then be analyzed for the presence of coincidences. The result obtained depends less on the stability and reproducibility of the electronic parameters, since many analog modules become unnecessary. Moreover, the data stored on a hard disk has a primary form, which enables different methods of statistical processing to be employed and compared over the same data set.

For these reasons, it was decided to use a digital module for the coincidence study. The main features of the digital module, as well as the data treatment code developed in our laboratory to analyze events registered by the module, will be detailed in the following sections.

4.3.1 Description of the digital module

Preamplifier outputs from PIPS and LEGe detectors are directly connected to a digital module N1728B from CAEN (see Figure 4.13, right side). This module consists of a pulse processor and wave shape digitizer of four input channels operating in parallel [89]. Integrated process occurs in a TNT card (Tracking Numerical Treatment [90]) and provides an on line pulse processing offering advanced high-resolution spectroscopy capabilities. An FPGA Xilinx Virtex II implements pulse processing and the hardware control. An additional FPGA Spartan II [91] provides system reconfiguration.

Figure 4.13: Comparison of the electronic modules used by the analogical coincidence system (left side) with the digital module (right side).

The digital module can work in two modes: "oscilloscope" and "energy". The "oscilloscope mode" is the simplest operating mode. The card works as an oscilloscope, sampled data from ADCs is continuously stored in memory. The context of the "energy mode"' is to process the detector output from the preamplifier stage used in nuclear physics experiments.

The amplitude of the registered signal is proportional to the energy of the particle which interacts with the detector. The calculation of the height of the pulse is carried out deconvolving in real time the preamplifier signal into a trapezoid shape using a wide range of programmable filter parameters [92].

Digital modeling provides a very good energy resolution, decreases ballistic deficit [93, 94], and presents a good base line stability for high count rates. An algorithm for digital trigger allows to operate with low energy thresholds, ensuring immunity to noise effects. Module control, signal treatment and classification, and data display and saving are carried out by the acquisition software TUC (TNT USB Control).

The digital module offers many possibilities and TUC has many options to widely control the measuring process. However, working in "energy mode"' (which allows to create energy spectra), the number of parameters to be controlled decreases. Mainly just the *trigger* values and the energy calculation parameters have to be optimized. The most important parameters are described below.

Trigger parameters

Different trigger parameters can be set in "Parameters of selected card 1/3" (Figure 4.14). The two most important are:

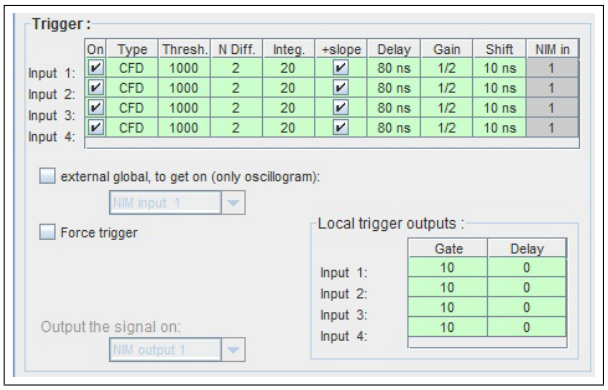

Figure 4.14: Trigger parameters from digital module to be optimized.

Type: simple, digital, CFD (Constant Fraction Discriminator) or external. In our case, a digital trigger was used. It compares a reference threshold value with the filtered preamplifier signal [91].

Threshold: it allows to discriminate noise pulses. It must be adjusted in each measurement because it depends on the kind of signal, the number of

inputs, etc. On average, a threshold value of +650 for gamma pulses and -650 for alpha pulses were used. The trigger signal creation process is summarized in Figure 4.15.

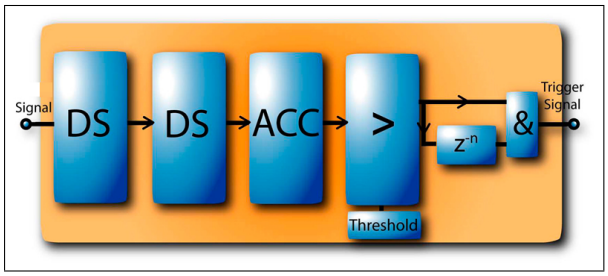

Figure 4.15: Trigger signal creation process as a function of the preamplifier pulse. [91].

Parameters for energy calculation

Each time a trigger occurs, the card calculates an average of the trapezoid height (modeled pulse amplitude) which will be proportional to the energy of the detected radiation. The parameters needed for this calculation can be set in "Parameters of selected card 2/3" (Figure 4.16). The most important are:

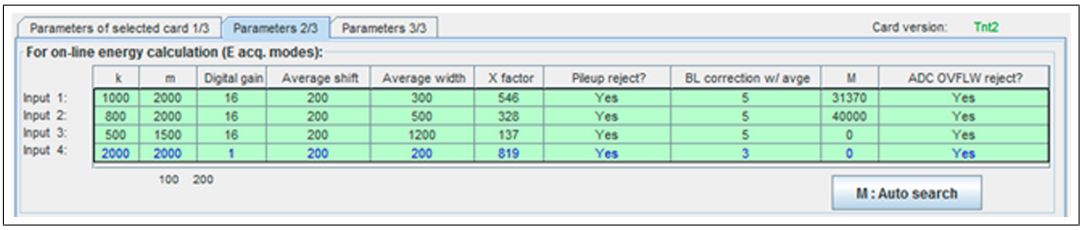

Figure 4.16: Trapezoid parameters to be optimized to calculate the height of the registered pulses (proportional to the energy of the detected radiation).

The shape parameters (Figure 4.17):

k: trapezoid rise time expressed as sampling periods (10 ns for each period). Values of 800 and 1000 were used for alpha and gamma pulses, respectively.

m: width of the trapezoid flat top expressed as sampling periods. In our case, a value of 2000 was used for both kind of pulses. The trapezoid height will be calculated $k + m$ points after the trigger point.

Average shift: value expressed in ns which indicates how many sampling points have to be counted from the beginning of the flat top to start to calculate an average value of the trapezoid height. It must be taken into account that $Shift + width \leq (m - 5)\, sampling\, periods$. The "average shift" was 200 for both kind of pulses.

Average width: parameter expressed in ns which indicates how many sampling points on the flat top will be considered to calculate the average trapezoid

height and, therefore, the energy. The greater the "average width", the better the trapezoid height calculation and, hence, the energy. A value of 1400 was used for both kinds of pulses.

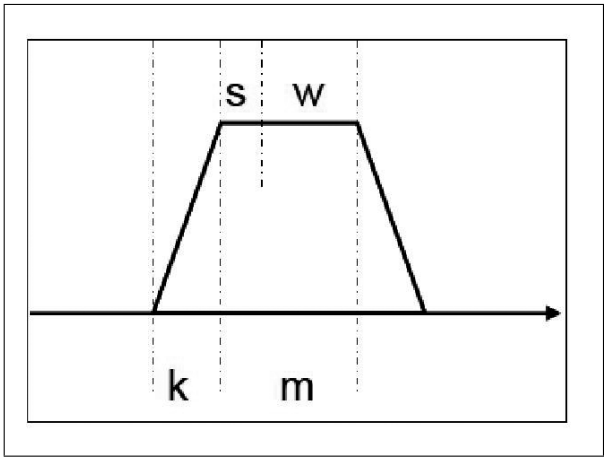

Figure 4.17: Trapezoid rise time (k), width of the trapezoid "flat top" (m), "average shift" (s) and "average width" (w).

Pile-up reject?: the program permits the possibility of reject or not reject pile-up events (being saved in the event file with an especial input number). A pile-up occurs if while the card is constructing the trapezoid, another trigger is detected before the end of the flat top has been reached. Two pile-up situations are possible:

- Both events will be considered as piled-up if the second trigger occurs before the energy related to the first trigger has been taken.
- Only the second event will be considered as piled-up if it occurs after the energy related to the first trigger has been taken.

In our case, measurements were carried out considering pile-up events. Afterward, during the decodification process and data treatment, the user decides to apply or not event discrimination.

M: time decay constant of the detected pulses. This value is calculated using "M: Auto search" (see Figure 4.16). Sometimes the value calculated by the program presents problems and the measurement is impossible to be carried out. Then, "M" will have to be slightly modified till measurement is possible. Values of 35580 and 40000 for gamma and alpha signals, respectively, were chosen.

ADC OVFLW reject?: this option allows to remove pulses with amplitudes out of ADCs limits. This option was selected in every measurements. However, against what happened with pile-up events, the digital module does not eliminate all ADC overflow events although the reason is unknown. This fact

has been checked with the data treatment software.

Once these parameters are set, the card is updated with "Update card" (Figure D.1) and the digital module is ready to measure in energy mode. Figure 4.18 shows a screenshot of the "Energy histograms" tab with two energy spectra of ^{241}Am: a gamma-ray spectrum (in red), and an alpha-particle spectrum (in green).

Before each measurement starts, the user should indicate if data will be stored or not. If stored, both the path ("Backup dir:") and the kind of file (binary or ASCII, see Figure 4.7) should be defined. Saving data with ASCII format is not recommended because information of all events is not stored, hence, binary files are more advisable. Mainly for that reason, the development of the code DIGDATA for data decodification and treatment was necessary. Its features are described in Section 4.3.2.

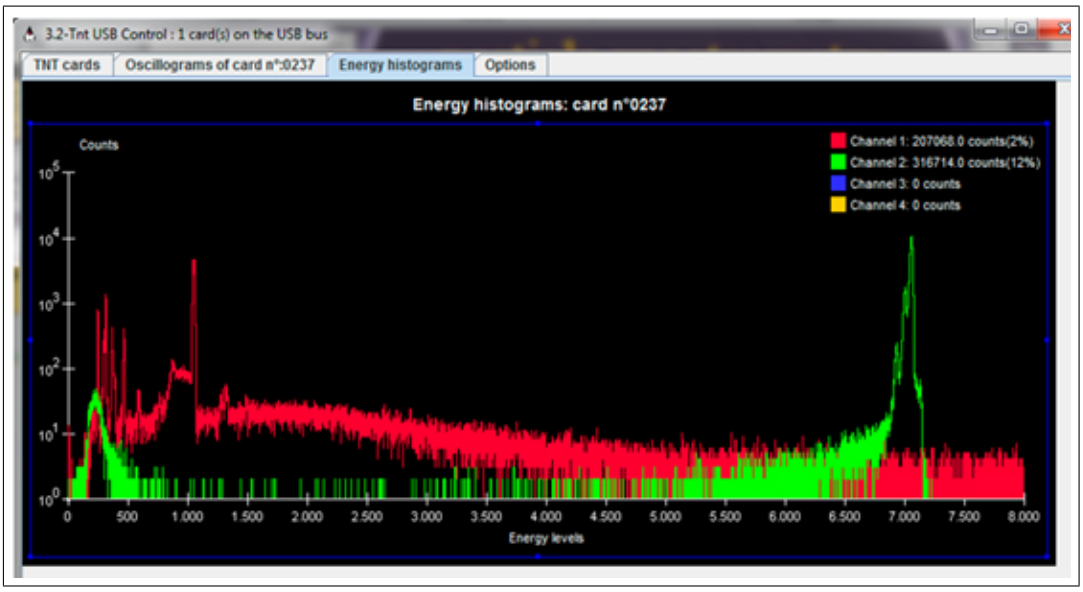

Figure 4.18: Screenshot of the "Energy histograms" tab showing two energy spectra from ^{241}Am: a gamma-ray spectrum (in red), and alpha-particle spectrum (in green), corresponding to ^{241}Am.

4.3.2 DIGDATA: decoding and data treatment program

Every time a trigger occurs in an input working in "energy mode" the so-called "energy event" is created. The information contained in the event is the following:

- Number of the module input.
- Trigger number.
- Timestamp (value that multiplied by 10 gives the registration time of the signal in *ns*).

- Associated channel, i.e. amplitude, as a function of the flat top height of the trapezoid and the pulse polarity.

In order to efficiently store these events, data are saved in binary files. Data are encoded following the "big endian order" as follow: 6 unsigned bytes for the registration time, 4 unsigned bytes for the trigger number, 2 signed bytes for the corresponding channel and 2 unsigned bytes to indicate the number of the input (existing special bits with information about pile-up, ADC overflow events, etc.).

With the purpose of decoding these files and carrying out their analysis, the data treatment code DIGDATA has been developed. It is a graphic user interface (GUI) written in Matlab R2010a©. It consists of five tabs:

- *Decodification*
- *Dead Time Control*
- *Time Histograms*
- *Energy Histograms*
- *Coincidences*

The software allows the binary file decodification, the application of the dead time correction, the energy and time histogram creation, and the coincidence analysis of the signals. All the features of the code are described bellow.

With "Open File" option from the "File" main menu, binary files with .evt extension are opened. Once the file is opened, the path and the file name appear in the "pop-up" menu placed just under the main menu (Figure 4.19).

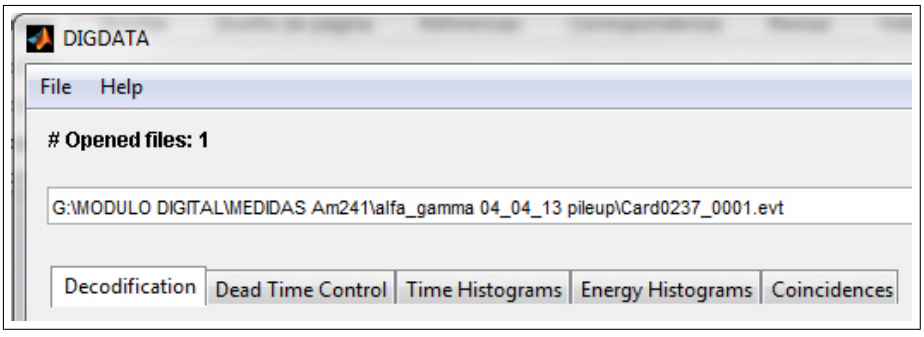

Figure 4.19: Screenshot of the main menu, the "pop-up" menu with the file name and the tabs of the data treatment software, DIGDATA.

The first working tab is ***Decodification*** (Figure C.1). Pressing "DECODE" button one or several files can be decoded and information about decodification time, measuring time and number of registered events is shown in the main screen. The code permits the decodification of the whole file (or

files) or just processing events occurred till a determined time. At the end of the process data can be saved in files with ".txt" extension using "Save Events Matrix" button.

After the decodification process, an event classification is carried out using "Input Discrimination" button, taking into account the used input. A message box will appear informing about the inputs registered in the file. Through "Input Selection" panel, the user indicates to the program what inputs have been used and what kind of signals have been registered. The code will distinguish pulses by polarity. The pulse polarity depends on the preamplifier configuration; in our case, alpha pulses have a negative polarity and gamma pulses have a positive polarity.

In other parts of the code the matrices with the classified events ("eventsdif") will be necessary so they will be saved with ".mat" extension in the current folder. In this way, processes from each different tab can be applied separately.

For detection systems that record discrete events, the *dead time* is the time after each event during which the system is not able to record another event. Through ***Dead Time Control*** tab (Figure C.2) it is possible to discriminate "detected" and "lost" events indicating a certain dead time for each input.

Two kinds of dead time can be carried out for each input, *nonparalyzable* and *paralyzable*. In the first case, events that happen during the dead time are lost and assumed to have no effect whatsoever the behavior of the detector. However, with a paralyzabled dead time, events that occur during the dead time, although are not registered as counts, extend the dead time by another period following the lost event [1]. Figure 4.20 shows an illustrative example. These two models substantially differ for high counting rates.

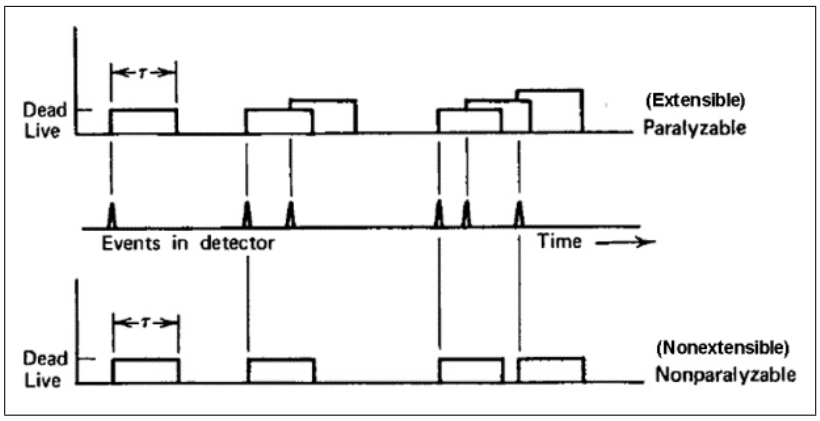

Figure 4.20: Examples of the paralyzable (top) and nonparalyzable (bottom) dead time models, taken from Knoll [1].

Correction is applied pressing "Dead Time Discrimination" button. An "open" dialog appears asking the user which ".mat" file (or files) containing the "eventsdif" matrices will have to be processed.

Information about the number of detected events, lost events, effective measurement time (in seconds) and the total dead time (in seconds and percentage) is displayed when the program ends. Matrices with the detected events ("eventsdead") are saved in the current folder with ".mat" extension. It is also possible to save information about these detected events in ".txt" files using "Save Matrices" button.

Dead time is introduced in micro seconds; the minimum value is 0.01 μs that is the time resolution of the digital module. Common times of 1 and 10 μs for alpha-particle and gamma-ray detection, respectively, were applied in our case.

The creation of time histograms corresponding to the four inputs of the digital module is possible using the ***Time Histograms*** tab (Figure C.3).The first step is indicating the time resolution of the histograms in microseconds taking into account that the minimum value is 0.01 μs. Once that is done, the "Create Histograms" button is pressed and then the code asks about the ".mat" file (or files) with the "eventsdead" matrices.

Time histograms are internally created and ready to be saved (using "Save Histograms") or to be plotted (using "Save Graphics"). In this last case, a time range has to be selected for the different inputs, an scale for the vertical axis (linear or logarithmic) has to be indicated, as well as the image resolution in "ppp" to save graphics with ".tif" extension. An example of a time histogram is shown in Figure 4.21.

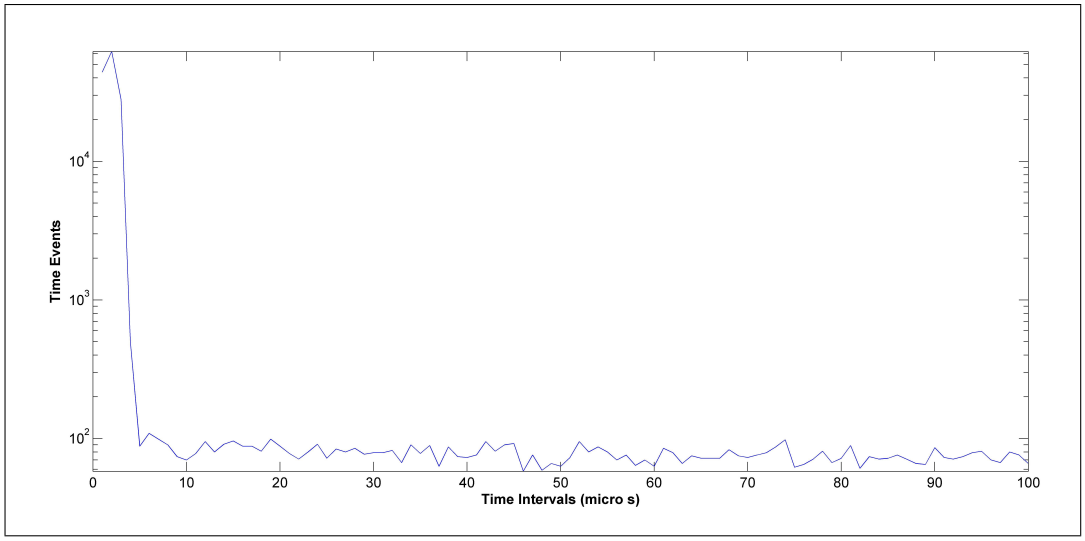

Figure 4.21: Time histogram of the electronic chain for gamma-ray detection of a ^{88}Y source. A dead time of 1 μs was applied.

In the ***Energy Histograms*** tab (Figure C.4) energy histograms corresponding to the four inputs of the module are created using the "Create Histograms" button. During this process, an event discrimination is carried out. The code identifies and dismisses "ADC overflow" events, "ADC overflow + Pile-up", signals with opposite polarity to the true pulses which are registered

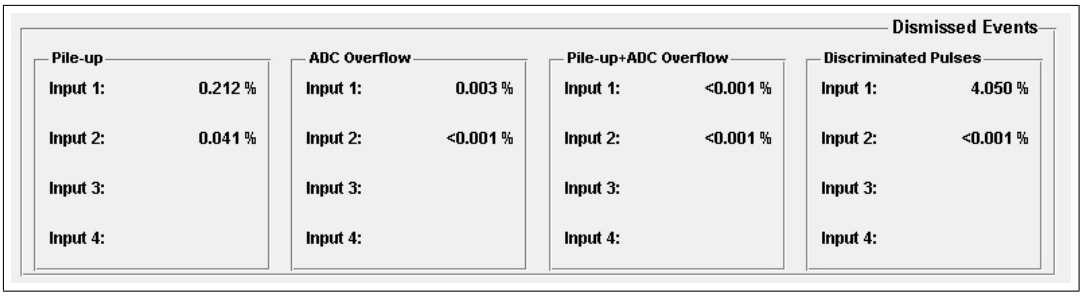

Figure 4.22: Percentages of dismissed events during the energy histogram creation in the "Energy Histograms" tab from DIGDATA.

in that input, and, optionally, "Pile-up" events. The percentage between these events and the detected events is shown in the "Dismissed Events" panel (Figure 4.22). The information referred to these events can be saved in ".txt" files through question dialogs which appear during the energy histogram creation process.

Once the histograms are created, they can be saved with ".txt" extension for their subsequent use with "Save Histograms" button or can be plotted through the "Save graphics". In this case, a range of channels for each input, the vertical axis scale (linear or logarithmic) and the resolution of the ".tif" files have to be selected. Counts can be plotted versus channel as well as energy indicating energy calibration parameters with "Use of Calibration".

The digital module classified events in 32768 channels by defect. Every event analysis is carried out using this number of channels. However, in some cases, working with less channels could be preferable, so the option of reducing the number of channels ("# of Channels Reduction" panel) will be useful. In the "pop-up" menus the number of channels for each input is selected.

Channel reduction is applied to save the energy histograms as well as to plot the corresponding energy spectra. Several message boxes inform the user of the number of channels with which the histograms will be saved or plotted. Figure 4.23 shows, as an example, an alpha energy histogram from the ^{243}Am source.

Finally, the ***Coincidences*** tab is described. The main advantage of a digital system is completely appreciated in this part of the program: the possibility of carrying out different analysis offline changing the values of some parameters, like the coincidence time, after just one measurement.

The code is programmed to establish coincidences between just two inputs. The first step is to indicate the signals from which input open the coincidence time window, "Start Input", through the "Coincidence Start Input" panel (Figure C.5).

The next step is the selection of a range of channels to create the coincidence matrix. Although coincidences are established for the whole range of channels (32768), in order to create the dual-parameter coincidence histogram (with dimensions $\#StartInputchannels \times \#Coin.Inputchannels$) a choice of a smaller range (to avoid exceeding the memory limit for the code) is necessary.

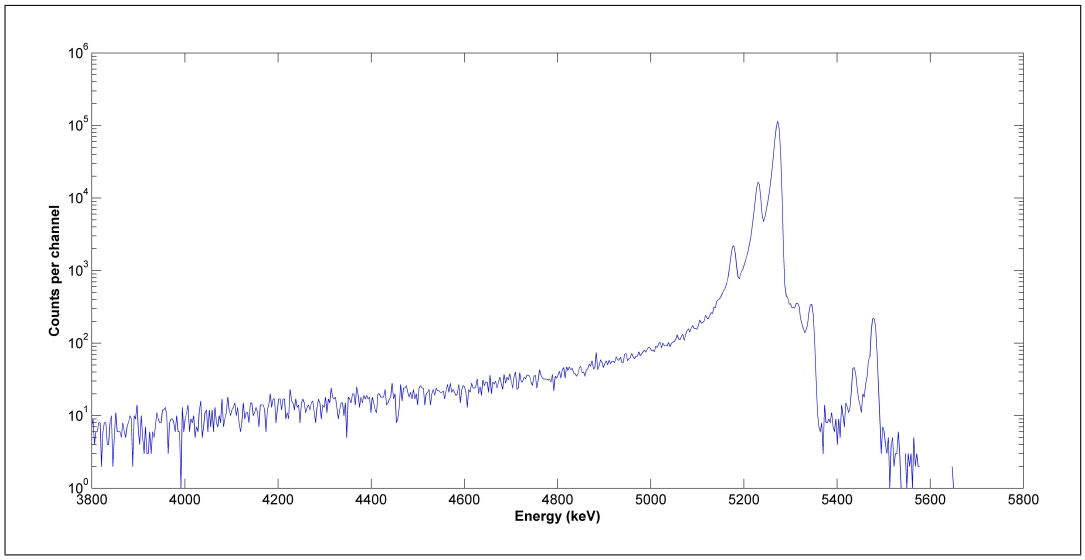

Figure 4.23: Alpha-particle spectrum of ^{243}Am reduced to 8192 channels.

The last step is the choice of the coincidence time (in μs). As mentioned above, the way of finding the optimal coincidence time is to construct the so called *coincidence curve*, measuring the time delay between two pulses. This curve is created using the "coincidence time" button. Both the graphic and the time histograms can be saved as ".fig" and ".txt" files. Ideally, this curve should have a Gaussian shape and be centered in the coordinate origin. The shift of the curve to the origin indicates the delay which should be applied to the events. The width of the curve gives the value of the coincidence time. Figure 4.24 shows the coincidence curve of ^{243}Am obtained from the timestamps registered by the digital module.

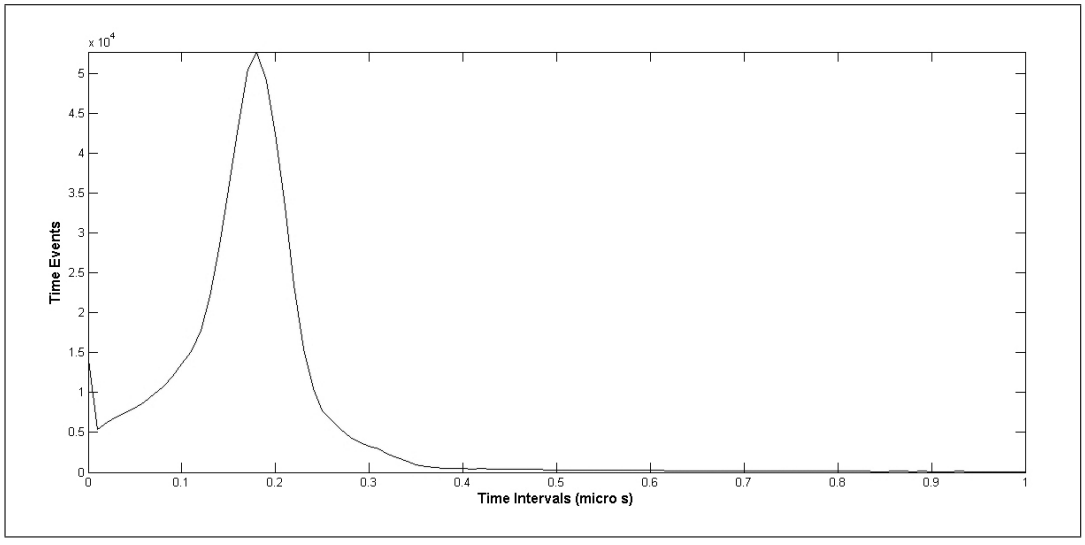

Figure 4.24: Coincidence curve of ^{243}Am obtained from the timestamps registered by the digital module.

When the "Set Coincidences" button is pressed the user has to select the ".mat" file (or files) with the "eventsdif" matrices. Coincidences are established taking into account all registered events. During this process, dead time correction and event discrimination are carried out with the aid of several question dialogs.

As a result, DIGDATA provides the following information: the coincidence setting time, the total number of coincidences, the number of rejected coincidences produced by dismissed events, the number of coincidences in cascade (just one "Start Event" coincident with several "Coincident Events")and the number of coincidences between several "Start Events" and just one "Coincident Event". A question dialog asks the user to save the information about the last kind of coincidence events in ".txt" files for its subsequent use, if necessary.

Once the dual-parameter histogram is created, it can be saved in ".txt" file pressing the "Save Coincidence Matrix" button. Dual-parameter plots and contour graphics can be created as a function of the number of channels or the energy, as well as in COLMA (see Section 4.2.1), using the "Save Graphics" button.

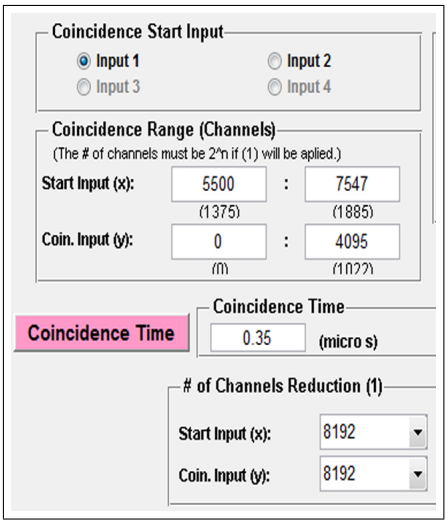

Figure 4.25: Detail of the "Coincidences" tab from DIGDATA corresponding to the reduction of the number of channels.

The option for the number of channel reduction is again available. It is important to note that if the user wants this option, the number of channels selected in "Coincidence Range" has to be a power of two (e.g., 512, 1024, etc) in order to a proper reduction of the dual-parameter histogram. Once the number of channels is chosen in the "pop-up" menu, the reduced number of channel equivalent to the original one appears under the "edit boxes" in "Coincidence Range" (see Figure 4.25).

As an example, a dual-parameter spectrum and a contour graphic of ^{243}Am are shown in Figure 4.26. The coincidence region of the three main alpha-particle emissions (5181, 5233.3 and 5275.3 keV) and the gamma region between 10 - 80 keV were plotted in this case.

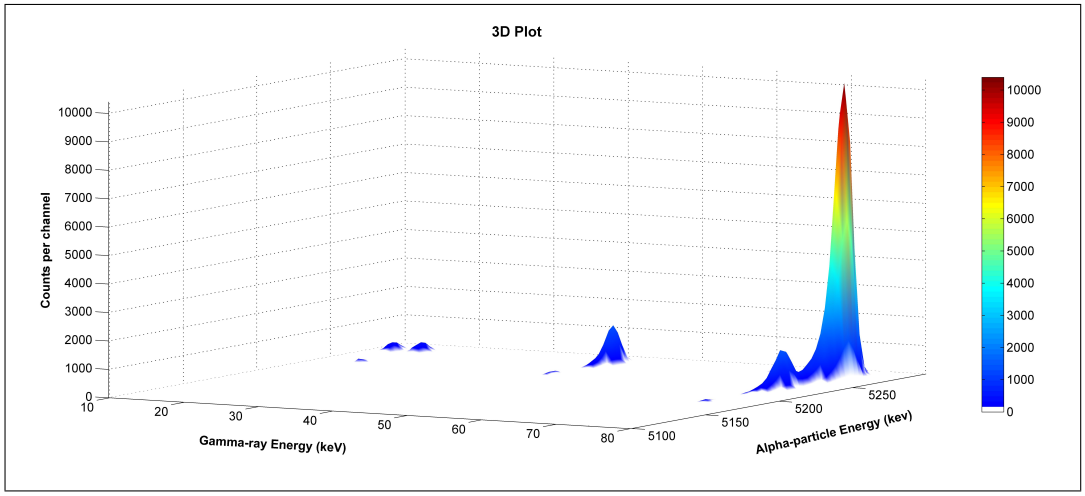

(a) Dual-parameter plot.

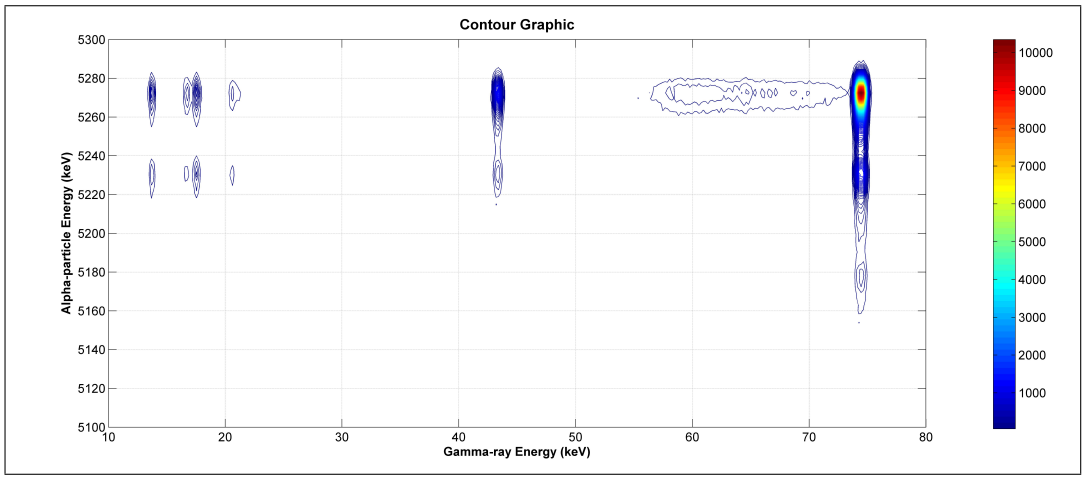

(b) Contour graphic.

Figure 4.26: Coincidence spectrum of ^{243}Am. A number of channels of 8192 and a coincidence time of 0.35 μs were chosen. The spectrum was measured forming $\theta_1 = \theta_2 = 45°$ (see Figure 4.2a).

Part III

Spectral analysis

Chapter 5

ALFITeX: A new code to fit alpha-particle spectra

This chapter describes the work done in the development of a new code, called ALFITeX [21], which combines parts of codes previously developed [58], and includes new features that have been added to improve its performances. The main requirements imposed in the development of the code are computational speed, a robust optimization method, and a very user-friendly interface. Technically, the computation algorithm is based on the Levenberg-Marquardt minimization method using the line shape formed by the convolution of a Gaussian curve with two or three left-handed exponentials in the low-energy-tail region[1].

An important issue found with previous codes is that the operations that are needed to perform matrix inversion frequently presented divergence problems, and in some cases the code failed to find the best values for the fitting parameters. The use of more robust matrix treatment techniques was therefore implemented, making the code both more accurate and reliable in computing the best fit to the experimental data. The ALFITeX code is written in Visual Basic for Microsoft Office Excel 2010© spreadsheets, incorporating several features aimed at making it a fast, robust and useful tool with a user-friendly interface.

5.1 Mathematical background

ALFITeX uses the line shape formed by the convolution of a Gaussian curve with the weighted sum of two left-handed exponentials in the low-energy-tail region proposed by Bortels and Collaers in 1987 [45]. In order to improve the tail approximation, they adapted L'Hoir's peak-shape function [33], which was based in the analytical function firstly proposed by L'Hoir [95] and later described by L'Hoir et al. [96] and Amsel et al. [97]. This line shape can be interpreted as a joint-probability-density function taking into consideration the symmetric (electronic noise and energy straggling) and asymmetric (incom-

[1]The last version of the code permits the selection of the use of two or three exponentials.

plete charge collection) effects in the alpha-particle detection process. Due to the agreement between the results obtained with this analytical function and experiments, other previously published codes are based in this peak-shape function, e.g. ALFA, developed by Babeliowsky and Bortels [54] and FITBOR, created by Martín Sánchez et al. [58].

In the present work, the contribution of a potential constant background due to the tailing of possible higher energy emissions or to unstructured noise is also considered. The mathematical expression for the total spectrum (understood as the sum of the component peaks and the background) is

$$\begin{aligned} F(u) = \sum_{i=1}^{npeaks} \frac{A_i \sigma \sqrt{2\pi}}{2} \Bigg[& \eta_1 \tau_1 exp\left((u-\mu_i)\,\tau_1 + \frac{\sigma^2 \tau_1^2}{2} \right) \\ & \times erfc\left(\frac{1}{\sqrt{2}} \left(\frac{u-\mu_i}{\sigma} + \sigma\tau_1 \right) \right) \\ & + (1-\eta_1)\,\tau_2 exp\left((u-\mu_i)\,\tau_2 + \frac{\sigma^2 \tau_2^2}{2} \right) \\ & \times erfc\left(\frac{1}{\sqrt{2}} \left(\frac{u-\mu_i}{\sigma} + \sigma\tau_2 \right) \right) \Bigg] + bck, \end{aligned} \tag{5.1}$$

where A_i is the height of each peak, σ is the Gaussian distribution parameter, $erfc$ is the complementary error function, η_1 is the weight of the first exponential (with $1-\eta_1$ being the weight of the second exponential), u the channel number, μ_i the peak positions, τ_j the exponential parameters (j = 1, 2), and bck the optional background contribution. σ, η_1, τ_j and bck are considered the same for all peaks.

Taking into account a fitting model depending on an array of parameters $\alpha_k\,(k = 1, ...N)$ in a nonlinear way, a function χ^2 is defined, and the best parameters which minimize this function are calculated by an iterative process. This process is repeated until a minimum value of χ^2 is found. The statistical significance level is given by the final reduced χ^2 value:

$$\chi_r^2 = \frac{1}{\nu} \sum_{j=1}^{N} \left(\frac{y_j - y\,(u_j; \boldsymbol{a})}{\sigma_j} \right)^2, \tag{5.2}$$

where ν is the number of degrees of freedom, N the number of channels considered in the fit, y_j the experimental values for each channel, σ_j their associated uncertainties, $y\,(u_j; \boldsymbol{a})$ the analytical value calculated with the fitting function in channel j (which depends on the set of fitting parameters included in the vector $\boldsymbol{a}$). The fitting procedure used is based on the ***Levenberg-Marquardt*** algorithm which seeks the minimum of the χ^2 function using jointly the inverse Hessian and the steepest descent methods [98]. Considering the gradient of χ^2 respect to the parameters $\boldsymbol{a}$

$$\frac{\partial \chi^2}{\partial a_k} = -2 \sum_{i=1}^{N} \frac{y_i - y\,(x_i; \boldsymbol{a})}{\sigma_i} \frac{\partial y\,(x_i; \boldsymbol{a})}{\partial a_k}, k = 1...M \tag{5.3}$$

and taking partial derivatives

$$\frac{\partial^2\chi^2}{\partial a_k \partial a_l} = 2\sum_{i=1}^{N}\frac{1}{\sigma_i^2}\left[\frac{\partial y\left(x_i;\boldsymbol{a}\right)}{\partial a_k}\frac{\partial y\left(x_i;\boldsymbol{a}\right)}{\partial a_l} - \left(y_i - y\left(x_i;\boldsymbol{a}\right)\right)\frac{\partial^2 y\left(x_i;\boldsymbol{a}\right)}{\partial a_k \partial a_l}\right], \tag{5.4}$$

it is possible to define a matrix equal to one-half times the Hessian matrix, called "curvature matrix" ($\boldsymbol{\alpha}$) in the context of least-squares, and a vector $\boldsymbol{\beta}$ which is one-half times the gradient of χ^2.

$$\alpha_{kl} = \frac{1}{2}\frac{\partial^2\chi^2}{\partial a_k \partial a_l}, \beta_k = -\frac{1}{2}\frac{\partial\chi^2}{\partial a_k} \tag{5.5}$$

The best value for the fitting parameters is obtained by solving the set of linear equations

$$\sum_{l=1}^{N}\alpha_{kl}^{'}\delta a_l = \beta_k, \tag{5.6}$$

where

$$\alpha_{kl}^{'} = \begin{cases} \alpha_{jj}(1+\lambda) \\ \alpha_{jk}, (j \neq k) \end{cases} \tag{5.7}$$

The diagonal elements of the covariance matrix $(\boldsymbol{\alpha})^{-1}$ are the *variances* of the fitting parameters, a_k. The square roots of these elements give the uncertainty associated with each ones. Applying the standard methods of error propagation the uncertainties of peak areas and emission probabilities can be calculated. If parameters are not correlated, and considering an ideal case, the non-diagonal elements of the matrix (called *covariances*) would be zero. However, in practice, these elements are not zero because some parameters can be correlated, due in part to numerical problems. The covariances must be taken into account for the uncertainty calculation only in the case that variables are correlated [99].

The uncertainty obtained from this procedure is underestimated because it just covers the effects of the fitting uncertainties and the counting statistics. In order to calculate an accurate uncertainty for the emission probabilities the contribution of other factors has to be considered, such as source impurity or the effect of the coincidence-summing corrections.

ALFITeX applies Singular Value Decomposition (SVD) as the matrix inversion method instead of the traditional Gauss-Jordan (GJ) method [98]. The minimization procedure is better performed with SVD than with GJ, especially when the curvature matrix is singular or quasi-singular (i.e., "ill-conditioned"). The SVD method also allows the identification of those parameters which do not strongly contribute to the χ^2 minimization [100]. The SVD method is based on the fact that any $M \times N$ matrix $\boldsymbol{A}(M \geq N)$ can be written as

$$\boldsymbol{A} = \boldsymbol{U} \cdot \boldsymbol{W} \cdot \boldsymbol{V}^T, \tag{5.8}$$

where $\boldsymbol{U}$ is an $M \times N$ column-orthogonal matrix, $\boldsymbol{W}$ an $N \times N$ diagonal matrix with positive or zero (ω_j) elements (the singular values), and the transpose of $\boldsymbol{V}$, an $N \times N$ orthogonal matrix. This decomposition can always be done, no matter how singular or ill-conditioned the matrix might be. In these cases, the pseudo-inverse matrix of $\boldsymbol{A}$ must be calculated as

$$\boldsymbol{A}^{-1} = \boldsymbol{V} \cdot \left[diag\left(\omega_j^{-1}\right) \right] \cdot \boldsymbol{U}^T, \tag{5.9}$$

where ω_j^{-1} is replaced by zero if $\omega_j = 0$ (singular matrix). If the ω_j values are non-zero but very small (ill-conditioned matrix), the solution obtained by zeroing small ω_j's will be better in the sense of the best approximation. In order to decide which values are "small", SVD requires a reference value (threshold) which will be provided by the user when the ω_j's are known.

Considering a general system of equations $\boldsymbol{A} \cdot \boldsymbol{x} = \boldsymbol{b}$, the pseudo-inverse matrix is the minimal solution of the system. On one hand, if there are no singularities and the system has a unique solution $\boldsymbol{x}$, the minimal solution coincides with $\boldsymbol{x}$. On the other, if there are singularities, $\boldsymbol{x}$ is the solution which minimizes the residual

$$r \equiv \left| \boldsymbol{A} \cdot \boldsymbol{x} - \boldsymbol{b} \right|. \tag{5.10}$$

In order to know the state of the matrix $\boldsymbol{A}$, the *condition number*, defined as the ratio of the largest (in magnitude) of the ω_j's to the smallest of the ω_j's, must also be known. A matrix is singular if its condition number is infinite, and is ill-conditioned if its condition number is too large, i.e., if its reciprocal approaches the machine's floating-point precision (for example, less than 10^{-12} for double precision) [98].

5.2 Description of the code

ALFITeX is written in Visual Basic for Microsoft Office Excel 2010 spreadsheets. One of the most important advantages of this approach is that all the data (both initial data and results)are stored in different sheets of the same workbook, which facilitates their verification and subsequent use. The program consists of six folders[2]: "Master", "Spectrum", "Fitting Parameters", "Graphics", "Matrix", and "INFO" (See Figure 5.1).

The control of the program and the introduction of the initial parameters are implemented in the folder **"Master"** (Figure B.1). From this folder, ALFITeX opens the spectrum file and calculates the optimal fitting parameters, starting with the values indicated by the user. Any initial parameter can be individually changed and the fitting process can be repeated whenever the user

[2]Screenshots of the program are shown in Appendix B.

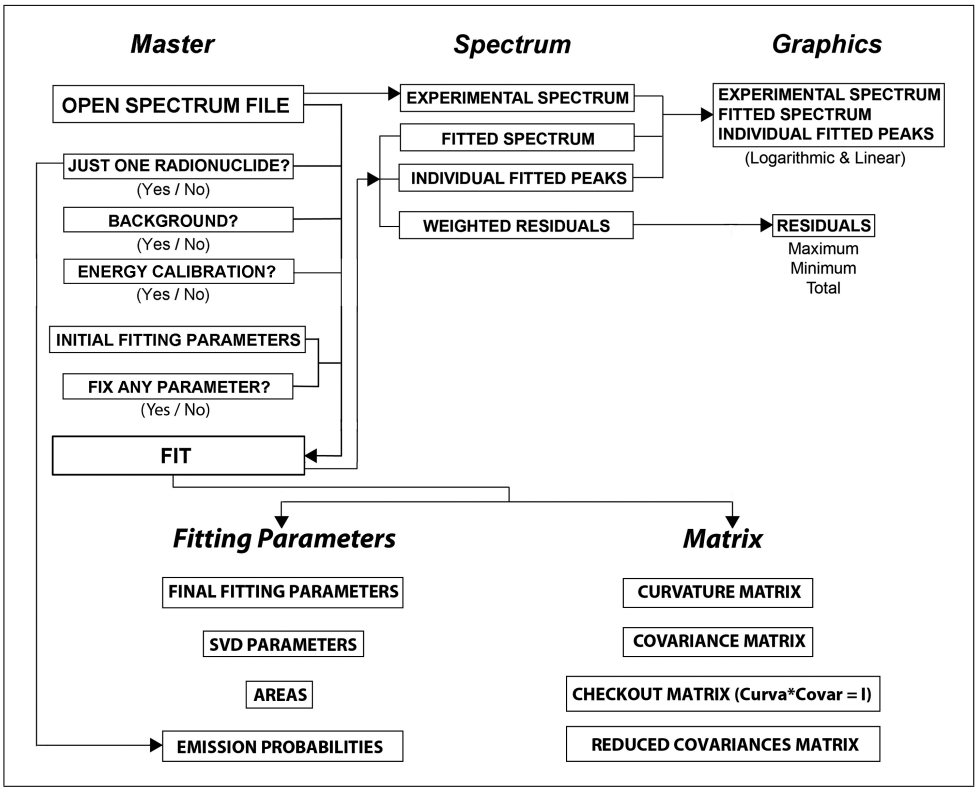

Figure 5.1: Diagram of ALFITeX.

wants without again having to enter all the values for the rest of the parameters each time. Another remarkable feature is that the program includes in this folder the following options:

- The selection of the region of the total spectrum where the fitting is applied.
- The possibility of using energy instead of channels. For this option the parameters of a linear energy calibration are necessary.
- The choice of whether or not to consider background contributions (which can also be fitted).
- The possibility of fixing the values of some initial parameters in the fitting process.
- The option that the user can indicate whether or not all the emissions studied are from the same radionuclide.
- The choice of a threshold for the SVD method in case the curvature matrix ($\boldsymbol{\alpha}$) is ill-conditioned.

Finally, the code also allows plotting the peak shape function corresponding to the initial fitting parameters before the fitting process begins. Thus, the

user can roughly check if the values of the parameters are close or far from the optimal solutions and change them.

In the folder **"Spectrum"** (Figure B.2), the experimental and fitted data, and the weighted $\left(\frac{N_{exp}-N_{fit}}{\sqrt{N_{exp}}}\right)$ residuals comprise the first three columns, respectively. The rest of the columns on this sheet are used to store the data corresponding to each individual fitted peak.

The folder **"Fitting Parameters"** (Figure B.3) presents the optimal values for the fitting parameters with their associated uncertainties, the parameters for the check of the SVD method, and the areas (with their uncertainties) for each peak in the spectrum. In the case of all the emissions belonging to the same radionuclide, the emission probabilities will be calculated and presented in this folder, as well as an improvement in the final data resulting from the constraint imposed that all the emission probabilities analyzed must sum to 100% [101].

Another advantage of ALFITeX is that the data can be plotted by the program in the folder **"Graphics"** (Figure B.4). This permits one to have all the plots together in the same worksheet, and check the fitting process graphically without having to use an external program. Three plots are shown simultaneously in this folder: the experimental and fitted spectrum on a linear scale, the same but on a logarithmic scale, and the weighted residuals from the best fit. In the first two plots, individual fitted peaks can also be shown. Some indicative values such as the sum and the maximum and minimum values of the residuals are also presented in some selected cells of this folder.

"Matrix" is a folder containing some important values for the matrices used to check the fitting process (see Figure B.5). The curvature matrix ($\boldsymbol{\alpha}$), the ordinary $(\boldsymbol{\alpha})^{-1}$ and the reduced covariance matrices, and even a check matrix (***curvature * covariance = identity***) are included.

Finally, in the last folder **"INFO"** (Figure B.6), a brief summary of the program and how it works can be consulted. Various "Info Marks" provide information about certain specifications of the program, such as the format of the spectrum files or what the proper threshold for the SVD process is.

5.3 Validation

In order to check the deconvolution procedure, tests were carried out using alpha spectra from several radionuclides. As a first example, ALFITeX was used to fit a spectrum of ^{239}Pu provided by CIEMAT that was previously used to check former similar computer codes in our laboratory [58]. Seventeen peaks were fitted and the graphical results are shown in Figure 5.2. In this case some fitting parameters were fixed. As all the peaks analyzed corresponded

to emissions from the same radionuclide, the emission probabilities were also calculated. The results were compared with data from [71, 102, 103] showing, in general, good agreement (Table 5.1). To have an idea of the computational speed of the code, ALFITeX was able to output the results of ^{239}Pu in few seconds (for a computer with an MC INTEL 1155 CORE I5 2300 2.8 GHz).

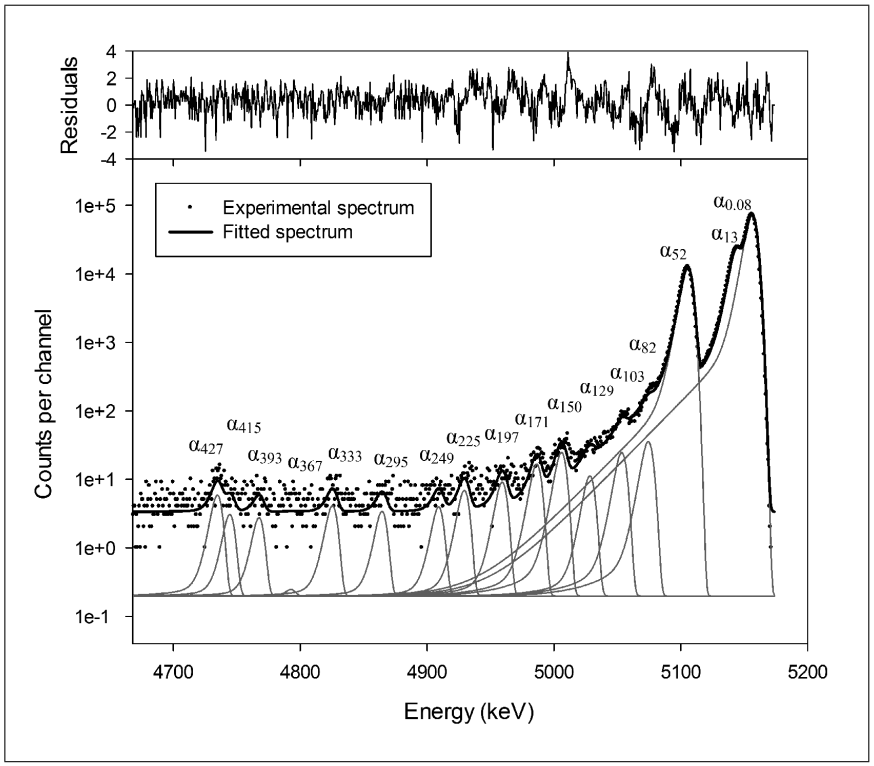

Figure 5.2: Alpha-particle spectrum of ^{239}Pu measured at CIEMAT showing the peaks deconvolved using ALFITeX. The weighted residuals of the fit are plotted in the *upper part* of the figure.

Another example of application is the deconvolution of a spectrum of ^{241}Am. The same source used in the optimization of the alpha-gamma coincidence system was measured with the semiconductor chamber (see Sections 3.1). The measurements were carried out with a source-to-detector distance of 61 mm and a room temperature of 20 ($\pm$ 2) °C. Two magnets and a diaphragm were coupled to the source support. A set of spectra were collected with short counting times and combined afterward applying an appropriate shifting correction using the code SHIFTER [29, 30]. The spectrum of ^{241}Am obtained under these measuring conditions had a resolution of 13.4 keV and a peak-to-valley ratio of 43.

The reduction of the conversion electrons using the magnets was not significant. It can be observed in Figure 5.3 that the fitted curve underestimates the experimental data between the α_{33} and α_0 emissions. This slight disagreement is due to the conversion electrons from ^{237}Np detected in coincidence with the 5511 keV alpha particles (α_{33} emission). Notice that the corresponding internal conversion coefficient for the subsequent transition to this α_{33} alpha

emission has a very high value ($\alpha_T \approx 175$) [71]. In this stage of the research the aim of the calculation of the emission probabilities was only checking that the code works properly. If supplying new or improved data had been the purpose of the calculations, coincidence summing corrections would have been then necessary.

α Branch	Emission probability (%)			
	Evaluations		Measurements	
	LNHB [71]	ToRI [102]	García-Toraño et al. [103]	ALFITeX
α_{427}	0.00570 (5)	-	0.0051 (8)	0.0055 (9)
α_{415}	0.00075 (11)	-	-	0.0028 (7)
α_{393}	0.00125 (3)	-	0.0015 (6)	0.0024 (7)
α_{367}	0.000944 (17)	-	0.0012 (6)	-
α_{333}	0.00354 (7)	-	0.0024 (7)	0.0038 (8)
α_{295}	0.0018 (5)	-	0.0019 (7)	0.0031 (7)
α_{249}	0.0030 (16)	-	0.0024 (9)	0.0036 (7)
α_{225}	0.0050 (7)	-	0.006 (1)	0.0064 (9)
α_{197}	0.007 (1)	-	0.007 (1)	0.0085 (10)
α_{171}	0.0034 (10)	-	0.013 (2)	0.016 (1)
α_{150}	0.0182 (27)	-	0.017(2)	0.023 (2)
α_{129}	0.013 (4)	-	0.0094 (30)	0.011 (2)
α_{103}	0.0375 (12)	-	0.047 (13)	0.023 (3)
α_{82}	0.052 (8)	-	0.078 (8)	0.034 (5)
α_{52}	11.87 (3)	11.5 (8)	11.94 (7)	11.82 (5)
α_{13}	17.14 (4)	15.1 (8)	17.11 (14)	17.01 (7)
$\alpha_{0.08}$	70.79 (10)	73.3 (8)	70.77 (14)	71.03 (9)

Table 5.1: Alpha-particle emission probabilities for ^{239}Pu obtained with the code ALFITeX compared with previously published values. Uncertainties are given in units of the last significant figures.

The spectrum of ^{241}Am was firstly fitted by ALFITeX into five peaks (Figure 5.3a). In the plot for the residuals, a structure similar to a "weak peak" can be observed in the region of the α_{226} emission of 5321.87 keV (marked by the second arrow). This alerts to the presence of a peak in the spectrum which had not been considered. The effect is, however, not so clearly observed in the region of the peak originating from the α_{305} emission of 5244.13 keV (first arrow on the plots of the residuals). A second fit considering seven peaks was carried out (Figure 5.3b). In this case, when the corresponding peaks were included in the fit, the structures firstly observed in the residuals shown in Figure 5.3 a were reduced (see Figure 5.3b).

To deconvolve the spectrum into five peaks, none of the fitting parameters were fixed, and no background was considered. In the case of the seven peaks, the position of the lower emissions with energies of 5244.13 keV and 5321.87 keV were fixed, and again no background was considered. The fit was improved with the inclusion of these two new peaks, and the values obtained for the

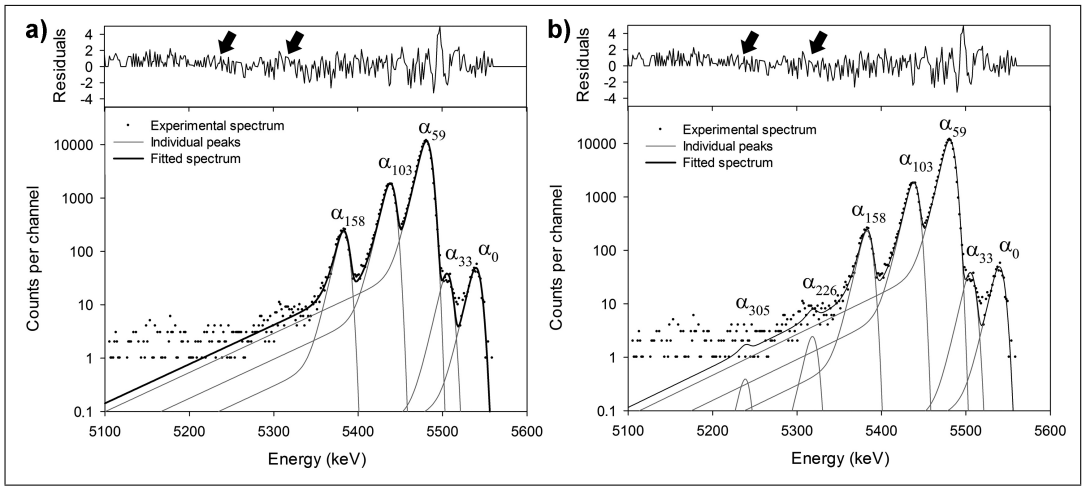

Figure 5.3: Deconvolution of an alpha-particle spectrum of ^{241}Am, considering (a) five peaks and (b) seven peaks. The two sets of weighted residuals are plotted in the *upper part* of the figure. In (a), two small structures (the first is less clear than the second) are marked in the region of the emissions α_{305} and α_{326}. Notice that in (b), the first structure is reduced, although the second remains practically unaffected after the seven-peak fitting process.

emission probabilities were also better. The results are given and compared with previously published data in Table 5.2, showing good agreement with the reference values [71, 102].

It is also appreciable in Figure 5.3 that the low-energy tail region is not well reproduced by using two exponentials. In such cases, the use of more exponentials or another kind of line shapes are required, as described below in Section 5.4.2.

α Branch	Emission probability (%)		
	Evaluations		Measurements
	LNHB [71]	ToRI [102]	ALFITeX
α_{305}	0.0022 (3)	0.0024	0.0028 (39)
α_{226}	0.014 (3)	0.015 (5)	0.018 (8)
α_{158}	1.66 (3)	1.6 (2)	1.67 (4)
α_{103}	13.23 (10)	13.0 (6)	13.37 (15)
α_{59}	84.45 (10)	84.50 (10)	84.31 (15)
α_{33}	0.23 (1)	0.22 (3)	0.27 (2)
α_0	0.38 (1)	0.34 (5)	0.36 (2)

Table 5.2: Comparison of the values obtained in this work using ALFITeX and previously published data for the alpha-particle emission probabilities from ^{241}Am. Uncertainties are given in units of the last significant figures. No corrections due to conversion electrons were carried out in this work.

Finally, to illustrate ALFITeX's capability of analysing very complex alpha-particle spectra, we considered an experimental spectrum of ^{235}U with a large number of overlapping emissions. This spectrum was obtained at the JRC's Institute for Reference Materials and Measurements (IRMM), and has previously been used by García-Toraño et al. [104] for the revision of previous nuclear data tables. Figure 5.4 shows graphically the results of the fit to this spectrum, in which the interfering emissions of ^{234}U and ^{236}U had to be accounted for in the fitting process.

The total spectrum for the analysis of ^{235}U was deconvolved using eighteen peaks including the emissions from ^{235}U, as well as the interfering emissions from ^{234}U and ^{236}U. These results were reached fixing (and therefore not fitting) the positions of the ^{235}U 4080.6 and 4283.2 keV peaks, the ^{236}U 4445 and 4494 keV peaks, and the ^{234}U 4603.5 keV peak. The amplitude of this last emission was also fixed in the fit, taking into account the ratio between this emission and that of 4774.6 keV from ^{234}U. Overall, 40 parameters were fitted by ALFITeX giving the results plotted in Figure 3. For this spectrum, little difference was found according to whether or not a background was considered. The values obtained for the emission probabilities, shown in Table 5.3, correspond to those without considering a background contribution. The results are in good agreement with previously published data [104].

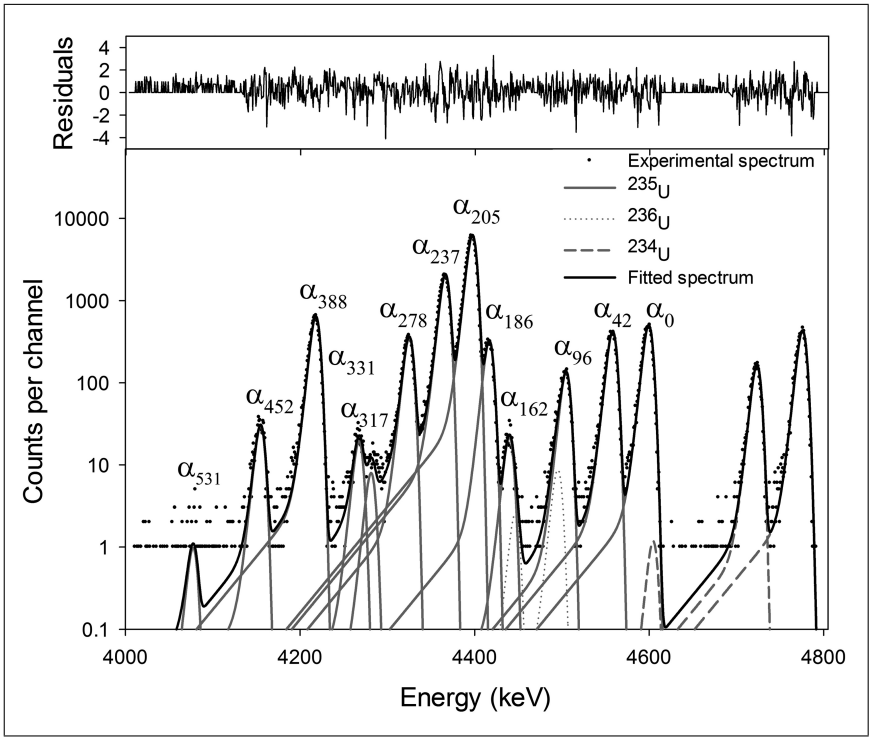

Figure 5.4: Alpha-particle spectrum of ^{235}U measured at IRMM showing the peaks deconvolved using ALFITeX. The weighted residuals of the fit are plotted in the *upper part* of the figure.

α Branch	Emission probability (%)	
	Measurements	
	García-Toraño et al. [104]	ALFITeX
α_{531}	0.016 (12)	0.009 (3)
α_{452}	0.286 (18)	0.277 (13)
α_{388}	5.91 (7)	5.96 (7)
α_{331}	0.200 (16)	0.179 (12)
α_{317}	0.066 (13)	0.074 (10)
α_{278}	3.37 (6)	3.28 (5)
α_{237}	19.00 (13)	19.13 (17)
α_{205}	57.98 (22)	58.04 (20)
α_{186}	3.11 (6)	3.03 (5)
α_{162}	0.219 (16)	0.204 (14)
α_{96}	1.25 (4)	1.25 (3)
α_{42}	3.87 (6)	3.91 (5)
α_0	4.74 (7)	4.65 (6)

Table 5.3: Alpha-particle emission probabilities for ^{235}U obtained with the code ALFITeX compared with previously published values. Uncertainties are given in units of the last significant figures.

5.4 Additional features

5.4.1 Prefittings

A common problem in the deconvolution of nuclear spectra is the instability of the non-linear optimization procedure; in particular, the selection of the initial set of parameters to start the minimization process constitutes a critical aspect. Since the physical meaning of some shape parameters is not clear, it becomes difficult to get meaningful information that could be used to build a first guess of these parameters. Hence, the process of trial and error is often required. In most cases, users will not be able to introduce good values, so it will be necessary that the program does it itself. For that reason, a set of prefittings for the most critical parameters have been implemented in ALFITeX. Each prefitting is described below.

Estimation of the sigma of the Gaussian component

A starting value for the sigma of the Gaussian component can be obtained following the method proposed by Mukoyama [105], which is based in a method previously proposed by Zimmermann [106]. Assuming that the pulse-height distribution near a peak can be represented by a Gaussian function:

$$y(x) = A\ exp\left[-\left(x - x_0\right)^2 / \ 2\sigma^2\right], \tag{5.11}$$

where A denotes the peak amplitude, x_0 is the peak position and σ is the standard deviation.

The standard deviation can be calculated from the following expression:

$$Q(x) = y(x-1) \,/\, y(x+1) = exp\left[2\,(x - x_0) \,/\, \sigma^2\right]. \tag{5.12}$$

$log\,(Q)$ is linear with x. Hence, $log\,(Q)$ defined by means of the Y_i data ($log\,(Y_{i-1}/Y_{i+1})$) can be linearly fitted by the conventional least-squares method.

For this prefitting process, a region of channels on the right side of the maximum of a reference peak must be provided. It must be taken into account that to calculate σ (as well as any other shape parameter), the selection of an isolated peak as reference is always the most convenient way to obtain an initial value, although a full minimization of all parameters can be carried out later over the whole spectral region to be analyzed.

Constant of the first exponential

It is very important that the initial shape parameters are correctly settled to avoid instabilities in the iterative nonlinear least-square process. Once the standard deviation of the Gaussian function has been estimated, the constants of the exponentials and their relative weights must be introduced.

ALFITeX allows prefitting the constants of the exponentials. They have been assumed to be correlated (the second one is the 10% of the first one and so on, when a third exponential is included). Therefore, once the constant of the first exponential is estimated, the rest of constants can also be obtained.

The Newton-Raphson method (described in Section 1.3) was followed in this case to calculate the constant of the first exponential. The function to be minimized is

$$\phi = F(u) - \frac{A}{2} = 0, \tag{5.13}$$

where $F(u)$ is the value of the line shape function (Eq. 5.1) in the position $u = \mu - 1.18\ AF\ \sigma$ and AF is the Asymmetry Factor. This value is calculated as the ratio between the width of the peak at the left and right sides of the maximum position for a height equal to the half maximum.

The method starts with an initial guess which is reasonably close to the true root and then the function is approximated by its tangent line, and the x-intercept of this tangent line is computed. The x-intercept will typically be a better approximation to the function's root than the original guess. In our case,

$$\tau_{1\,n+1} = \tau_{1\,n} - \frac{\phi\,(\tau_{1\,n})}{\phi'\,(\tau_{1\,n})}. \tag{5.14}$$

It is important to point out that the estimation of the standard deviation of the Gaussian, the relative weights and initial peak positions and heights must be introduced in order to estimate the constants of the exponentials. The user

will also have to provide the position and height of a reference peak (normally the main peak), as well as AF.

Peak amplitudes

Once the initial shape parameters have been obtained by the procedures described in the previous paragraph, a first estimation of peak positions and amplitudes is required to complete the set of initial parameters needed to start the minimization process. Peak positions can be obtained either by using an energy calibration, if all spectral components are known, or by visual inspection. Then, it becomes possible to estimate the initial values for the peak amplitudes by reducing the set of equations 5.6:

$$\sum_{l=1}^{N} \alpha_{kl}^{'} \delta a_l = \beta_k,$$

to a simplified one where the only unknowns are the peak amplitudes.

$$\alpha_{kl} = \frac{1}{2}\frac{\partial^2 \chi^2}{\partial A_k \partial A_l}, \beta_k = -\frac{1}{2}\frac{\partial \chi^2}{\partial A_k},$$

$$\frac{\partial^2 \chi^2}{\partial A_k \partial A_l} = 2\sum_{i=1}^{N} \frac{1}{\sigma_i^2}\left[\frac{\partial y\left(x_i;\boldsymbol{a}\right)}{\partial A_k}\frac{\partial y\left(x_i;\boldsymbol{a}\right)}{\partial A_l} - \left(y_i - y\left(x_i;\boldsymbol{a}\right)\right)\frac{\partial^2 y\left(x_i;\boldsymbol{a}\right)}{\partial A_k \partial A_l}\right].$$

In this case, the system reduces to a linear set of equations that can be solved in a straightforward manner to obtain starting values for the peak amplitudes.

5.4.2 Adding a third exponential

As described in Section 1.3, in most cases alpha-particle spectra measured with semiconductor detectors are complex. The limited energy resolution of Si detectors, the high stopping power of alpha particles or the coincidence summing between alpha particles and conversion electrons difficult the analysis of the alpha spectra. Moreover, experimental factors such as the source preparation, the detector size, and the solid angle of the measurement, also strongly influence on spectral parameters such as energy resolution and peak tailings.

The low-energy tail can be modeled in several ways, such as using a hyperbolic function [47] or adding left-handed exponentials. Based on the last option, a new line shape has been recently proposed by Pommé and Caro Marroyo [107] and it is described in detail in Appendix A. This line shape can contain up to ten left-handed exponentials for the low-energy part and four right-handed tailing functions to try to reproduce some tailing at the high-energy side.

In some cases, it is difficult to reproduce the tail region. For example, Figure 5.5 (a) presents a spectrum of ^{210}Po fitted by ALFITeX using only two

exponentials. The residuals of this fit clearly show that the fitting underestimates the number of counts in the low-energy part of the spectrum. Increasing the number of left-handed exponentials could improve the shape of the spectrum in the low-energy tail region. When the use of only two exponentials fails reproducing the low-energy tail, ALFITeX allows the addition of a third left-handed exponential. The new fitting function is now

$$
\begin{aligned}
F(u) = \sum_{i=1}^{npeaks} \frac{A_i \sigma \sqrt{2\pi}}{2} \Bigg[& \eta_1 \tau_1 exp\left((u-\mu_i)\,\tau_1 + \frac{\sigma^2 \tau_1^2}{2} \right) \\
& \times erfc\left(\frac{1}{\sqrt{2}} \left(\frac{u-\mu_i}{\sigma} + \sigma\tau_1 \right) \right) \\
& + \eta_2 \tau_2 exp\left((u-\mu_i)\,\tau_2 + \frac{\sigma^2 \tau_2^2}{2} \right) \\
& \times erfc\left(\frac{1}{\sqrt{2}} \left(\frac{u-\mu_i}{\sigma} + \sigma\tau_2 \right) \right) \\
& + (1-(\eta_1+\eta_2))\,\tau_3 exp\left((u-\mu_i)\,\tau_3 + \frac{\sigma^2 \tau_3^2}{2} \right) \\
& \times erfc\left(\frac{1}{\sqrt{2}} \left(\frac{u-\mu_i}{\sigma} + \sigma\tau_3 \right) \right) \Bigg] + bck,
\end{aligned}
\tag{5.15}
$$

where η_2 and τ_3 are the weight of the second exponential and the constant of the third exponential, respectively, and must be introduced by the user.

In the case of the spectrum of ^{210}Po, the use of the third exponential improves the fitting in the region of the low-energy tail (Figure 5.5 (b)). As it was expected, more exponentials give a better fitting of the tail. However, depending on the spectrum, this fact does not always mean a significant improvement in the emission probabilities. In some cases the results are worse. In other situations the behavior of the use of three exponentials can be reproduced quite suitably using two exponentials and a constant background.

A more complicate situation is presented in Figure 5.6. A spectrum of ^{233}U measured at IRMM was fitted using two (green line) and three (red line) exponentials. The use of the third exponential improves again the fitting in the low energy tail part. This fact influences the emission probabilities values as shown in Table 5.4. The results corresponding to the low-energy region obtained using three exponentials are, in this case, closer to those from literature [108].

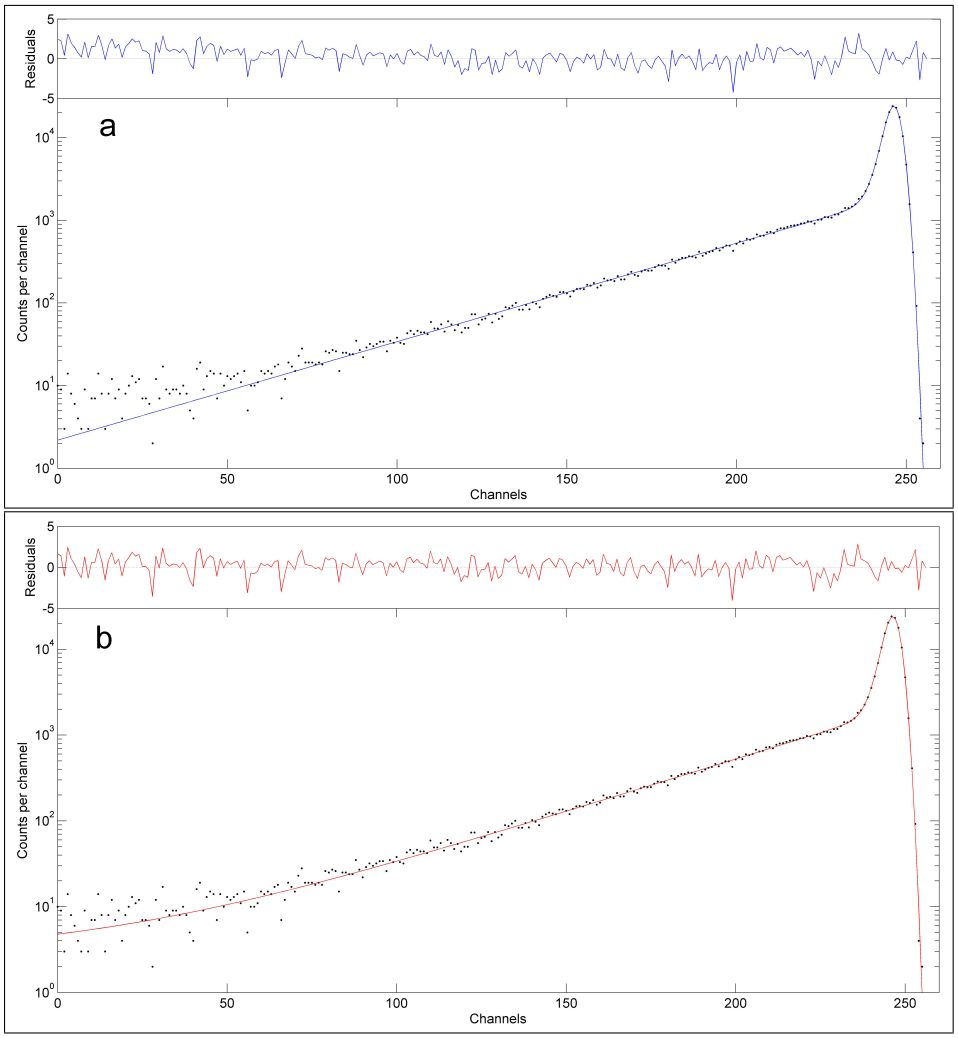

Figure 5.5: Comparison of a spectrum of ^{210}Po fitted with ALFITeX using two (a) and three exponentials (b). The weighted residuals of the fits are plotted in the *upper part* of each figure.

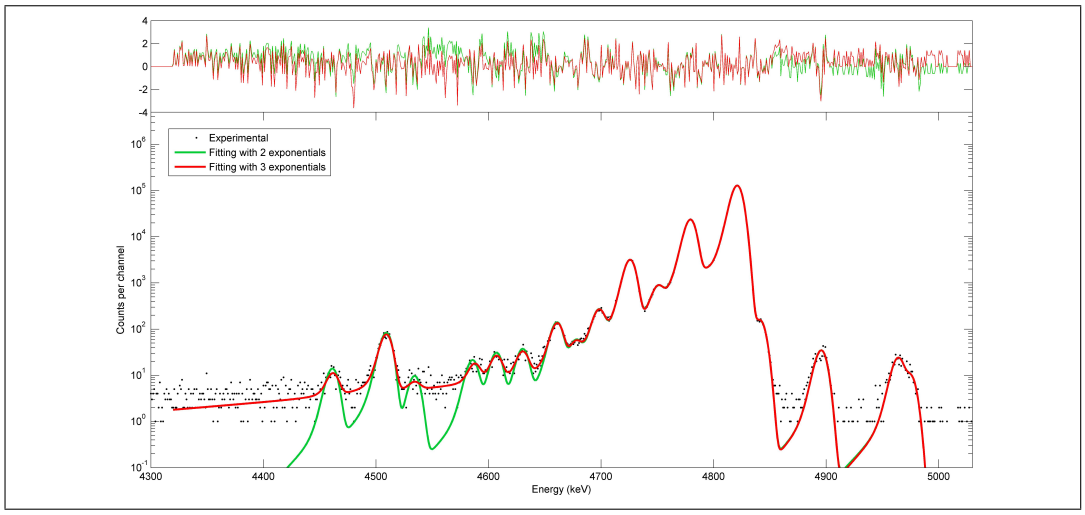

Figure 5.6: Comparison of the ALFITeX fittings of a spectrum of ^{233}U using two and three exponentials.

α Branch	Emission probability (%)		
	Evaluations	Measurements	
	Browne [108]	ALFITeX 2 exponentials	ALFITeX 3 exponentials
α_{366}	0.003	0.0088 (5)	0.0049 (6)
$\alpha_{328} + \alpha_{320} + \alpha_{317}$	0.031	0.0535 (27)	0.0467 (16)
α_{288}	0.004	0.0062 (3)	0.0015 (6)
α_{103}	0.007	0.0131 (3)	0.0068 (9)
$\alpha_{217} + \alpha_{212}$	0.01	0.0191 (12)	0.0118 (10)
α_{196}	0.01	0.0224 (5)	0.0144 (12)
α_{163}	0.042	0.0853 (6)	0.0761 (23)
$\alpha_{146} + \alpha_{141}$	0.0128	0.0250 (7)	0.0185 (17)
α_{125}	0.06	0.1398 (7)	0.134 (3)
α_{97}	1.61	1.99 (1)	1.99 (2)
$\alpha_{75} + \alpha_{72} + \alpha_{68}$	0.189	0.328 (23)	0.348 (9)
α_{42}	13.2	14.67 (7)	14.72 (13)
α_{29}	0.28	0.2832 (14)	0.31 (2)
α_0	84.3	82.36 (7)	82.31 (13)

Table 5.4: Comparison of the alpha-particle emission probabilities for ^{233}U obtained by ALFITeX with two and three exponentials and also compared with previously published values. Uncertainties are given in units of the last significant figures.

Part IV

Applications

Chapter 6

Determination of the alpha-particle emission probabilities of ^{242}Pu

The nuclide ^{242}Pu decays 100 % by alpha-particle emission to ^{238}U with a half-life of 3.73 x 10^5 years [109]. Figure 6.1 shows its decay scheme.

During the 1980s, the International Atomic Energy Agency (IAEA) undertook a Coordinated Research Project (CRP) that resulted in the production of a library of evaluated decay data for 23 transactinium nuclei [110]. An update of this library was carried out under the CRP entitled "Updated Decay Data Library for Actinides" [111–114], following the methodology adopted for the Decay Data Evaluation Project (DDEP) (Browne et al. [115]). The results of the evaluation program were presented by Kellet [116]. This document requests new measurements of some alpha-particle emission probabilities for some actinides, such as the ^{242}Pu and ^{243}Am.

6.1 Previous measurements and evaluations

The results of previous measurements and evaluations for this nuclide are contained in Tables 6.1 and 6.2. In 1953, Asaro [117], and in 1956, Hummel [63], measured by magnetic spectrometry the alpha-particle emission energies and probabilities for the two major emissions. Also in 1956 Kondratev et al. [118] reported the alpha-particle energies for the α_0 and α_{45} emissions, which were determined by magnetic spectrometry. In 1968 and 1976, new measurements by magnetic spectrometry were carried out by Baranov et al. [2, 119] who obtained new alpha-particle emission energies and probabilities for the two major emissions. The results of Asaro [117], Hummel [63] and Baranov et al. [2, 119] were revised by Ellis and Haese in 1977 [120]. The original energy values obtained by Baranov et al. were increased by 0.6 keV because of a calibration problem. They also reported the emission probabilities of α_{148} and α_{307} that were not observed but deduced from gamma-ray emission probabilities. In 1986 the measurements carried out by Vaninbroukx et al. [121] using surface-barrier detectors provided new values of the alpha-particle probabilities for the

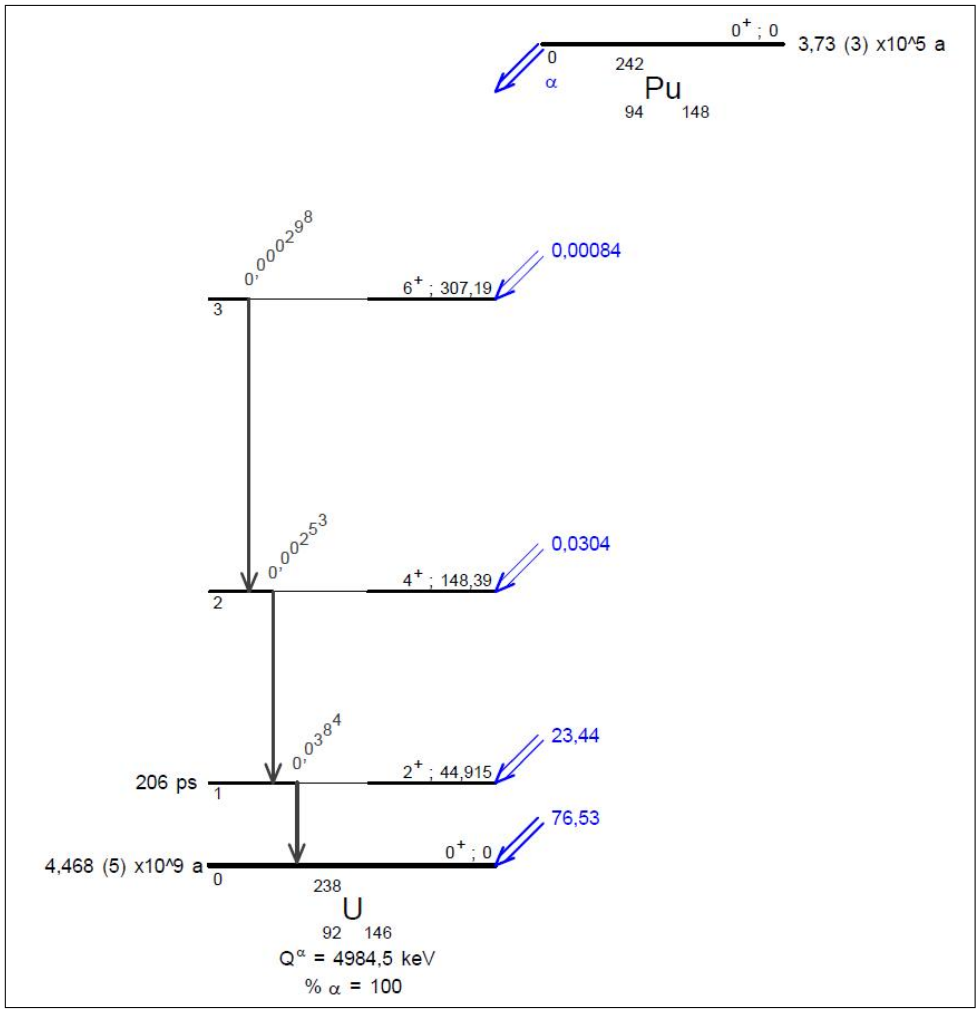

Figure 6.1: Decay scheme of ^{242}Pu taken from Chechev [109].

α_0, α_{45} and α_{148} emissions. The study also included gamma-ray emission probability values obtained by measuring with calibrated high-purity-Ge detectors. The emission probability for the α_{307} particles was derived from the gamma-ray emission probability of the 158.8 keV transition and the corresponding internal-conversion coefficient. Their results provide the first complete set of data.

Afterward, some evaluations were carried out by Lorentz [110] giving information related to the uncertainties of the alpha-particle emission probabilities reported by Asaro [117], Hummel [63] and Baranov et al. [119]. The study of Rytz [122] suggested an adjustment of the energies of the α_0 and α_{45} emissions. Finally, Chechev [109] reported, after the evaluation of all available data, a set of alpha-particle emission energies and probabilities for ^{242}Pu that are the last recommended data by the DDEP [71] for this radionuclide.

New measurements of alpha-particle emission energies and probabilities for ^{242}Pu were requested after the evaluation program presented by Kellet [116]. This chapter presents new values of the α_0, α_{45} and α_{148} emission probabilities obtained with the alpha-particle spectrometry devices described in Section 3.2.

α Branch	α Energy (keV)	Measurements				Evaluation
		Asaro [117]	Hummel [63]	Baranov et al. [119]	Vaninbroukx et al. [121]	Chechev [109]
α_{307}	4600	-	-	-	-	0.00084 (6)
α_{148}	4756	-	-	-	0.0290 (14)	0.0304 (13)
α_{45}	4858	20 (6)	26 (4)	20.2 (20)	23.52 (17)	23.44 (17)
α_0	4902	80 (6)	74 (4)	79.7 (20)	76.45 (17)	76.53 (17)

Table 6.1: Experimental and evaluated alpha-particle emission probabilities for ^{242}Pu (%).

α Branch	Measurements			Evaluation		
	Asaro [117]	Hummel [63]	Kondratev [118]	Baranov [2]	Rytz [122]	Chechev [109]
α_{307}	-	-	-	-	-	4600.1 (10)
α_{148}	-	-	-	-	-	4756.2 (10)
α_{45}	4860.6 (20)	4859.7 (30)	4863.2 (30)	4856.1 (12)	4858.1 (15)	4858.2 (10)
α_0	4904.6 (20)	4903.7 (30)	4907.2 (30)	4900.4 (12)	4902.3 (14)	4902.3 (10)

Table 6.2: Measured and evaluated alpha-particle energies for ^{242}Pu (keV).

6.2 Experimental

6.2.1 Sources

Two sources of about 20 Bq each were prepared at CIEMAT by electrodeposition from a ^{242}Pu solution, following the procedure described by Pommé et al. [123] which is a modification of the method proposed by dos Santos et al. [124]. An aliquot of the ^{242}Pu solution was transferred into a 10 cm^3 glass beaker and evaporated to dryness. The dry residue was dissolved in saturated NH_4NO_3 solution and transferred into the electrodeposition cell. The beaker was rinsed with 12 cm^3 portions of saturated NH_4NO_3 to obtain a total volume of electrolyte of 10 cm^3. The pH was adjusted to pH=1 with drops of concentrated HNO_3. The deposition was performed onto mirror polished stainless steel disks (25 mm diameter, 1 mm thickness),which acted as the cathode of the electrodeposition cell, while the anode was an 1 mm diameter platinum (Pt) wire folded in the base with spiral shape. Deposition was performed with 1 A current intensity and 10 mm distance between electrodes were used. The electrodeposition time was 120 minutes. One minute before switching off the current, 1 cm^3 of concentrated NH_4OH was added to the solution to prevent the re-dissolution of the deposited layer. The source was rinsed with deionized water, and then the electrodeposition cell was disassembled. The source was rinsed once again with water and finally with ethanol and dried at ambient temperature. This resulted in a deposit covering an area of approximately 22 mm diameter.

The sources also contain impurities of ^{238}Pu, ^{239}Pu, ^{240}Pu and ^{241}Am. At the reference date of 15/11/2013, the ratios between these nuclides and the ^{242}Pu were:

$$\frac{^{238}Pu +^{241} Am}{^{242}Pu} \approx 2.5\% \ , \ \frac{^{239}Pu +^{240} Pu}{^{242}Pu} \approx 2.0\%.$$

6.2.2 Measurements

Alpha spectra of both sources of ^{242}Pu, N9 and N10, were obtained at CIEMAT using the high-stability alpha-particle chamber and the α-e$_c$ coincidence chamber (see description in Section 3.2), although the latter was only used as an spectroscopy alpha chamber in the same way as the first one. In this way two sets of results were obtained each one characterized by a different counting efficiency. The aim of this was to obtain the best estimation for the emission probabilities by the extrapolation to zero effective efficiency.

A total number of 129 spectra were measured in 1-day cycles without interruption with the high-stability alpha-particle chamber using a PIPS detector with 50 mm^2 active area and 300 μm Si thickness. Two cubic magnets creating a magnetic field of about 1 kG for 15 mm distance between poles were used for the measurements. A collimator composed of a tantalum diaphragm (0.1 mm thick and 9 mm opening diameter) was coaxially placed with the source and detector. With this configuration the geometrical efficiency reached was about

$\epsilon = 0.005$. In order to obtain significant statistics in the α_{148} peak, the individual spectra were combined in a total sum spectrum with 1.8 x 10^6 counts in the region corresponding to the ^{242}Pu. The computed peak resolution was 9.5 keV FWHM and the peak-to-valley ratio was 127. In spite of the temperature stabilization, some electronic drift remained and it was necessary to use special techniques to combine all data. Therefore a numerical gain stabilization method based on the Stieltjes integral of spectra was applied to determine the shifting correction [29, 30].

A total of 54 single alpha spectra were measured with the α-e$_c$ coincidence chamber in 100000 s cycles using two PIPS detectors with 450 mm^2 active area and 100 μm Si thickness. The magnetic field created by the two cylindrical magnets used for the measurements was about 0.05 kG for 20 mm distance between poles. A diaphragm with 22 mm diameter was fixed at an intermediate distance between the source and the detector. With this configuration the geometrical efficiency was about $\epsilon = 0.035$. First, 29 spectra were measured with the detector No 84488 (group No 1). After some time, this detector started to fail and it was necessary to be replaced with the detector No 59871. Another set of 25 spectra were measured with the second detector (group No 2). Therefore, the spectra were combined in two groups after the application of shifting corrections. The total number of counts of the group No 1 spectrum was 2.2 x 10^6, the energy resolution was 12.5 keV FWHM and the peak-to-valley ratio was 25. Respect to the group No 2, the total counting was 2.4 x 10^6, the energy resolution was 11.5 keV FWHM and the peak-to-valley ratio was 48.

Figure 6.2 shows the total sum spectrum of ^{242}Pu measured with the high-stability alpha-particle chamber (a) and the group No 2 spectrum measured with the α-e$_c$ coincidence chamber (b). Background spectra were collected in both measuring systems but no indication was found of any significant structure in the region of analysis. Typical background counting rates were 1 x 10^{-5} s^{-1} for the high-stability alpha-particle chamber and 2 x 10^{-5} s^{-1} for the α-e$_c$ coincidence chamber. These can be considered negligible compared to the counting rates of the source spectra, 1.6 x 10^{-1} s^{-1} and 9.7 x 10^{-1} s^{-1}, respectively measured with the high-stability alpha-particle chamber and the α-e$_c$ coincidence chamber.

6.3 Spectral analysis

6.3.1 Deconvolution procedure

In the case of the high-stability alpha-particle chamber a spectrum was obtained by the combination of the individual spectra. Two additional spectra (No 1 and No 2) were also considered resulting of the addition of 29 and 25 individual spectra measured with the α-e$_c$ coincidence chamber.

The three sum spectra were fitted by the ALFITeX code, extensively described in Section 5. The sequence of minimization started by a set of prefittings: an estimation of the sigma of the Gaussian component, the constant of the first exponential and the peak amplitudes. Once the initial values of these parameters were set, the *Levenberg-Marquardt* optimization algorithm implemented in the code provided the final values for the parameters and the uncertainties. The final peak intensities and their uncertainties were calculated taking into account the covariance matrix and the constraint that all the emission probabilities analyzed must sum to 100% [101].

A region of interest delimited by 4550 and 4950 keV was selected in all cases. Three left-handed exponentials were used for the fits and no background contribution was considered. Minimization was carried out for all parameters.

For the spectrum measured with the high-stability alpha-particle chamber, the reduced chi-square value was 1.27. The fitting of this total sum spectrum is presented in Figure 6.2.a, showing the component peaks and the weighted residuals $(Y_{exp} - Y_{fit}) / \sqrt{Y_{exp}}$, where Y_{exp} and Y_{fit} are the counts in a given channel of the experimental and the fitted spectrum, respectively. No evidence for unfitted peaks was observed.

The peak-fitting process in the case of the spectra measured with α-e_c coincidence chamber was more complicated and the fits were worse than in the previous situation of the spectrum registered with the high-stability alpha-particle chamber. This is reflected in the values of the reduced chi-square, which were 7.4 and 12.2 for the spectrum groups No 1 and 2, respectively. The fitted spectrum of the group No 2 is presented in Figure 6.2.b. The weighted residuals clearly show that the fitting function was unable to accurately reproduce the experimental counts of the region between the α_0 and α_{45} peaks and also the tail of the α_{45} emission. A plausible explanation is the spectral deformation in these regions caused by α-e_c coincidence summing events. The higher geometrical efficiency of the set-up and the use of less strong magnetic fields caused the detection of a higher number of conversion electrons, and then the corrections for coincidence summing were greater.

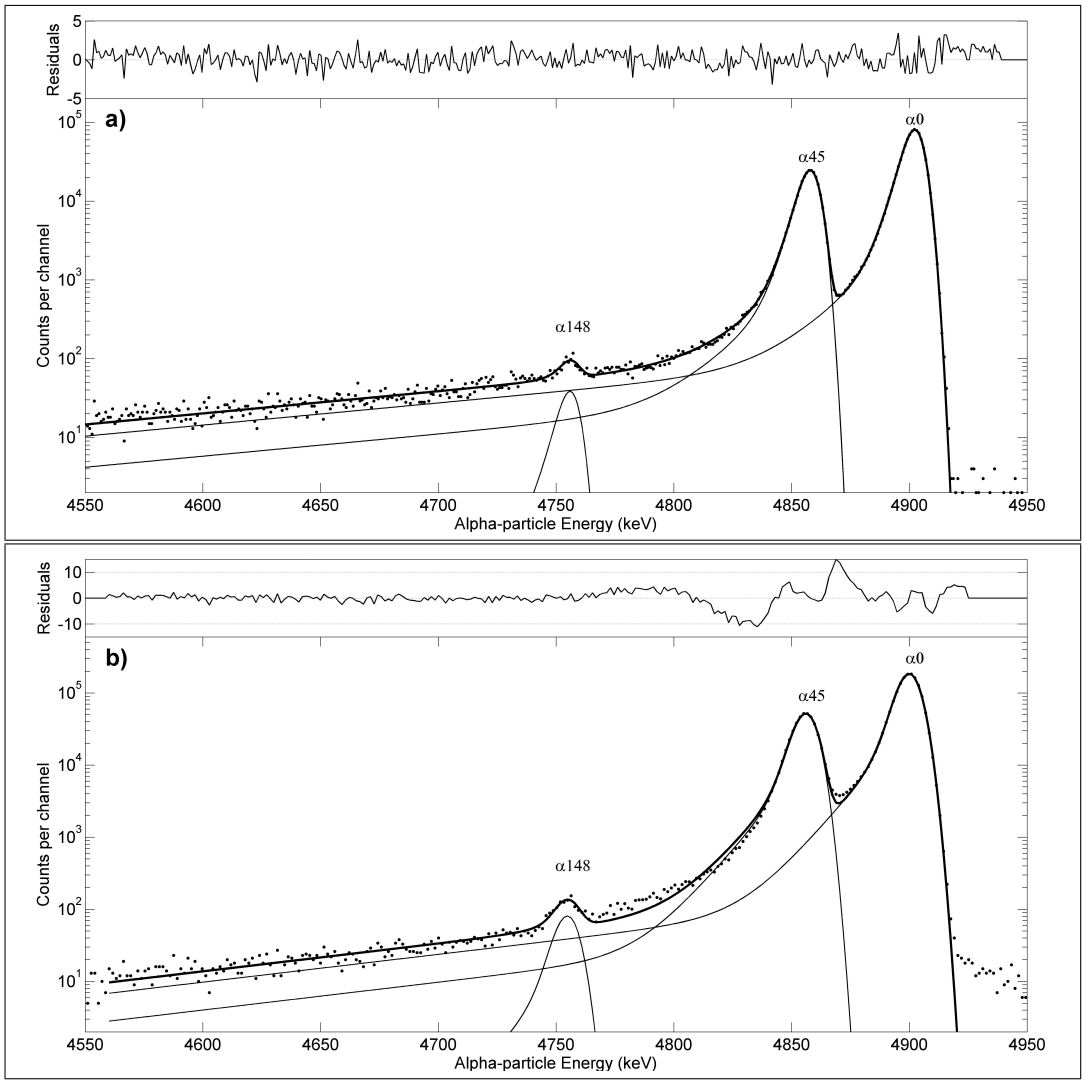

Figure 6.2: ALFITeX fit of the total sum spectrum of ^{242}Pu measured with the high-stability chamber (a) and of the group No 2 spectrum of ^{242}Pu measured with the α-e$_c$ coincidence chamber (b). Three exponentials were used in both cases. The weighted residuals of the fit are plotted in the *upper part* of the figures. The measuring times were 129 and 30 days, respectively.

6.3.2 Spectral interferences

Two effects were evaluated to determine their degree of interference in the measurements of ^{242}Pu: (a) coincidence-summing between alpha-particles and conversion electrons from gamma transitions depopulating the levels fed by the alpha decay; and (b) contributions of other plutonium isotopes and ^{241}Am that are present as impurities in the sources.

(a) The number of coincidence-summing pulses between alpha-particles and conversion electrons depends on the overall detection efficiency of the set-up. Although the relative importance of this effect is reduced by the combination of measuring under low solid angles and using magnets, a number of coincidences remained that could deteriorate the spectral quality and disturb

the peak intensities calculation. The simultaneous detection of alpha-particles and conversion electrons gives rise to a combined pulse in another region of the spectrum. Coincidence-summing between X-rays of low-energy and alpha-particles are also possible but their effect was estimated to be less important than that of the conversion electrons.

The evaluation and further correction of these processes involves a detailed calculation of the most probable events, using the energies and relative intensities of the alpha particles and conversion electrons. The value obtained for the probability of a given alpha-particle emission should be corrected by:

1. **summing in** between alpha-particles from lower energy emissions in coincidence with conversion-electrons whose summing energy reaches the energy range of the emission considered.

2. **summing out** between alpha-particles from the current emission in coincidence with conversion-electrons whose summing energy is out of the energy range.

In order to estimate these contributions, the first step is to find the location of the $\alpha + e_c^-$ coincidence summing region and the renormalization of the e_c^- emission probabilities. The use of magnets in the measurements modifies the detection efficiency and the value of this new efficiency, called *effective efficiency*, is calculated multiplying the geometrical efficiency by a reduction factor of conversion electrons. This factor is experimentally obtained calculating the ratio between the conversion-electron areas in spectra measured with and without magnets. The modification of the efficiency implies the correction of the e_c^- probability. The final $\alpha + e_c^-$ coincidence summing probability is then obtained multiplying the alpha-particle probability by the corrected e_c^- emission probability. The $\alpha + e_c^-$ coincidence summing probabilities should be added to the alpha-particle probability of the emission considered (summing out) and subtracted from the probability of higher energy emissions (summing in). Two examples of the correction procedure for the α_{45} and α_{148} emission probabilities obtained with both measuring chambers are summarized in Table 6.3.

The reduction factors were experimentally determined in this work measuring several spectra with and without magnets and calculating the ratio between the conversion-electron areas in both cases. As an example, Figure 6.3 shows the conversion-electron region in two spectra measured with and without magnets using the high-stability alpha-particle chamber. For this set-up, the reduction factors obtained for the two groups of 20 and 70 keV electrons were about 0.13 in both cases.

With the α-e_c coincidence chamber, the reduction factor for 20 keV electrons could not be determined from the spectra due to the high contribution of the electronic noise. However, for 70 keV electrons this factor could be calculated, obtaining a value of about 0.93. The reduction factor in the case of 20 keV electrons was estimated considering the value for 70 keV electrons and

B_α	P_α	E_α (keV)	E_γ (keV)	$E_{e_c^-}$ (keV)	Shell	$E_{\alpha+e_c^-}$ (keV)	C.S region	$P_{e_c^-}$	$A_{detec.}$ (mm^2)	ϵ_g	F	$\epsilon_{eff.}$	$P'_{e_c^-}$ (x 10^{-3})	P_α x $P'_{e_c^-}$ (x 10^{-5})	C.S in (x 10^{-7})	C.S out (x 10^{-4})	P'_α
α_{45}	0.2321	4858.2	44.9	23.2	L	4881.4	α_0	0.728	50	0.005	0.13	0.0007	0.5	11.9	2.3	1.63	0.2322
				39.4	M	4897.6		0.270					0.2	4.4			
α_{148}	0.000342	4756.2	103.5	81.7	L	4837.9	α_{45}	0.669	450	0.035	0.55	0.019	12.9	0.4	0.0	0.07	0.000350
				97.9	M	4854.2		0.250	(No 2)		0.93	0.033	8.2	0.3			

Table 6.3: Examples of the detailed calculation for the coincidence summing corrections applied to the α_{45} and α_{148} emission probabilities of ^{242}Pu obtained with both measuring chambers. Headings refer to: alpha-particle branch (B_α), α emission probability (P_α), α energy (E_α), gamma-ray energy (E_γ), conversion-electron energy ($E_{e_c^-}$), electronic shell (Shell), $\alpha + e_c^-$ energy ($E_{\alpha+e_c^-}$), $\alpha + e_c^-$ coincidence summing region (C.S region), normalized e_c^- probability ($P_{e_c^-}$), detector active area ($A_{detec.}$), geometrical efficiency (ϵ_g), reduction factor (F), effective efficiency ($\epsilon_{eff.}$), normalized e_c^- probability corrected by $\epsilon_{eff.}$ ($P'_{e_c^-}$), $\alpha + e_c^-$ coincidence summing probability (P_α x $P'_{e_c^-}$), coincidence summing probability from previous emissions (C.S in), coincidence summing probability contributing to higher energy emissions (C.S out) and α emission probability corrected by coincidence summing (P'_α).

the expression for the gyroradius of the circular trajectory of an alpha particle deflected by a magnetic field $\vec{B}$ as explained by Paepen et al. [28]:

$$r = \frac{m_0 c}{|q|\, B}\sqrt{(\gamma^2 - 1)} \tag{6.1}$$

where the Lorentz factor γ is given by:

$$\gamma = 1 + \frac{K}{m_0 c^2} \tag{6.2}$$

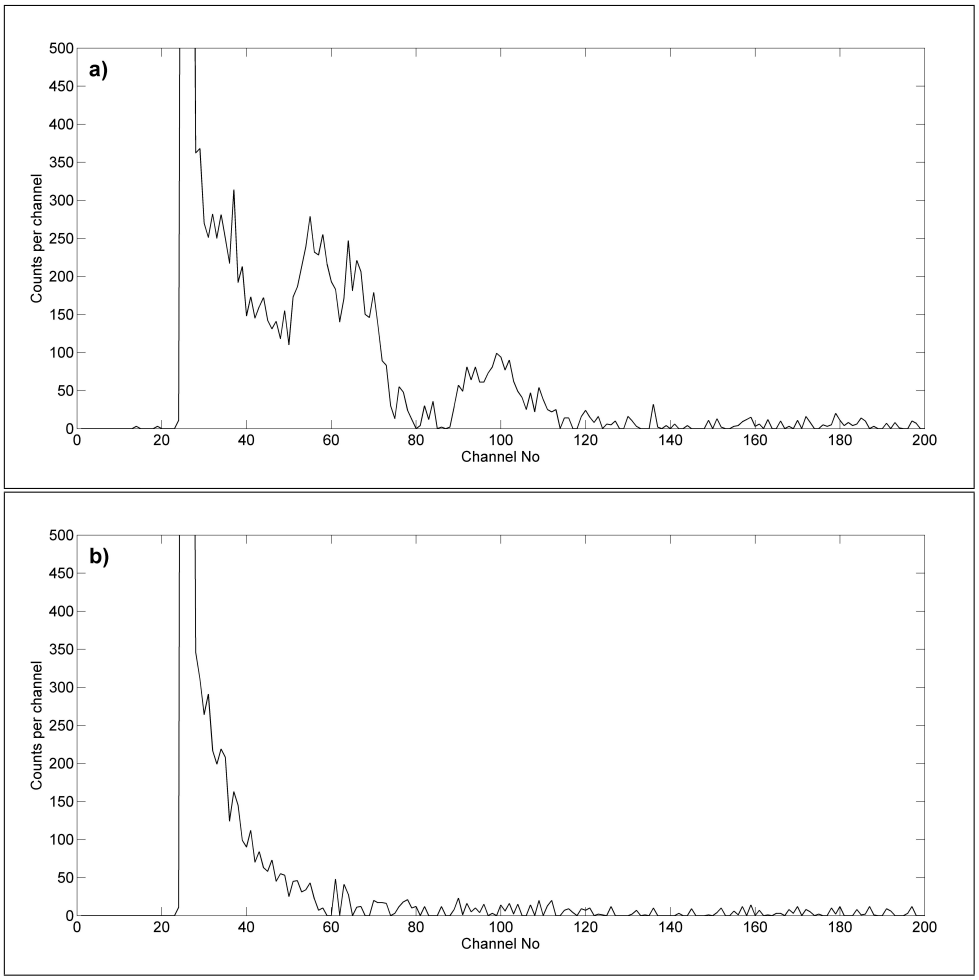

Figure 6.3: Conversion-electron region in two spectra measured without (a) and with (b) magnets using the high-stability alpha-particle chamber. The background contribution was removed from both spectra. The measuring time was 200000 s.

The ratio between the gyroradius for 20 and 70 keV electrons is about 60 %. Then the reduction factor considered for 20 keV electrons was about 0.55. Table 6.4 and Figure 6.4 present the results obtained for the emission probabilities values as a function of the effective efficiency. An average of the reduction factors was considered in the case of the α-e_c coincidence chamber.

Both the table and figure include both the raw values obtained in the fits and the values corrected by coincidence summing for each geometry.

In spite of the coincidence summing corrections, a small trend can still be observed in the values that can be removed extrapolating to zero efficiency. As can be seen in Figure 6.4, extrapolated values to zero efficiency for corrected and uncorrected results agree very well.

Detector active area (mm^2)	Effective efficiency	α Branch	Emission probability	
			Uncorrected	Corrected
50	0.0007	α_0	0.7676 (6)	0.7674 (6)
		α_{45}	0.2321 (6)	0.2322 (6)
		α_{148}	0.000365 (36)	0.000365 (36)
450	0.0264	α_0	0.7817 (5) 0.7824 (5)	0.7768 (5) 0.7774 (5)
		α_{45}	0.2128 (5) 0.2173 (5)	0.2229 (5) 0.2223 (5)
		α_{148}	0.000286 (24) 0.000342 (21)	0.000292 (25) 0.000350 (22)

Table 6.4: Alpha-particle emission probabilities for ^{242}Pu as a function of effective efficiency with and without coincidence-summing corrections. For the measurements made with the highest effective efficiency (450 mm^2 active area detectors), two values are presented for each emission probability: one obtained with the detector No 84488 (upper values) and one measured with the detector No 59871 (bottom values).

(b) Given the isotopic composition of the sources and the energies of the emitted alpha-particles, the ^{238}Pu+^{241}Am contribution can be neglected. From the remaining isotopes, only week peaks from ^{239}Pu and ^{240}Pu could show up in the region of interest (see Figure 6.5 and Table 6.5). The contributions of the interfering emissions were calculated for each measuring system. The multiplet composed by the 5105.81, 5143.82 and 5156.59 keV emissions from ^{239}Pu and the 5123.6 and 5168.13 keV from ^{240}Pu was deconvolved using ALFITeX, and the areas of the interfering emissions were calculated for the main peaks. The following counting rates were obtained: 2.3 x 10^{-7} s^{-1} for the high-stability chamber and 1.7 x 10^{-6} s^{-1} for the α-e_c coincidence chamber. These values are even lower than the background counting rates. Hence, the ^{239}Pu+^{240}Pu contribution could also be neglected in this case, although its corresponding uncertainty component was calculated and added to the final proposed values for the emission probabilities.

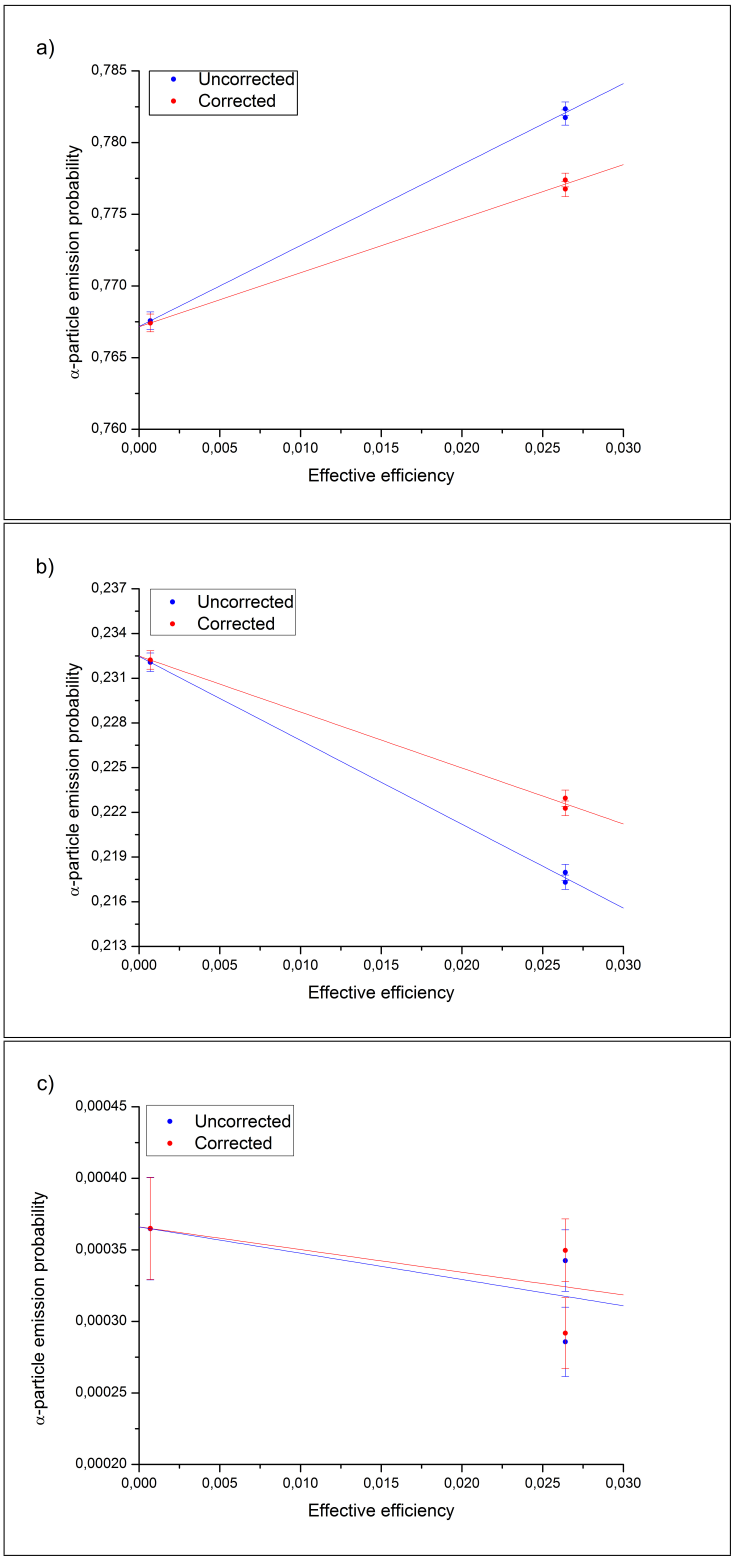

Figure 6.4: Emission probability values of the α_0 (a), α_{45} (b) and α_{148} (c) peaks, derived from the fitting of the spectra measured with the high-stability chamber and the α-e$_c$ chamber. Values corrected by coincidence summing are plotted in red while those without corrections are in blue. The extrapolation of the values to zero efficiency provides the best estimations for the alpha emission probabilities.

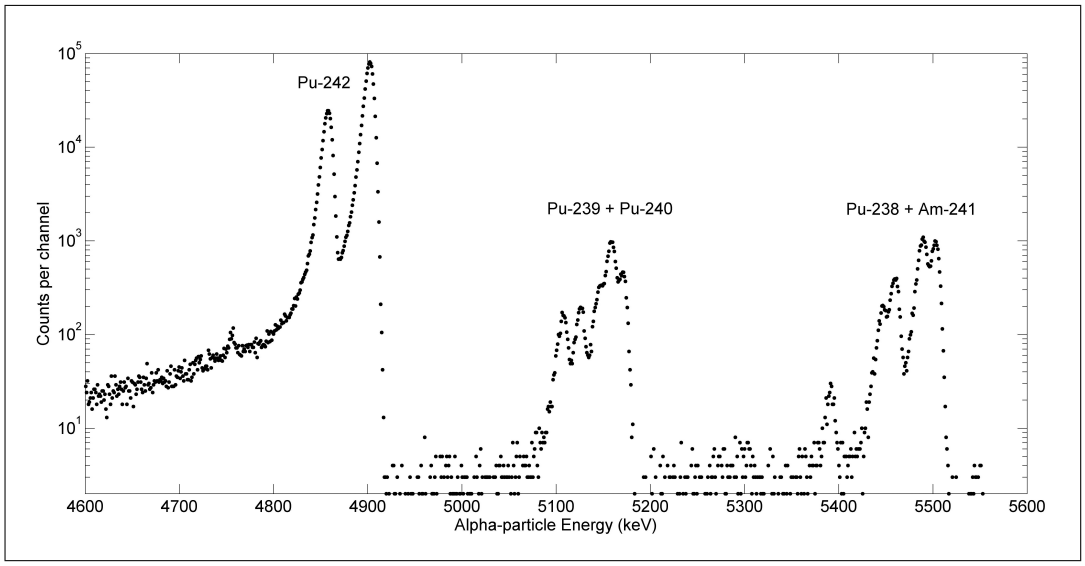

Figure 6.5: Total sum spectrum of ^{242}Pu measured with the high-stability chamber showing the peaks corresponding to the impurities of the other plutonium isotopes and ^{241}Am present in the source.

^{239}Pu		^{240}Pu	
E_α (keV)	P_α (%)	E_α (keV)	P_α (%)
4911.69 (21)	0.0030 (16)		
4866.91 (21)	0.0018 (5)	4863.5 (2)	0.001082 (18)
4829.38 (21)	0.00354 (7)		
4770.01 (21)	0.00125 (3)		
4737.05 (21)	0.00570 (5)		

Table 6.5: Interfering alpha-particle emissions of ^{239}Pu and ^{240}Pu present in the region of interest. Uncertainties are given in units of the last significant figures. Data are taken from the Decay Data Evaluation Project (DDEP) [71].

6.4 Results

The extrapolation to zero efficiency of the peak intensity values (see Figure 6.4) provides the best estimations for the alpha emission probabilities of ^{242}Pu. The final values were calculated as the extrapolation of the result obtained from the measurements with the high-stability chamber and the average of the values calculated from the measurements with the α-e_c chamber. Table 6.6 shows a comparison between the recommended emission probabilities [109] and the values proposed in this work.

α Branch	α Energy (keV)	Evaluation [109]	This work
α_{148}	4756	0.000304 (13)	0.000366 (36)
α_{45}	4858	0.2344 (17)	0.2324 (6)
α_0	4902	0.7653 (17)	0.7673 (6)

Table 6.6: Comparison between the alpha-particle emission probabilities of ^{242}Pu obtained in this work and the evaluated values [109]. The alpha energies were not measured in this work, the values presented in this table were taken from Chechev [109].

The uncertainty components for the experimental values are summarized in Table 1.8. They include:

α Branch	P_α	s_o	Uncertainty components (%)					
			s_e	s_f	s_c	s_i	s_p	s_b
α_{148}	0.000366	0.000036	0.434	9.8	0.52	1.8 x 10^{-4}	3.1 x 10^{-7}	2.1 x 10^{-3}
α_{45}	0.2324	0.0006	0.008	0.3	0.02	1.4 x 10^{-4}	2.0 x 10^{-4}	6.2 x 10^{-3}
α_0	0.7673	0.0006	0.002	0.1	0.02	1.4 x 10^{-4}	6.4 x 10^{-4}	6.2 x 10^{-3}

Table 6.7: The uncertainty components refer to: s_o overall uncertainties (see text), s_e extrapolation process, s_f fitting procedure (covariance matrix), s_c coincidence summing corrections, s_i impurities in the source, s_p omitted small peaks and s_b background contribution. The quoted overall uncertainties correspond to one standard deviation.

- s_e: uncertainty related to the extrapolation process. For each emission probability it was calculated as the difference between the results of the extrapolations of the value obtained with the high-stability chamber and each value from the α-e_c chamber.
- s_f: uncertainty associated to the fitting process and obtained from the covariance matrix as it is described in Chapter 5.
- s_c: additional uncertainty produced by the coincidence summing corrections. It was calculated as the sum of the summing-in and summing-out contributions and divided by a factor of four.
- s_i: contribution resulted from the interfering small emissions of ^{239}Pu and ^{240}Pu impurities, for which no correction was made.
- s_p: uncertainty associated to the fact that the weak peak α_{307}, deduced by Vaninbroukx et al. [121] from the 158.8 keV $\gamma + ce$ transition, was not observed and therefore neglected in the analysis. This relative uncertainty was calculated multiplying the measured peak intensities by the α_{307} emission probability value.

- s_b: uncertainty component related to the background contribution.
- s_o denotes the overall uncertainty obtained as the square root of the quadratic sum of the uncertainty components.

Although six sources of uncertainty have been considered, that associated with the spectral fitting process is the largest remaining uncertainty component.

6.5 Discussion

Although there are some older data obtained by magnetic spectrometry, the only set of values with an explicit calculation of uncertainties was published by Vaninbroukx et al. [121] and includes both alpha-particle and gamma-ray emission probabilities measured with semiconductor detectors. Alpha-particle emission probabilities measured in this work agree well with the values reported by them for the two major emissions and are compatible with that of the weakest emission.

In general, our values exhibit lower uncertainties than those of Vaninbroukx et al. [121], a consequence of the intensive numerical analysis of spectra, the higher statistical contents of our measurements and the purity of the measured samples. The only exception corresponds to the emission probability of the weakest peak, for which the uncertainty considered in this study doubles that declared by these authors. Given all factors mentioned in the precedent paragraph we consider that their uncertainty evaluation for the minor emission could not be realistic. For the same reason, a new evaluation of P_α values for this nuclide should be considered.

Chapter 7

Study of ^{243}Am decay

^{243}Am decays 100 % by alpha-particle emission to ^{239}Np and with a minute branch of 3.8 (7) x 10^{-9} % by spontaneous fission. Its half-life is 7367 (23) years [125]. A simplified decay scheme of this radionuclide is shown in Figure 7.1.

As noted in the previous chapter, the Coordinated Research Project (CRP) "Updated Decay Data Library for Actinides" [116] highlighted the need to review several nuclear data for some actinides, such as ^{243}Am. This evaluation requests new measurements of the half-life and some alpha-particle and gamma-ray emission probabilities of this nuclide.

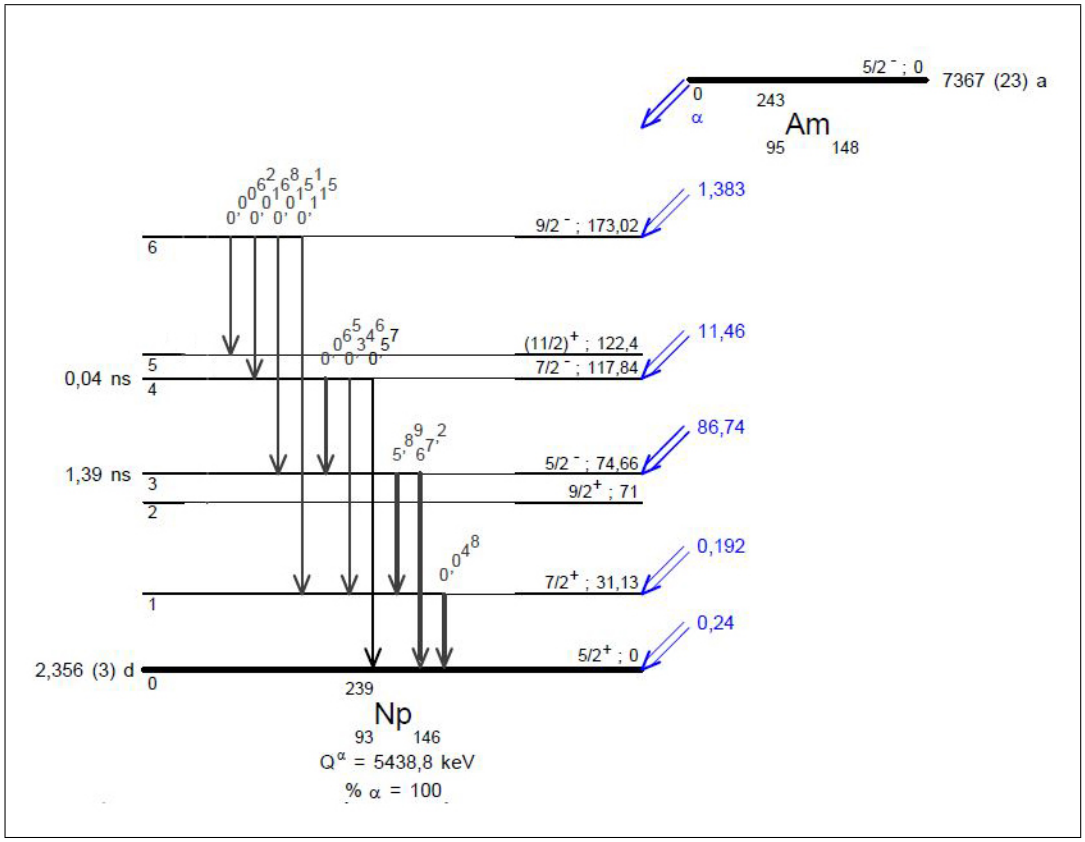

Figure 7.1: Simplified decay scheme of ^{243}Am taken from Browne et al. [125].

7.1 Previous measurements and evaluations

The results of previous measurements and evaluations of the gamma-ray emissions and energies for ^{243}Am are contained in Tables 7.1 and 7.2. In 1960, Asaro et al. [126] firstly proposed gamma-ray emission probabilities for the 43.53, 74.66 and 117.84 keV transitions obtained by measurements with scintillator detectors. In 1968, Van Hise and Engelkemeir [127] published a detailed study of the decay of ^{243}Am by measuring alpha-gamma coincidences using Si(Au) surface-barrier and Ge(Li) detectors with a two-parameter multichannel analyzer and applying the usual fast-slow coincidence technique. Besides the three transitions already observed, they found new transitions at 31.14, 50.62, 55.18, 86.71, 141.89, 169, 195 and 220 keV. Also in 1968 Aleksandrov et al. [128] measured the gamma-ray emissions of 43.53, 74.66 and 117.84 keV by the alpha-gamma coincidence method. They used a silicon surface-barrier detector for alpha particles and both a proportional gas-discharge counter and a scintillation spectrometer for LX radiation and gamma rays.

In 1972, Ahmad and Wahlgren [129] obtained gamma-ray emission probabilities by gamma spectrometry using coaxial Ge(Li) detectors. They reported gamma intensities for ^{243}Am and also K X-rays from plutonium and gamma rays corresponding to ^{239}Np. Gamma spectrometry and gamma-gamma coincidences were used by Pate et al. [130] to determine the gamma-ray energies and emission probabilities from both ^{243}Am and ^{239}Np decays. Latter, in 1982, Ahmad [131] measured again the ^{243}Am-^{239}Np gamma-ray emission probabilities by gamma-ray spectrometry but this time using planar intrinsic Ge detectors. He was the first author who reported the gamma intensity of the 31.14 keV transition. Vaninbroukx et al. [132] deduced in 1984 the ^{243}Am-^{239}Np photon-emission probabilities from the photon-emission rates, measuring with a High-Purity germanium (HPGe) detector, and the disintegration rates determined by alpha-particle counting in well-defined solid angles.

In 1996, Woods et al. [133] and Sardari et al. [134] measured the latest published values of gamma-ray emission probabilities for ^{243}Am. The first authors measured by gamma-ray spectrometry using intrinsic Ge detectors. Sardari et al. applied two methods: i) deducing the gamma probability from the gamma-emission rates (measuring with a planar Ge detector) and the absolute ^{243}Am disintegration rate (measured with a surface-barrier Si detector and well-known solid angles, and with the $4\pi\beta-\gamma$ coincidence system); and ii) measuring alpha-gamma coincidences using a fast-slow system with a Si(Au) surface-barrier detector for alpha-particles and a planar Ge detector for gamma rays. With the second method, the authors found three new transitions: 46.84, 98.36 and 102.02 keV.

Finally, Browne et al. [125] reported, after the evaluation of all available data, a set of gamma-ray emission energies and probabilities for ^{243}Am that are the last recommended data by the DDEP [71] for this radionuclide. In this evaluation, the gamma-ray emission probabilities for 46.84 and 102.02 transitions obtained by Sardari et al. [134] are not included. The aim of the present work was trying to find experimental evidences that confirm the existence

Transition	γ Energy (keV)	Measurements											Evaluation
		Asaro et al. [126]	Van Hise and Engelkemeir [127]	Aleksandrov et al. [128]	Ahmad and Wahlgren [129]	Pate et al. [130]	Starozhukov et al. [135]	Popov et al. [136]	Ahmad [131]	Vaninbroukx et al. [132]	Woods et al. [133]	Sardari et al. [134]	Browne et al. [125]
$1 \rightarrow 0$	31.14	-	-	-	-	-	-	-	0.069 (7)	-	-	0.0477 (13)	0.048 (4)
$4 \rightarrow 3$	43.1	-	0.03	-	-	-	-	-	-	-	-	-	0.065
$3 \rightarrow 1$	43.53	4 (1)	5.3	5 (1)	5.5 (3)	-	-	5.3 (12)	6.20 (30)	6.04 (13)	5.93 (10)	5.72 (17)	5.89 (10)
$6 \rightarrow 5$	50.6	-	0.0027	-	-	-	-	-	-	-	-	0.0168 (11)	0.0168 (11)
$6 \rightarrow 4$	55.18	-	0.0094	-	-	-	-	-	-	-	-	0.0168 (11)	0.0168 (11)
$3 \rightarrow 0$	74.66	69 (3)	61	-	66 (3)	-	59.1 (40)	60 (4)	68.0 (20)	68.5 (15)	66.7 (12)	68.4 (13)	67.2 (12)
$4 \rightarrow 1$	86.71	-	0.37	-	-	-	-	-	0.340 (15)	0.35 (1)	0.342 (15)	0.344 (9)	0.346 (9)
$6 \rightarrow 3$	98.5	-	-	-	-	-	-	-	-	-	-	0.0151 (21)	0.0151 (21)
$4 \rightarrow 0$	117.60	-	0.75	-	-	-	-	-	-	-	-	0.57 (5)	0.57 (5)
$6 \rightarrow 1$	141.90	-	0.13	-	-	-	-	-	0.128 (6)	0.13 (1)	0.117 (5)	0.1068 (26)	0.115 (8)
$7 \rightarrow 2$	169	-	0.0012	87.9 (3)	-	-	-	-	-	-	-	-	0.0012
$9 \rightarrow 5$	195	-	0.00085	-	-	-	-	-	-	-	-	-	0.00085

Table 7.1: Experimental and evaluated gamma-ray emission probabilities (%) for ^{243}Am-daughter, ^{239}Np.

Transition	Measurements					Evaluation
	Van Hise and Engelkemeir [127]	Engelkemeir [137]	Pate et al. [130]	Ahmad [131]	Sardari et al. [134]	Browne et al. [125]
$1 \rightarrow 0$	31.2	-	31.10 (15)	31.14 (3)	31.13	31.14 (3)
$4 \rightarrow 3$	-	43.1	43.1	-	-	43.1
$3 \rightarrow 1$	43.6	-	43.53 (15)	43.53 (2)	43.53	43.53 (2)
$6 \rightarrow 5$	50.6	-	-	-	50.6	50.6
$6 \rightarrow 4$	55.4	55.4	-	-	55.18	55.18
$3 \rightarrow 0$	74.8	74.7	74.67 (15)	74.66 (2)	74.66	74.66 (2)
$4 \rightarrow 1$	86.7	86.7	86.79 (15)	86.71 (2)	86.71	86.71 (2)
$6 \rightarrow 3$	-	98.5	-	-	98.5	98.5
$4 \rightarrow 0$	117.8	117.8	117.60 (15)	-	117.84	117.60 (15)
$6 \rightarrow 1$	142	142	142.18 (15)	141.89 (3)	141.89	141.90 (6)
$7 \rightarrow 2$	169	-	-	-	169	169
$9 \rightarrow 5$	195	-	-	-	195	195

Table 7.2: Measured and evaluated gamma-ray energies (keV) for ^{243}Am-daughter, ^{239}Np.

of these two transitions as well as reviewing some of the gamma-ray emission probabilities previously reported. For that purpose, gamma-ray spectrometry and alpha-gamma coincidence measurements were used in this work.

7.2 Experimental

7.2.1 Source calibration

The source used for the measurements was previously measured by García-Toraño and Aceña [16] to determine the alpha-particle emission probabilities of ^{243}Am. It was prepared at the Central Bureau for Nuclear Measurements (CBNM, now JRC-IRMM) by vacuum evaporation onto a stainless-steel disk, resulting in a deposit covering an area of approximately 8 mm diameter. The ^{243}Am material was originally obtained from the Oak Ridge National Laboratory (ORNL) and purified at CBNM to eliminate traces of ^{239}Pu following the procedure described by Mast et al. [138].

The source was recently re-standardized in activity at CIEMAT using absolute alpha counting under 2π geometry with a grid ionization chamber. The activity of the source was (2804 ± 14) Bq at the reference date of 11/09/2014. The uncertainty components are: 0.1 % due to standard deviation of three measurements, 0.3 % due to counting statistics and 0.4 % due to backscattering correction (a correction of 1.2 % was applied [6, 139, 140]).

7.2.2 Measurements

The ^{243}Am source was measured with the alpha-gamma coincidence device described in detail in Section 4.1. A PIPS detector was placed at the top of the chamber to measure alpha particles and a LEGe detector was coupled to the back of the chamber to register gamma rays. The radioactive source was placed on the rotary support so that the normal axis of the source formed 45° angle with the normal axes of both detectors. The digital module, detailed in Section 4.3.1, was preferred to the analog dual-parameter multichannel setup (see Section 4.2) due to the possibility of implementing an "offline" post-processing of registered data with different parameters (such as dead times and others) to evaluate their effect and the associated uncertainties.

The measurements were carried out for 132 days without interruptions. A total number of 316 binary data files were obtained and processed using the code DIGDATA (see Section 4.3.2). Dead times were selected according to the detector characteristics; thus, while dead times of 10 μs were required to reach a good signal shaping in the planar LEGe detector, due to the small size of the alpha silicon detector, a similar condition can be obtained using a few microseconds (3 μs). As a result, one alpha-particle, one gamma-ray and one alpha-gamma coincidence spectra were created.

Alpha-particles

Alpha-particles were measured by a PIPS detector with 50 mm^2 active area and 100 μm Si thickness placed at the top of the chamber. The source-to-detector distance was 30 mm and the source-to-detector angle was 45°. Neither magnets to reduce the number of conversion-electrons detected nor any collimator to improve energy resolution were used for the measurements. With this configuration the geometrical efficiency reached was about $\epsilon = 0.0049$. The total number of counts was 1.6 x 10^8, the energy resolution was 13.2 keV FWHM and the peak-to-valley ratio was 20. Since no temperature stabilization was available, some electronic drift appeared and it was necessary to use numerical techniques to combine all spectra. The numerical gain stabilization method developed by Pommé and Sibbens [29,30] was applied to determine and correct the shift. Nevertheless, the quality of the spectrum was limited by the fact that alpha particles registered by the detector are emitted in angles far from the normal, thus suffering a significant straggling in the source. Therefore, the spectrum was not suitable for a precise determination of alpha-particle emission probabilities.

Figure 7.2 shows the total alpha-particle spectrum of ^{243}Am obtained after 132 days of measurement. The five most intense emissions were clearly identified in the spectrum. Since a small contamination of ^{241}Am was also present in the sample, the corresponding α_0, α_{60}, α_{103} and α_{158} emissions were also observed. There are no interfering peaks in the region of interest for the ^{243}Am, the alpha particles from ^{241}Am are being emitted at higher energies. Only the contribution of the tails should be considered in this region, however, the sum of the tail areas is only 0.02 % of the ^{243}Am total area. Therefore, area corrections due to interfering emissions could be considered negligible.

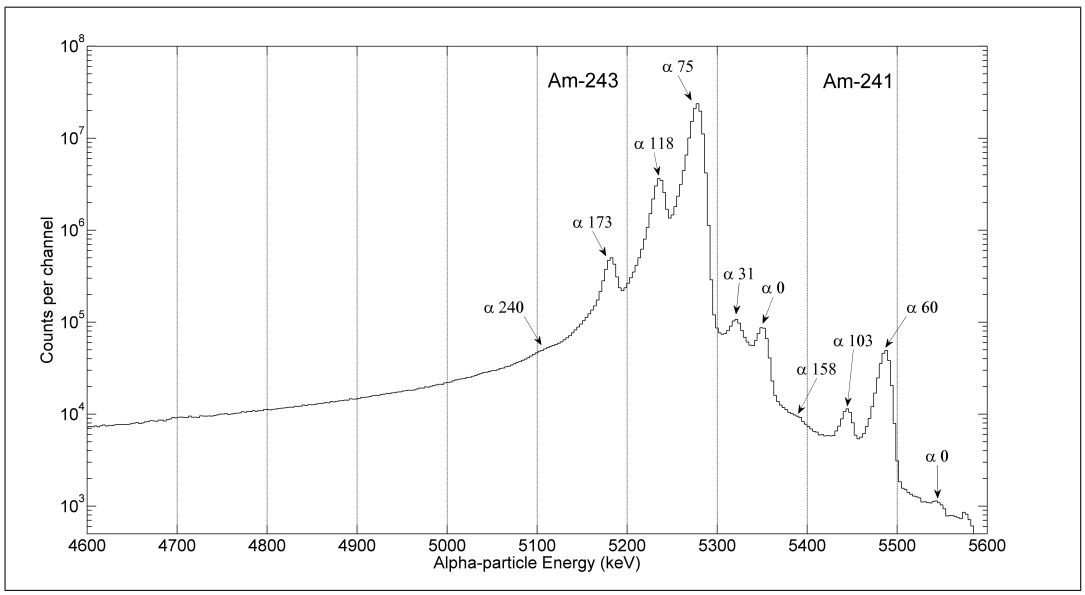

Figure 7.2: Alpha-particle spectrum of ^{243}Am obtained with the PIPS detector from the $\alpha - \gamma$ coincidence measuring system. The measuring time was 132 days.

Since no magnets were used for the measurements, a large number of conversion-electrons were also detected by the PIPS detector under the same geometrical measuring conditions. The conversion-electron spectrum is shown in Figure 7.3. Conversion-electrons corresponding to the most intense L and M emissions were identified in the spectrum.

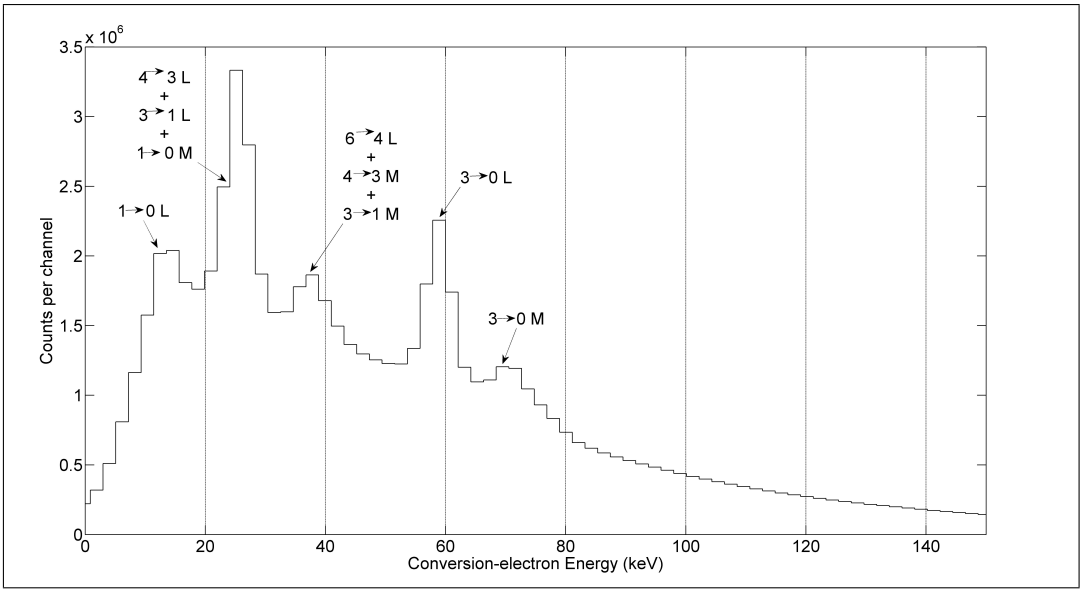

Figure 7.3: Conversion-electron spectrum of ^{243}Am measured with the PIPS detector from the measuring setup. The measuring time was 132 days.

Gamma-rays

Gamma-rays were measured by a LEGe detector with 100 mm^2 active area and 10 mm thick coupled to the back of the chamber. The source-to-detector distance was about 40 mm and the source-to-detector angle was 45°. A total number of 2.7 x 10^8 counts and an energy resolution of 0.8 keV FWHM for 74.66 keV were obtained with this measuring configuration.

Figure 7.4 shows the total gamma-ray spectrum obtained after 132 days. The main gamma-ray emissions of ^{243}Am and L X-rays from Np were identified. Since ^{243}Am-daughter, ^{239}Np, was in equilibrium with the parent, K and L X-Rays and gamma rays of ^{239}Pu were also registered with the measuring set-up. Moreover, it was also identified in the spectrum the 59.54 keV emission from the small contamination of ^{241}Am.

It is necessary to point out the presence of deformed peaks at higher energy regions. A revision of the measurement system indicated a failure in the preamplifier operation. An attempt was made to correct this effect changing the pulse modeling parameters by the digital module. However, it was not possible to remove it completely. This deformation was directly proportional to energy and only affected peak shape but not peak areas, so it did not significantly influence the gamma-ray emission probability values.

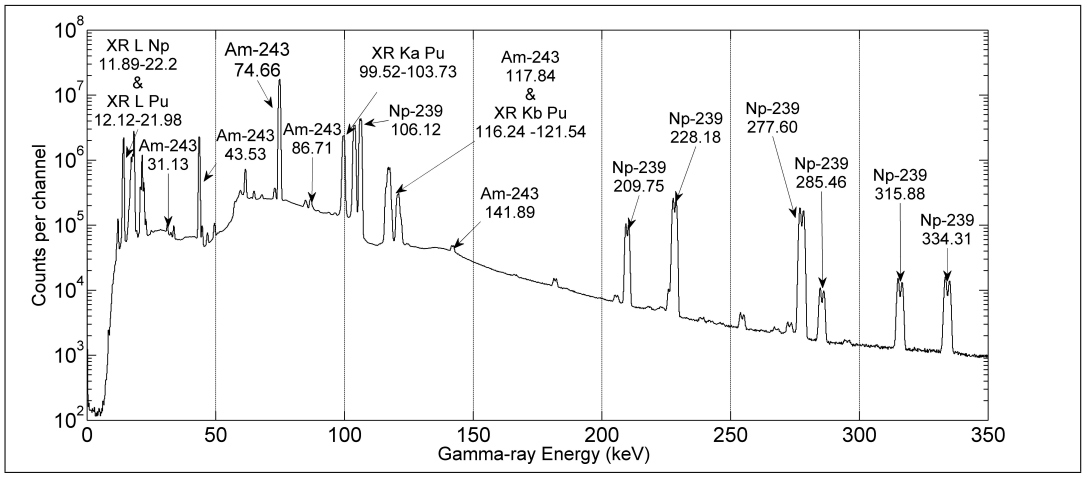

Figure 7.4: Gamma-ray spectrum of ^{243}Am and ^{239}Np obtained with the LEGe detector from the $\alpha-\gamma$ coincidence system. The measuring time was 132 days.

Efficiency calibration of the LEGe detector

In order to carry out a precise efficiency calibration of the LEGe detector for the specific measuring geometry of the ^{243}Am source, a set of three sources (two prepared and standardized at CIEMAT and one at NIST) were used:

- An ^{241}Am source with an active area of approximately 7 mm diameter and (66.1 ± 0.7) Bq activity at the reference date of 12/12/2014.
- A ^{133}Ba source with an active area of approximately 9 mm diameter and (347.7 ± 2.8) Bq activity at the reference date of 12/12/2014.
- A multigamma source of ^{154}Eu, ^{155}Eu and ^{125}Sb with an active area of approximately 7 mm diameter and (3990 ± 24), (268.4 ± 2.1) and (11.2 ± 0.1) Bq activity, respectively, at the reference date of 12/12/2014.

The efficiencies were calculated as $\epsilon_{peak} = \frac{R}{AP_\gamma}$, where ϵ_{peak} is the peak efficiency, R is the counting rate calculated on the basis of the net peak area, A is the radionuclide activity and P_γ is the corresponding gamma-ray emission probability. The peak areas were determined using the analysis code developed by the International Atomic Energy Agency (IAEA), GRILS. The gamma-ray emission probabilities were taken from the Decay Data Evaluation Project (DDEP) [71].

Experimental peak efficiencies obtained from the analysis of the emissions from ^{133}Ba, ^{154}Eu, ^{155}Eu and ^{125}Sb had to be corrected for coincidence-summing. For that purpose, a revised version of the expressions originally proposed by Schina and Hoppes [141] was used. All possible combinations of cascade photons and summing with K X-rays were considered while outer-shell X-Rays, electrons and bremsstrahlung summing were ignored. The peak and the total efficiencies for each energy and radionuclide were used for the calculation of the correction factors. Both the peak and total efficiencies were obtained by a fitting code that implements the following semi-empirical function [142]:

$$\epsilon = \frac{\Omega}{4\pi} e^{-\sum \mu_i t_i} \left[1 - \left(\frac{e^{-\mu_p t} + e^{-k\mu_p t}}{2} \right) \right] f_e, \tag{7.1}$$

where $\frac{\Omega}{4\pi}$ represents the relative measuring solid angle, $e^{-\sum \mu_i t_i}$ is the attenuation factor due to the different absorbers placed between the source and the active volume of the detector taking into account that μ_i is the linear attenuation coefficient and t_i the thickness of the different materials. The term in square brackets represents the photoelectric interaction probability with a germanium detector of thickness t and linear attenuation coefficient μ_p. The additional term $e^{-k\mu_p t}$ takes into account the effect of close geometries. Finally, f_e is a function that accounts for the escape of X-Rays from Ge. After the fitting procedure, optimal solid angle and thickness parameters were obtained and subsequently used to calculate the total efficiencies from the peak efficiencies by using the total interaction cross sections in place of the photoelectric ones. The photon cross sections were taken from the code XCOM, developed by the National Institute of Standards and Technology (NIST) [143].

Once the experimental peak efficiencies were corrected by coincidence-summing, data were fitted a second time using the fitting code described above. Figure 7.5 presents the experimental peak efficiency values (corrected by coincidence summing) and both the fitted peak and total gamma-ray efficiency curves.

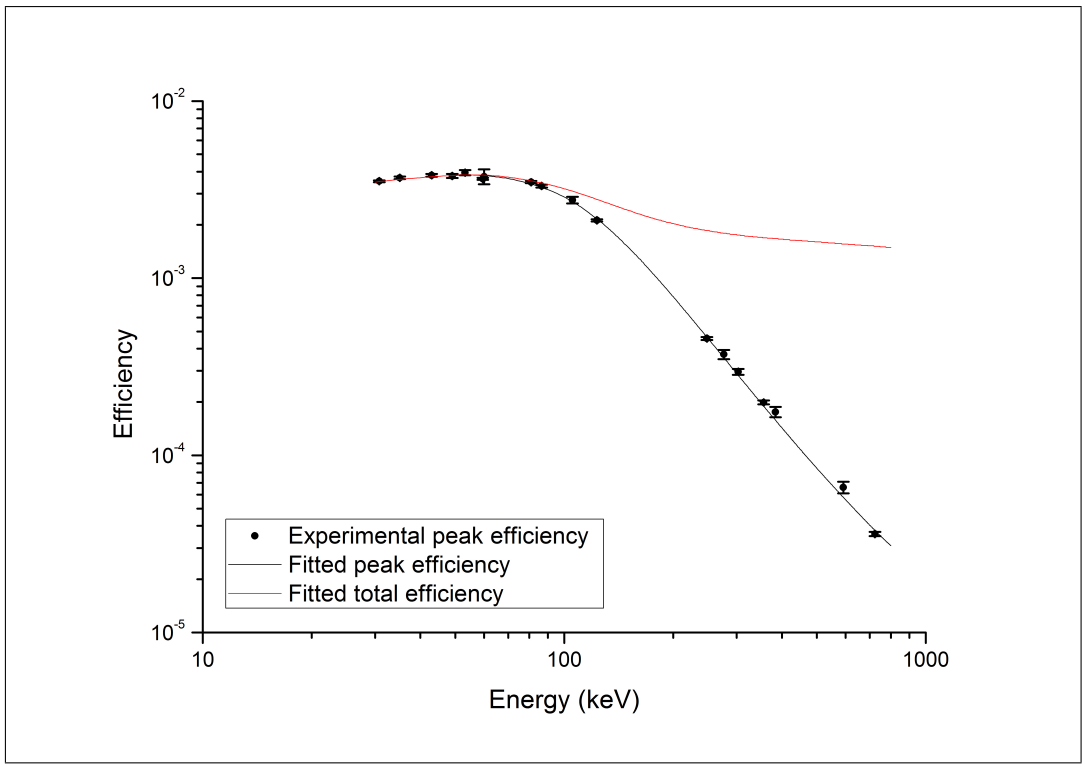

Figure 7.5: Experimental (scatter) and fitted (black solid line) peak efficiency curves of the 100 mm^2 x 10 mm planar LEGe detector. The red solid line represents the fitted total efficiency curve obtained from the peak efficiency values.

Table 7.3 lists the measured peak efficiencies (corrected by coincidence summing) and the corresponding fitted efficiencies at the specific gamma-ray energies required for the ^{243}Am study. The energy range of interest was from 30 to 800 keV. From an examination of the fit, the uncertainties of the interpolated values have been estimated as 2%.

Radionuclide	γ Energy (keV)	Measured ϵ	Fitted ϵ
^{133}Ba	30.78*	0.00353 (4)	0.00351 (4)
^{133}Ba	35.10*	0.00369 (6)	0.00361 (6)
^{154}Eu	43.00*	0.00381 (7)	0.00374 (7)
^{243}Am	43.53	-	0.00374 (7)
^{243}Am	46.84	-	0.00378 (8)
^{154}Eu	49.00*	0.00377 (10)	0.00380 (10)
^{243}Am	50.62	-	0.00381 (8)
^{133}Ba	53.16	0.00394 (13)	0.00382 (13)
^{243}Am	55.18	-	0.00382 (8)
^{241}Am	59.54	0.00364 (5)	0.00380 (5)
^{155}Eu	60.01	0.00375 (36)	0.00379 (36)
^{243}Am	74.66	-	0.00355 (7)
^{133}Ba	81.00	0.00349 (5)	0.00340 (5)
^{155}Eu	86.55	0.00331 (6)	0.00326 (6)
^{243}Am	86.71	-	0.00325 (7)
^{243}Am	98.36	-	0.00292 (6)
^{243}Am	102.02	-	0.00281 (6)
^{155}Eu	105.3	0.00276 (12)	0.00270 (12)
^{243}Am	117.84	-	0.00232 (5)
^{154}Eu	123.07	0.00212 (3)	0.00216 (3)
^{243}Am	141.89	-	0.00168 (3)
^{154}Eu	247.93	0.000457 (9)	0.000466 (9)
^{133}Ba	276.40	0.000371 (22)	0.000355 (22)
^{133}Ba	302.85	0.000296 (11)	0.00283 (11)
^{133}Ba	356.01	0.000199 (5)	0.000190 (5)
^{133}Ba	383.85	0.000176 (12)	0.000158 (12)
^{154}Eu	591.76	0.000066 (5)	0.000058 (5)
^{154}Eu	723.30	0.000036 (1)	0.000038 (1)

Table 7.3: Measured and fitted gamma-ray peak efficiencies. *X-Rays.

Coincidence measurements

Alpha-gamma coincidence spectra were created by offline processing of raw data using the code DIGDATA. In the ^{243}Am decay scheme, gamma-ray transitions are very fast (the life-times are in the order of nanoseconds) so the accurate coincidence calculation was guaranteed. Moreover, ^{239}Np has a half-life of 2.3 days, hence no coincidences between alpha particles (gamma rays) from ^{243}Am and gamma rays (alpha particles) from ^{239}Np could be registered.

The first step was the creation of the *coincidence curve* measuring the

time delay between alpha ("start input"') and gamma ("stop input") pulses. Figure 7.6 shows the coincidence curve of ^{243}Am obtained from the timestamps registered by the digital module. It has a Gaussian-like shape and is practically symmetric. Moreover, it shows that alpha events are advanced 180 ns to gamma pulses. It is necessary to correct the so-called Gandy effect [69], i.e. spurious coincidences that appear when the average delay is not zero. For that purpose, the advanced events, alpha pulses in this case, should be delayed to center the curve in zero. This effect was corrected in the coincidence analysis algorithm. Taking into account this curve, the coincidence time chosen was 300 ns.

Although coincidences were established for all events, the coincidence matrix was only built for alpha-particle energies between 4250 and 5800 keV and gamma-ray energies between 0 and 200 keV. The number of channels was reduced from 32768 to 8192. The contour graphics of the coincidence regions delimited by 5150 - 5300 keV alpha-particles and 30 - 150 keV gamma-rays are shown in Figures 7.7 - 7.10. Figures 7.7 and 7.8 show the alpha region between 5150 and 5200 keV with a lower z-scale for a clearer identification of the coincidence peaks.

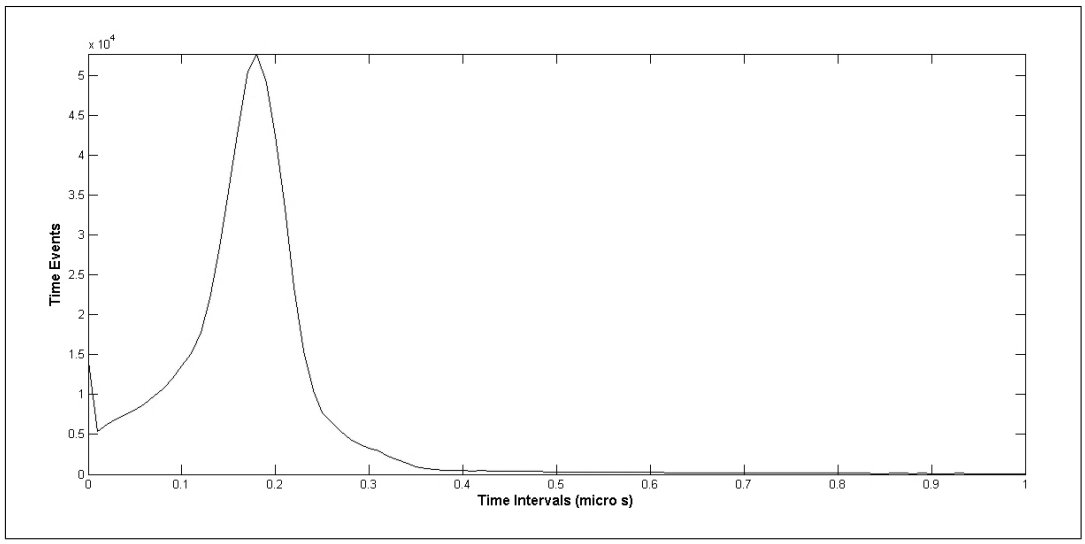

Figure 7.6: Coincidence curve of ^{243}Am obtained from the timestamps registered by the digital module.

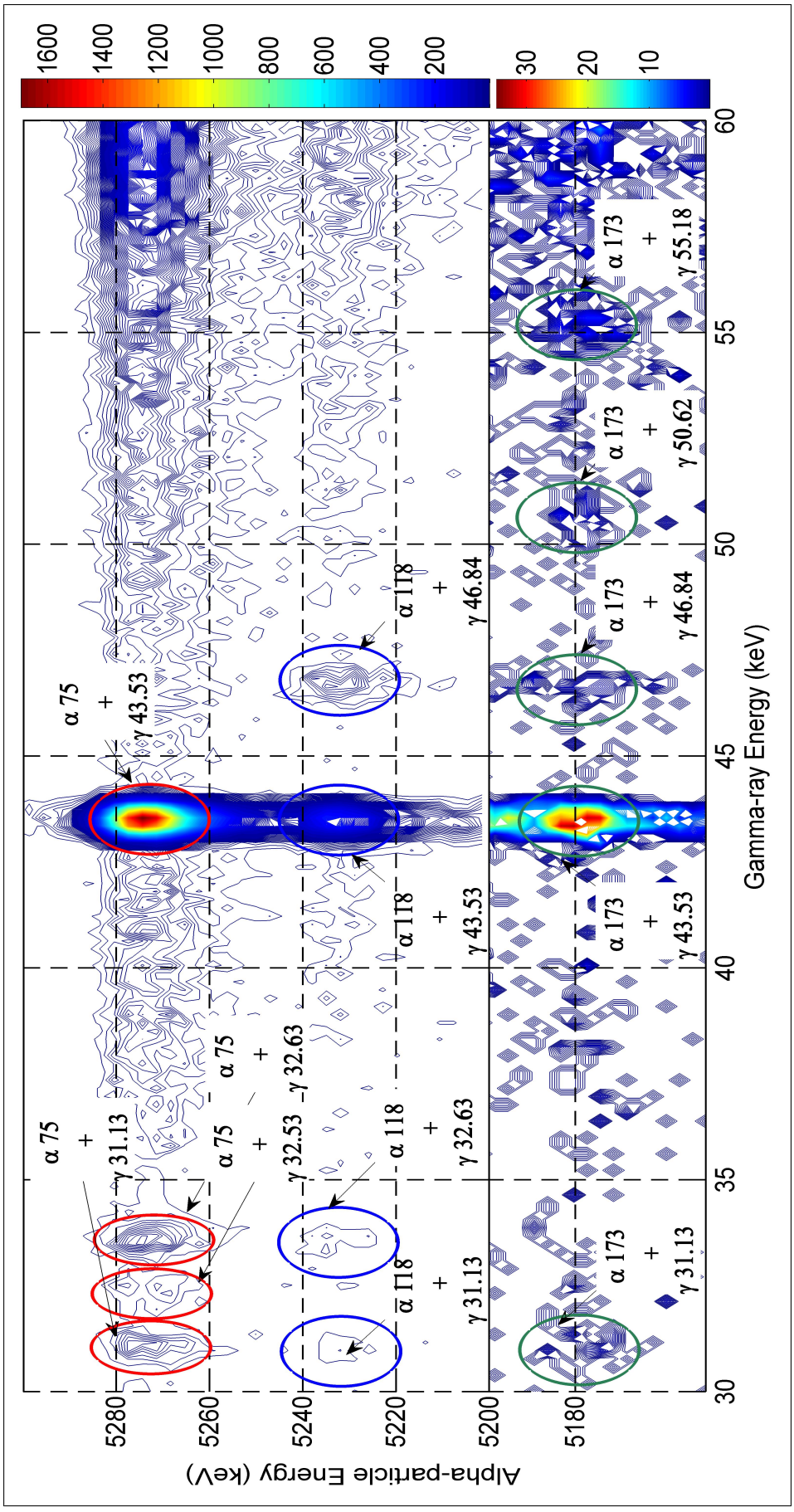

Figure 7.7: Contour plot of the coincidence region delimited by 5150 - 5300 keV alpha particles and 30 - 60 keV gamma rays. The alpha-particle region between 5150 and 5200 keV is represented in a different z-scale.

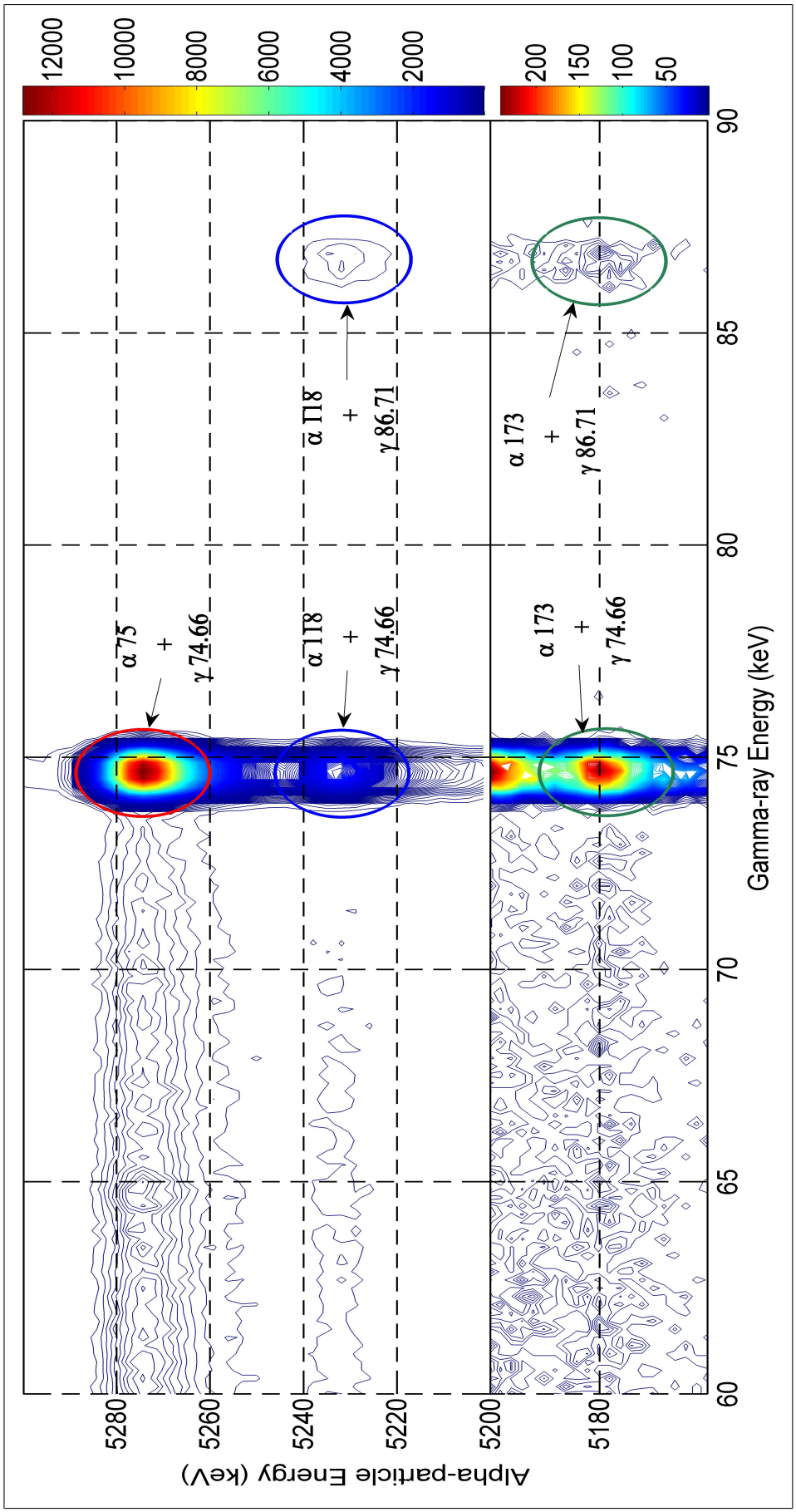

Figure 7.8: Contour plot of the coincidence region delimited by 5150 - 5300 keV alpha particles and 60 - 90 keV gamma rays. The alpha-particle region between 5150 and 5200 keV is represented in a different z-scale.

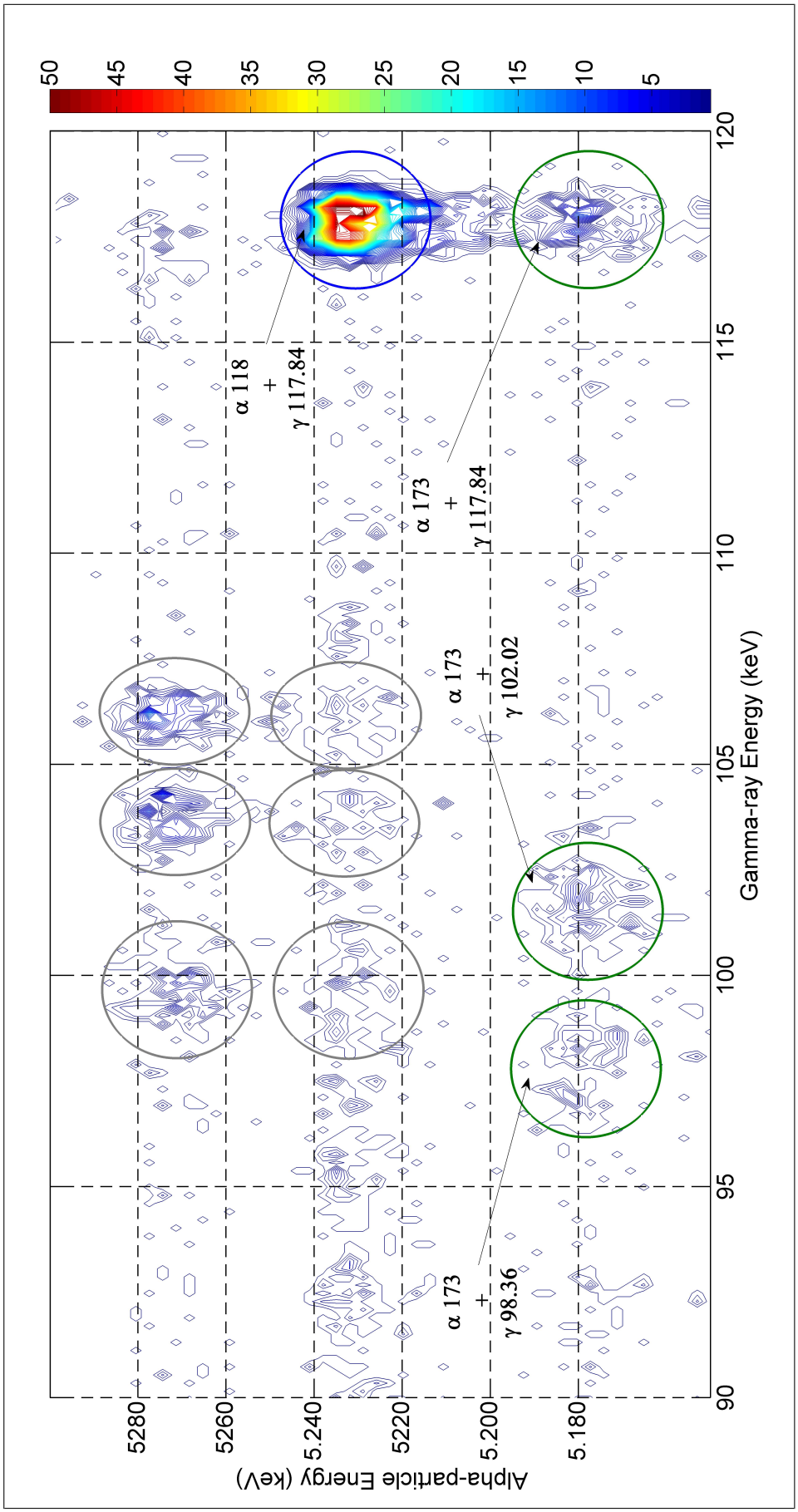

Figure 7.9: Contour plot of the coincidence region delimited by 5150 - 5300 keV alpha particles and 90 - 120 keV gamma rays.

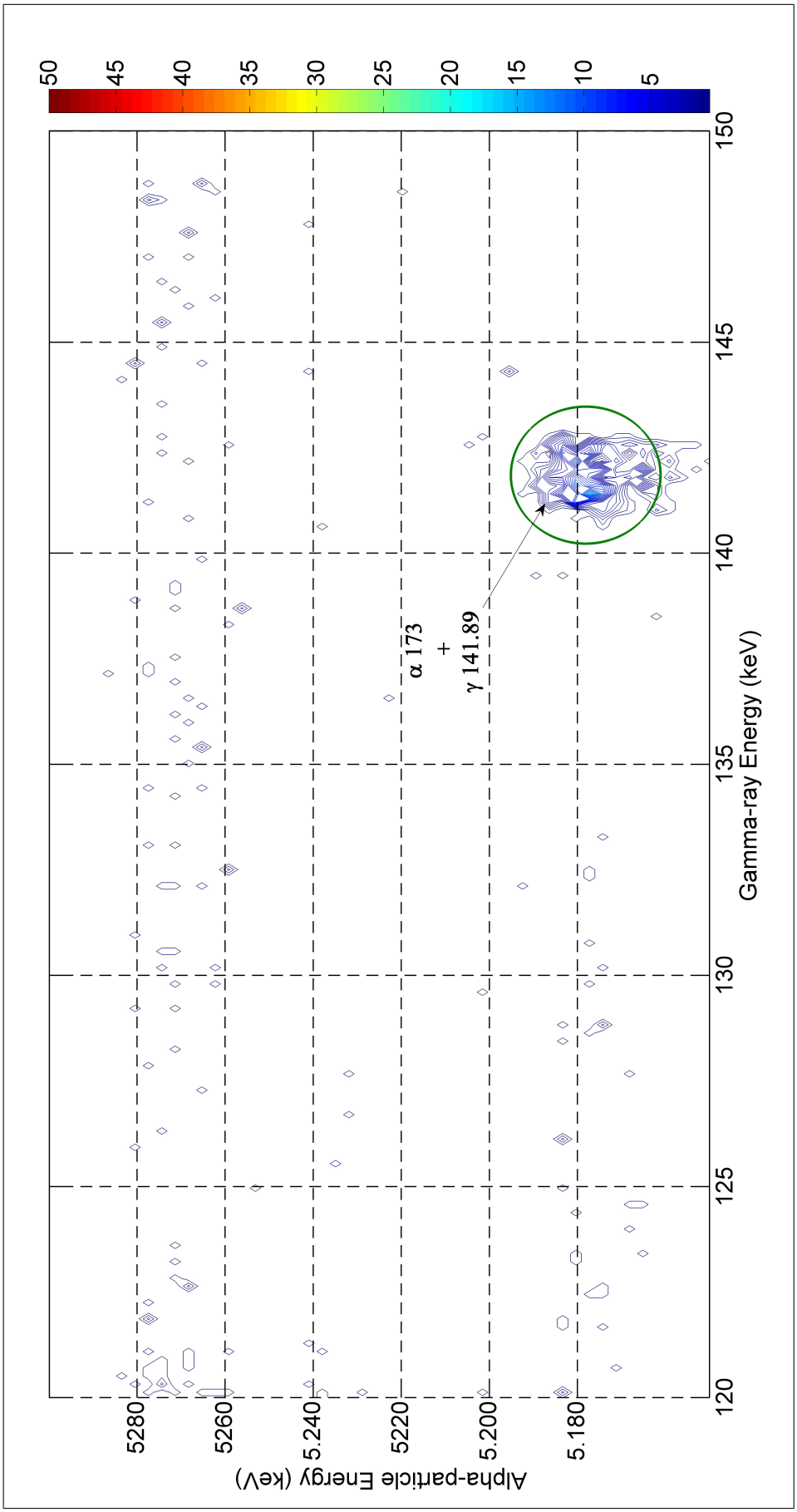

Figure 7.10: Contour plot of the coincidence region delimited by 5150 - 5300 keV alpha particles and 120 - 150 keV gamma rays.

7.3 Detailed analysis of gamma-ray transitions

As mentioned in Section 7.1, this work was focused on trying to find experimental evidences that confirm the existence of the two gamma transitions from the alpha-particle decay of ^{243}Am obtained by Sardari et al. [134] and not included in the Nuclear Data Tables [125] and reviewing some of the gamma-ray emission probabilities (P_γ) previously reported. The experimental P_γ for 31.13, 43.53, 46.84, 74.66, 86.71 and 141.89 keV emissions were calculated by gamma-ray spectrometry. Lines that were hidden or peaks distorted by the presence of gamma-photons or X-Rays from Pu were studied by alpha-gamma coincidence measurements. In that case, the experimental gamma-ray emission probability conditioned by the corresponding energy level desexcitation ($P_\gamma|_\alpha$), i.e. normalized by the sum of the probabilities of all transitions from the corresponding level, was calculated.

7.3.1 Transitions not included in the Nuclear Data Tables

The following two transitions were previously reported by Sardari et al. [134], but are not placed in the decay scheme (Nuclear Data Tables):

- 46.84 keV, from the 117.84 to the 71 keV energy level.
- 102.02 keV, from the 173.02 to the 71 keV energy level.

These transitions have been observed in the course of our measurements. They were firstly identified using the alpha-gamma coincidence measurements. Afterward, the corresponding P_γ and $P_\gamma|_\alpha$ were obtained by a rigorous analysis of the coincidence and non-coincidence spectra.

46.84 keV transition

A well-defined peak was observed at 46.80 keV (according to the experimental energy calibration) in the regular gamma-ray spectrum. It was believed to be the E1 transition from the $7/2^-$ 117.84 keV level to the $9/2^+$ 71 keV energy level.

Identification

In order to check that this spectral line actually corresponded to the transition from 117.84 keV energy level to 71 keV level, alpha-gamma coincidences were measured. Two coincidence peaks were observed in the gamma-ray energy region of 46.84 keV (see Figure 7.11): one for 5233 keV alpha particles (α_{118}) and a smaller one for 5181 keV alpha particles (α_{173}). The first peak should correspond to the direct coincidences between alpha particles that populate the 117.84 keV energy level and gamma rays that de-populate that level to the 71 keV level. The second peak should be attributed to the cascade coincidences with alpha particles that populate the 173.02 keV level. This

level will be de-populated to the 117.84 keV level and this, in turn, will be desexcited emitting 46.84 keV gamma rays, reaching the 71 keV level.

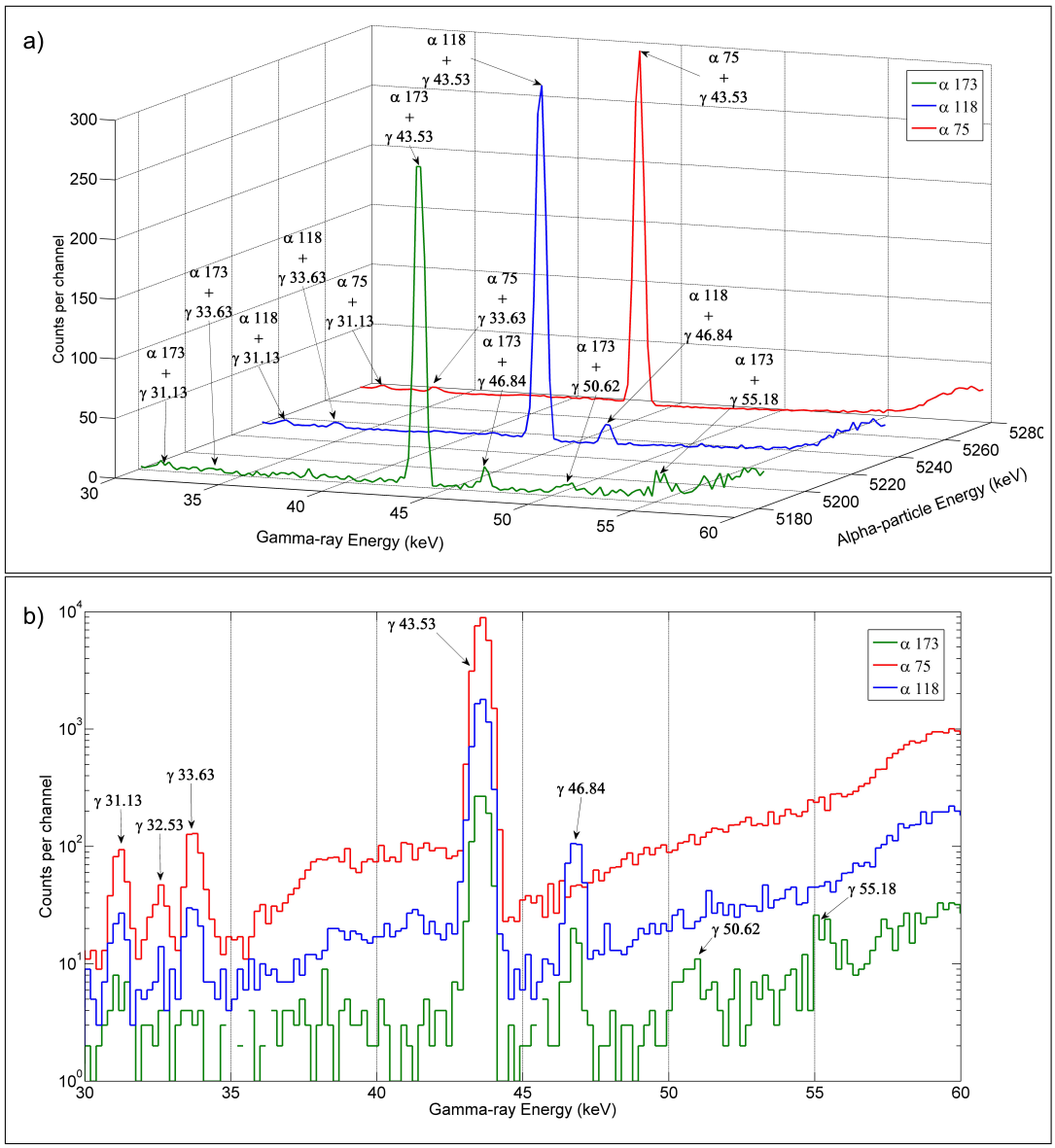

Figure 7.11: (a) 3D representation of the 30 - 60 keV energy region of the gamma coincidence spectra corresponding to α_{173} (green line), α_{118} (blue line) and α_{75} (red line). Spectra are normalized to the lower counting spectrum, α_{173}. (b) 30 - 60 keV region of the regular gamma coincidence spectra corresponding to α_{173}, α_{118} and α_{75}. It can be seen in both representations that a peak is present at 46.84 keV in both the α_{173} and α_{118} gamma coincidence spectra but not in the α_{75} spectrum.

According to the decay scheme (see Figure 7.1), there cannot be coincidences between 5275 keV alpha particles (α_{75}) and 46.84 keV gamma rays. As can be seen in Figure 7.11, no coincidence peak was raised in the 5275 keV alpha energy region.

The qualitative analysis can be reinforced by the comparison of the random and total coincidences corresponding to α_{75}, α_{118} and α_{173} and 46.84 keV transition. The random coincidences were calculated following Equation 2.3, already described in Section 2.1. Considering a coincidence time (τ) of 300 ns and the corresponding alpha and gamma counting rates in each case, the random coincidence results are shown in Table 7.4 for comparison with the total number of coincident events found.

γ Energy (keV)	Calculated random coincidences			Measured total coincidences		
	α_{75}	α_{118}	α_{173}	α_{75}	α_{118}	α_{173}
46.84	0.40 (1)	0.048 (2)	0.0061 (5)	-	320 (31)	42 (3)

Table 7.4: Calculated random coincidences and measured total gamma coincidences for α_{75}, α_{118} and α_{173} in coincidence with 46.84 keV γ-ray. The measuring time in both cases was 132 days.

The total number of coincidences were obtained from the coincidence matrix. Three gamma coincidence spectra were extracted from this matrix selecting three proper rectangular alpha ROIs and summing the gamma channel contents along these ROIs. These gamma coincidence spectra are those presented in Figure 7.11. The total coincidence counts for 46.84 keV peak were determined using the analysis code GRILS for each gamma spectrum. Table 7.4 also shows these values compared to the random coincidence results. No coincidence peak corresponding to 46.84 keV gamma rays and α_{75} was identified after the analysis of the spectrum, there was only background in this region. However, for α_{118} and α_{173} a well-defined peak was present and, in both cases, the area of the measured coincidence peak was very much higher (about 7000 times) than the calculated random coincidences.

The quantitative analysis confirmed then that only α_{118} and α_{173} were in true coincidence with the 46.84 keV line. From both approaches it seems that 46.84 keV gamma emission belongs to ^{243}Am and originates in the depopulation of 117.84 keV energy level to 71 keV level.

Gamma-ray emission probability

From direct gamma-ray spectrum

The gamma-ray emission probability of the 46.84 keV transition was calculated from the regular gamma-ray spectrum as $P_\gamma = \frac{R}{A\epsilon}$, where R corresponds to the peak areas determined using the analysis code GRILS and ϵ is the peak efficiency interpolated from the calibration curve. The result obtained is shown in Table 7.5 and compared with the value reported by Sardari et al. [134].

From coincidence measurements

Assuming no angular correlations, the true coincidence counting can be expressed as:

γ Energy (keV)	P_γ	
	Sardari et al. [134]	This work
46.84	0.000498 (13)	0.000670 (16)

Table 7.5: Gamma-ray emission probability of the 46.84 keV line.

$$N_c = N_0 P_\alpha \epsilon_\alpha P_\gamma|_\alpha \epsilon_\gamma \tag{7.2}$$

where N_0 is the number of particles emitted by the source, P_α and ϵ_α are the alpha-particle emission probability and efficiency, respectively, $P_\gamma|_\alpha$ is the gamma-ray emission probability conditioned to the desexcitation of the energy level and ϵ_γ the gamma-ray peak efficiency.

$N_0 P_\alpha \epsilon_\alpha$ corresponds to the number of alpha-particles with an specific energy detected by the detector. This value can be obtained from the alpha-particle spectrum by fitting the experimental data using the code ALFITeX, and it will be denoted hereinafter as $N_{\alpha\ ALFITeX}$. The peak efficiency (ϵ_γ) can be obtained from the calibration curve. Thus, knowing the coincidence peak area, the conditioned gamma-ray emission probability can be experimentally determined as

$$P_\gamma|_\alpha = \frac{N_c}{N_{\alpha\ ALFITeX}\epsilon_\gamma}. \tag{7.3}$$

$P_\gamma|_\alpha$ is the only gamma probability that can be purely obtained experimentally by alpha-gamma coincidence measurements. It must be noted, however, that this gamma probability can be subject to angular correlations because it is influenced by the measuring geometry (detectors forming 90°). For both reasons, it was decided to study $P_\gamma|_\alpha$ instead of the regular P_γ by the coincidence technique.

In order to improve the consistency of the measurements for this transition, two values of $P_\gamma|_\alpha$ were calculated from the direct coincidences between alpha particles that populate the 117.84 keV energy level and gamma rays that depopulate that level to the 71 keV level. The coincidence peak area (N_c) was calculated from the coincidence matrix by two approaches:

- Gamma coincidence spectrum

  A gamma coincidence spectrum was extracted from the matrix selecting the rectangular alpha ROI corresponding to α_{118} (5189-5241 keV) and summing the gamma channel contents along this ROI (see Figure 7.11 blue solid line). The coincidence counts for the 46.84 keV peak were determined using the analysis code GRILS.

  In this approach, the alpha ROI selected in the coincidence matrix did not take into account the contribution of the tail of the alpha peak.

This contribution should be added, hence, the total counting should be corrected dividing the value by the ratio between the peak and the total area. Considering this, the value obtained was 0.00551 (57).

- Alpha coincidence spectrum

  An alpha coincidence spectrum was extracted from the matrix selecting the rectangular gamma ROI corresponding to 46.84 keV (45.7-47.4 keV) and summing the alpha channel contents along this ROI. The alpha coincidence spectrum is shown in Figure 7.12. The coincidence counts for the 46.84 keV emission was determined fitting the spectrum by ALFITeX and considering the peak area corresponding to α_{118} (blue line in Figure 7.12).

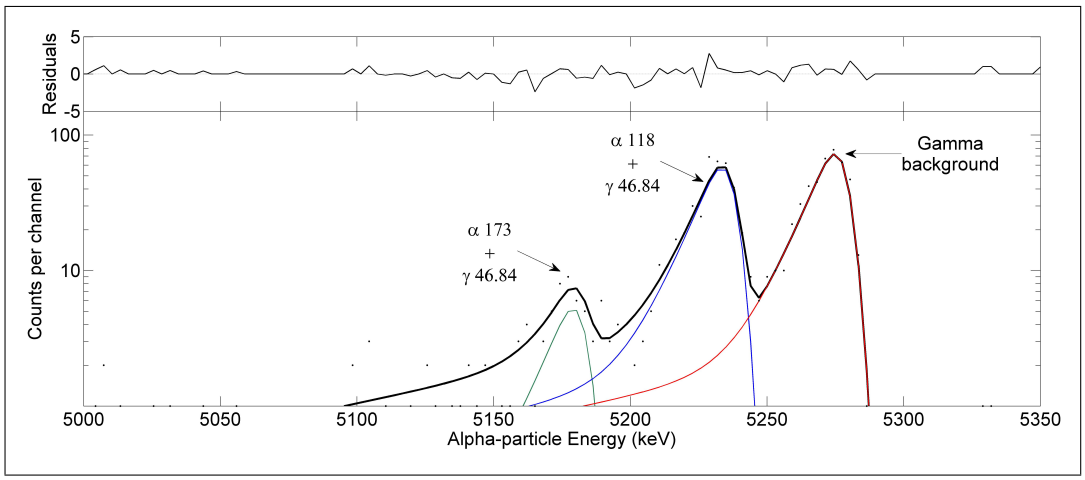

Figure 7.12: Alpha coincidence spectrum corresponding to the 46.84 keV line.

In this approach, the gamma ROI selected in the coincidence matrix took into account the contribution of both the net gamma peak and the background. Since the background is attributed to other gamma photons with higher energies, these counts do not correspond to true coincidences with 46.84 keV gamma rays. In order to disregard the wrong background contribution, the total coincidence counting should be multiplied by the ratio between the net and the total peak area. In this approach, the value obtained was 0.00521 (106).

The values were corrected by random coincidences. Other corrections like backscattering were neglected because the maximum contribution of this effect is significantly lower that the uncertainties affecting the results considering the measuring geometry.

The $P_\gamma|_\alpha$ was calculated as the weighted mean of the values obtained by both approaches as

$$\bar{x} = \frac{\sum_i^2 \frac{x_i}{\sigma_i^2}}{\sum_i^2 \frac{1}{\sigma_i^2}}, \quad \frac{1}{\sigma^2} = \sum_i^2 \frac{1}{\sigma_i^2} \tag{7.4}$$

The final experimental $P_\gamma|_\alpha$ of the 46.84 keV transition is shown in Table 7.6. This result can be compared with a reference value calculated from the corresponding P_γ value recommended in the Nuclear Data Tables [125]. The gamma-ray emission probability conditioned to the desexcitation of a specific energy level N can be calculated normalizing the gamma emission probability by the sum of the probabilities of all transitions from the corresponding level as

$$P_\gamma|_\alpha = \frac{P_\gamma}{\sum_i^p P_{T_i\ N\to M_i}}, \tag{7.5}$$

where p is the total number of transitions and $P_{T_i\ N\to M_i}$ is the transition probability from the energy level N to the final level M_i.

In the case of 46.84 keV transition, the P_γ reported by Sardari et al. [134] was normalized taking into account the transition probabilities of the 117.84 keV energy level listed in Table 7.7 and taken from Browne et al. [125]. The value obtained is also shown in Table 7.6.

γ Energy (keV)	$P_\gamma\|_\alpha$ (Isotropy)	$P_\gamma\|_\alpha$ (90 °)
	Sardari et al. [134] & Evaluation [125]	This work
46.84	0.00447 (12)	0.00544 (50)

Table 7.6: Gamma-ray emission probability of the 46.84 keV line conditioned to the desexcitation of the 117.84 keV energy level.

Final energy level (keV)	Transition Energy (keV)	P_T
74.66	43.18	0.101
31.13	86.71	0.0041 (1)
0	117.84	0.0062 (5)

Table 7.7: Transition probabilities from the 117.84 keV energy level taken from Browne et al. [125].

Discussion

Experimental evidences presented confirm the existence of the 46.84 keV transition from the $7/2^-$ 117.84 keV level to the $9/2^+$ 71 keV energy level. A new P_γ value experimentally obtained by gamma-ray spectrometry has been proposed for this transition. Moreover, the corresponding $P_\gamma|_\alpha$ has also been experimentally determined by coincidences and compared with reference values.

As can be seen in Table 7.5, the P_γ obtained in this work by gamma-ray spectrometry (0.000670 (16)) was not compatible with the value published by Sardari et al. [134] (0.000498 (13)), even considering 3 σ.

The experimental $P_\gamma|_\alpha$ obtained in this work by alpha-gamma coincidence measurements was 0.00544 (50) (see Table 7.6). It must be pointed out that this value could be subject to angular correlation effects because the measuring geometry. In spite of that, as a check, the value was compared with the $P_\gamma|_\alpha$ calculated from the data reported in the Nuclear Data Tables [125], 0.00447 (12), that was not influenced by angular correlations. In this case, both values were compatible considering 2 σ.

Since the experimental P_γ obtained in this work by gamma-ray spectrometry considerably differed from Sardari's value, it was decided to calculate the isometric reference $P_\gamma|_\alpha$ with our result, obtaining 0.00602 (20). In that case, the value determined from coincidence measurements (0.00544 (50)) was in agreement considering 1 σ. This fact showed the consistency of our measurements and suggested that a new evaluation of the P_γ for the 46.84 keV transition should be considered.

102.02 keV transition

The second line found by Sardari et al. [134] and not included in the Nuclear Data Tables [125] was believed to be the E1 transition from the $9/2^-$ 173.02 keV level to the $9/2^+$ 71 keV energy level. In this case, the peak observed in our regular gamma-ray spectrum was very deformed by the K_α X-Rays interfering emissions from plutonium so the study of this transition was limited to the alpha-gamma coincidence measurements.

Identification

Alpha-gamma coincidence measurements were done in order to check that the spectral line 102.02 keV actually corresponded to the transition from 173.02 keV energy level to 71 keV level. Figure 7.13 shows two representations of the 90 - 120 keV region of the gamma coincidence spectra corresponding to the 5181, 5233 and 5275 keV alpha regions. It can be seen that one peak is present at 102.02 keV in the α_{173} gamma coincidence spectrum (green line) but neither in the α_{118} nor in the α_{75} spectra, as it was expected according to the decay scheme (see Figure 7.1). The peak should correspond to the direct coincidences between alpha particles that populate the 173.02 keV energy level and gamma rays that de-populate that level to the 71 keV level.

It can also be seen in Figure 7.13.b that coincidence measurements permitted to discriminate between the 102.02 keV transition and the coincidence peaks corresponding to the K_α X-Rays from plutonium, which only raised in the α_{118} and α_{75} spectra. The qualitative analysis can be reinforced by the comparison of the random and total coincidences corresponding to α_{75}, α_{118} and α_{173} and 102.02 keV transition. The corresponding calculated random coincidences are shown in Table 7.8 for comparison with the total number of coincident events found. The quantitative analysis confirmed that only α_{173} was in true coincidence with the 102.02 keV line. The measured coincidences are about 30 times higher than the random value. However, the coincidence peaks that appeared at 103.73 keV (corresponding to the K_α X-Rays from plutonium) coincident with both α_{118} and α_{75} were random coincidences. The

ratios between the measured and the random coincidences were about 1, respectively. From both approaches it seems that 102.02 keV gamma emission belongs to ^{243}Am and originates in the depopulation of 173.02 keV energy level to 71 keV level.

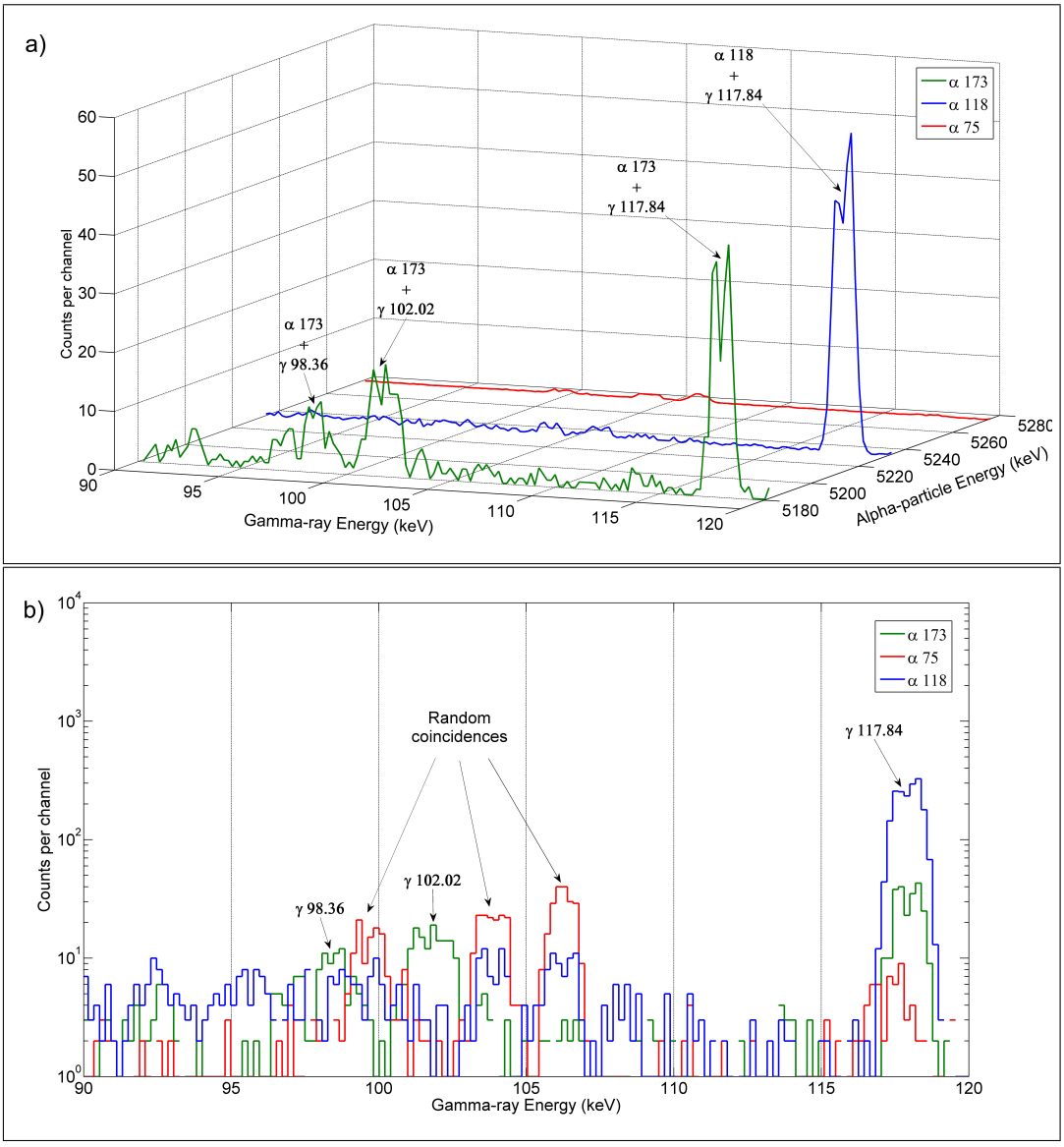

Figure 7.13: (a) 3D representation of the 90 - 120 keV region of the normalized gamma coincidence spectra corresponding to the 5181, 5233 and 5275 keV alpha regions. (b) 90 - 120 keV region of the regular gamma coincidence spectra corresponding to the 5181, 5233 and 5275 keV alpha regions. It can be seen in both representations that one peak is present at 102.02 keV in the α_{173} gamma coincidence spectrum but neither in the α_{118} nor in the α_{75} spectra.

γ Energy (keV)	Calculated random coincidences			Measured total coincidences		
	α_{75}	α_{118}	α_{173}	α_{75}	α_{118}	α_{173}
102.02 + 103.73	149 (2)	17.7 (5)	2.3 (2)	146 (19)	28 (4)	65 (16)

Table 7.8: Calculated random coincidences and measured total gamma coincidences for α_{75}, α_{118} and α_{173} in coincidence with 102.02 keV γ-ray. The measuring time in both cases was 132 days.

Gamma-ray emission probability

From coincidence measurements

In the case of the 102.02 keV transition it was only possible to calculate the $P_\gamma|_\alpha$ from the coincidence measurements. It was determined from the direct coincidences between alpha particles that populate the 173.02 keV energy level and gamma rays that de-populate that level to the 71 keV level. The $P_\gamma|_\alpha$ was calculated as the weighted mean of the values obtained by both the gamma and the alpha approaches previously described in the study of the 46.84 keV transition.

- Gamma coincidence spectrum

  A gamma coincidence spectrum was extracted from the matrix selecting the rectangular alpha ROI corresponding to α_{173} (5135-5189 keV) and summing the gamma channel contents along this ROI (see Figure 7.13 green solid line). The value was corrected to take into account the contribution of the coincident alpha tail counts. The value obtained in this approach was 0.0113 (30).

- Alpha coincidence spectrum

  An alpha coincidence spectrum was extracted from the matrix selecting the rectangular gamma ROI corresponding to 102.02 keV (100.2-102.7 keV) and summing the alpha channel contents along this ROI. The alpha coincidence spectrum is shown in Figure 7.14. The coincidence counts for the 102.02 keV emission was determined fitting the spectrum by ALFITeX and considering the peak area corresponding to α_{1173} (green line in Figure 7.14). The value was corrected to disregard the gamma background contribution. Considering this, the value obtained was 0.0116 (40).

The final experimental $P_\gamma|_\alpha$ of the 102.02 keV transition is shown in Table 7.9 and compared with the isotropic reference value calculated from the P_γ reported by Sardari et al. [134] and the P_{T_i} listed in Table 7.10 and taken from Browne et al. [125]. Only random coincidence corrections were applied to our value in this case.

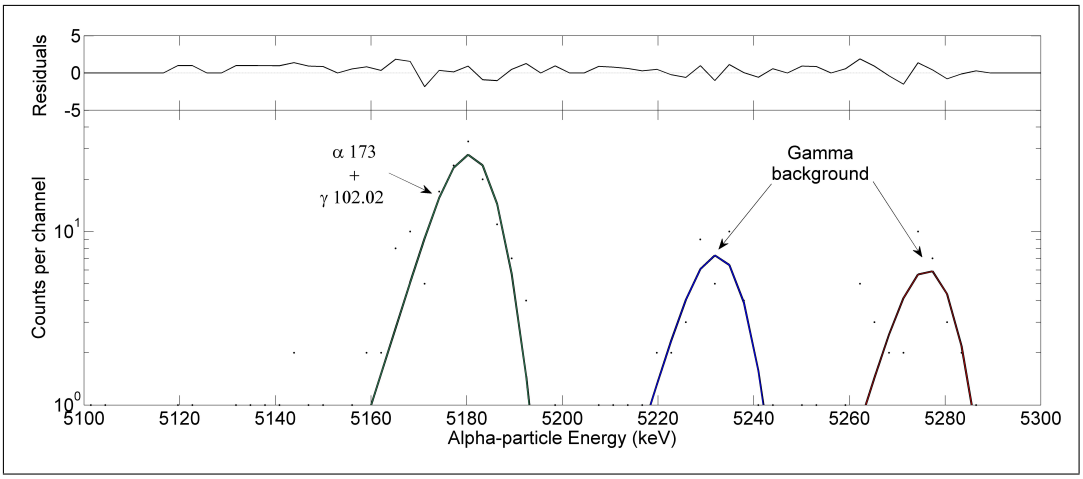

Figure 7.14: Alpha coincidence spectrum corresponding to the 102.02 keV line.

Discussion

Experimental evidences observed confirm the presence of the 102.02 keV transition from the $9/2^-$ 173.02 keV level to the $9/2^+$ 71 keV energy level. The corresponding $P_\gamma|_\alpha$ has been experimentally determined by coincidences and compared with reference values.

The experimental $P_\gamma|_\alpha$ obtained in this work was 0.0114 (24) (see Table 7.9). Although this value could be affected by angular correlations, it was compared as a check with the $P_\gamma|_\alpha$ calculated from the data reported in the Nuclear Data Tables [125] (see Table 7.10), 0.0127 (20), that was not influenced by angular correlations. In this case, both values were in good agreement considering 1 σ. This fact seemed to confirm the value reported by Sardari et al. [134] with the limitation that our value was obtained with a measuring geometry where detectors formed 90° angle.

γ Energy (keV)	$P_\gamma\|_\alpha$ (Isotropy)	$P_\gamma\|_\alpha$ (90 °)
	Sardari et al. [134] & Evaluation [125]	This work
102.02	0.0127 (20)	0.0114 (24)

Table 7.9: Gamma-ray emission probability of the 102.02 keV line conditioned to the desexcitation of the 173.02 keV energy level.

Final energy level (keV)	Transition Energy (keV)	P_T
122.4	50.62	0.00011 (2)
117.84	55.18	0.0181 (26)
74.66	98.36	0.0025 (4)
31.13	141.89	0.00141 (10)

Table 7.10: Transition probabilities from the 173.02 keV energy level taken from Browne et al. [125].

7.3.2 Other transitions

Additional values corresponding to the 31.13, 43.53, 74.66, 86.71 and 141.89 keV emissions were studied by gamma-ray spectrometry and compared with previous published data. As a check of the coincidence system, the experimental $P_\gamma|_\alpha$ of the well-determined 43.53, 50.62, 55.18, 74.66, 86.71, 117.84 and 141.89 keV transitions were calculated by alpha-gamma coincidence measurements.

31.13 keV transition

This is a transition depopulating the 31.13 keV energy level to the ground level. The 31.13 keV level is populated by 5321 keV alpha particles (α_{31}). The direct coincidences between these alpha particles and 31.13 keV gamma rays were not observed in the coincidence spectrum. However, in Figure 7.11 three coincidence peaks could be identified at 31.13 keV for α_{173}, α_{118} and α_{75}. These peaks were attributed to the cascade coincidences with alpha particles that populate the higher energy levels 173.02, 117.84 and 74.66 keV, respectively. Since expression 7.3 is used for direct coincidences and the direct coincidence peak was not observed in the spectrum, it was decided not to carry out the study of this emission by coincidence measurements.

Gamma-ray emission probability

From direct gamma-ray spectrum

The gamma-ray emission probability of the 31.13 keV transition was calculated from the regular gamma-ray spectrum following the procedure described in Section 7.3.1. The result obtained is shown in Table 7.11 and compared with the value recommended in the Nuclear Data Tables [125].

γ Energy (keV)	P_γ	
	Evaluation [125]	This work
31.13	0.00048 (4)	0.00067 (2)

Table 7.11: Gamma-ray emission probability of the 31.13 keV line.

Discussion

As can be seen in Table 7.11, the P_γ obtained in this work by gamma-ray spectrometry (0.00067 (2)) was compatible with the reference value (0.00048 (4)) considering 3 σ. Only two experimental values have been previously reported for this transition: 0.00069 (7) by Ahmad [131] and 0.000477 (13) by Sardari et al. [134]. Considering this, our proposed value is totally in agreement (1 σ) with that measured by Ahmad and, moreover, exhibits a lower uncertainty.

43.53 keV transition

One of the well-known gamma transitions used to check the measuring system was 43.53 keV. This is the transition from 74.66 keV energy level to the 31.13 keV level. The 74.66 keV level is populated by 5275 keV alpha particles (α_{75}).

In the alpha-gamma coincidence spectrum (see Figure 7.11) three peaks were observed in the gamma-ray energy region of 43.53 keV for α_{173}, α_{118} and α_{75}. The last peak corresponds to direct coincidences between alpha particles that populate the 74.66 keV energy level and gamma rays that de-populate that level to the 31.13 keV level. The other two peaks were attributed to the cascade coincidences with alpha particles that populate the higher energy levels 173.02 and 117.84 keV.

Gamma-ray emission probability

From direct gamma-ray spectrum

The gamma-ray emission probability of the 43.53 keV transition was calculated from the regular gamma-ray spectrum following the procedure described in Section 7.3.1. The result obtained is shown in Table 7.12 and compared with the value recommended in the Nuclear Data Tables [125].

γ Energy (keV)	P_γ	
	Evaluation [125]	This work
43.53	0.0589 (10)	0.0607 (13)

Table 7.12: Gamma-ray emission probability of the 43.53 keV line.

From coincidence measurements

- Gamma coincidence spectrum.

  A gamma coincidence spectrum was extracted from the matrix selecting the rectangular alpha ROI corresponding to α_{75} (5241-5300 keV) and summing the gamma channel contents along this ROI (see Figure 7.11 red solid line). The value was corrected to take into account the contribution of the coincident alpha tail counts. Taking into account this consideration, the value obtained was 0.0591 (16).

- Alpha coincidence spectrum.

  An alpha coincidence spectrum was extracted from the matrix selecting the rectangular gamma ROI corresponding to 43.53 keV (42.0-44.5 keV) and summing the alpha channel contents along this ROI. The value was corrected to discard the gamma background contribution. Considering this, the value obtained was 0.0586 (19).

These values were corrected by two effects: random coincidences and X-Rays escape peaks. The final experimental $P_\gamma|_\alpha$ of the 43.53 keV transition

γ Energy (keV)	$P_\gamma\|_\alpha$ (Isotropy)	$P_\gamma\|_\alpha$ (90 °)
	Evaluation [125]	This work
43.53	0.0599 (14)	0.0588 (12)

Table 7.13: Gamma-ray emission probability of the 43.53 keV line conditioned to the desexcitation of the 74.66 keV energy level.

was obtained as the weighted mean of both approaches. Table 7.13 shows the experimental $P_\gamma|_\alpha$ and the isotropic reference value calculated from the P_γ and the P_{T_i} recommended by Browne et al. [125].

Discussion

As can be seen in Table 7.12, the P_γ obtained in this work by gamma-ray spectrometry (0.0607 (13)) was in agreement with the value recommended by Browne et al. [125] (0.0589 (10)) considering 1 σ. Moreover, the experimental $P_\gamma|_\alpha$ obtained in this work by alpha-gamma coincidence measurements was 0.0588 (12) (see Table 7.13). Although this value could be influenced by angular correlations, it was compared as a check with the $P_\gamma|_\alpha$ calculated from the data reported in the Nuclear Data Tables [125], 0.0599 (14), that was not influenced by angular correlations. In this case, both values were compatible considering 1 σ. The good agreement reached in both cases permitted to validate the measuring system.

50.62 keV transition

This is the transition from 173.02 keV energy level to the 122.4 keV level. The 173.02 keV level is populated by α_{173}. It can be seen in the gamma coincindence spectrum shown in Figure 7.11 that one peak is present at 50.62 keV in the α_{173} gamma coincidence spectrum (green line) but neither in the α_{118} nor in the α_{75} spectra, as it was expected according to the decay scheme (see Figure 7.1). In this case, no peak was observed in our regular gamma-ray spectrum so the study of this transition was limited to the alpha-gamma coincidence measurements.

Gamma-ray emission probability

In the case of the 50.62 keV transition it was only possible to calculate the $P_\gamma|_\alpha$ from the coincidence measurements. It was determined from the direct coincidences between alpha particles that populate the 173.02 keV energy level and gamma rays that de-populate that level to the 122.4 keV level. The $P_\gamma|_\alpha$ was calculated as the weighted mean of the values obtained by both the gamma and the alpha approaches.

From coincidence measurements

- Gamma coincidence spectrum.

  A gamma coincidence spectrum was extracted from the matrix selecting the rectangular alpha ROI corresponding to α_{173} and summing the gamma channel contents along this ROI (see Figure 7.11 green solid line). The value was corrected to take into account the contribution of the coincident alpha tail counts. Considering this, the value obtained was 0.0040 (16).

- Alpha coincidence spectrum.

  An alpha coincidence spectrum was extracted from the matrix selecting the rectangular gamma ROI corresponding to 50.62 keV (49.1-51.5 keV) and summing the alpha channel contents along this ROI. The value was corrected to disregard the gamma background contribution. In this approach the value obtained was 0.0038 (14).

The final experimental $P_\gamma|_\alpha$ of the 50.62 keV transition is shown in Table 7.14 and compared with the isotropic reference value calculated from the values recommended in the Nuclear Data Tables [125]. In this case, our value was only corrected by random coincidences.

γ Energy (keV)	$P_\gamma\|_\alpha$ (Isotropy)	$P_\gamma\|_\alpha$ (90 °)
	Evaluation [125]	This work
50.62	0.0028 (6)	0.0039 (11)

Table 7.14: Gamma-ray emission probability of the 50.62 keV line conditioned to the desexcitation of the 173.02 energy level.

Discussion

The corresponding $P_\gamma|_\alpha$ for 50.62 keV transition has been experimentally determined by coincidences and compared with reference values. The $P_\gamma|_\alpha$ obtained in this work was 0.0039 (11) (see Table 7.14). Although this value could be subject to angular correlations, as a check it was compared with the $P_\gamma|_\alpha$ calculated from the data reported in the Nuclear Data Tables [125], 0.0028 (6), that was not influenced by angular correlations. In this case, both values were in good agreement considering 1 σ, although our value was obtained with a measuring geometry where detectors formed 90° angle. The high uncertainty of our value is due to the low statistics of the coincidence peak.

55.18 keV transition

This is the transition from 173.02 keV energy level to the 117.84 keV level. In the gamma coincindence spectrum shown in Figure 7.11 it can be seen that one peak is present at 55.18 keV in the α_{173} gamma coincidence spectrum

(green line) but neither in the α_{118} nor in the α_{75} spectra, as it was expected according to the decay scheme (see Figure 7.1). The study of this transition was limited to the alpha-gamma coincidence measurements because no peak was observed in our regular gamma-ray spectrum.

Gamma-ray emission probability

Since it was only possible to calculate the $P_\gamma|_\alpha$ for this transition, it was determined from the direct coincidences between alpha particles that populate the 173.02 keV energy level and gamma rays that de-populate that level to the 117.84 keV level. The $P_\gamma|_\alpha$ was calculated as the weighted mean of the values obtained by both analysis approaches.

From coincidence measurements

- Gamma coincidence spectrum.

  A gamma coincidence spectrum was extracted from the matrix selecting the rectangular alpha ROI corresponding to α_{173} and summing the gamma channel contents along this ROI (see Figure 7.11 green solid line). The value was corrected to take into account the contribution of the coincident alpha tail counts. Taking into account this correction, the value obtained was 0.0069 (8).

- Alpha coincidence spectrum.

  An alpha coincidence spectrum was extracted from the matrix selecting the rectangular gamma ROI corresponding to 50.62 keV (54.2-56.1 keV) and summing the alpha channel contents along this ROI. The value was also corrected to discard the gamma background contribution. In this case, $P_\gamma|_\alpha$ was a little lower than the value obtained in the gamma approach, 0.0043 (10).

The values were corrected by random coincidences. The final experimental $P_\gamma|_\alpha$ of the 50.62 keV transition is shown in Table 7.15 and compared with the isotropic reference value calculated from the values recommended in the Nuclear Data Tables [125].

γ Energy (keV)	$P_\gamma\|_\alpha$ (Isotropy)	$P_\gamma\|_\alpha$ (90 °)
	Evaluation [125]	This work
55.18	0.0076 (10)	0.0059 (13)

Table 7.15: Gamma-ray emission probability of the 55.18 keV line conditioned to the desexcitation of the 173.02 keV energy level.

Discussion

The $P_\gamma|_\alpha$ corresponding to the 55.18 keV transition has been experimentally determined by coincidences and compared with reference values. As can

be seen in Table 7.15, a value of 0.0059 (13) was obtained in this work. The uncertainty of this value was not calculated following the expression shown in Equation 7.4 because it was overly small to cover the values obtained by both the γ and α approaches. Thus, the uncertainty was arbitrarily increased as

$$\sigma = \frac{P_{\gamma}|_{\alpha}\ from\ \gamma\ approach\ -\ P_{\gamma}|_{\alpha}\ from\ \alpha\ approach}{2}. \qquad (7.6)$$

As a check, the mean value was compared with the $P_{\gamma}|_{\alpha}$ calculated from the data reported in the Nuclear Data Tables [125], 0.0076 (10). In this case, both values were compatible considering 2 σ. Taking into account the low counting statistics of the peak and the fact that our value was obtained with a measuring geometry where detectors formed a 90° angle, the difference between both values can be been considered acceptable.

74.66 keV transition

The most intense and the best-known gamma transition is 74.66 keV. This is the transition from 74.66 keV energy level to the ground level.

In the alpha-gamma coincidence spectrum three well-formed peaks were observed in the gamma-ray energy region of 74.66 keV for α_{173}, α_{118} and α_{75}. The last peak corresponded to the direct coincidences between alpha particles that populate the 74.66 keV energy level and gamma rays that de-populate that level to the ground level. The other two peaks were attributed to the cascade coincidences with alpha particles that populate the higher energy levels 173.02 and 117.84 keV.

Gamma-ray emission probability

From direct gamma-ray spectrum

The gamma-ray emission probability of the 74.66 keV transition was calculated from the regular gamma-ray spectrum following the procedure described in Section 7.3.1. The result obtained is shown in Table 7.16 and compared with the value recommended in the Nuclear Data Tables [125].

γ Energy (keV)	P_{γ}	
	Evaluation [125]	This work
74.66	0.672 (12)	0.672 (13)

Table 7.16: Gamma-ray emission probability of the 74.66 keV line.

From coincidence measurements

- Gamma coincidence spectrum.

  A gamma coincidence spectrum was extracted from the matrix selecting the rectangular alpha ROI corresponding to α_{75} and summing the gamma

channel contents along this ROI. The value was corrected to take into account the contribution of the coincident alpha tail counts. Considering this, the value obtained was 0.664 (17).

- Alpha coincidence spectrum.

  An alpha coincidence spectrum was extracted from the matrix selecting the rectangular gamma ROI corresponding to 43.53 keV (72.4-76.2 keV) and summing the alpha channel contents along this ROI. The value was corrected to discard the gamma background contribution. In this approach, a value of 0.660 (17) was obtained.

The final experimental $P_\gamma|_\alpha$ of the 74.66 keV transition was obtained as the weighted mean of both approaches. In this case, the value was only corrected by random coincidences. The X-Rays escape peak corrections only supposed 0.5 % so it was considered negligible. Table 7.17 shows the experimental $P_\gamma|_\alpha$ and the isotropic reference value calculated from the P_γ and the P_{T_i} recommended by Browne et al. [125].

γ Energy (keV)	$P_\gamma\|_\alpha$ (Isotropy)	$P_\gamma\|_\alpha$ (90 °)
	Evaluation [125]	This work
74.66	0.683 (17)	0.662 (12)

Table 7.17: Gamma-ray emission probability of the 74.66 keV line conditioned to the desexcitation of the 74.66 keV energy level.

Discussion

As can be seen in Table 7.16, the P_γ obtained in this work by gamma-ray spectrometry (0.672 (13)) was in very good agreement with the value recommended in the Nuclear Data Tables [125] (0.672 (12)) considering 1 σ. Moreover, the experimental $P_\gamma|_\alpha$ obtained in this work by alpha-gamma coincidence measurements was 0.662 (12) (see Table 7.17). In spite of the possibility of this value could be affected by angular correlations, as a check it was compared with the $P_\gamma|_\alpha$ calculated from the data reported in the Nuclear Data Tables [125], 0.683 (17). Also in this case, both values were totally compatible considering 1 σ. The good agreement reached for this emission in both approaches was considered as another check that also validated the measuring system.

86.71 keV transition

This is the transition from 117.84 keV energy level to the 31.13 keV level. This peak was clearly observed in both the regular gamma-ray and the alpha-gamma coincidence spectra. In this last spectrum two peaks were observed at 86.71 keV for α_{173} and α_{118}. The last peak corresponded to the direct coincidences between alpha particles that populate the 117.84 keV energy level and gamma

rays that de-populate that level to the 31.13 keV level. The other peak was attributed to the cascade coincidences with alpha particles that populate the higher energy level 173.02 keV.

Gamma-ray emission probability

From direct gamma-ray spectrum

The gamma-ray emission probability of the 86.71 keV transition is shown in Table 7.18 and compared with the value recommended by Browne et al. [125].

γ Energy (keV)	P_γ	
	Evaluation [125]	This work
86.71	0.00346 (9)	0.00355 (10)

Table 7.18: Gamma-ray emission probability of the 86.71 keV line.

From coincidence measurements

- Gamma coincidence spectrum.

  A gamma coincidence spectrum was extracted from the matrix selecting the rectangular alpha ROI corresponding to α_{118} and summing the gamma channel contents along this ROI. The value was corrected to take into account the contribution of the coincident alpha tail counts. Considering this, a value of 0.0282 (15) was obtained.

- Alpha coincidence spectrum.

  An alpha coincidence spectrum was extracted from the matrix selecting the rectangular gamma ROI corresponding to 86.71 keV (85.3-87.8 keV) and summing the alpha channel contents along this ROI. The value was corrected to not take into account the gamma background contribution. The value obtained in this approach was 0.0279 (24).

The final experimental $P_\gamma|_\alpha$ of the 86.71 keV transition was obtained as the weighted mean of both approaches. In this case, the values were only corrected by random coincidences. Table 7.19 shows the experimental $P_\gamma|_\alpha$ and the isotropic reference value calculated from the P_γ and the P_{T_i} recommended in the Nuclear Data Tables [125].

γ Energy (keV)	$P_\gamma\|_\alpha$ (Isotropy)	$P_\gamma\|_\alpha$ (90 °)
	Evaluation [125]	This work
86.71	0.0311 (8)	0.0281 (13)

Table 7.19: Gamma-ray emission probability of the 86.71 keV line conditioned to the desexcitation of the 117.84 keV energy level.

Discussion

Table 7.18 proposes a new value for the P_γ transition considered, 0.00355 (10), that was in good agreement with the value recommended by Browne et al. [125], 0.00346 (9) (1 σ). Moreover, this transition was studied by alpha-gamma coincidence measurements obtaining an experimental $P_\gamma|_\alpha$ of 0.0281 (13) (see Table 7.19). This value was compared with the $P_\gamma|_\alpha$ calculated from the data reported in the Nuclear Data Tables [125], 0.0311 (11). In this case, both values were compatible considering 2 σ. Taking into account the possibility of an angular correlation influence in the experimental value obtained in this work, this difference can be accepted, confirming the consistency of our measurements.

98.36 keV transition

Sardari et al. [134] found another weak line that, in this case, was included in the Nuclear Data Tables [125]. It is the E2 transition from the $9/2^-$ 173.02 keV level to the $5/2^-$ 74.66 keV energy level. Since only Sardari's value has been reported, it was decided to do a deeper study of this transition.

The peak observed in our regular gamma-ray spectrum was seriously affected by the K_α X-Rays interfering emissions from plutonium so the study of this transition was limited to the alpha-gamma coincidence measurements.

Identification

Alpha-gamma coincidence measurements were done in order to confirm that the spectral line 98.36 keV actually corresponds to the transition from 173.02 keV energy level to 74.66 keV level. Figure 7.13 shows that one peak was raised at 98.36 keV in the α_{173} gamma coincidence spectrum (green line) but neither in the α_{118} nor in the α_{75} spectra, as it was expected according to the decay scheme (see Figure 7.1). The peak should then correspond to the direct coincidences between alpha particles that populate the 173.02 keV energy level and gamma rays that de-populate that level to the 74.66 keV level.

As in the case of the 102.02 keV transition, coincidence measurements permitted to discriminate between the 98.36 keV transition and the random coincidence peaks corresponding to the K_α X-Rays from plutonium. The random and total coincidences corresponding to α_{75}, α_{118} and α_{173} and 98.36 keV transitions were calculated and compared in Table 7.20. The quantitative analysis confirmed that only α_{173} was in true coincidence with the 98.36 keV line, while the coincidence peaks that appeared at 99.52 keV (corresponding to the K_α X-Rays from plutonium) coincident with α_{118} and α_{75} were random coincidences. From both approaches it was confirmed that 98.36 keV gamma emission indeed belongs to ^{243}Am and originates in the depopulation of 173.02 keV energy level to 74.66 keV level.

Gamma-ray emission probability

From coincidence measurements

In the case of the 98.36 keV transition it was only possible to calculate the

γ Energy (keV)	Random coincidences			Total coincidences					
	α_{75}	α_{118}	α_{173}	α_{75}		α_{118}		α_{173}	
98.36 + 99.52	98 (1)	11.7 (4)	1.5 (1)	100 (17)	R	13 (2)	R	63 (20)	T

Table 7.20: Random coincidences and total gamma coincidence counting for α_{75}, α_{118} and α_{173} in coincidence with 98.36 keV γ-ray.

$P_\gamma|_\alpha$ from the coincidence measurements. It was determined from the direct coincidences between alpha particles that populate the 173.02 keV energy level and gamma rays that de-populate that level to the 74.66 keV level. The $P_\gamma|_\alpha$ was calculated as the weighted mean of the values obtained by both the gamma and the alpha approaches.

- Gamma coincidence spectrum.

  A gamma coincidence spectrum was extracted from the matrix selecting the rectangular alpha ROI corresponding to α_{173} and summing the gamma channel contents along this ROI (see Figure 7.13 green solid line). The value was corrected to take into account the contribution of the coincident alpha tail counts. The result obtained in this approach was 0.0106 (36).

- Alpha coincidence spectrum.

  An alpha coincidence spectrum was extracted from the matrix selecting the rectangular gamma ROI corresponding to 98.36 keV (95.8-99.6 keV) and summing the alpha channel contents along this ROI. The coincidence counts for the 98.36 keV emission was determined fitting the spectrum by ALFITeX and considering the peak area corresponding to α_{1173}. The value was corrected to reject the gamma background contribution. Considering this, a value of 0.0095 (37) was obtained in this case.

The final experimental $P_\gamma|_\alpha$ of the 98.36 keV transition is shown in Table 7.21. The value was compared with the isotropic reference value calculated from the P_γ and the P_{T_i} recommended by Browne et al. [125]. Only corrections for random coincidences were applied in this case.

γ Energy (keV)	$P_\gamma\|_\alpha$ (Isotropy)	$P_\gamma\|_\alpha$ (90 °)
	Evaluation [125]	This work
98.36	0.0068 (12)	0.0101 (26)

Table 7.21: Gamma-ray emission probability of the 98.36 keV line conditioned to the desexcitation of the 173.02 keV energy level.

Discussion

In this work the presence of the 98.36 keV transition from the $9/2^-$ 173.02 keV level to the $5/2^-$ 74.66 keV energy level has been confirmed by alpha-gamma coincidence measurements. The corresponding $P_\gamma|_\alpha$ has been experimentally determined by coincidences and compared with reference values.

The $P_\gamma|_\alpha$ obtained in this work was 0.0101 (26) (see Table 7.21). The high uncertainty was due to the low statistic of the coincidence peak. The value was compared with the $P_\gamma|_\alpha$ calculated from the data reported in the Nuclear Data Tables [125], 0.0068 (12). In this case, both values were compatible considering 1 σ, although our value could be subject to angular correlations because the measuring geometry. In spite of both values were in agreement, we consider that a new evaluation of the P_γ of the 98.36 keV transition should be considered.

117.84 keV transition

This is the transition from 117.84 keV energy level to the ground level. In the alpha-gamma coincidence spectrum (see Figure 7.13) it can be seen that two peaks are present at 117.84 keV in the α_{173} and α_{118} gamma coincidence spectra (green and blue lines) but not in the α_{75} spectrum. The peak observed in our regular gamma-ray spectrum was very deformed by the K_β X-Rays interfering emissions from plutonium so the study of this transition was limited to the alpha-gamma coincidence measurements.

Gamma-ray emission probability

From coincidence measurements

The $P_\gamma|_\alpha$ was determined from the direct coincidences between alpha particles that populate the 117.84 keV energy level and gamma rays that depopulate that level to ground level. The $P_\gamma|_\alpha$ was calculated as the weighted mean of the values obtained by both analysis approaches.

- Gamma coincidence spectrum.

  A gamma coincidence spectrum was extracted from the matrix selecting the rectangular alpha ROI corresponding to α_{118} and summing the gamma channel contents along this ROI. The value was corrected to take into account the contribution of the coincident alpha tail counts. The value obtained in this approach was 0.0510 (26).

- Alpha coincidence spectrum.

  An alpha coincidence spectrum was extracted from the matrix selecting the rectangular gamma ROI corresponding to 117.84 keV (116.0-119.0 keV) and summing the alpha channel contents along this ROI. The value was corrected to disregard the gamma background contribution. Considering this, a value of 0.0510 (46) was obtained.

The values were corrected by random coincidences. The final experimental $P_\gamma|_\alpha$ of the 117.84 keV transition was compared with the isotropic reference

value calculated from the emission and transition probabilities recommended in the Nuclear Data Tables [125]. Table 7.22 shows both values.

γ Energy (keV)	$P_\gamma\|_\alpha$ (Isotropy)	$P_\gamma\|_\alpha$ (90 °)
	Evaluation [125]	This work
117.84	0.0512 (5)	0.0510 (23)

Table 7.22: Gamma-ray emission probability of the 117.84 keV line conditioned to the desexcitation of the 117.84 keV energy level.

Discussion

The $P_\gamma|_\alpha$ corresponding to the 117.84 keV transition has been experimentally determined by coincidences and compared with reference values. The $P_\gamma|_\alpha$ obtained in this work was 0.0510 (23) (see Table 7.22). Although this value could be subject to angular correlations, as a check it was compared with the $P_\gamma|_\alpha$ calculated from the data reported in the Nuclear Data Tables [125], 0.0512 (45), that was not influenced by angular correlations. Both values were in very good agreement considering 1 σ. Moreover, the uncertainty of our value is lower than that obtained from the Nuclear Data Tables.

141.89 keV transition

The last gamma emission probability obtained in this work was 141.89 keV. This is the transition from 173.02 keV energy level to the 31.13 keV level. In this case, well-formed peaks were observed in both the regular gamma-ray and the coincidence spectra.

In the alpha-gamma coincidence spectrum one peak was observed in the gamma-ray energy region of 141.89 keV for α_{173} but neither in the α_{118} nor in the α_{75} spectra, as it was expected according to the decay scheme (see Figure 7.1). The peak corresponded to the direct coincidences between alpha particles that populate the 173.02 keV energy level and gamma rays that de-populate that level to the ground level.

Gamma-ray emission probability

From direct gamma-ray spectrum

The gamma-ray emission probability of the 141.89 keV transition was calculated from the regular gamma-ray spectrum following the procedure described in Section 7.3.1. The result obtained is shown in Table 7.23 and compared with the value recommended in the Nuclear Data Tables [125].

From coincidence measurements

- Gamma coincidence spectrum.

  A gamma coincidence spectrum was extracted from the matrix selecting the rectangular alpha ROI corresponding to α_{173} and summing the

γ Energy (keV)	P_γ	
	Evaluation [125]	This work
141.89	0.00115 (8)	0.00129 (5)

Table 7.23: Gamma-ray emission probability of the 141.89 keV line.

gamma channel contents along this ROI. The value was corrected to take into account the contribution of the coincident alpha tail counts. The value obtained in this case was 0.099 (22).

- Alpha coincidence spectrum.

  An alpha coincidence spectrum was extracted from the matrix selecting the rectangular gamma ROI corresponding to 141.89 keV (139.7-143.5 keV) and summing the alpha channel contents along this ROI. The value was corrected to reject the gamma background contribution. Taking into account this consideration, the value obtained was 0.096 (23).

The final experimental $P_\gamma|_\alpha$ of the 141.89 keV transition was obtained as the weighted mean of both approaches and corrected by random coincidences. Table 7.24 shows the experimental $P_\gamma|_\alpha$ and the isotropic reference value calculated from the P_γ and the P_{T_i} recommended by Browne et al. [125].

γ Energy (keV)	$P_\gamma\|_\alpha$ (Isotropy)	$P_\gamma\|_\alpha$ (90 °)
	Evaluation [125]	This work
141.89	0.052 (7)	0.098 (16)

Table 7.24: Gamma-ray emission probability of the 141.89 keV line conditioned to the desexcitation of the 173.02 keV energy level.

Discussion

As can be seen in Table 7.23, the P_γ obtained in this work by gamma-ray spectrometry (0.00129 (5)) was compatible with the reference value (0.00115 (8)) considering 2 σ. However, our value is totally in agreement with the values obtained by Van Hise and Engelkemeir [127], Ahmad [131] and Vaninbroukx et al. [132] considering 1 σ (see Table 7.1). Moreover, our proposed value exhibits lower uncertainty.

The $P_\gamma|_\alpha$ obtained in this work was 0.098 (16) (see Table 7.24). It was compared with the $P_\gamma|_\alpha$ calculated from the data reported in the Nuclear Data Tables [125], 0.052 (7). Both values were compatible considering 2 σ, however, the relative difference is quite high. Although our value could be affected by angular correlations, this effect does not seem to be the explanation of the discrepancy. Further studies will be carried out in the future to find the

cause of the poor agreement between the measured and the reference values for 141.89 keV transition.

7.3.3 Summary

In this section, a summary of the gamma-ray emission probabilities obtained in this work is presented in Table 7.25. Figure 7.15 shows a modification of the simplified decay scheme of ^{243}Am considering the values measured in this work. On one hand, pure experimental P_γ were determined by gamma-ray spectrometry for 31.13, 43.53, 46.84, 74.66, 86.71 and 141.89 keV transitions. On the other hand, combined P_γ values were calculated from the experimental $P_\gamma|_\alpha$ obtained by alpha-gamma coincidences and a 90° measuring angle and the isotropic reference transition probabilities recommended in the Nuclear Data Tables [125]. These last probabilities were calculated for 43.53, 46.84, 50.62, 55.18, 74.66, 86.71, 98.36, 102.02, 117.84 and 141.89 keV transitions. In most cases, our results were in good agreement with the reference data.

γ Energy (keV)	Evaluated P_γ	Experimental P_γ	Combined P_γ
	Browne et al. [125]	This work	
31.13	0.00048 (4)	0.00067 (2)	-
43.53	0.0589 (10)	0.0607 (13)	0.0579 (15)
46.84	0.000498 (13)*	0.000670 (16)	0.000605 (56)
50.62	0.000062 (10)	-	0.000086 (25)
55.18	0.000168 (11)	-	0.000130 (32)
74.66	0.672 (12)	0.672 (13)	0.651 (16)
86.71	0.00346 (9)	0.00355 (10)	0.00313 (14)
98.36	0.000151 (21)	-	0.000223 (63)
102.02	0.000280 (30)*	-	0.000252 (61)
117.84	0.0057 (5)	-	0.0057 (3)
141.89	0.00115 (8)	0.00129 (5)	0.00217 (44)

Table 7.25: Summary of the gamma-ray emission probabilities obtained in this work. *Values not included in the Nuclear Data Tables [125], only reported by Sardari et al. [134].

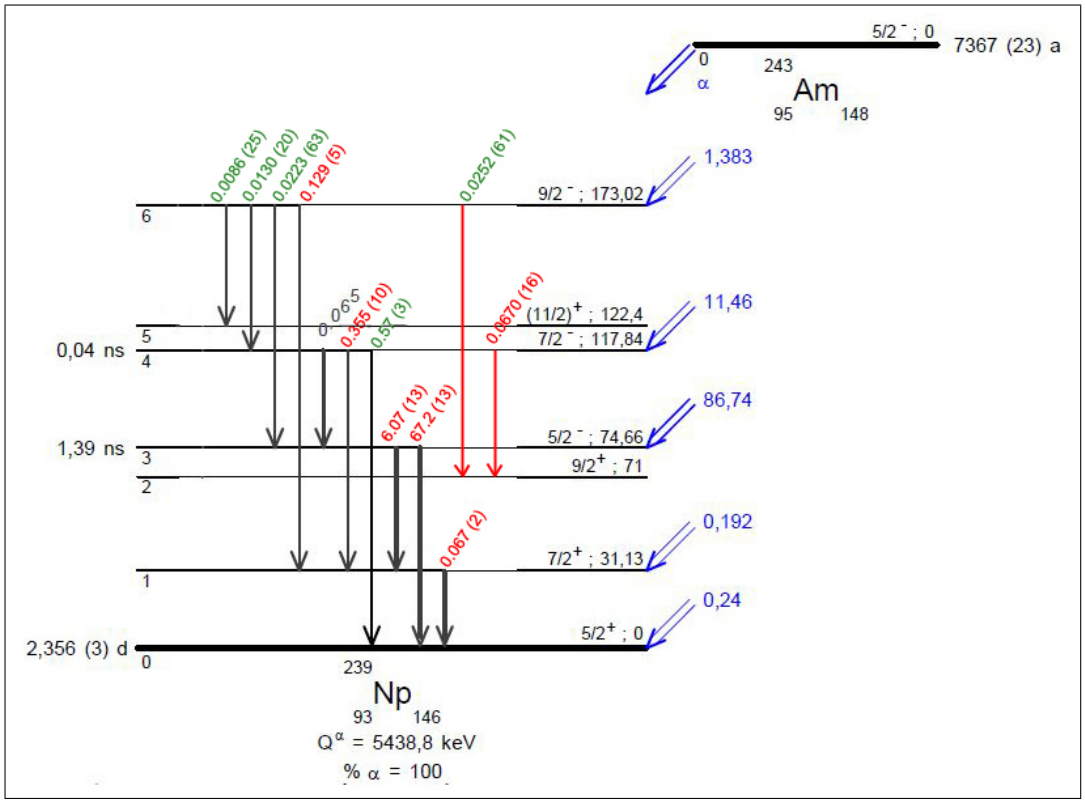

Figure 7.15: Modification of the simplified decay scheme of ^{243}Am (taken from Browne et al. [125]) considering the results obtained in this work. Two red arrows corresponding to the 46.84 and 102.02 keV transitions have been added to the decay scheme. Values in red are those measured by gamma-ray spectrometry while values in green are those only obtained by alpha-gamma coincidence measurements. The corresponding combined P_γ values were calculated from the experimental $P_\gamma|_\alpha$ measured by coincidences (90° measuring angle) and the isotropic transition probabilities recommended in the Nuclear Data Tables [125]. The value written in black corresponds to a transition not observed in this study due to the energy resolution limitation of the measuring set-up; it was taken from Browne et al. [125].

Chapter 8

Summary & Conclusions

The aim of this work was to improve techniques and analysis methods in alpha-particle spectrometry and alpha-gamma coincidence measurements and their application to the study of two alpha-particle emitters: ^{242}Pu and ^{243}Am. These nuclides are mentioned in a recent document from a group of nuclear data evaluators that calls for additional measurements.

The evolution and the state of the art of the alpha-particle spectrometry and the basic set-ups used for coincidence measurements are summarized in Chapters 1 and 2. A detailed description of the evolution of the spectrometric devices, a set of particular effects inherent to measure with Si detectors and a complete review of the deconvolution procedure of alpha-particle spectra are present in Chapter 1. Meanwhile, the main applications of the coincidence technique and a comparison between the basic and the modern coincidence set-ups, highlighting the distorting effects that should be considered, are described in Chapter 2.

The first step of this study focused on the design and characterization of several measuring set-ups. The experimental equipments used in this work are described in detail in Chapters 3 and 4. Firstly, the characteristics of the alpha-particle spectrometry devices are shown in Chapter 3. Details of the Si detectors, the electronic modules and the geometrical measuring conditions are presented for the semiconductor chamber from the University of Extremadura and the high-stability and α-e$_c$ coincidence chambers from CIEMAT.

Secondly, Chapter 4 describes the alpha-gamma coincidence chamber designed and characterized at the University of Extremadura, pointing out the features of the detectors and the electronic modules. Two measuring configurations were used: i) one based on the use of common amplifier and ADC modules and a dual-parameter multichannel analyzer; ii) a second one based on an unique digital module. The optimization of the parameters needed in each configuration is detailed in this chapter. Moreover, it was necessary to develop data treatment and analysis programs, COLMA and DIGDATA. A detailed description of both codes is also shown in Chapter 4. Although both measuring configurations gave compatible coincidence results, the advantages

of a digital module (such as the possibility of implementing "offline" the post-processing of registered data with different parameters), prevailed over the use of the analog dual-parameter multichannel set-up.

The improvement in the alpha-particle spectrometry measuring set-ups was complemented with the development of a new fitting code called ALFITeX. This software is described in detail in Chapter 5. ALFITeX has several advantages compared to some previous programs to fit alpha-particle spectra. The spreadsheet format makes it particularly easy and user-friendly to handle and the presentation of results both numerically and graphically allows a fast evaluation of the quality of the fitting process. The possibility of selecting the use of two or three left-handed exponentials permits to obtain a more adequate reproduction of the low-energy tail region of the peaks when the spectrum so requires. The capability of fitting a possible background contribution is also included in the code. The calculation of the emission probabilities with accurate uncertainty estimation (taking into account the constraint that all the emission probabilities must sum to 100 %) is also implemented. Applying the SVD method as a robust algorithm for matrix inversion permits to fit even alpha-particle spectra presenting singularities or an ill-conditioned curvature matrix in the fitting process. Moreover, the set of prefittings implemented in ALFITeX reduces the instability of the non-linear optimization procedure providing a suitable initial set of fitting parameters.

The ALFITeX code is applicable to the analysis of standard samples of single or mixed radionuclides. The tests carried out in this work showed the program to be very suitable for the fitting of complex alpha-particle spectra, with very short computation times.

The improved experimental devices and analysis codes were applied to the study of two alpha-particle emitters, ^{242}Pu and ^{243}Am. First of all, a new set of alpha-particle emission probabilities for ^{242}Pu is proposed in Chapter 6. The sources were measured by the alpha-particle chambers based on the use of ion-implanted Si detectors described in Chapter 3. The measurements were done under high-stability conditions and under several different configurations to obtain the best estimation for the emission probabilities by extrapolating to zero effective efficiency. The spectra were fitted by the ALFITeX code and the intensity values were corrected by the interfering effect of coincidence-summing between alpha-particles and conversion electrons from gamma transitions depopulating the levels fed by the alpha decay.

The alpha-particle emission probabilities measured in this work agree well with the values reported by Vaninbroukx et al. [121] for the two major emissions and are compatible with that of the weakest emission. Due to the intensive numerical analysis of spectra, the higher statistical contents of our measurements and the purity of the measured samples, our values exhibit, in general, lower uncertainties than those from Vaninbroukx et al. [121]. The only exception corresponds to the P_α of the weakest peak, for which the uncertainty considered in this study doubles that given by these authors. Taken

into account all factors mentioned in the precedent paragraph we consider that their uncertainty evaluation for the minor emission could be underestimated. For the same reason, a new evaluation of alpha-particle emission probabilities for ^{242}Pu should be considered.

Otherwise, Chapter 7 describes in detail the experimental evidences that confirm the existence of two gamma transitions from the alpha-particle decay of ^{243}Am not included in the Nuclear Data Tables [125] and the review of some values of gamma-ray emission probabilities previously reported. For that purpose, gamma-ray spectrometry and alpha-gamma coincidence measurements were carried out. The ^{243}Am source was measured with the alpha-gamma coincidence set-up described in Chapter 4. The device consisted of a vacuum chamber with an ion-implanted Si detector to measure alpha particles and a low-energy Ge detector to register gamma photons. Due to the possibility of implementing "offline" the post-processing of registered data with different parameters (such as dead times and others), a digital module was used instead of an analog dual-parameter multichannel set-up. Decodification and data treatment were done with the DIGDAT code described in Chapter 4.

A detailed analysis of selected gamma transitions was carried out in this work. Our main interest was focused on the study of the 46.84 and 102.02 keV transitions, previously reported by Sardari et al. [134] but not placed in the decay scheme (Nuclear Data Tables). Moreover, a set of previously reported transitions was also reviewed. The P_γ of emissions with well-formed peaks in the non-coincidence gamma-ray spectrum were calculated by gamma-ray spectrometry. Lines that were hidden or peaks distorted by the presence of gamma-photons or X-Rays from Pu were studied by alpha-gamma coincidence measurements. In those cases, it was not possible to obtain P_γ values; instead of that, $P_\gamma|_\alpha$ was determined, i.e. the gamma-ray probability normalized by the sum of the probabilities of all transitions from the corresponding level. It has to be noted that in this work $P_\gamma|_\alpha$ values can be influenced by angular correlation effects due to the 90° measuring angle.

The 46.84 and 102.02 keV transitions were experimentally identified by alpha-gamma coincidence measurements. For 46.84 keV P_γ and $P_\gamma|_\alpha$ were calculated by gamma-ray spectrometry and alpha-gamma coincidences, respectively, showing very good agreement between them but differing from the value reported by Sardari et al. [134]. Therefore, a new evaluation of the P_γ of the 46.84 keV transition should be considered. Results obtained for 102.02 keV transition seemed to confirm the Sardari's emission probability with the limitation that our value was obtained with a 90° measuring angle.

Additional values corresponding to the 31.13, 43.53, 74.66, 86.71 and 141.89 keV emissions were studied by gamma-ray spectrometry and compared with previous published data. In most cases, our results were in good agreement with the reference data. As a check of the coincidence system, the experimental $P_\gamma|_\alpha$ for a set of well-determined transitions were calculated by alpha-gamma coincidence measurements. Despite of the fact that the experimental values could be influenced by angular correlation effects, the good agreement reached

for the most intense emissions permitted to validate the measuring coincidence system. Moreover, the results obtained for the rest of transitions were also in agreement with previous published data. The only exception found was the case of 141.89 keV for which the differences almost exceed 2 σ. The reason for this discrepancy is, for the moment, unknown and will require further studies.

Chapter 9

Resumen & Conclusiones

El objetivo de este trabajo fue la mejora de técnicas y métodos de análisis en espectrometría de partículas alfa y medidas de coincidencias alfa-gamma, y su aplicación al estudio de dos emisores de partículas alfa: ^{242}Pu y ^{243}Am. Estos radionucleidos son algunos de los mencionados en un reciente documento publicado por un grupo de evaluadores de datos nucleares en el que se reclaman medidas adicionales.

La evolución y el estado de la espectrometría de partículas alfa y los equipos básicos utilizados en medidas de coincidencias están resumidos en los Capítulos 1 y 2. Una descripción detallada de la evolución de los dispositivos espectrométricos, el conjunto de efectos característicos inherentes a la medida con detectores de silicio y una completa revisión de los procedimientos de deconvolución de espectros alfa se presentan en el Capítulo 1. Por otra parte, el Capítulo 2 describe las principales aplicaciones de la técnica de coincidencias y una comparación entre los sistemas de medida básicos y más actuales, estudiando los efectos distorsionadores que deben considerarse.

El primer paso de este estudio se enfocó al diseño y puesta a punto de varios sistemas de medida. Los equipos experimentales utilizados en este trabajo se describen detalladamente en los Capítulos 3 y 4. En primer lugar, las características de los dispositivos de espectrometría alfa se presentan en el Capítulo 3. Se muestran los detalles de los detectores de silicio, los módulos electrónicos y las condiciones geométricas de medida de la cámara con detector de semiconductor de la Universidad de Extremadura y de las cámaras de alta estabilidad y de coincidencias alfa-electrón de conversión del CIEMAT.

En segundo lugar, el Capítulo 4 describe la cámara de coincidencias alfa-gamma diseñada y puesta a punto en la Universidad de Extremadura, resaltando las características de los detectores y de los módulos electrónicos. Se utilizaron dos configuraciones de medida: i) una basada en el uso de amplificadores y ADCs convencionales y un analizador multicanal biparamétrico; ii) una segunda configuración basada en el uso de un único módulo digital. La optimización de los parámetros necesarios en cada configuración está detallada en este capítulo. Además, fue necesario el desarrollo de programas de

tratamiento y análisis de datos, COLMA y DIGDATA. Ambos códigos también se describen detalladamente en el Capítulo 4. Aunque las dos configuraciones de medida dieran resultados compatibles, las ventajas de un módulo digital (como la posibilidad de implentar de manera "offline" el procesamiento de los datos registrados utilizando diferentes parámetros) prevalecieron sobre el uso del dispositivo analógico con el analizador multicanal biparamétrico.

La mejora de los dispositivos de medida para espectrometría alfa se complementó con el desarrollo de un nuevo código de ajuste, llamado ALFITeX, descrito con detalle en el Capítulo 5. ALFITeX tiene varias ventajas comparado con algunos programas para el ajuste de espectros alfa previamente desarrollados. Su formato de hoja de cálculo lo hace sencillo de manejar y atractivo para los usuarios, y la presentación numérica y gráfica de los resultados permite una evaluación rápida de la calidad del proceso de ajuste. La posibilidad de seleccionar el uso de dos o tres exponenciales permite reproducir de manera más adecuada la región de la cola de baja energía del pico cuando el espectro lo requiere. También está incluída en el código la capacidad de ajustar la posible contribución de un fondo. El cálculo de las probabilidades de emisión con una estimación de las incertidumbres más correcta (considerando la restricción de que todas las probabilidades de emisión deben sumar el 100 %) también está implementado en el programa. La aplicación del método SVD como un algoritmo más robusto para la inversión de matrices permite ajustar incluso espectros alfa que presentan durante el proceso de ajuste singularidades o matrices de curvatura mal condicionadas. Además, un conjunto de preajustes implementados en ALFITeX reduce la inestabilidad del proceso de optimización no lineal proporcionando un conjunto de parámetros de ajuste iniciales adecuado.

El código ALFITeX se aplica al análisis de muestras estándar de uno o varios radionucleidos. Las pruebas realizadas durante este trabajo mostraron que el programa era muy adecuado para el ajuste de espectros de partículas alfa complejos, con tiempos de computación muy cortos.

Los dispositivos experimentales y códigos de análisis mejorados se aplicaron al estudio de dos emisores de partículas alfa, el ^{242}Pu y el ^{243}Am. En primer lugar, en el Capítulo 6 se propone un nuevo conjunto de probabilidades de emisión alfa para el ^{242}Pu. Las fuentes se midieron con las cámaras de espectrometría alfa basadas en el uso de detectores de silicio tipo PIPS, descritas en el Capítulo 3. Las medidas se realizaron bajo condiciones de alta estabilidad y con varias configuraciones de medida diferentes para obtener la mejor estimación de las probabilidades de emisión mediante la extrapolación a eficiencia efectiva cero. Los espectros se ajustaron con el código ALFITeX y los valores de intensidad se corrigieron por los efectos interferentes de las sumas por coincidencia entre partículas alfa y electrones de conversión de las transiciones gamma que se desexcitan desde los niveles alimentados por la desintegración alfa.

Las probabilidades de emisión obtenidas en este trabajo muestran un buen

acuerdo con los valores propuestos por Vaninbroukx et al. [121] para las dos emisiones principales y son compatibles en el caso de la emisión más débil. Debido al intenso análisis numérico de los espectros, al mayor contenido estadístico de nuestras medidas y a la pureza de las muestras, nuestros valores exhiben, por lo general, menor incertidumbre que los propuestos por Vaninbroukx et al. [121]. La única excepción corresponde a la P_α del pico de menor intensidad, para el que la incertidumbre considerada en este estudio dobla el valor dado por estos autores. Teniendo en cuenta todos los factores mencionados anteriormente, consideramos que su evaluación de incertidumbres para la emisión menor podía estar subestimada. Por la misma razón, debería considerarse una nueva evaluación de las probabilidades de emisión alfa para el ^{242}Pu.

Por otro lado, el Capítulo 7 describe con detalle las evidencias experimentales que confirman la existencia de dos transiciones gamma del esquema de desintegración del ^{243}Am no incluídas en las Tablas de Datos Nucleares [125], y la revisión de algunas probabilidades de emisión gamma anteriormente publicadas. Para ello, se han llevado a cabo medidas de espectrometría gamma y de coincidencias alfa-gamma. La fuente de ^{243}Am se midió con el sistema de coincidencias alfa-gamma descrito en el Capítulo 4. El dispositivo consiste en una cámara de vacío con un detector silicio para medir partículas alfa y un detector de germanio de baja energía para registrar fotones gamma. Debido a la posibilidad de implementar "offline" el procesamiento de los datos registrados utilizando diferentes parámetros (como tiempos muertos y otros), se utilizó un módulo digital, en vez de un montaje analógico con analizador multicanal biparamétrico. La decodificación y el tratamiento de datos se llevó a cabo con el código DIGDATA, descrito en el Capítulo 4.

En este trabajo se desarrolló un detallado análisis de determinadas transiciones gamma. Nuestro interés se centró en el estudio de las transiciones de 46.84 y 102.02 keV, previamente presentadas por Sardari et al. [134] pero que no están consideradas en el esquema de desintegración (Tablas de Datos Nucleares). Además, también se revisó un conjunto de transiciones gamma previamente publicadas. Las P_γ de emisiones con picos bien formados en el espectro gamma sin coincidencias se calcularon mediante espectrometría gamma. Las líneas escondidas o los picos deformados por la presencia de fotones gamma o Rayos-X pertenecientes al Pu se estudiaron mediante medidas de coincidencias alfa-gamma. En esos casos no fue posible obtener los valores de P_γ; sin embargo, se determinó $P_\gamma|_\alpha$, es decir, la probabilidad gamma normalizada por la suma de las probabilidades de todas las transiciones con origen en el correspondiente nivel. Hay que resaltar que en este trabajo los valores de $P_\gamma|_\alpha$ pueden estar influídos por efectos de correlación angular debido a que el ángulo de medida fue 90°.

Las transiciones de 46.84 y 102.02 keV se identificaron experimentalmente mediante medidas de coincidencias alfa-gamma. Para 46.84 keV, se calcularon P_γ y $P_\gamma|_\alpha$ mediante espectrometría gamma y coincidencias alfa-gamma, respectivamente, alcanzándose un muy buen acuerdo entre los valores obtenidos

por ambas técnicas, pero difiriendo de los propuestos por Sardari et al. [134]. Por lo tanto, debería considerarse una nueva evaluación de la probabilidad de emisión de la transición de 46.84 keV. Los resultados obtenidos para la transición de 102.02 keV parecieron cofirmar la probabilidad de Sardari con la limitación de que nuestro valor se obtuvo con un ángulo de medida de 90°.

Mediante espectrometría gamma se estudiaron valores adicionales de P_γ para las transiciones de 31.13, 43.53, 74.66, 86.71 and 141.89 keV y se compararon con datos anteriormente publicados. En la mayoría de los casos, nuestros resultados mostraron buen acuerdo con los valores de referencia. Como chequeo del sistema de coincidencias, se calcularon valores experimentales de $P_\gamma|_\alpha$ para una selección de transiciones bien conocidas. A pesar del hecho de que los valores experimentales pueden estar influídos por efectos de correlaciones angulares, el buen acuerdo alcanzado para las emisiones más intensas permitió validar el dispositivo de coincidencias. Además, los resultados obtenidos para el resto de las transiciones también estuvieron de acuerdo con datos previamente publicados. La única excepción fue el caso de la transición de 141.89 keV para la que la diferencia casi excedó 2 σ. La razón de esta discrepancia se desconoce por el momento y requerirá estudios adicionales.

Appendix A

Improved peak shape fitting in alpha spectra

A.1 Introduction

Whereas alpha peak models based on the convolution of a Gaussian curve with two or three left-handed exponentials in the low-energy-tail region, such as those implemented in the ALPHA [30] and ALFITeX [21] codes, generally perform very well, there are still noticeable residuals when fitting spectra that have millions of counts in each energy bin, since the extremely low random variations in the spectra reveal the slightest mismatch between fit and experiment.

A more adequate fit of the most challenging spectra requires more elaborate modeling. This adds to the complexity and computing time for reaching the optimum fit parameters via search routines. This work proposes a logical extension to the analytical model

$$F(u) = \sum_{i=1}^{3} \eta_i \frac{A}{2\tau_i} exp\left(\frac{u-\mu_i}{\tau_i} + \frac{\sigma_E^2}{2\tau_i^2}\right) efrc\left[\frac{1}{\sqrt{2}}\left(\frac{u-\mu_i}{\tau_i} + \frac{\sigma_E}{\tau_i}\right)\right], \quad \text{(A.1)}$$

in which A is the peak area, $u - \mu_i$ the distance to the peak position, $\sigma_E = \sigma + F(E_{max} - E_{peak})$ the standard deviation of the Gaussian that is a function of the energy, τ_i the tailing parameter and η_1, η_2 and $\eta_3 = 1 - (\eta_1 + \eta 2)$ normalized weighting factors.

The analytical model is implemented as a call function in an Excel spreadsheet and the built-in optimization routine SOLVER is used to find the best match between fitted and measured spectrum. This spectral analysis tool will be referred to as "BEST" and its performance will be tested on recently published ^{240}Pu and ^{236}Pu spectra and compared with ALPHA results.

A.2 The new algorithm

The typical line shape of a peak with triple tailing as defined in Eq. A.1 is shown in Fig. A.1, with indications where the peak width σ and the tailing

parameters $\tau_1 < \tau_2 < \tau_3$ determinate the peak shape. With increasing distance from the peak top, the tailing is dominated by exponentials with larger τ values. The analytical peak shape is not completely smooth in transition regions where the dominance changes from one exponential tail to another.

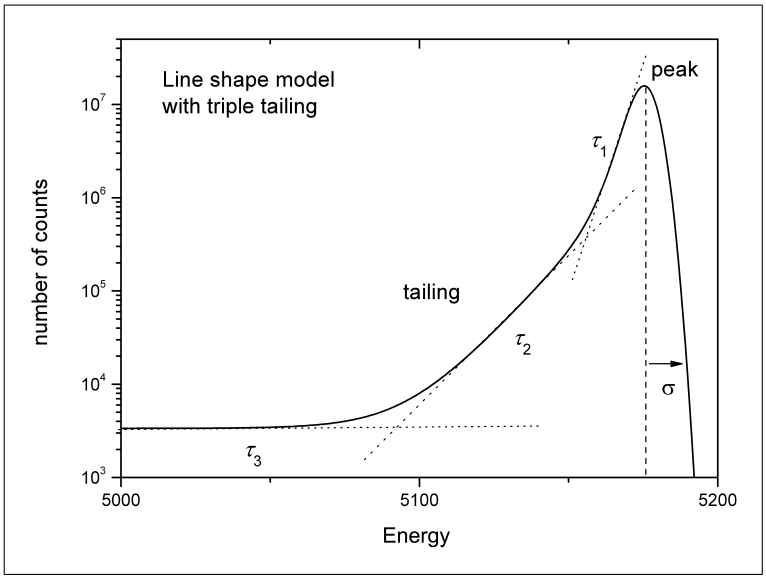

Figure A.1: Typical line shape applying a convolution of a Gaussian with three left-handed exponentials (Eq. A.1) and indication where the peak width σ and the tailing parameters $\tau_1 < \tau_2 < \tau_3$ are the most influential.

One way of mitigating the abrupt changes in the slope of the tailing is adding more exponential tails with progressively increasing τ values. On the other hand, the experimental spectra are also not perfectly smooth and may show mild curvatures that are not well reproduced by monotonic functions. Therefore the fit would not only benefit from a higher number of exponential tailing functions, but also from flexibility in the weighting factors, allowing some of them to be negative or larger than 1 on condition that the sum of all weighting factors remains one.

Another observation is that alpha peaks show slight distortions and even some tailing at the high-energy side. This aspect can be taken into account by applying also right-handed exponential tailing in addition to the left-handed tailing. The inversion of the tailing is easily established by changing the sign of the position in the function call, i.e. by replacing $u - \mu$ by $\mu - u$. In the current implementation of the BEST algorithm, the peak shape can contain up to ten left-handed and four right-handed tailing functions:

$$F(u) = \sum_{i=-3}^{0} \eta_i f\left(\mu_i - u; \sigma_{Ei}, \tau_i\right) + \sum_{i=1}^{10} \eta_i f\left(u - \mu_i; \sigma_{Ei}, \tau_i\right) \qquad \text{(A.2)}$$

The sum of the weighting factors is normalized to one, but this is the only constraint on the individual values. In practice, this constraint is implemented by excluding η_1 from the list of free parameters in the fit and setting it equal to 1 minus the sum of the other factors:

$$\sum_{i=-3}^{10} \eta_i = 1 \; or \; \eta_1 = 1 - \sum_{i=-3}^{10} \eta_i \; (i \neq 1) \tag{A.3}$$

In the decay of an alpha-emitting radionuclide, usually there are several alpha transitions involved with different energy and relative emission probabilities. Each of them corresponds to an individual peak in the alpha spectrum and the peak area A_k of peak k can be represented as the product of the total number of alpha decays A_{tot} of this particular nuclide multiplied by the relative intensity I_k:

$$A_k = A_{tot} I_k = \sum_{k=1}^{n_{peaks}} I_k F_k(u) \tag{A.4}$$

It is convenient to use A_{tot} as a free fitting parameter to adjust all peaks of a radionuclide to the number of counts in a spectrum, without changing the spectral shape through the relative peak intensities. This feature can be used, e.g., to determine the activity ratio of radionuclides in a mixed source. Some of the intensities may be released for more precise fitting, while others may be kept fixed, e.g. because literature values may be more accurate. The normalization of the intensities is enforced by constraining the intensity of the major peak to the value of 1 minus the sum of the intensities of the other peaks:

$$\sum_{k=1}^{n_{peaks}} I_k = 1 \; or \; I_1 = 1 - \sum_{k=2}^{n_{peaks}} I_k \tag{A.5}$$

Additional functional relationships between parameters, e.g. a constant ratio between emission probabilities, can be introduced as a constraint in the spreadsheet. Also the energy calibration, e.g. through a linear relationship between bin number and keV, can be part of the optimization process, before individual peak positions are released in the fit for more precise positioning.

When fitting a spectrum within a selected energy region, all peaks contributing to it should be included, including the tailing of possible high-energy peaks situated outside the considered energy region. This may include peaks from interfering nuclides, the spectrum of which can be introduced using the same energy calibration. In principle it is possible that there is a misalignment of the peak energies between two radionuclides, for example through a mismatch of the energy calibrations in the experiments on which the literature values are based. In that case, one can easily introduce a separate energy calibration for both nuclides to align both spectral shapes to the measured aggregate spectrum. Multiple energy calibration can also be useful in conversion electron spectrometry, involving mixed spectra of photons and particles [144].

A.3 Examples

A.3.1 High-resolution ^{240}Pu spectrum

Demonstrating the adequacy of analytical functions by means of a fit to spectra with a low number of counts is not enough. Visually the fit may appear convincing, certainly in a log scale plot, and the residuals are bound to look stochastically distributed since the randomness of the Poisson process would be the dominant uncertainty component. Systematic functional misrepresentations of the spectral shape can only surface when they supersede statistical uncertainty. For this reason, a high-resolution ^{240}Pu spectrum with extremely good statistical accuracy (3.6×10^8 events) was selected for a test of the algorithm.

In Figure A.2.a classical fit with triple tailing is shown, which was the best available fit for the determination of the alpha emission probabilities [82]. The fit reproduces the spectral shape quite well, but slight discrepancies between model and reality do show up. The regions around the peak tops are well fitted, but the slope of the tailing is not rigorously reproduced by the model. The apparent subtle tailing at the high energy side was not included in the model and therefore the fit could not be extended to that region. The residuals varied between -22 and +27, owing to the extremely low statistical uncertainty in each bin.

For comparison, this challenging spectrum was fitted with BEST using the full capacity of 10 exponentials at the low-energy side and 4 at the high-energy side of the peak. The same shaping was applied to the three peaks and the result is shown in Figure A.2.b. It is clear that the increased flexibility of the model has made it possible to fit the tailing and the changes in its slope more adequately. Also the high-energy part of the spectrum could be reproduced more rigorously, including the high-energy tailing of the main peak and the interfering tailing from peaks around 5.5 MeV. The overall fit has been drastically improved and the residuals being confined between -4 and +4 approaches the desired level of perfection.

The fitted intensities of the three main peaks were 72.63 %, 27.29 % and 0.084 %, with a negligible statistical uncertainty. The provided data in this work are not intended to replace the previously published values and, therefore, no extensive uncertainty budget is provided. The values the values fitted by BEST agree by one standard uncertainty with the data obtained by Sibbens et al. [82], i.e. 72.70 (7) %, 27.21 (7) % and 0.085 (4) %. Nevertheless, the difference is significant compared to the uncertainty on model dependence estimated from a comparison among six participants with different software packages [82]. On the basis of the closer fit to the spectrum, it could seem reasonable to assign a higher credibility to the result obtained with the BEST model than with the simpler models. However, this issue is open to future scrutiny.

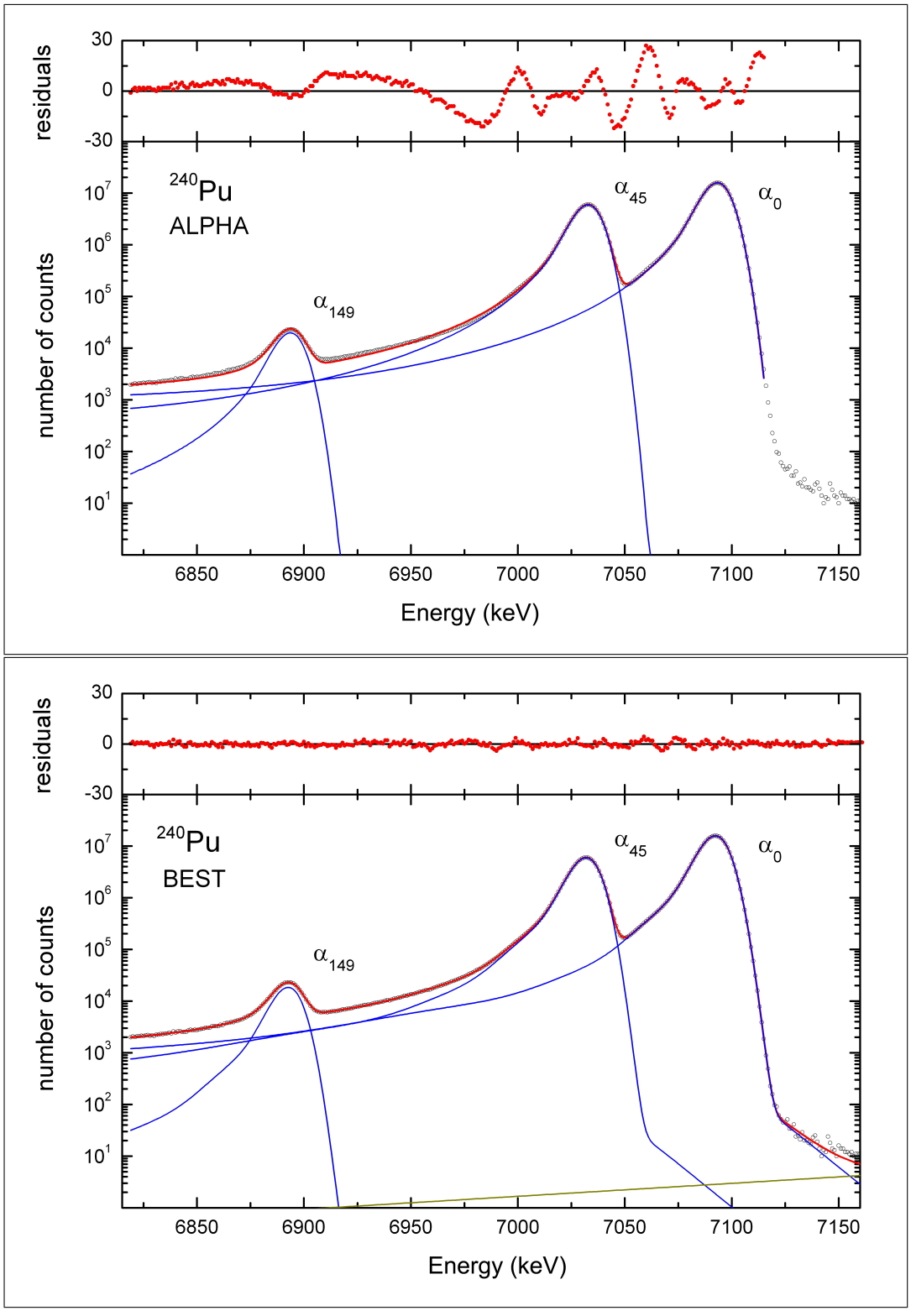

Figure A.2: Measured ^{240}Pu alpha-particle spectrum 'IRMM HR01' from Sibbens et al. [82] and fitted line shapes using the ALPHA software (a), based on a convolution of a Gaussian and triple exponential low-energy tailing; and the BEST algorithm (b), using a convolution of a Gaussian with 10 exponential low-energy tails and 4 high-energy tails (Eqs. 1,3). The residuals spectrum (top) is shown in units of one standard deviation of the channel contents.

A.3.2 High-resolution ^{236}U spectrum

The example of the ^{240}Pu spectrum is extreme in the number of counted events and the complexity of the fit function used, i.e. with 14 exponentials. This level of complexity is not needed in more common spectra which are usually well reproduced with a double or triple tailing and lack the statistical accuracy to require or even justify the free fit of additional shaping parameters. The new algorithm is implemented in a way that the number of exponentials is freely chosen by resetting the weighting factors η_i of the superfluous exponentials to zero, or by simply erasing these numbers in their respective spreadsheet cells.

As an example of a spectrum with "intermediate complexity", a ^{236}U spectrum was fitted without using the full potential of the model. In Figure A.3.a the classical fit with triple tailing is shown [145] as well as the residuals, which vary between -15 and +15. Figure A.3.b shows a fit result obtained with BEST, using 6 left-handed and 1 right-handed exponential. The fit has improved considerably, the most extreme residuals being reduced to -5 and +5, but there are still issues with reproducing the finer details of the shape of the main peak. Also in this example, the fitted intensities of the main peaks 74.25 %, 25.64 % and 0.119 % , agree by one standard uncertainty by the data obtained by Marouli et al. [145], i.e. 74.20 (5) %, 25.68 (5) % and 0.123 (5) % and have the same uncertainty budget. The evaluated statistical uncertainty of the main published emission probabilities was very small, 0.02 %, but the uncertainties were increased to 0.05 % to take into account spectral distortions [145]. Apparently, the introduction of a more sophisticated line shape demonstrates that an uncertainty increase of this magnitude was indeed needed.

A.3.3 Thick-source spectra of ^{238}U

Whereas the algorithm was primarily designed for high-resolution spectrometry, it can also be tested on spectra from thick sources, having a poor energy resolution. Two alpha spectra from the decay of ^{238}U were selected from the work of Semkow et al. [146], in which samples of various thicknesses were prepared and counted with a grid ionization chamber suitable for fast alpha spectrometry in bulky matrices. Figures A.4.a and A.4.b show spectra from a relatively thin (0.11 mg cm^{-2}) and thick (1.3 mg cm^{-2}) ^{238}U source (with ^{230}Th tracer), respectively. As the source mass increases, the peaks become broader and less intense due to energy loss and self-absorption in the sample. Nevertheless, there is always a fraction emitted from the top layer that can be measured close to the emission energy.

The line shapes fitted to the spectra were based on 5 left-handed and 4 right-handed exponentials. The exponential models are well suited to reproduce the long tailing part (also below 3.5 MeV), but residuals remain between the maxima of the two main peaks. No substantial gain in quality was found by increasing the number of exponentials. For this type of spectra, the fit result is fairly good but not superior to the functions proposed by Semkow et al. [146].

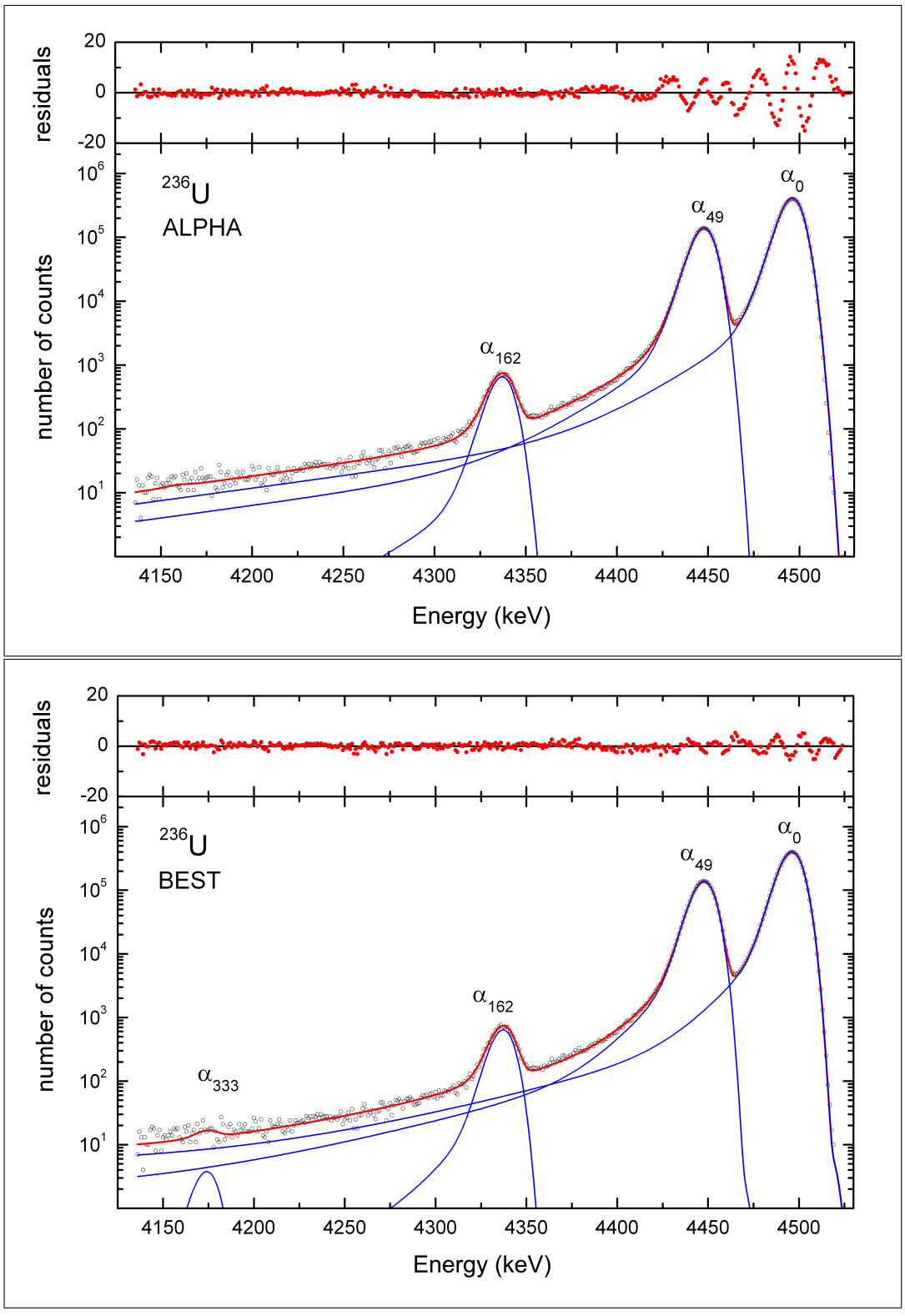

Figure A.3: Measured ^{236}U alpha-particle spectrum (with magnet) from Marouli et al. [145] and fitted line shapes using the ALPHA software (a) and the BEST algorithm (b), using a convolution of a Gaussian with 6 exponential low-energy tails and 1 high-energy tail. The residuals spectrum (top) is shown in units of one standard deviation of the channel contents.

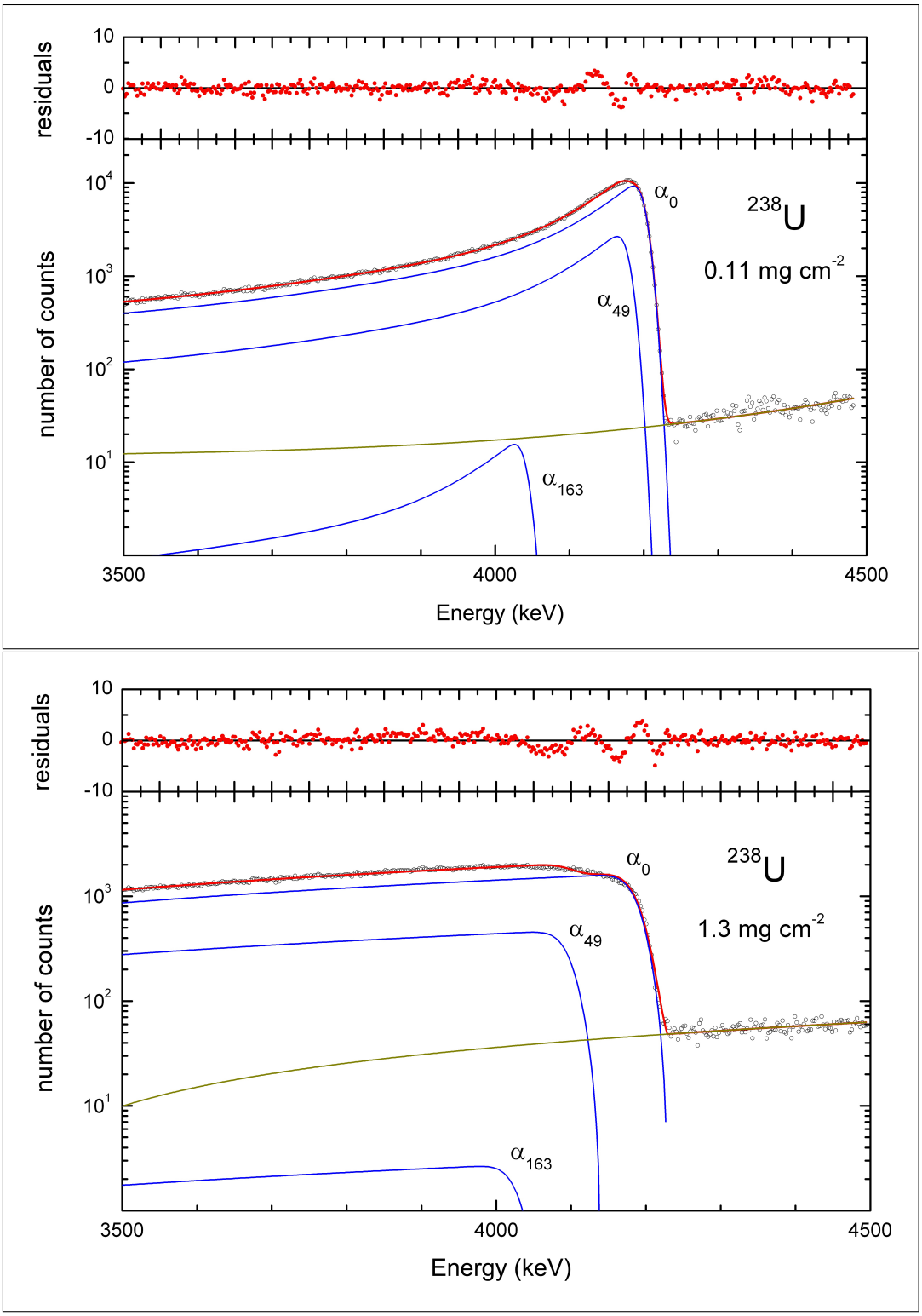

Figure A.4: Fit of peak shape with 5 left-handed and 4 right-handed exponentials to alpha spectra from ^{238}U thick-samples of 0.11 (a) and 1.3 mg cm^{-2} (b) [146]. The residuals spectrum (top) is shown in units of one standard deviation of the channel contents.

A.4 Uncertainty

The issue of uncertainty in alpha spectrometry has been discussed in a recent review paper [147]. The statistical uncertainties on the fitted parameters, including the peak areas, can in principle be calculated from the covariance matrix. The corresponding equations have been published by Sibbens [148], Ihantola et al. [149] and Caro Marroyo et al. [21]. However,a minimum requirement is that the residuals are purely stochastic. This condition is not fulfilled in most of the spectra presented in this work.

Experience with complex spectra shows that fit results are badly defined if a spectrum can be fitted in several ways, e.g. increasing a tailing can have similar effects as adding a small additional peak,changing the peak width or energy calibration can significantly influence the areas of overlapping peaks, the area of small peaks interfered by the tailing of a dominant peak are crucially dependent on the exact representation of the latter, not taking into account underlying peaks from impurities can change relative positions of freely fitted peaks and alter relative peak areas. Also scattering effects, electronic drift and coincidences between signals from alpha particles with beta particles, conversion electrons, X-Rays or electronic noise give rise to a distortion of the energy spectrum which is not explicitly implemented in the analytical model [123], [145].

For these reasons, the uncertainties obtained from the covariance matrix may perhaps suffice in routine measurements with low statistical accuracy, but should be interpreted with caution in reference measurements with high statistical precision in the measurement data.Comparison of fit results with different codes does reveal biases that are not under statistical control [82].

The preferred way of dealing with uncertainties in radionuclide metrology is to make for each peak a detailed uncertainty budget and perform proper uncertainty propagation towards the final result (see e.g. Sibbens et al. [82], Pommé et al. [123], P*öllä*nen and Siiskonen [150]). Uncertainty components include counting statistics, spectral interferences, impurities and background, residual deviations between fit and measurement, physical effects not included in the model and model dependence of the fit result. Normalization and (anti-) correlation of uncertainty components are constraints that require specific propagation formulas. Equations and numerical examples can be found in [147].

The alpha emission probability P_k is derived from the peak area A_k relative to the total area A_{tot} of all peaks in the emission spectrum of the same radionuclide. The sum of all relative intensities $\sum P_k$ equals 100 % by definition. Through normalization, all intensities receive a degree of correlation which comes on top of the (anti-) correlation of the peak areas due to imperfect deconvolution of spectral interferences. In the hypothetical case in which the alpha peaks are perfectly separated, i.e.their peak areas are uncorrelated, the uncertainties on the areas propagate to P_k via

$$\sigma^2(P_k) = P_k^2(1-P_k)^2\left[\frac{\sigma^2(A_k)}{\sigma^2 A_k^2} + \frac{\sigma^2\left(\sum_{i\neq k} A_i\right)}{\left(\sum_{i\neq k} A_i\right)^2}\right] \tag{A.6}$$

Statistical uncertainties are readily introduced into Equation A.6, and the same equation can be used to propagate the interference of an impurity that affects part of the spectrum [147]. Also a mismatch between fit and measured spectrum can be included in the uncertainty budget. Explicit uncertainties can be assigned to fit model dependence, contrary to ignoring this component when relying on the covariance matrix.

Another propagation formula is required in the ubiquitous cases in which the uncertainties in the peak areas are anti-correlated

$$\sigma^2(P_k) = \frac{\sigma^2(A_k)}{\left(\sum_i A_i\right)^2} \tag{A.7}$$

Equation A.7 is applicable in any situation in which adding an amount $\Delta(A_k)$ to peak k implies the subtraction of the same amount from the rest of the spectrum, so that the total area $\sum A$ remains invariable and the corresponding emission probability changes to $P_k = (A_k + \Delta[A_k])/\sum A$. This situation occurs in the fit of an unresolved doublet, subtraction of tailing from a higher-energy peak and correction for coincidence summing-in and summing-out effects [147].

To a lesser extent, positively correlated uncertainties may also appear for which the propagation factor is smaller [147]. If the relative deviation is the same for all peaks, there is no change in the emission probabilities. Equation A.6 gives an upper limit for the propagated uncertainty.

A.5 Discussion

Whereas the convolution of a Gaussian with three left-handed exponentials is very successful in satisfactorily reproducing most high-resolution alpha particle spectra, a more elaborate modeling is needed to fit the most demanding spectra with extremely good counting statistics. A line shape model was proposed that expands the number of left-handed exponentials and also incorporates a number of righted-handed exponentials, which allows obtaining a smoother function, better reproducing changes of slope in the tailing and incorporating spectral broadening at the high-energy side.

A line model with up to 10 left-handed and 4 right-handed exponentials was implemented as a function in the spreadsheet application BEST. It uses the functionality of a spreadsheet to perform the search for optimum fit parameters, to select which parameters to keep fixed or to define a relationship between a set of parameters (e.g. normalization, fixed reference data, maintain a ratio between parameters), to store spectral data and all specifics of the fit together in one file, to plot and export the results. Applications include the free fit of individual peaks to determinate alpha emission probabilities or of

complete radionuclide emission spectra to determine activity ratios in a mixed sample. The new algorithm seemed to outperform existing software at deconvoluting high-resolution ^{240}Pu and ^{236}U spectra with high count numbers. Its applicability extends to thick alpha sources of which the spectrum almost resembles a step function. Further extensions are possible in which different functional shapes are combined, e.g for application with mixed spectra of mono-energetic electrons and X-Rays.

Appendix B

ALFITeX's folders

Screenshots of the code ALFITeX are shown as follow. The program consists of six folders:

- *Master*
- *Spectrum*
- *Fitting Parameters*
- *Graphics*
- *Matrix*
- *INFO*

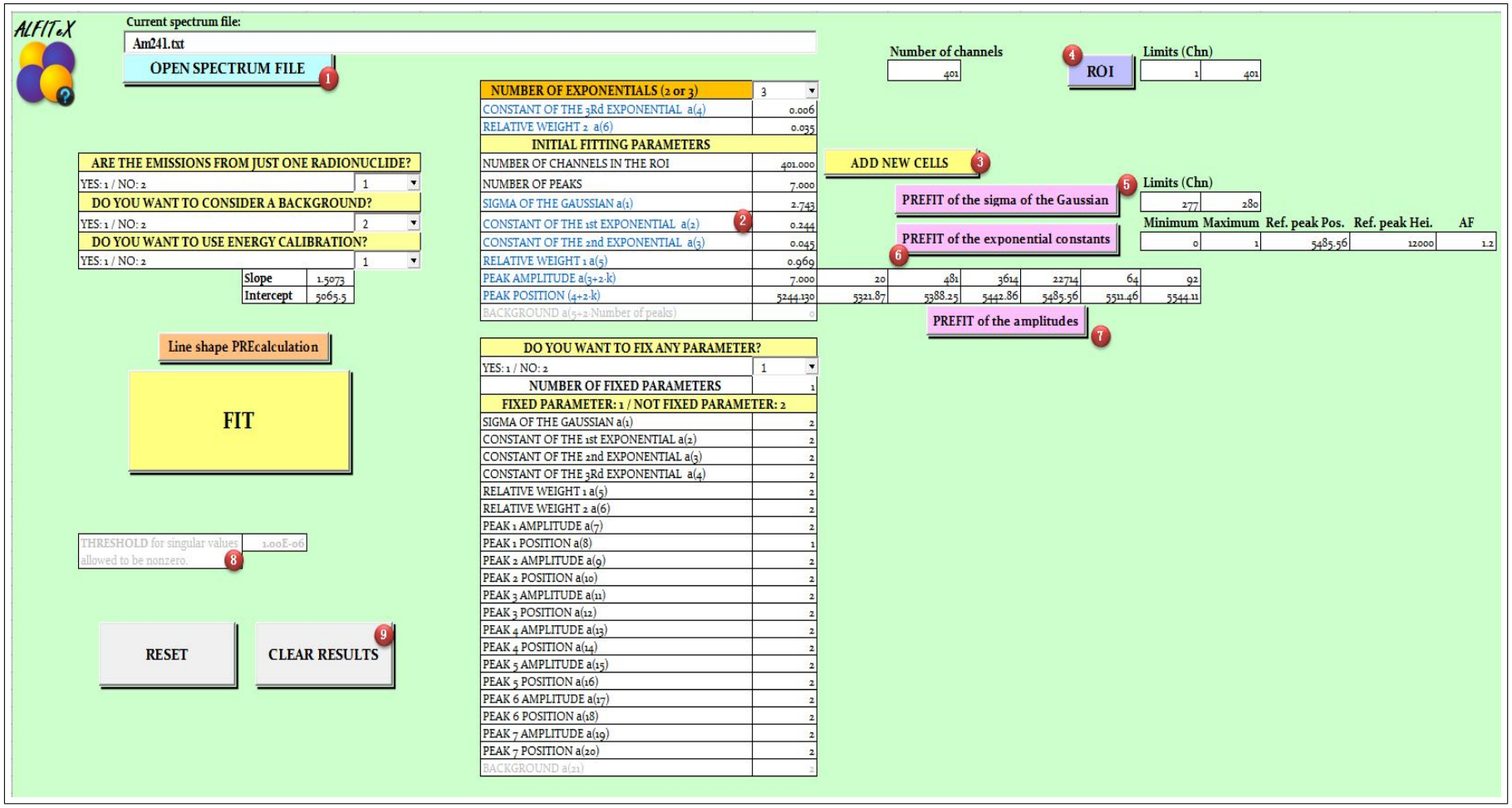

Figure B.1: Screenshot of the folder "Master".

32	36	-0.7	0	0	26	3	7	0	0
49	43	0.8	0	0	33	4	7	0	0
37	52	-2.5	0	0	41	4	7	0	0
56	63	-1.0	0	0	52	4	8	0	0
75	78	-0.3	0	0	66	4	8	0	0
82	95	-1.5	0	0	83	4	8	0	0
132	117	1.3	0	0	105	4	8	0	0
165	144	1.7	0	0	130	5	9	0	0
181	174	0.6	0	0	159	5	9	0	0
193	204	-0.8	0	0	189	5	10	0	0
238	230	0.5	0	0	215	5	10	0	0
235	247	-0.8	0	0	231	6	10	0	0
260	247	0.8	0	0	230	6	11	0	0
255	229	1.6	0	0	212	6	11	0	0
178	196	-1.3	0	0	177	7	12	0	0
160	154	0.5	0	0	134	7	12	0	0
105	112	-0.7	0	0	92	8	13	0	0
84	77	0.7	0	0	56	8	13	0	0
52	53	-0.2	0	0	30	9	14	0	0
30	39	-1.6	0	0	15	10	14	0	0
36	32	0.6	0	0	6	11	15	0	0
36	30	1.0	0	0	2	12	15	0	0
33	31	0.4	0	0	1	14	16	0	0
35	33	0.4	0	0	0	15	17	0	0
36	35	0.1	0	0	0	18	18	0	0
30	39	-1.6	0	0	0	20	18	0	0
54	43	1.5	0	0	0	24	19	0	0
52	48	0.6	0	0	0	28	20	0	0
52	54	-0.3	0	0	0	33	21	0	0
50	61	-1.6	0	0	0	39	22	0	0
70	70	0.0	0	0	0	47	23	0	0
88	82	0.7	0	0	0	58	24	0	0
81	96	-1.6	0	0	0	71	25	0	0
107	113	-0.6	0	0	0	87	26	0	0
130	135	-0.5	0	0	0	108	27	0	0
170	163	0.5	0	0	0	134	29	0	0
197	198	-0.1	0	0	0	168	30	0	0
221	243	-1.4	0	0	0	211	32	0	0
315	299	0.9	0	0	0	265	34	0	0
359	370	-0.6	0	0	0	334	35	0	0
489	460	1.3	0	0	0	422	37	0	0
587	574	0.5	0	0	0	534	40	0	0
743	717	1.0	0	0	0	675	42	0	0
887	894	-0.2	0	0	0	848	45	0	0
1121	1104	0.5	0	0	0	1056	48	0	0
1357	1339	0.5	0	0	0	1287	52	0	0
1633	1576	1.4	0	0	0	1520	56	0	0

Experimental data are in column A.
Fitted data are in column B.
Weighted residuals from de fits are in column C.
Fitted data per peaks are in columns (4+k). (k goes from 1 to "Number of peaks").

Figure B.2: Screenshot of the folder “Spectrum”.

FINAL FITTING PARAMETERS			
Chi-squared =	392		
chisqr =	1.026		
a(1) =	4.150	±	0.024
a(2) =	0.162	±	0.002
a(3) =	0.031	±	0.004
a(4) =	0.003	±	0.002
a(5) =	0.960	±	0.006
a(6) =	0.036	±	0.005
a(7) =	0.060	±	0.866
a(8) =	5244.130	±	0.000
a(9) =	6.796	±	1.722
a(10) =	5321.495	±	1.853
a(11) =	351.286	±	8.579
a(12) =	5387.931	±	0.159
a(13) =	2763.934	±	30.051
a(14) =	5443.493	±	0.064
a(15) =	17664.545	±	113.614
a(16) =	5486.526	±	0.039
a(17) =	57.121	±	3.364
a(18) =	5511.161	±	0.459
a(19) =	74.913	±	3.383
a(20) =	5545.518	±	0.288

Iterations
8

W(k) VECTOR
17539553.788
3013820.933
1522450.331
204708.563
28874.402
11283.288
1358.374
294.511
41.474
12.173
4.967
1.359
0.352
0.284
0.091
0.088
0.014
0.002
0.000
0.000

CONDITION NUMBER OF ALPHA
2.30704E+11

RESIDUAL
-1.8779E-179

The option 'Fixed parameters' has been selected.
Do not take into account the components of w(k) which are zero
to set a threshold if the curvature matrix is ill-conditioned.

PEAK AREAS								
Peak 1 :	exp1 =	0.60	exp2 =	0.02	Total peak area =	0.62	±	8.65
Peak 2 :	exp1 =	67.87	exp2 =	2.55	Total peak area =	70.70	±	17.30
Peak 3 :	exp1 =	3508.21	exp2 =	131.82	Total peak area =	3654.69	±	123.30
Peak 4 :	exp1 =	27602.74	exp2 =	1037.15	Total peak area =	28755.30	±	759.15
Peak 5 :	exp1 =	176411.56	exp2 =	6628.54	Total peak area =	183777.69	±	4598.34
Peak 6 :	exp1 =	570.45	exp2 =	21.43	Total peak area =	594.27	±	36.58
Peak 7 :	exp1 =	748.14	exp2 =	28.11	Total peak area =	779.38	±	38.73

TOTAL AREA =	217632.6607	±	4662.557915
AREA PER COUNTS =	144603	±	380.2670115
BACKGROUND AREA =	0		

EMISSION PROBABILITIES (%)			
Peak 1:	0.000	±	0.004
Peak 2:	0.032	±	0.008
Peak 3:	1.679	±	0.067
Peak 4:	13.213	±	0.449
Peak 5:	84.444	±	2.782
Peak 6:	0.273	±	0.018
Peak 7:	0.358	±	0.019

IMPROVED EMISSION PROBABILITIES (%)			
Peak 1:	0.000	±	0.004
Peak 2:	0.032	±	0.008
Peak 3:	1.679	±	0.067
Peak 4:	13.213	±	0.443
Peak 5:	84.444	±	0.449
Peak 6:	0.273	±	0.018
Peak 7:	0.358	±	0.019

Figure B.3: Screenshot of the folder "Fitting Parameters".

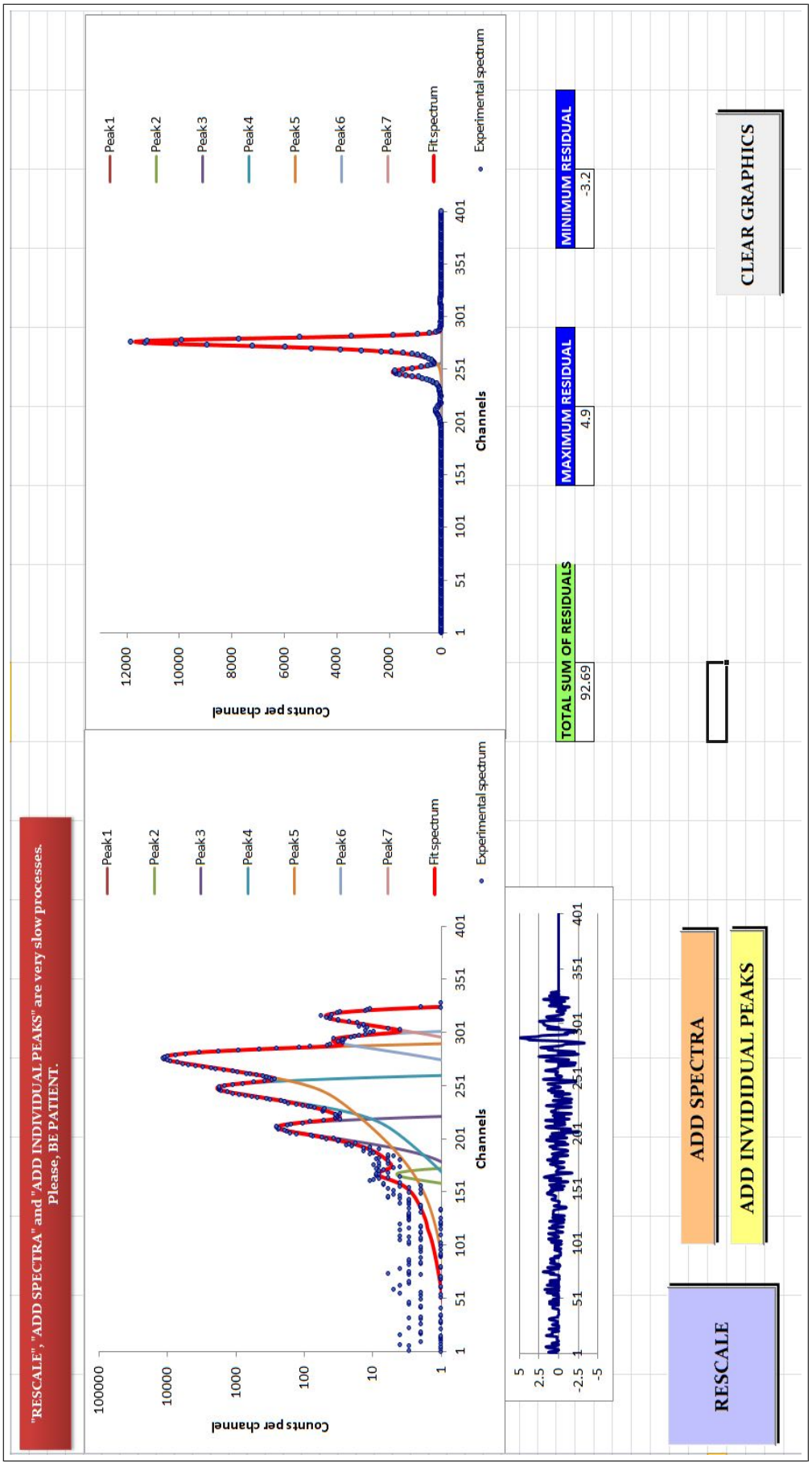

Figure B.4: Screenshot of the folder "Graphics".

Curvature matrix																									
12308.68	-25656.07	-1995.84	17207.97	6639.82	14689.99	1.51	0	1.52	0.01	1.57	8.23	1.58	69.08	1.67	1131.69	2.55	-9.01	1.67	4.59
-25656.07	2856155.86	129518.07	-247737.40	300906.87	-356035.46	0.13	0	2.79	4.42	0.51	790.90	-4.25	4421.30	0.59	57802.63	13.65	1.47	4.14	208.29
-1995.84	129518.07	1072717.28	-857099.18	1746723.82	1246980.84	-142.36	0	-225.95	-14.49	-43.83	-95.12	-6.59	1297.26	1.99	-2182.35	1.52	0.03	2.51	-8.71
17207.97	-247737.40	-857099.18	1031054.52	-1155128.77	-766774.98	269.00	0	231.46	-3.53	29.14	-70.89	6.99	-516.25	1.55	-1460.43	1.27	1.71	0.90	-3.77
6639.82	300906.87	1746723.82	-1155128.77	9073283.16	8450073.67	-1336.99	0	-461.63	33.74	-37.08	200.62	-3.19	645.78	3.81	1611.04	4.34	-1.88	4.96	3.47
14689.99	-356035.46	1246980.84	-766774.98	8450073.67	8273470.23	-1314.77	0	-403.36	41.57	-17.94	394.25	5.47	346.45	2.07	-5101.23	1.71	4.71	1.86	-14.96
1.51	0.13	-142.36	269.00	-1336.99	-1314.77	1.71	0	0.00	0.00	0.00	0.00	0.00	0.00	0.00	0.00	0.00	0.00	0.00	0.00
0	0	0	0	0	0	0	0	0	0	0	0	0	0	0	0	0	0	0	0
1.52	2.79	-225.95	231.46	-461.63	-403.36	0.00	0	0.42	-0.02	0.00	0.00	0.00	0.00	0.00	0.00	0.00	0.00	0.00	0.00
0.01	4.42	-14.49	-3.53	33.74	41.57	0.00	0	-0.02	0.30	0.00	0.00	0.00	0.00	0.00	0.00	0.00	0.00	0.00	0.00
1.57	0.51	-43.83	29.14	-37.08	-17.94	0.00	0	0.00	0.00	0.02	-0.03	0.00	0.00	0.00	0.00	0.00	0.00	0.00	0.00
8.23	790.90	-95.12	-70.89	200.62	394.25	0.00	0	0.00	0.00	-0.03	44.29	0.00	-0.41	0.00	-0.03	0.00	0.00	0.00	0.00
1.58	-4.25	-6.59	6.99	-3.19	5.47	0.00	0	0.00	0.00	0.00	0.00	0.00	-0.05	0.00	-0.03	0.00	0.00	0.00	0.00
69.08	4421.30	1297.26	-516.25	645.78	346.45	0.00	0	0.00	0.00	0.00	-0.41	-0.05	362.07	0.01	-18.90	0.00	0.00	0.00	0.00
1.67	0.59	1.99	1.55	3.81	2.07	0.00	0	0.00	0.00	0.00	0.00	0.00	0.01	0.00	0.00	0.00	0.00	0.00	0.00
1131.69	57802.63	-2182.35	-1460.43	1611.04	-5101.23	0.00	0	0.00	0.00	0.00	0.00	-0.03	-18.90	0.00	2989.05	0.54	-4.71	0.01	-0.02
2.55	13.65	1.52	1.27	4.34	1.71	0.00	0	0.00	0.00	0.00	0.00	0.00	0.00	0.00	0.54	0.10	0.14	0.00	-0.02
-9.01	1.47	0.03	1.71	-1.88	4.71	0.00	0	0.00	0.00	0.00	0.00	0.00	0.00	0.00	-4.71	0.14	4.99	0.02	-0.24
1.67	4.14	2.51	0.90	4.96	1.86	0.00	0	0.00	0.00	0.00	0.00	0.00	0.00	0.00	0.01	0.00	0.02	0.09	0.01
4.59	208.29	-8.71	-3.77	3.47	-14.96	0.00	0	0.00	0.00	0.00	0.00	0.00	0.00	0.00	-0.02	-0.02	-0.24	0.01	12.23
Covariances matrix																			
0.00	0.00	0.00	0.00	0.00	0.00	0.00	0	0.00	0.00	-0.05	0.00	-0.43	0.00	-2.36	0.00	-0.01	0.00	-0.01	0.00
0.00	0.00	0.00	0.00	0.00	0.00	0.00	0	0.00	0.00	0.00	0.00	-0.04	0.00	-0.12	0.00	0.00	0.00	0.00	0.00
0.00	0.00	0.00	0.00	0.00	0.00	0.00	0	0.00	0.00	0.01	0.00	-0.05	0.00	-0.12	0.00	0.00	0.00	0.00	0.00
0.00	0.00	0.00	0.00	0.00	0.00	0.00	0	0.00	0.00	0.00	0.00	-0.02	0.00	-0.06	0.00	0.00	0.00	0.00	0.00
0.00	0.00	0.00	0.00	0.00	0.00	0.00	0	0.00	0.00	0.00	0.00	0.09	0.00	0.16	0.00	0.00	0.00	0.00	0.00
0.00	0.00	0.00	0.00	0.00	0.00	0.00	0	0.00	0.00	0.00	0.00	0.00	0.00	0.00	0.00	0.00	0.00	0.00	0.00
0.00	0.00	0.00	0.00	0.00	0.00	0.00	0	0.00	0.00	0.00	0.00	0.00	0.00	0.00	0.00	0.00	0.00	0.00	0.00
0	0	0	0	0	0	0	0	0	0	0	0	0	0	0	0	0	0	0	0
0.00	0.00	0.00	0.00	0.00	0.00	0.12	0	2.97	0.25	1.31	-0.01	-2.89	-0.01	-3.49	0.00	-0.03	0.00	-0.01	0.00
0.00	0.00	0.00	0.00	0.00	0.00	-0.04	0	0.25	3.43	0.44	0.00	-0.43	0.00	-2.17	0.00	-0.01	0.00	-0.01	0.00
-0.05	0.00	0.01	0.00	0.00	0.00	-0.23	0	1.31	0.44	73.60	0.11	34.95	0.02	158.66	0.06	0.98	-0.04	0.74	0.05
0.00	0.00	0.00	0.00	0.00	0.00	0.00	0	-0.01	0.00	0.11	0.03	0.94	0.00	2.77	0.00	0.02	0.00	0.01	0.00
-0.43	-0.04	-0.05	-0.02	0.09	-0.09	1.49	0	-2.89	-0.43	34.95	0.94	903.08	0.73	1724.85	0.64	10.31	-0.15	7.68	0.62
0.00	0.00	0.00	0.00	0.00	0.00	0.00	0	-0.01	0.00	0.02	0.00	0.73	0.00	2.19	0.00	0.01	0.00	0.01	0.00
-2.36	-0.12	-0.12	-0.06	0.16	-0.16	5.72	0	-3.49	-2.17	158.66	2.77	1724.85	2.19	12908.06	2.67	54.66	-1.68	45.80	2.55
0.00	0.00	0.00	0.00	0.00	0.00	0.00	0	0.00	0.00	0.06	0.00	0.64	0.00	2.67	0.00	0.01	0.00	0.01	0.00
-0.01	0.00	0.00	0.00	0.00	0.00	0.03	0	-0.03	-0.01	0.98	0.02	10.31	0.01	54.66	0.01	11.32	-0.33	0.07	0.02
0.00	0.00	0.00	0.00	0.00	0.00	0.00	0	0.00	0.00	-0.04	0.00	-0.15	0.00	-1.68	0.00	-0.33	0.21	-0.06	0.00
-0.01	0.00	0.00	0.00	0.00	0.00	0.02	0	-0.01	-0.01	0.74	0.01	7.68	0.01	45.80	0.01	0.07	-0.06	11.45	0.01
0.00	0.00	0.00	0.00	0.00	0.00	0.00	0	0.00	0.00	0.05	0.00	0.62	0.00	2.55	0.00	0.02	0.00	0.01	0.08
Checkout matrix (CURVA*COVAR=I)																			
1.00	0.00	0.00	0.00	0.00	0.00	0.00	0	0.00	0.00	0.00	0.00	0.00	0.00	0.00	0.00	0.00	0.00	0.00	0.00
0.00	1.00	0.00	0.00	0.00	0.00	0.00	0	0.00	0.00	0.00	0.00	0.00	0.00	0.00	0.00	0.00	0.00	0.00	0.00

Figure B.5: Screenshot of the folder "Matrix".

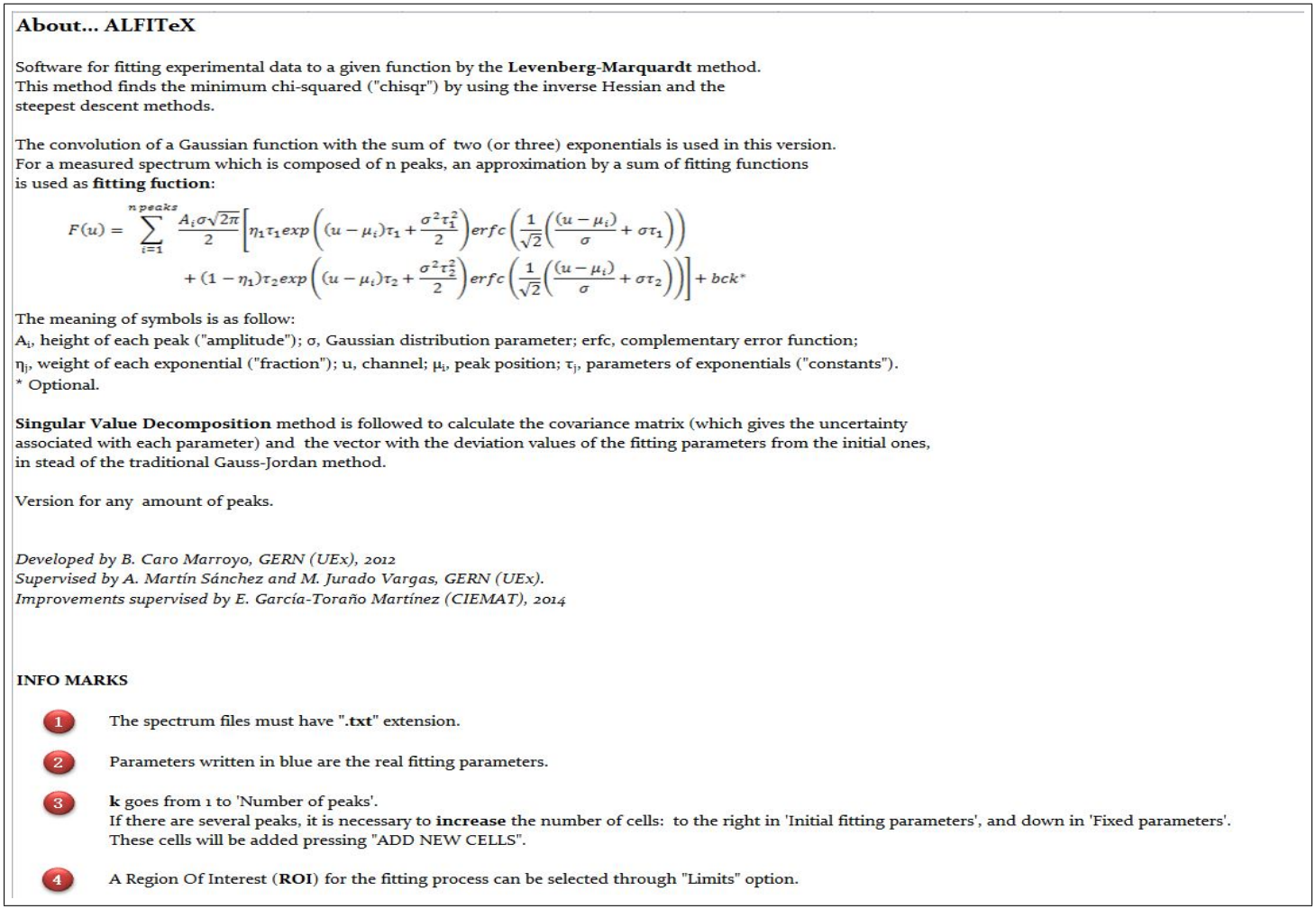

About... ALFITeX

Software for fitting experimental data to a given function by the **Levenberg-Marquardt** method.
This method finds the minimum chi-squared ("chisqr") by using the inverse Hessian and the steepest descent methods.

The convolution of a Gaussian function with the sum of two (or three) exponentials is used in this version.
For a measured spectrum which is composed of n peaks, an approximation by a sum of fitting functions is used as **fitting fuction**:

$$F(u) = \sum_{i=1}^{n\,peaks} \frac{A_i \sigma\sqrt{2\pi}}{2}\left[\eta_1\tau_1 exp\left((u-\mu_i)\tau_1 + \frac{\sigma^2\tau_1^2}{2}\right) erfc\left(\frac{1}{\sqrt{2}}\left(\frac{(u-\mu_i)}{\sigma} + \sigma\tau_1\right)\right)\right.$$
$$\left. + (1-\eta_1)\tau_2 exp\left((u-\mu_i)\tau_2 + \frac{\sigma^2\tau_2^2}{2}\right) erfc\left(\frac{1}{\sqrt{2}}\left(\frac{(u-\mu_i)}{\sigma} + \sigma\tau_2\right)\right)\right] + bck^*$$

The meaning of symbols is as follow:
A_i, height of each peak ("amplitude"); σ, Gaussian distribution parameter; erfc, complementary error function;
η_j, weight of each exponential ("fraction"); u, channel; μ_i, peak position; τ_j, parameters of exponentials ("constants").
* Optional.

Singular Value Decomposition method is followed to calculate the covariance matrix (which gives the uncertainty associated with each parameter) and the vector with the deviation values of the fitting parameters from the initial ones, in stead of the traditional Gauss-Jordan method.

Version for any amount of peaks.

Developed by B. Caro Marroyo, GERN (UEx), 2012
Supervised by A. Martín Sánchez and M. Jurado Vargas, GERN (UEx).
Improvements supervised by E. García-Toraño Martínez (CIEMAT), 2014

INFO MARKS

1. The spectrum files must have "**.txt**" extension.
2. Parameters written in blue are the real fitting parameters.
3. **k** goes from 1 to 'Number of peaks'.
   If there are several peaks, it is necessary to **increase** the number of cells: to the right in 'Initial fitting parameters', and down in 'Fixed parameters'.
   These cells will be added pressing "ADD NEW CELLS".
4. A Region Of Interest (**ROI**) for the fitting process can be selected through "Limits" option.

Figure B.6: Screenshot of the folder "INFO".

Appendix C

DIGDATA tabs

Screenshots of the code DIGDATA are shown as follow. The program consists of five tabs:

- *Decodification*
- *Dead Time Control*
- *Time Histograms*
- *Energy Histograms*
- *Coincidences*

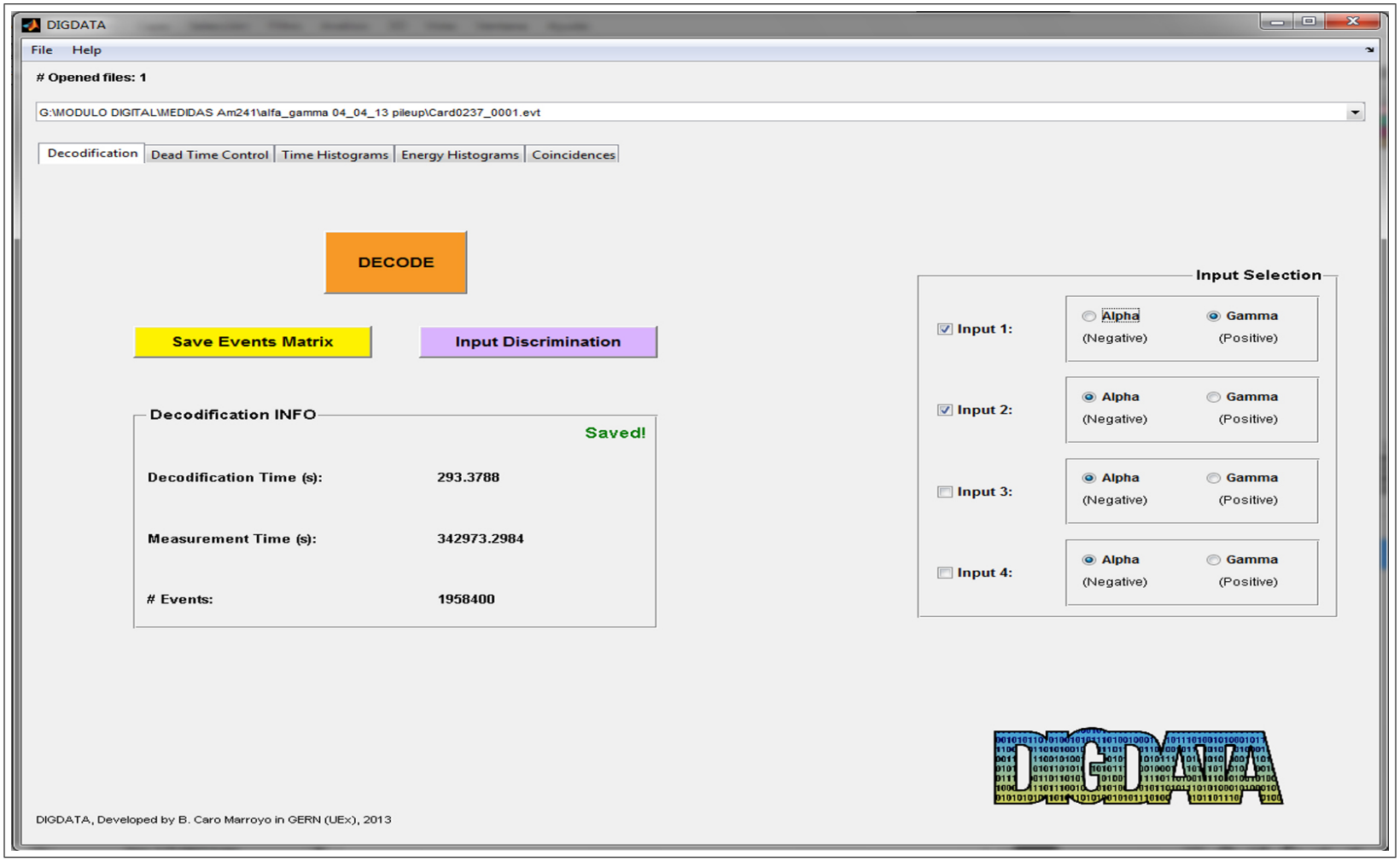

Figure C.1: Screenshot of the "Decodification" tab from DIGDATA.

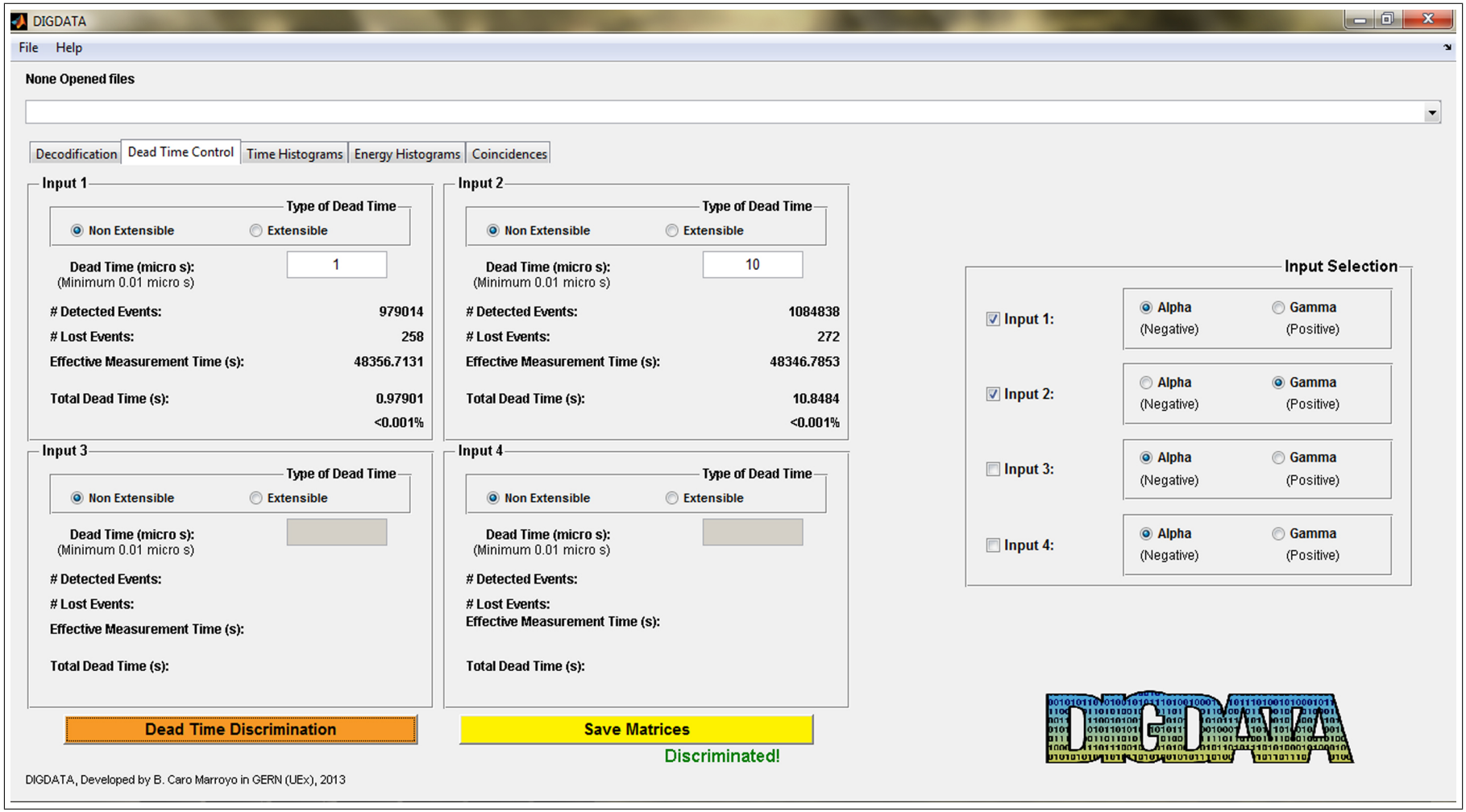

Figure C.2: Screenshot of the "Dead Time Control" tab from DIGDATA.

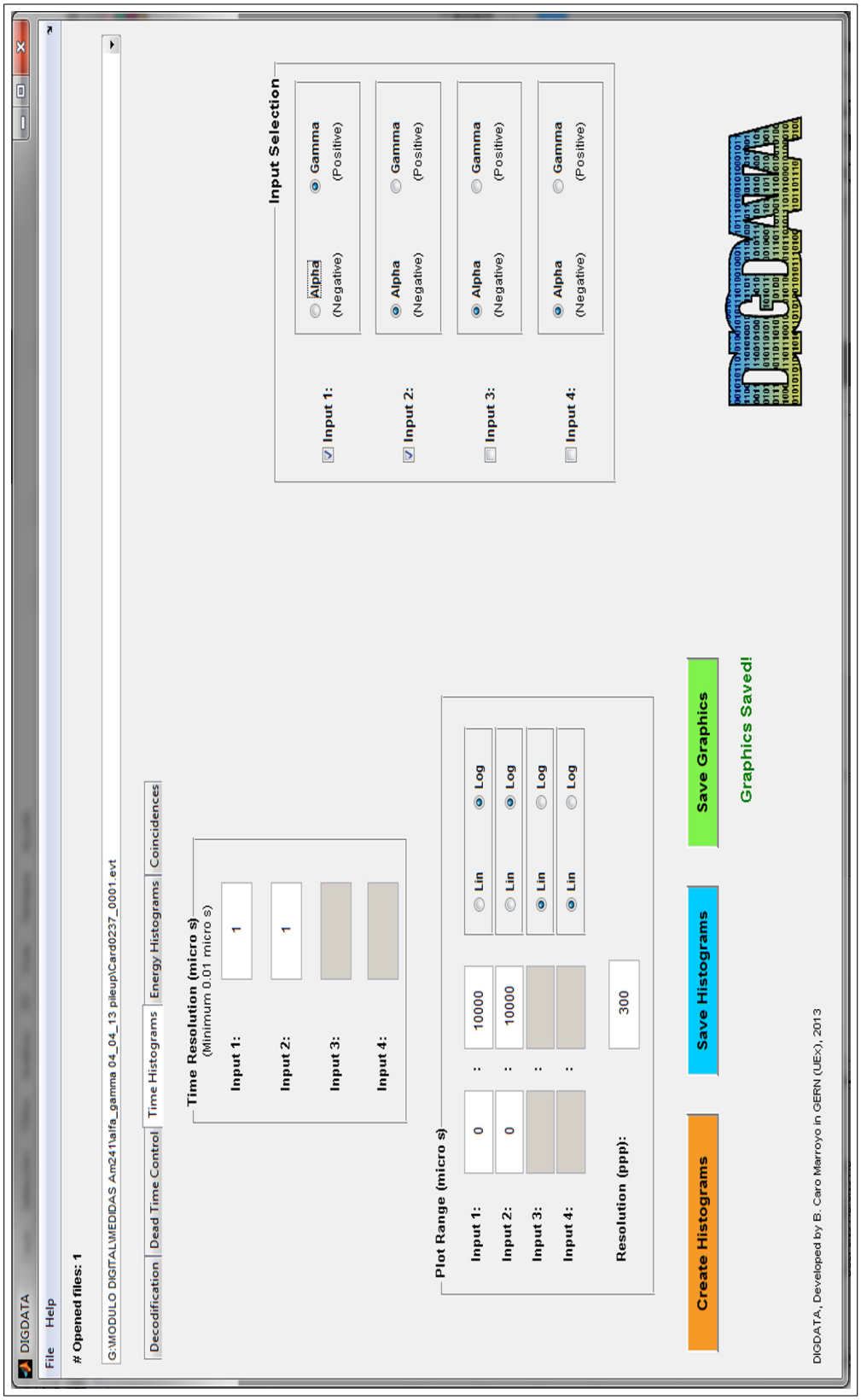

Figure C.3: Screenshot of the "Time Histograms" tab from DIGDATA.

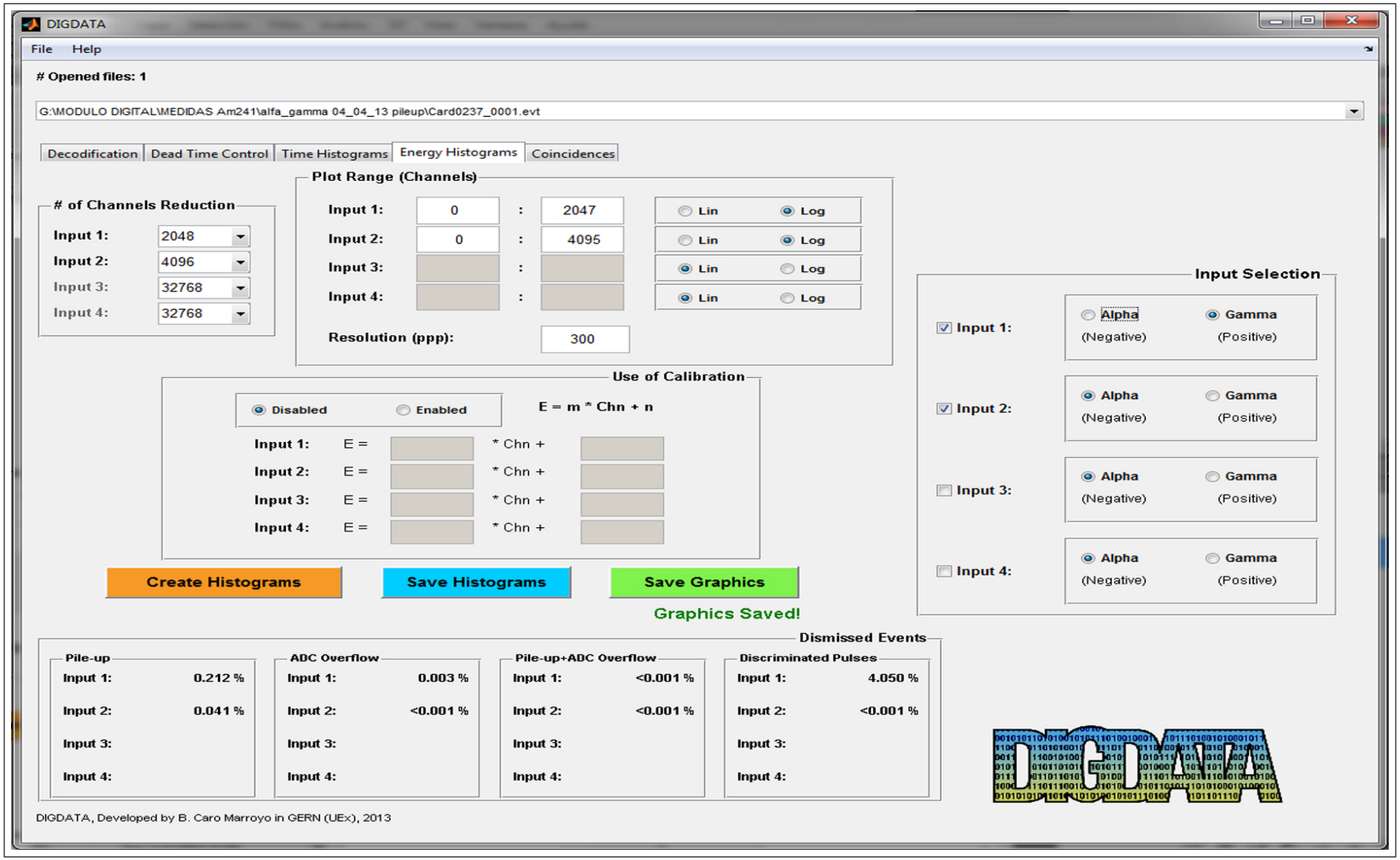

Figure C.4: Screenshot of the "Energy Histograms" tab from DIGDATA.

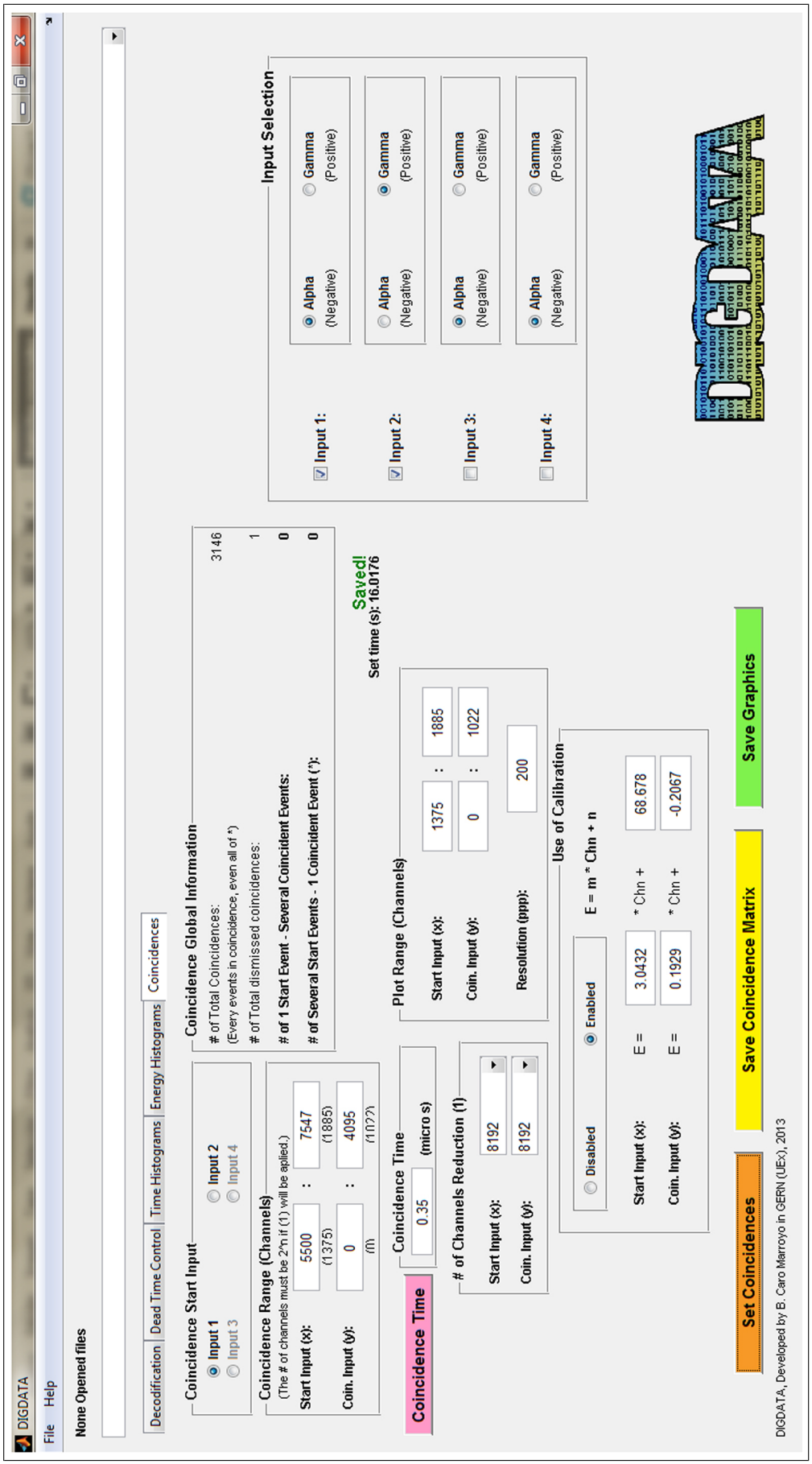

Figure C.5: Screenshot of the "Coincidences" tab from DIGDATA.

Appendix D

TUC parameters

The acquisition software TNT USB Control (TUC) was used to control the digital module and process the pulses. To work in "energy mode", it is necessary to indicate through "Card inputs" in "Parameters of selected card 1/3" (Figure D.1) the following information:

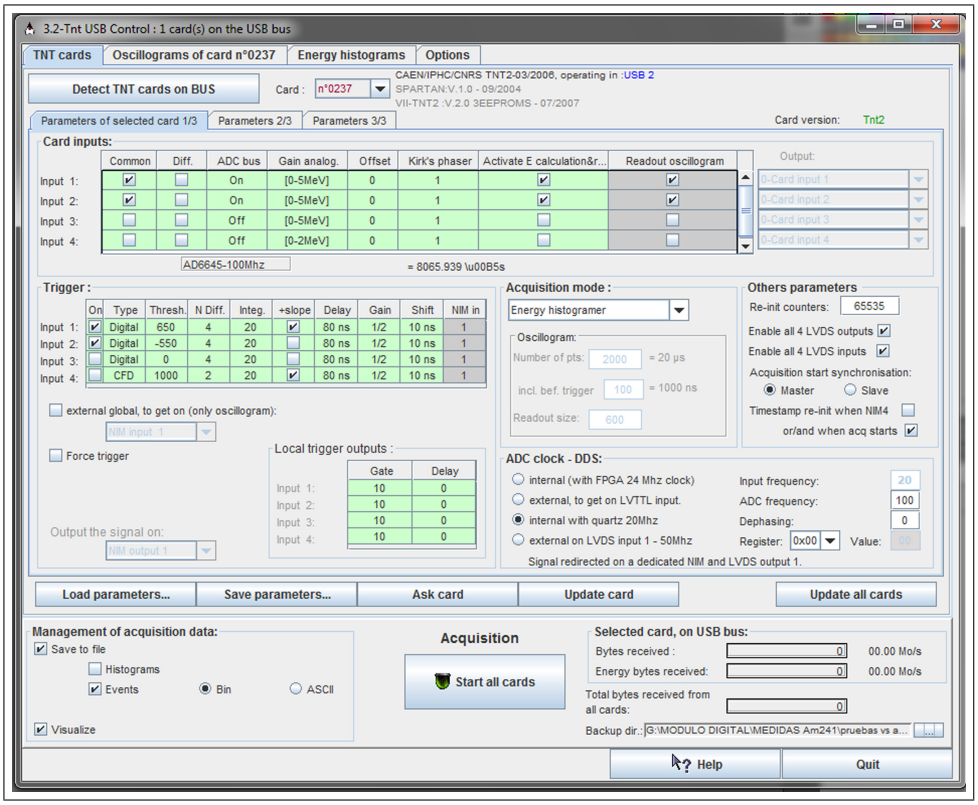

Figure D.1: Screenshot of the "TNT cards" tab of the digital module control software, TUC.

- Use of the "Common" working mode.
- Activation of the corresponding "ADC bus" for the used inputs.

- Analogical gain (in our case, 0-5 MeV).
- Selection of "Activate E calculation & rea..." for each input.

Mainly *trigger* (Figure D.2) and energy calculation (Figure D.3) values have to be optimized to work in energy mode. The most important parameters are described below.

Trigger parameters

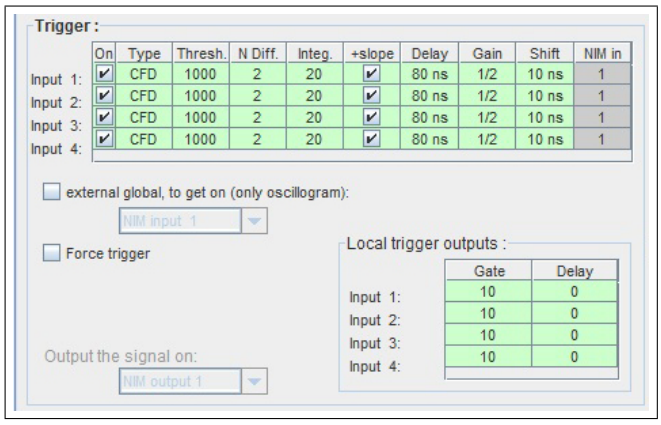

Figure D.2: Trigger parameters from digital module to be optimized.

Type: simple, digital, CFD (Constant Fraction Discriminator) or external. In our case, a digital trigger was used. It compares a reference threshold value with the filtered preamplifier signal [91].

Threshold: it allows to discriminate noise pulses. It must be adjusted in each measurement because it depends on the kind of signal, the number of inputs, etc. On average, a threshold value of +650 for gamma pulses and -650 for alpha pulses were used.

Differentiation constant: using a digital trigger, the preamplifier signal is filtered. In a first step, the pulse is differentiated. The low frequency components are cut out, removing the tail of the preamplifier signal. In order to obtain the differentiated signal, difference between the current point nx and the previous one $nx - N$ is calculated, where N is the "Differentiation constant". In our case, the parameter value was 4 for both kind of signals (alpha and gamma).

Integration constant: the second step is the integration of the differentiated pulse. High frequencies (noise) are removed. The integration constant refers to the number of samples used in the integration process and, in our case, a value of 20 was chosen for both signals.

+Slope: it indicates the polarity of the preamplifier signal, positive (for our gamma pulses) or negative (for our alpha pulses). When the integrated signal crosses the threshold with an specific slope, a trigger is launched by the card.

Parameters for energy calculation

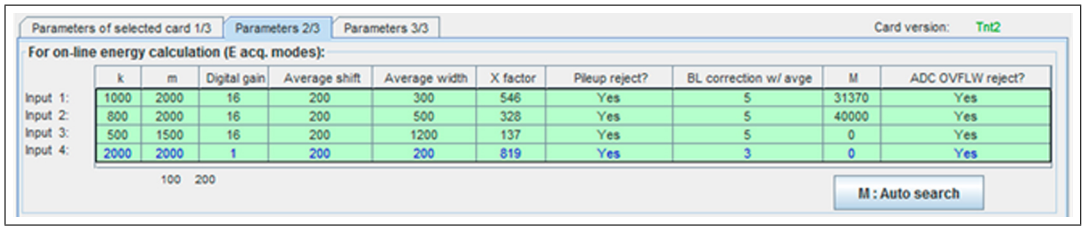

Figure D.3: Trapezoid parameters to be optimized to calculate the height of the registered pulses (proportional to the energy of the detected radiation).

Each time a trigger occurs, the card calculates an average of the trapezoid height which will be proportional to the energy of the detected radiation. This height will be calculated $k + m$ points after the trigger point. The following parameters are essential for the trapezoid height calculation (Figure D.3):

k: it is the trapezoid rise time expressed as sampling periods (10 ns for each period). Values of 800 and 1000 were used for alpha and gamma pulses, respectively.

m: it is the width of the trapezoid flat top expressed as sampling periods. In our case, a value of 2000 was used for both kind of pulses.

Digital gain: it is a parameter which increases the trapezoid height and, hence, pulses are classified in channels corresponded to higher energies. A value of 16 was used for each kind of pulses.

Average shift: value expressed in ns which indicates how many sampling points have to be counted from the beginning of the flat top to start to calculate an average value of the trapezoid height. It must be taken into account that $Shift + width \leq (m - 5)\, sampling\, periods$. The "average shift" was 200 for both kind of pulses.

Average width: parameter expressed in ns which indicates how many sampling points on the flat top will be considered to calculate the average trapezoid height and, therefore, the energy. The greater the "average width", the better the trapezoid height calculation and, hence, the energy. A value of 1400 was used for both kinds of pulses.

X factor: it is some information related to "Average width" but expressed in a more efficient way for the FPGA Virtex 2 in order to operate arithmetic division smoother and rapidly. This parameter is calculated by the program

itself when the "Average width" value is introduced. For both kinds of pulses "X factor" was 117.

Pile-up reject?: the program permits the possibility of reject or not reject pile-up events (being saved in the event file with an especial input number). A pile-up occurs if while the card is constructing the trapezoid, another trigger is detected before the end of the flat top has been reached. Two pile-up situations are possible:

- Both events will be considered as piled-up if the second trigger also occurs before energy related to first trigger has been taken.
- Only the second event will be considered as piled-up if it occurs after the energy related to first trigger has been taken.

In our case, measurements were carried out considering pile-up events. Afterward, during the decodification process and data treatment, the user decides to apply or not event discrimination.

BL correction/w avge: this parameter is necessary to be set to calculate a baseline average taking sampling points outside trapezoid shape. A proper trapezoid height and baseline calculations will allow to suitably classify pulses. A value of 5 was used for both kind of pulses.

M: time decay constant of the detected pulses. This value is calculated using "M: Auto search" (see Figure D.3). Sometimes the value calculated by the program presents problems and the measurement is impossible to be carried out. Then, "M" will have to be slightly modified till measurement is possible. Values of 35580 and 40000 for gamma and alpha signals, respectively, were chosen.

ADC OVFLW reject?: this option allows to remove pulses with amplitudes out of ADCs limits. This option was selected in every measurements. However, against what happened with pile-up events, the digital module does not eliminate all ADC overflow events although the reason is unknown. This fact has been checked with the data treatment software.

List of Figures

List of Tables

Bibliography

[1] G.F. Knoll. *Radiation Detection and Measurement*. John Wiley & Sons Inc., 1999.

[2] S. A. Baranov, V. M. Kulakov, and V. M. Shatinskiĭ. Relative determination of the energy of the most intense groups of α particles of certain isotopes ($T_{1/2} > 50$ years) of heavy elements. *Yad. Fiz. 7 (1968) 727; Sov. J. Nucl. Phys.*, 7(4):442–445, 1968.

[3] I. Ahmad, J. Milsted, R. K. Sjoblom, J. Lerner, and P. R. Fields. Alpha decay of Fm251. *Phys. Rev. C*, 8(2):737–744, 1973.

[4] G. Bertolini. Alpha particle spectroscopy by gridded ionization chamber. *Nucl. Instrum. Methods*, 223(2-3):285–289, 1984.

[5] E. García-Toraño. Current status of alpha-particle spectrometry. *Appl. Radiat. Isot.*, 64(10-11):1273–1280, 2006.

[6] A. Martín Sánchez, C. J. Bland, and A. F. Timón. Computer simulation of backscattered alpha particles. *Appl. Radiat. Isot.*, 52(3):341–346, 2000.

[7] M. Jurado Vargas and A. Fernández Timón. Scattering and self-absorption corrections in the measurement of α-particle emitters in 2π geometry. *Nucl. Instrum. Methods B*, 217(4):564–571, 2004.

[8] M. Jurado Vargas and A. Fernández Timón. Dependence of self-absorption on thickness for thin and thick alpha-particle sources of UO_2. *Nucl. Instrum. Methods A*, 548:432–438, 2005.

[9] G. E. Kocharov and G. A. Korolev. A high-resolution ionization alpha-spectrometer. *Bull. Acad. Sci. USSR, Phys. Ser*, 25:227, 1961.

[10] C. Budtz-Jorgensen and H. H. Knitter. A precise method for charged particle counting employing energy and angle information from gridded ion chambers. *Nucl. Instrum. Methods*, 223:295, 1984.

[11] A. Al-Adili, F. . Hambsch, S. Oberstedt, S. Pomp, and S. Zeynalov. Comparison of digital and analogue data acquisition systems for nuclear spectroscopy. *Nucl. Instrum. Methods*, 624(3):684–690, 2010.

[12] H. Ammi and M. Chekirine. Electronic collimation for precise measurement of resolution, with a gridded ionization chamber. *Vacuum*, 47(1):33–34, 1996.

[13] M. Jurado Vargas and A. Fernández Timón. Study of backscattering in alpha-particle sources with the new code AlfaMC. *Radiat. Phys. Chem.*, 106:199–203, 2015.

[14] E. Steinbauer, P. Bauer, M. Geretschlager, G. Bortels, J. P. Biersack, and P. Burger. Energy resolution of silicon detectors: Approaching the physical limit. *Nucl. Instrum. Methods B*, 85:642–649, 1994.

[15] E. Steinbauer, G. Bortels, P. Bauer, Biersack, J. P. Burger, and P. I. Ahmad. A survey of the physical processes which determine the response function of silicon detectors to alpha particles. *Nucl. Instrum. Methods A*, 339(1-2):102–108, 1994.

[16] E. García-Toraño, M. L. Aceña, G. Bortels, and D. Mouchel. Alpha-particle emission probabilities in the decay of Am243. *Nucl. Instrum. Methods A*, 312:317–322, 1992.

[17] P. Burger, K. De Backker, and W. Schoenmakers. Performance of large area particle detectors spie. *The International Society for Optical Engineering*, 591, 1985.

[18] A. Martín Sánchez, F. Vera Tomé, and C. J. Bland. *Low-level measurements of man-made radionuclides in the environment.* M. García León and G. Madurga. World Scientific, Singapore, 1991.

[19] A. Martín Sánchez, F. Vera Tomé, D. Marzal Cáceres, and C. J. Bland. Experimental study of symmetric and asymmetric peak-fitting parameters for alpha-particle spectrometry. *Nucl. Instrum. Methods A*, A339(1-2):127–130, 1994.

[20] A. Martín Sánchez and D. Cáceres Marzal. Experimental study of the curve-shape variations in alpha-particle spectrometry. *Nucl. Instrum. Methods A*, 414(2-3):265–273, 1998.

[21] B. Caro Marroyo, A. Martín Sánchez, and M. Jurado Vargas. ALFITeX: a new code for the deconvolution of complex alpha-particle spectra. *J. Radioanal. Nucl.Chem.*, 296:1247–1252, 2013.

[22] E. A. Frolov. A precision facility for measuring alpha-particle energies and flux density. *Appl. Radiat. Isot.*, 43(1-2):211–222, 1992.

[23] A. Rytz and R. A. P. Wiltshire. Absolute determination of the energies of alpha particles emitted by ^{236}Pu. *Nucl. Instrum. Methods*, 223(2-3):325–328, 1984.

[24] N. Coron, G. Dambier, G. J. Focker, P. G. Hansen, G. Jegoudez, B. Jonson, J. Leblanc, J. P. Moalic, H. L. Ravn, H. H. Stroke, and O. Testard. A composite bolometer as a charged-particle spectrometer. *Nature*, 314(6006):75–76, 1985.

[25] R.D. Horansky, J.N. Ullom, J.A. Beall, G.C. Hilton, K.D. Irwin, D. E. Dry, E.P Hastings, S. P Lamont, C.R. Rudy, and M.W. Rabin. Superconducting calorimetric alpha-particle sensors for nuclear nonproliferation applications. *Appl. Phys. Lett.*, 93:123504, 2008.

[26] P. C. Ranitzsch, S. Kempf, A. Pabinger, C. Pies, J. . Porst, S. Schfer, A. Fleischmann, L. Gastaldo, C. Enss, Y. S. Jang, I. H. Kim, M. S. Kim, Y. H. Kim, J. S. Lee, K. B. Lee, M. K. Lee, S. J. Lee, W. S. Yoon, and Y. N. Yuryev. Development of cryogenic alpha spectrometers using metallic magnetic calorimeters. *Nucl. Instrum. Methods A*, 652:299–301, 2011.

[27] F. P. Hessberger, S. Hofmann, G. Muenzenberg, K.-. Schmidt, P. Armbruster, and R. Hingmann. Influence of energy summing of α-particles and conversion electrons on the shapes of a-spectra in the region of the heaviest nuclei. *Nucl. Instrum. Methods*, 274(3):522–527, 1989.

[28] J. Paepen, A. Dirican, M. Marouli, S. Pommé, R. Van Ammel, and H. Stroh. A magnet system for the supression of conversions electrons ain alpha spectrometry. *Appl. Radiat. Isot.*, 87:320–324, 2014.

[29] S. Pommé and G. Sibbens. Concept for an off-line gain stabilisation method. *Appl. Radiat. Isot.*, 60(2-4):151–154, 2004.

[30] S. Pommé and G. Sibbens. A new off-line gain stabilization method applied to alpha-particle spectrometry. *Adv. Math. Comput. Tools Metrol.*, VI:327–329, 2004.

[31] P. M. Rubio Montero and E. García-Toraño. Use of discrete Fourier transform to sum spectra in measurements with long counting times. *Nucl. Instrum. Methods A*, 577(3):715–718, 2007.

[32] E. Oran Brigham. *The Fast Fourier Transform.* Prentice-Hall Inc., 1974.

[33] A. L'Hoir. Study of the asymmetrical response of silicon surface barrier detectors to MeV light ions. Application to the precise analysis of light ions energy spectra. I. Helium ions. *Nucl. Instrum. Methods*, 223:336–345, 1984.

[34] W. N. Lennard, H. Geissel, K. B. Winterbon, D. Phillips, T. K. Alexander, and J. S. Forster. Nonlinear reponse of Si detectors for low-Z ions. *Nucl. Instrum. Methods A*, 248(2-3):454–460, 1986.

[35] W. N. Lennard and G. R. Massoumi. Anomalous pulse heights in silicon detectors. *Nucl. Instrum. Methods B*, 48(1-4):47–50, 1990.

[36] P. Bauer and G. Bortels. Response of Si detectors to electrons, deuterons and alpha particles. *Nucl. Instrum. Methods A*, 299:205, 1990.

[37] A. Fernández Timón, M. Jurado Vargas, and A. Martín Sánchez. A method to reproduce alpha-particle spectra measured with semiconductor detectors. *Appl. Radiat. Isot.*, 68(4-5):941–945, 2010.

[38] W. N. Lennard and K. B. Winterbon. Response of silicon detectors to H-1 and He-4 ions. *Nucl. Instrum. Methods B*, 24-25(2):1035–1038, 1987.

[39] E. García-Toraño and M.L. Aceña. GEAL, un programa general para el análisis de espectros alfa. *JEN Report*, (409), 1976.

[40] Trivedi M.P. Least squares analysis of experimental alpha spectra. Technical Report NYO-844-81, USAEC, 1969.

[41] H. Baba. A computer program for alpha spectrum analysis. *Nucl. Instrum. Methods*, 148:173–178, 1978.

[42] Wätzig W. and Westemeier W. ALFUN - a program for the evaluation of complex alpha-spectra. *Nucl. Instrum. Methods*, 153:517–524, 1978.

[43] Basova B.G. et al. Automatic analysis of complex alpha spectra using a computer. *Soviet Radiochemistry*, 21(3):362–367, 1979.

[44] E. García-Toraño and M. L. Aceña. Nolin: Nonlinear analysis of complex alpha spectra. *Nucl. Instrum. Methods*, 185(1-3):261–269, 1981.

[45] G. Bortels and P. Collaers. Analytical function for fitting peaks in alpha-particle spectra from Si detectors. *Int. J. Rad. Appl. Instrum. A*, 38(10):831–837, 1987.

[46] M. J. Koskelo, W. C. Burnett, and P. H. Cable. An advanced analysis program for alpha-particle spectrometry. *Radioactivity Radiochem.*, 7(1):18–26, 1996.

[47] E. García-Toraño. Advances in alpha-, beta and gamma-ray spectrometry. *Proceedings of A Meeting in St. Petersburg*, pages 17–23, 1997.

[48] J. C. Lozano, S. Madruga, and F. Fernández. Function using cubic splines for the analysis of alpha-particle spectra from silicon detectors. *Nucl. Instrum. Methods A*, 449(1):356–365, 2000.

[49] E. García-Toraño. A model shape for the analysis of alpha-particle spectra. *Nucl. Instrum. Methods A*, 498(1-3):289–291, 2003.

[50] R. C. Noy, E. García-Toraño, E. Mainegra, and E. López. The WinALPHA code for the analysis of alpha-particle spectra. *Nucl. Instrum. Methods A*, 525(3):522–528, 2004.

[51] S. Pommé and J. Keightley. *Count rate estimation of a Poisson process: unbiased fit versus central moment analysis of time interval spectra*, volume 945 of *ACS Symposium Series*. 2007.

[52] E. García-Torano. Fitting of low-statistics peaks in alpha-particle spectra. *Nucl. Instrum. Methods A*, A339(1-2):122–126, 1994.

[53] M. A Wolfe. *Numerical Methods for Unconstrained Optimization: An Introduction*. Van Nostrand Reinhold, New York, USA, 1978.

[54] T. Babeliowsky and G. Bortels. ALFA: A program for accurate analysis of complex alpha-particle spectra on a PC. *Appl. Radiat. Isot.*, 44(10-11):1349–1358, 1993.

[55] J. Yang and J. Ni. Analysis technique of multiplet alpha spectra. *Nucl. Instrum. Methods A*, A338(2-3):498–505, 1994.

[56] J. Yang and J. Ni. New data on alpha-particle emission probabilities of several actinide nuclides. *Nucl. Instrum. Methods A*, 413(2-3):239–241, 1998.

[57] E. García-Toraño. A comparative study of minimization methods in the fitting of alpha-particle spectra. *Nucl. Instrum. Methods A*, 369(2-3):608–612, 1996.

[58] A. Martín Sánchez, P. Rubio Montero, and F. Vera Tomé. FITBOR: A new program for the analysis of complex alpha spectra. *Nucl. Instrum. Methods A*, 369(2-3):593–596, 1996.

[59] H. Ruellan, M. C. Lepy, M. Etcheverry, J. Plagnard, and J. Morel. A new spectra processing code applied to the analysis of ^{235}U and ^{238}U in the 60 to 200 keV energy range. *Nucl. Instrum. Methods A*, 369(2-3):651–656, 1996.

[60] A. Martín Sánchez and P. R. Montero. Simplifying data fitting using branching ratios as constraints in alpha spectrometry. *Nucl. Instrum. Methods A*, 420(3):481–488, 1999.

[61] J. C. Lozano and F. Fernández. ALFIT: A code for the analysis of low statistic alpha-particle spectra from silicon semiconductor detectors. *Nucl. Instrum. Methods A*, 413(2-3):357–366, 1998.

[62] K.S. Krane. *Introductory Nuclear Physics*. John Wiley & Sons Inc., 1988.

[63] J.P. Hummel. *Alpha-decay studies in the heavy-element region.* Doctoral Thesis. University of California, 1956.

[64] R. C. Pilger Jr. *Nuclear decay schemes in the actinium family.* Doctoral Thesis. University of California, 1957.

[65] T.F. Wang. Determination of the ^{242}Pu Branching Ratio via Alpha-Gamma Coincidence. *INMM 53rd Annual Meeting*, 2012.

[66] P. C. Simms, N. Benczer-Koller, and C. S. Wu. New application of delayed coincidence techniques for measuring lifetimes of excited nuclear states- Ca^{42} and Sc^{47}. *Phys. Rev.*, 121:1169, 1961.

[67] A. Z. Schwarzschild and E. K. Warburton. The measurement of short nuclear lifetimes. *Annual Review of Nuclear Science*, 18(1):265–290, 1968.

[68] P. J. Campion. The standardization of radioisotopes by the beta-gamma coincidence method using high efficiency detectors. *Appl. Radiat. Isot.*, 4(3-4):232–240, 1959.

[69] A. Gandy. Absolute measurement of the activity of radionuclides by the beta-gamma coincidence method with high efficiency detectors. Study of instrumental coincidences. *Appl. Radiat. Isot.*, 11(2-3):75–91, 1961.

[70] C. Bobin. Primary standardization of activity using the coincidence method based on analogue instrumentation. *Metrologia*, 44:S27–S31, 2007.

[71] Decay Data Evaluation Project. http://www.nucleide.org/nucdata.htm.

[72] E. Flamm and F. Asaro. Perturbation of Alpha Particle-Gamma Ray Angular Correlations in Am^{241},Am^{243}, and Cm^{243}. *Phys. Rev.*, 129:290–296, 1963.

[73] M. Roteta Ibarra. *Determinación de parámetros nucleares mediante técnicas de correlación angular: aplicación a algunos casos prácticos.* Doctoral Thesis. Universidad Complutense de Madrid, 2009.

[74] A. Martín Sánchez and B. Caro Marroyo. Assembly of an alpha-gamma coincidence measuring device for checking alpha decay schemes. *Appl. Radiat. Isot.*, 70(9):2263–2266, 2012.

[75] M. Jurado Vargas, B. Caro Marroyo, and A. Martín Sánchez. Measurements of alpha-gamma coincidences with an optimized dual-parameter multichannel system. *Appl. Radiat. Isot.*, 82(0):308 – 313, 2013.

[76] B. Caro Marroyo, A. Martín Sánchez, and M. Jurado Vargas. Improvements to alpha-particle spectrometry techniques. *Appl. Radiat. Isot.*, 87(0):328 – 330, 2014.

[77] C. Bobin, J. Bouchard, and B. Censier. First results in the development of an on-line digital counting platform dedicated to primary measurements. *Appl. Radiat. Isot.*, 68(7-8):1519–1522, 2010.

[78] C. Bobin, J. Bouchard, S. Pierre, and C. Thiam. Overview of a FPGA-based nuclear instrumentation dedicated to primary activity measurements. *Appl. Radiat. Isot.*, 70(9):2012–2017, 2012.

[79] J. Keightley and T. S. Park. Digital coincidence counting for radionuclide standardization. *Metrologia*, 44(4):S32–S35, 2007.

[80] E. García-Toraño, T. Durán Ramiro, C. Burgos, and M. Begoña Ahedo. Defined solid angle counter with variable geometry. *Appl. Radiat. Isot.*, 2008.

[81] S. Pommé and G. Sibbens. Alpha-particle counting and spectrometry in a primary standardisation laboratory. *Acta Chimica Slovenica*, 55(1):111–119, 2008.

[82] G. Sibbens, S. Pommé, T. Altzitzoglou, E. García-Toraño, H. Janßen, R. Dersch, O. Ott, A. Martín Sánchez, M. P. Rubio Montero, M. Loidl, N. Coron, P. de Marcillac, and T. M. Semkow. Alpha-particle emission probabilities in the decay of ^{240}Pu. *Appl. Radiat. Isot.*, 68(7-8):1459–1466, 2010.

[83] N. A. Cornejo Díaz, A. Martín Sánchez, and J. de la Torre Pérez. SOLANG: A user-friendly code to calculate the geometry factor using Monte Carlo simulations. Application to alpha-particle spectrometry. *Appl. Radiat. Isot.*, 69(5):822–824, 2011.

[84] A. Martín Sánchez, M.J. Nuevo, M. Jurado Vargas, J. Díaz Bejarano, M.F. da Silva, C. Roldán García, A. Paúl, J.L. Ferrero Calabuig, A. Méndez Vilas, and D. Juanes Barber. Application of atomic and nuclear techniques to the study of inhomogeneities in electrodeposited α-particle sources. *Nucl. Instrum. Methods B*, 190(14):747 – 750, 2002.

[85] G. Bortels, D. Mouchel, R. Eykens, E. García-Toraño, M.L. Aceña, R.A.P. Wiltshire, M. King, A.J. Fudge, and P. Burger. Alpha-particle emission probabilities in the decay of ^{237}Np. *Nucl. Instrum. Methods A*, 295(12):199 – 206, 1990.

[86] K. Breitenecker, D. Donohue, H. Eisenwagner, A.P. Maddison, and H. Siegmund. Configuration of an alpha-gamma coincidence spectrometer for utilization of safeguards measurements. *Appl. Radiat. Isot.*, 67:2088–2091, 2009.

[87] B. Caro Marroyo. *Medidas de radiaciones alfa y gamma en coincidencia.* Trabajo de Grado de Licenciatura en Física. Facultad de Ciencias, Universidad de Extremadura, Spain, 2012.

[88] N. A. Cornejo Díaz and M. Jurado Vargas. DETEFF: An improved Monte Carlo computer program for evaluating the efficiency in coaxial gamma-ray detectors. *Nuclear Inst.and Methods A*, 586(2):204–210, 2008.

[89] M. Richer and C. Santos. *TNT2 Digital Pulse Processor Funcionalities & TUC control software.* Institut Pluridisciplinaire Hubert Curien, Université de Strasbourg, France, 2007.

[90] L. Arnold, R. Baumann, E. Chambit, M. Filliger, C. Fuchs, C. Kieber, D. Klein, P. Medina, C. Parisel, M. Richer, C. Santos, and C. Weber. TNT digital pulse processor. *IEEE Transactions on Nuclear Science*, 53(3):723–728, 2006.

[91] M. Lauer. *Digital Signal Processing for segmented HPGe detectors. Preprocessing algorithms and pulse shape analysis.* Doctoral Thesis. Ruprecht-Karls-Universität Heidelberg, Germany., 2004.

[92] V. T. Jordanov and G. F. Knoll. Digital synthesis of pulse shapes in real time for high resolution radiation spectroscopy. *Nucl. Instrum. Methods A*, 345(2):337–345, 1994.

[93] A. Doehring, S. Kalbitzer, and W. Melzer. On the ballistic deficit and the signal-to-noise ratio of semiconductor spectrometers for energy and position spectroscopy. *Nucl. Instrum. Methods*, 59(1):40–44, 1968.

[94] F. S. Goulding and D. A. Landis. Ballistic deficit correction in semiconductor detector spectrometers. *IEEE Transactions on Nuclear Science*, 35(1), 1987.

[95] A. L'Hoir. *Thèse 3ème cycle*, volume Unpublished. 1975.

[96] A. L'Hoir, C. Cohe, and G. Amsel. volume 2. Proc. Int. Conf. on Ion Beam Surface Layer Analysis, Karlsruhe, Germany, Sept. 15-19, 1975, 1976.

[97] G. Amsel, C. Cohe, and A. L'Hoir. volume 2. Proc. Int. Conf. on Ion Beam Surface Layer Analysis, Karlsruhe, Germany, Sept. 15-19, 1975, 1976.

[98] W.H. Press, S.A. Teukolsky, W.T Vetterling, and B.P. Flannery. *Numerical recipes in Fortran 77: the art of scientific computing (Vol. 1 of Fortran numerical recipes).* Cambridge University Press, 1997.

[99] S. Brandt. *Statistical and Computational Methods in Data Analisis.* North-Holland, Amsterdam, Netherlands, 1989.

[100] J. C. Lozano and F. Fernández. Application of singular value decomposition to the analysis of alpha-particle spectra. *Nucl. Instrum. Methods*, 413(2-3):233–238, 1998.

[101] A. Martín Sánchez, F. Vera Tomé, and J. Díaz Bejarano. Constraints on uncertainties and their application to the emission probabilities of alpha-particles. *Nucl. Instrum. Methods A*, 340:509, 1994.

[102] Table of Radioactive Isotopes. http://ie.lbl.gov/education/isotopes.htm.

[103] E. García-Toraño, M. L. Aceña, G. Bortels, and D. Mouchel. Alpha-particle emission probabilities in the decay of ^{239}Pu. *Nuclear Inst.and Methods A*, 334(2-3):477–484, 1993.

[104] E. García-Toraño, M. T. Crespo, M. Roteta, G. Sibbens, S. Pommé, A. M. Sánchez, M. P. R. Montero, S. Woods, and A. Pearce. α-particle emission probabilities in the decay of ^{235}U. *Nucl. Instrum. Methods A*, 550(3):581–592, 2005.

[105] T. Mukoyama. Fitting of Gaussian to peaks by non-iterative method. *Nucl. Instrum. Methods*, 125(2):289–291, 1975.

[106] W. Zimmermann. Evaluation of photopeaks in scintillation gamma-ray spectroscopy. *Review of Scientific Instruments*, 32(9):1063–1065, 1961.

[107] S. Pommé and B. Caro Marroyo. Improved peak shape fitting in alpha spectra. *Appl. Radiat. Isot.*, 96:148–153, 2015.

[108] E. Browne. *Nucl. Data Sheets*, 109:2657, 2008.

[109] V. P. Chechev. The evaluation of ^{238}Pu, ^{240}Pu, and ^{242}Pu Decay Data. *Proc. Intern. Conf. Nuclear Data for Science and Technology, Santa Fé, New Mexico, 26 September-1 October 2004*, pages 91–94, 2005.

[110] A. Lorenz. Decay data of the transactinium nuclides. *IAEA Tech. Rep.*, (261):75–76, 1986.

[111] M. A. Kellett. Summary report of the first research coordination meeting on updated decay data library for actinides. *17-19 October 2005, IAEA Report*, (INDC(NDS)-0479), 2006.

[112] M. A. Kellett. Summary report of the second research coordination meeting on updated decay data library for actinides. *28-30 March 2007, IAEA Report*, (INDC(NDS)-0508), 2007.

[113] M.A. Kellett, F.G. Kondev, and A.L. Nichols. IAEA coordinated research project: Updated decay data library for actinides. *Appl. Radiat. Isot.*, 66(67):694 – 700, 2008.

[114] M. A. Kellett. Summary report of the third research coordination meeting on updated decay data library for actinides. *8-10 October 2009, IAEA Report*, (INDC(NDS)-0539), 2009.

[115] E. Browne, M. M. Bé, T. D. MacMahon, and R. G. Helmer. Report on the Activities of the Decay Data Evaluation Project (DDEP). *CEA Report*, CEA-R-5990(E), 2001.

[116] M. A. Kellett. Assessment of actinide decay data evaluations: Findings of an IAEA coordinated research project. *Appl. Radiat. Isot.*, 70(9):1919–1923, 2012.

[117] F. Asaro. *The complex alpha spectra of the heavy elements*. PhD Thesis, Univ. of California, Livermore, CA, Report UCRL-2180, 1953.

[118] L. M. Kondratev, G. I. Novikova, Y. P. Sobolev, and L. L. Goldin. Alpha decay of ^{240}Pu. *Zh. Eksp. Teor. Fiz. 31 (1956) 771; Sov. Phys. JETP*, 4(5):645–647, 1956.

[119] S. A. Baranov, A. G. Zelenkov, and V. M. Kulakov. Experimental investigation of α decay of actinoid elements (current state of results on α decay). *Sov. At. Energy*, 41(5):987–992, 1976.

[120] Y. A Ellis and R. L. Haese. *Nucl. Data Sheets*, 21:621–626, 1977.

[121] R. Vaninbroukx, G. Bortels, and B. Denecke. Alpha-particle and gamma-ray emission probabilities in the decay of ^{242}Pu. *Appl. Radiat. Isot.*, 37(12):1167–1172, 1986.

[122] A. Rytz. Recommended energy and intensity values of alpha particles from radioactive decay. *At. Data. Nucl. Data Tables*, 47(2):205–239, 1991.

[123] S. Pommé, E. García-Toraño, M. Marouli, M.T. Crespo, V. Jobbágy, R. Van Ammel, J. Paepen, and H. Stroh. High-resolution alpha-particle spectrometry of ^{238}U. *Appl. Radiat. Isot.*, 87:315 – 319, 2014.

[124] L.R. dos Santos, M.E. Sbampato, and A.M. dos Santos. Characterization of electrodeposited uranium films. *J. Radioanal. Nucl.Chem.*, 261(1):203–209, 2004.

[125] E. Browne, M.M. Bé, and R. G. Helmer. ^{243}Am - Comments on evaluation of decay data. *Decay Data Evaluation Project*, 2009.

[126] F. Asaro, F. S. Stephens, J. M. Hollander, and I. Perlman. Anomalous Electric Dipole Conversion Coefficients in Odd-Mass Isotopes of the Heavy Elements. *Phys. Rev.*, 117:492–505, 1960.

[127] J. R. Van Hise and D. Engelkemeir. Alpha Decay of ^{243}Am. *Phys. Rev.*, 171:1325–1330, 1968.

[128] B. M. Aleksandrov, O. I. Grigor'ev, and N. S. Shimanskaya. LX AND γ EMISSION OF ^{243}Am. *Sov. J. Nucl. Phys.*, 70:8–9, 1969.

[129] I. Ahmad and M. Wahlgren. Long-lived standards for the efficiency calibration of Ge(Li) detectors. *Nucl. Instrum. Methods*, 99:333 – 337, 1972.

[130] J. C. Pate, K. R. Baker, and R. W. Fink. A $\gamma\gamma$ Coincidence Study of Transitions in ^{239}Np and ^{239}Pu from Decay of ^{243}Am. *Z. Phys. A.*, 272:169 – 174, 1975.

[131] I. Ahmad. Alpha-emitting nucleides as absolute efficiency calibration sources for germanium detectors. *Nucl. Instrum. Methods*, 193:9 – 13, 1982.

[132] R. Vaninbroukx, G. Bortels, and B. Denecke. Alpha-Particle-Emission Probabilities in the Decay of ^{234}U and Photon-Emission Probabilities in the Decays of ^{234}U, ^{239}Np and ^{243}Am. *Int. J. Appl. Radiat. Isot.*, 35(12):1081–1087, 1984.

[133] S. A. Woods, D. H. Woods, M. J. Woods, S. M. Jerome, M. Burke, N. E. Bowles, S. E. M. Lucas, and C. Paton Walsh. Standardisation and measurement of the decay scheme data of ^{243}Am and ^{239}Np. *Nucl. Instrum. Methods A*, 369:472 – 476, 1996.

[134] D. Sardari, T. D. Mac Mahon, and S. P. Holloway. ^{239}U and ^{243}Am decay data. *Nucl. Instrum. Methods A*, 369:486 – 490, 1996.

[135] D. I. Starozhukov, Y. S. Popov, and P. A. Privalova. *At. Energy*, 42:319 – 321, 1977.

[136] Y. S. Popov, D. I. Starozhukov, V. B. Mishenev, P. A. Privalova, and A. I. Mishchenko. *At. Energy*, 46:111 – 113, 1979.

[137] D. Engelkemeir. ^{243}Am α decay: Multipolarity of γ transitions. *Phys. Rev.*, 181:1675–1681, 1969.

[138] H. Mast, R. Eykens, J. Pauwels, and C. Wagemans. ^{243}Am targets for nuclear fission experiments: Requirements and realisation. *Nucl. Instrum. Methods A*, 282(1):107 – 109, 1989.

[139] M.Jurado Vargas, A. Fernández Timón, E. García-Toraño, and A Martín Sánchez. Application of ion transport simulation to the backscattering in α-particle sources. *Nucl. Instrum. Methods B*, 213:129 – 133, 2004.

[140] A. Fernández Timón and M. Jurado Vargas. Dependence of α-particle backscattering on energy and source backing. *Nucl. Instrum. Methods A*, 580(1):350 – 353, 2007.

[141] F. J. Schima and D.D. Hoppes. Tables for cascade-summing corrections in gamma-ray spectrometry. *Int. J. Appl. Radiat. Isot.*, 34 (8):1109–1114, 1983.

[142] M. Roteta and E. García-Toraño. An evaluation of the influence of $\gamma - \gamma$ angular correlation on the coincidence-summing corrections in γ-ray spectrometry. *Nucl. Instrum. Methods A*, 369:665 – 670, 1996.

[143] M.J. Berger, J.H. Hubbell, S.M. Seltzer, J. Chang, J.S. Coursey, R. Sukumar, D.S. Zucker, and K. Olsen. XCOM: Photon Cross Section Database (version 1.5). *National Institute of Standards and Technology, Gaithersburg, MD, USA*, http://physics.nist.gov/xcom, 2010.

[144] K. Peräjärvi, J. Turunen, S. Ihantola, V. Kämäräinen, S. Pommé, R. Pöllänen, T. Siiskonen, H. Sipilä, and H. Toivonen. Feasibility of conversion electron spectrometry using a Peltier-cooled silicon drift detector. *J. Radioanal. Nucl.Chem.*, 299:229–234, 2014.

[145] M. Marouli, S. Pommé, V. Jobbágy, R. Van Ammel, J. Paepen, H. Stroh, and L. Benedik. Alpha-particle emission probabilities of ^{236}U obtained by alpha spectrometry. *Appl. Radiat. Isot.*, 87:292–296, 2014.

[146] T.M. Semkow, A. J. Khan, D. K. Haines, A. Bari, G. Sibbens, S. Pommé, S. E. Beach, I. AlMahamid, and G. L. Beach. *Alpha Spectrometry of Thick Samples for Environmental and Bioassay Monitoring.* Nuclear Energy and the Environment, ACS Symposium Series, Vol. 1046, 2010.

[147] S. Pommé. Typical uncertainties in alpha-particle spectrometry. *Metrologia*, In press.

[148] G. Sibbens. Uncertainty assessment in the analysis of alpha-particle spectra. *Appl. Radiat. Isot.*, 49(9-11):1241–1244, 1998.

[149] S. Ihantola, A. Pelikan, R. Pöllänen, and H. Toivonen. Advanced alpha spectrum analysis based on the fitting and covariance analysis of dependent variables. *Nucl. Instrum. Methods A*, 656:55–60, 2011.

[150] R. Pöllänen and T. Siiskonen. Unfolding alpha-particle energy spectrum from a membrane air filter containing radon progeny. *Radiat. Meas.*, 70:15–20, 2014.